ADDIS ABABA UNIVERSITY

COLLEGE OF TECHNOLOGY AND BUILT ENVIRONMENT

School of Civil and Environmental Engineering

Water Resource Engineering and Management Stream

Integrated Three-Layer Groundwater Flow Modeling for Resource Assessment and Management for Part of the Upper Awash Basin, Central Ethiopia

Ephrem Tadesse Tagegne

Addis Ababa, Ethiopia
March 2026

ADDIS ABABA UNIVERSITY

COLLEGE OF TECHNOLOGY AND BUILT ENVIRONMENT

School of Civil and Environmental Engineering

Water Resource Engineering and Management Stream

Integrated Three-Layer Groundwater Flow Modeling for Resource Assessment and Management for Part of the Upper Awash Basin, Central Ethiopia

Ephrem Tadesse Tagegne

A Dissertation Submitted to Addis Ababa University, College of Technology and Built Environment, School of Civil and Environmental Engineering, PhD Program in Water Resources Engineering and Management (Specialization in Groundwater Engineering and Management)

March 2026

Declaration

I, the undersigned, declare that this dissertation has been composed solely by me and that it has not been submitted, in whole or in part, in any previous application for a degree or any other qualification. Except where duly stated by references or acknowledgments, the work presented in this dissertation is entirely my own.

This Dissertation has been submitted for examination with my approval as the student's supervisor.

Author: Signature Date

Ephrem Tadesse Tagegne ________________ ______________

Witnessed by:

Main Advisor:

Tilahun Azagegn (Associate Professor) _______________ ______________

Co-advisor:

Taye Alemayehu (Associate Professor) ________________ ______________

DOCTORAL DISSERTATION APPROVAL SHEET

Addis Ababa University

College of Technology and Built Environment

School of Civil and Environmental Engineering

Water Resource Engineering and Management Stream

This is to certify that the dissertation prepared by Ephrem Tadesse, entitled as "**Integrated Three-Layer Groundwater Flow Modelling for Resource Assessment and Management for Part of the Upper Awash Basin, Central Ethiopia**" and submitted in partial fulfillment of the requirements for the Degree of Doctor of Philosophy (PhD) in Water Resources Engineering and Management (Specialization in Groundwater Engineering and Management) complies with the regulations of the University and meets the accepted standards for originality and quality.

Ephrem Tadesse Tagegne ____________ Date: March 2026

APPROVED BY THE BOARD OF EXAMINERS

Name	Signature	Date
Dr. Tilahun Azagegn (Main Advisor)		19/03/2026
Dr. Taye Alemayehu (Co-Advisor)		23/3/2026
Dr. Dessie Nedaw (Internal Examiner)		19 March 2026
Prof. Seifu Kebede (External Examiner)		16 March 2026
Dr. Ing. Yenesew Mengiste (Dean, SCEE and Chairperson)		08 Mar 2026

Abstract

Integrated Three-Layer Groundwater Flow Modelling for Resource Assessment and Management for Part of the Upper Awash Basin, Central Ethiopia

Ephrem Tadesse

Addis Ababa University, 2026

Effective management of future groundwater resources relies on mathematical models. This study presents a three-layer groundwater flow model for a segment of the Upper Awash Basin, aimed at identifying aquifers suitable for long-term use without significant depletion. Additionally, it offers a framework applicable to similar wellfields or areas. The model incorporates a variety of datasets, including measurements of ^{222}Rn and Electrical Conductivity, resistivity soundings, hydrochemical and isotopic data, as well as streamflow records from 11 gauging stations collected over periods spanning 8 to 20 years. Four primary aquifer units have been identified through geological and hydrogeological assessments: the superficial deposit aquifer, the fractured Rift basalt aquifer, the acidic rock units (aquiclude), and the confined scoriaceous basalt aquifer. The superficial deposits and Rift basalt aquifers (layer 1) receive recharge from precipitation and nearby streams, characterized by mixed $CaHCO_3$ or $CaMgHCO_3$ water types with low TDS (< 200 mg/l), a high Ca^{2+}/Na^{+} ratio (> 5), a low residual alkalinity (RA) (< 2.0), enriched isotopic signatures, and a high deuterium excess of 13.3. Conversely, the confined scoriaceous basalt aquifer (layer 3) is replenished by groundwater flow from the adjacent Muger Watershed, part of the Blue Nile Basin, as well as from surrounding highlands or escarpments. This is demonstrated by a high lineament density ranging from 0.96 to 3.0 km/km^2, high TDS (> 468 mg/l), a $NaHCO_3$ water type, a low Ca^{2+}/Na^{+} ratio (< 1.0), a high residual alkalinity (RA > 2.0), significantly depleted isotopic signals, and a low deuterium excess of less than 11. The headwaters of both basins, parts of the Upper Awash and Blue Nile Basins, are closely linked to aquifers, as evidenced by high ^{222}Rn and BFI values. The southern and southeastern areas act as the primary groundwater outlet zones, exhibiting very high ^{222}Rn levels (ranging from 400 to 1467 Bq/m^3) and BFI values (between 0.35 and 0.5). In contrast, the central plain area shows minimal connection with values (^{222}Rn < 100 Bq/m^3) and correspondingly low BFI values. Recharge rates calculated using the WTF and Darcy methods are 47.4 mm/y for the unconfined aquifer and 59.2 mm/y for the confined aquifer. The model area spans 3,440 km² and features a three-layer aquifer system composed of 113,825 active grid cells of 500 m x 500 m each. Utilizing Visual MODFLOW Flex, the model uses hydrogeological conditions of the year 2025 and projects stress-based scenario simulations extending to 2055 to assess system dynamics for management purposes. Calibration, achieved through a trial-and-error approach, exhibited a high degree of accuracy (RMS error: 9.16, mean residual: 0.81 m, R^2: 0.99). A water balance analysis confirmed a state of equilibrium between inflows and outflows. Sensitivity analysis indicated that the unconfined aquifer is particularly sensitive to changes in hydraulic conductivity and recharge, while the confined aquifer responds to fluctuations in hydraulic conductivity and flux. Scenario-based simulations after a steady-state calibration were conducted to assess aquifer responses to various scenarios, including drought, pumping, and injection. During drought conditions, recharge and flux were reduced by 50%, resulting in groundwater level declines of 25.8 meters in the unconfined aquifer and 4.3 meters in the confined aquifer. While river leakage inflow increased by 10.5%, outflows decreased by 43%. In the pumping scenarios, which involved the use of 100 and 150 boreholes at a rate of 50 l/s, the unconfined aquifer experienced drawdowns of 50 and 85 meters, respectively. Meanwhile, the confined aquifer experienced more modest declines of 2 and 4.2 meters. River discharge was reduced by 23.3%, while inflows saw an increase of 16.13%. In the fourth scenario, simulations involving the injection of water through 50 hypothetical deep wells, with varied daily injection volumes, resulted in an increase in groundwater levels by 1.05 to 4.45 meters. The water balance results indicated that higher injection rates enhanced groundwater outflow to rivers while concurrently reducing river leakage into the aquifer. The model simulations indicate that the regional confined aquifer (layer 3) can sustain long-term water withdrawals while ensuring groundwater stability and preserving its hydraulic properties. This study's model provides a framework for evaluating other wellfields, promoting sustainable resource management, and assisting policymakers in making informed decisions to safeguard the aquifer from long-term depletion.

Keywords

Part of the Upper Awash Basin, hydro-lithostratigraphy, Aquifers, Recharge area, Aquifer-surface water interaction, three-layer, Groundwater flow modelling, Ethiopia

Acknowledgment

First and foremost, I express my deepest gratitude to the Almighty God for his blessings and strength that have guided me throughout this journey.

I am deeply thankful to Addis Ababa University and the Ethiopian Institute of Water Resources for allowing me to pursue my PhD. I also sincerely appreciate the Ethiopian Engineering Corporation, Water and Energy Sector, for their logistical assistance and provision of data. Additionally, I am grateful to the Ministry of Water and Energy, the National Meteorological Agency, private firms, and individuals for their invaluable contributions.

I extend my deepest gratitude to my advisor, Dr. Tilahun Azagegn, for his invaluable guidance, expertise, and unwavering patience throughout this journey. His insightful contributions have shaped this dissertation and greatly enhanced my academic growth. From shaping ideas to finalizing manuscripts, his support has been instrumental in the success of this work. I sincerely thank my co-advisor, Dr. Taye Alemayehu, for his time, expertise, and invaluable contributions in refining manuscripts and this PhD thesis. His guidance has been instrumental in shaping the quality of this work. I also extend my deepest gratitude to Mr. Engida Zemedagegnehu, a passionate and dedicated hydrogeologist, for his generosity in sharing fundamental insights into Ethiopia's hydrogeology.

I also acknowledge my colleagues, particularly Dr. Endaweke Asegid, Mr. Adisu Deresa, and Mr. Ashebir Gebre, whose stimulating discussions, collaboration, and friendship have enriched my academic experience. Their invaluable support in the modeling work and problem-solving alongside me has been instrumental in shaping this research.

Finally, I extend my deepest gratitude to my lovely wife, Dr. Sosina Gebremichael, whose unwavering love, support, and encouragement have been my greatest source of strength. Her belief in me has carried me through every challenge. To my three wonderful children, Kidus, Tsion, and Barok, your joy and inspiration have been my driving force, motivating me to persevere even in the most difficult times.

Table of contents

List of Figures

List of Figures (Cont'd)

List of Figures (Cont'd)

List of Tables

List of Tables (Cont'd)

Acronyms and Abbreviations

AAWSA	Addis Ababa Water Supply and Sewerage Authority
BFI	Baseflow index
BH	Borehole
Bq/m^3	Becquerel per cubic meter
EC	Electrical Conductivity
ECDSWCO	Ethiopian Construction Design Supervision Works Corporation
EEA	European Economic Area
FAO	Food and Agricultural Organization
GIS	Geographic Information System
GPS	Global Positioning System
IAEA	International Atomic Energy Agency
IRIS	Information Research Inquiry System
L/s	Liter per second
LMWL	Local Meteoric Water Line
LSC	Liquid Scintillation Counting
LULC	Land use / Land cover
m.a.s.l	meter above sea level
m.b.g.l	meter below ground level
m/d	meter per day
m^3/d	Cubic meter per day
Ma	Millions of years ago
MCM/y	Millions of cubic meters per year
MER	Main Ethiopian Rift
MKm^3	Millions cubic kilometers
mm/y	millimeter per year
MoWE	Ministry of Water and Energy
NMA	National Meteorological Agency
NW-SE	Northwest-Southeast
PCi/L	Picocuries per liter
RAP	River Analysis Package
TDS	Total Dissolved Solids
UN	United Nations
UNESCO	United Nations Educational, Scientific, and Cultural Organization
UNICEF	United Nations International Children's Emergency Fund
WEDSWS	Water and Energy Design Supervision Works Sector
WHO	World Health Organization
WTF	Water Table Fluctuation
WWDSE	Water Works Design and Supervision Enterprise
µS/cm	Micro Siemens per centimeter
ρ_{app}	Apparent resistivity

List of Appendices

1. INTRODUCTION

1.1 Background

Groundwater, the largest freshwater resource on Earth, is vital as a climate-resilient water supply for drinking, industry, and agriculture that sustains economies (Müller Schemed et al., 2021). It is preferred as the best alternative to surface water because it naturally filters as it percolates through layers of rock and soil, is resilient to seasonal fluctuations, sustains Baseflow in rivers and wetlands, and requires less costly regulation infrastructure than surface water (Zektser & Everett, 2004; MacDonald et al., 2021).

Groundwater is a crucial water source for many cities and towns worldwide (European Commission, 2008; Dieter et al., 2018). It is the sole water source in countries like Denmark, Malta, and Saudi Arabia. Furthermore, it meets over 70% of the water needs in nations such as the Netherlands, Germany, and Austria, and approximately 80% in Tunisia and Morocco. Groundwater is also heavily utilized for agriculture, with 45% usage in the U.S. and up to 67% in Algeria. Many European cities, including Rome and Budapest, rely entirely on groundwater for municipal drinking and domestic water. Cities like Amsterdam and Brussels depend on it for more than half of their water consumption (EEA, 2019; UN/UNESCO, 2022).

Groundwater resources in Africa are crucial for socioeconomic development (Grey & Sadoff, 2007; Foster et al., 2012). Hydrogeological studies indicate that Africa has significant groundwater reserves, with an estimated total storage of around 0.66 Million cubic kilometers (Mkm^3) (MacDonald et al., 2012; World Bank, 2018a; MacAllister et al., 2020). While climate change may impact surface water, it is unlikely to affect groundwater negatively, as recharge relies on strong rainfall events expected to increase in frequency (Cuthbert et al., 2019a).

Africa is expected to increasingly rely on groundwater as a reliable source of water supply (Giordano, 2009; MacDonald & Calow, 2009; UNEP, 2010; Gaye & Tindimugaya, 2019). However, the sub-regions that stand to benefit the most from groundwater resources will differ due to variations in recharge rates, aquifer storage, and aquifer permeability. Important factors such as aquifer storage, recharge capacity, and the resilience of groundwater systems to climate change will all play vital roles in determining future water security. Besides, Sub-Saharan Africa has much potential for developing groundwater, but several challenges prevent its regular use. Many of these problems are similar across countries, with the main issue being that policymakers do not pay enough attention to groundwater (WHO/UNICEF, 2021). Even though some nations around the world started creating hydrogeological maps and groundwater databases in the 1970s and 1980s, these are still rare in Africa, including Ethiopia. Only a few countries regularly check the quality and amount of their groundwater, which is an important first step in managing this resource (IGRAC, 2020).

In Ethiopia, over 60 % (about 469,000 m^3/d) of Addis Ababa's water supply comes from groundwater. Furthermore, many regional cities, rural towns, and villages, as well as almost every community within a 100-kilometer radius of Addis Ababa, depend mainly on groundwater. However, there is almost no experience in monitoring its quality and quantity or in creating a database for this information (ECDSWC-WEDSWS, 2017). Ethiopia has realized that developing its groundwater resources is crucial to the nation's economic growth, poverty alleviation, environmental preservation, and climate change adaptation over the last two decades. Owing to the country's fast population growth, groundwater serves as the main source of water, and several water supply wells have been drilled, including areas within the present study area that are intended for irrigation development.

Since 1997, hydrogeological investigation for Awash and the nearby Blue Nile Basins has been advanced from a conventional technique to a recent integrated approach by different researchers (Cherinet, 1997; BCEOM, 1997; Kebede et al., 2005; Alemayehu, 2006; Kebede et al., 2007; Ayenew et al., 2007; Ayenew et al., 2008; WWDSE, 2008; Azagegn, 2008; Demlie et al., 2008; Yitbarek, 2009; Tesfaye, 2009; Rango et al., 2010; Bretzler et al., 2011; Furi, 2011; Kebede & Travi, 2012; Yitbarek et al., 2012; Kebede, 2013; Azagegn et al., 2014; Azagegn, 2015; Kebede et al., 2016; Berehanu et al., 2017; Berehanu et al., 2018; Kebede et al., 2021). Aside from such comprehensive studies, the lack of relevant groundwater-related data meant that only a few numerical simulations were run in some areas of the Country to examine the groundwater system's response to various conditions, like the Akaki watershed (AAWSA, 2000; Ayenew et al., 2008), Ada'a plain (WWDSE, 2009), Kobo-Raya valley (WWDSE, 2010), and Upper Awash Basin (Yitbarek et al., 2012 & Azagegn, 2015) are limited practices of numerical modeling.

While future groundwater management will increasingly rely on calibrated mathematical simulation models that account for the inherent variability in aquifer properties, recharge rates, and groundwater withdrawals (Cook, 2003; Lubczynski & Gurwin, 2005), it is essential to have a comprehensive understanding of aquifer characteristics (Anderson & Woessner, 1992). The response of an aquifer is significantly influenced by the spatial and temporal variation of its parameters, boundary conditions, and the stresses it experiences. This study uses a quasi-3D finite difference visual MODFLOW flex code (Waterloo Hydrogeologic, 2011) to estimate the available groundwater resources in the area with greater accuracy in defining aquifer parameters, leading to more efficient modeling outcomes. Thus, the main purpose of this research is to develop the area-specific (Becho plain/Melkakunture catchment) hydrogeological conceptual model and simulate a three-layer stress-based scenario simulation for part of the Upper Awash Basin to determine the optimum rate relevant for sustainable utilization without environmental impacts.

1.2 Description of the study area

The study area encompasses significant portions of the Upper Awash Basin and the adjacent eastern edge of the Blue Nile Basin, specifically known as the Melkakunture and Muger Watershed. These regions are recognized as hydraulically interconnected systems, as thought by various studies (Kebede et al., 2007; WWDSE, 2008; Yitbarek et al., 2012; Azagegn et al., 2014), covering a total area of 9,200 km². It is situated at the western edge of the Main Ethiopian Rift (MER) system and partially within the northwestern plateau, which is defined by the following geographic coordinates. 37^0 57´19.36´´E to 38^0 50´58.57´´E longitude; 8^0 26´46.11´´N to 9^0 50´14.42´´N latitude; and at an elevation between 2050 and 2850 m.a.s.l (Figure 1.1a). The main criteria used to define the boundary of the study area by excluding the Akaki catchment are for its better aquifer stratification, less urban impact, limited prior studies, and better-defined boundaries, making it ideal for three-layer groundwater modeling, which will be gradually extended to nearby or other well fields.

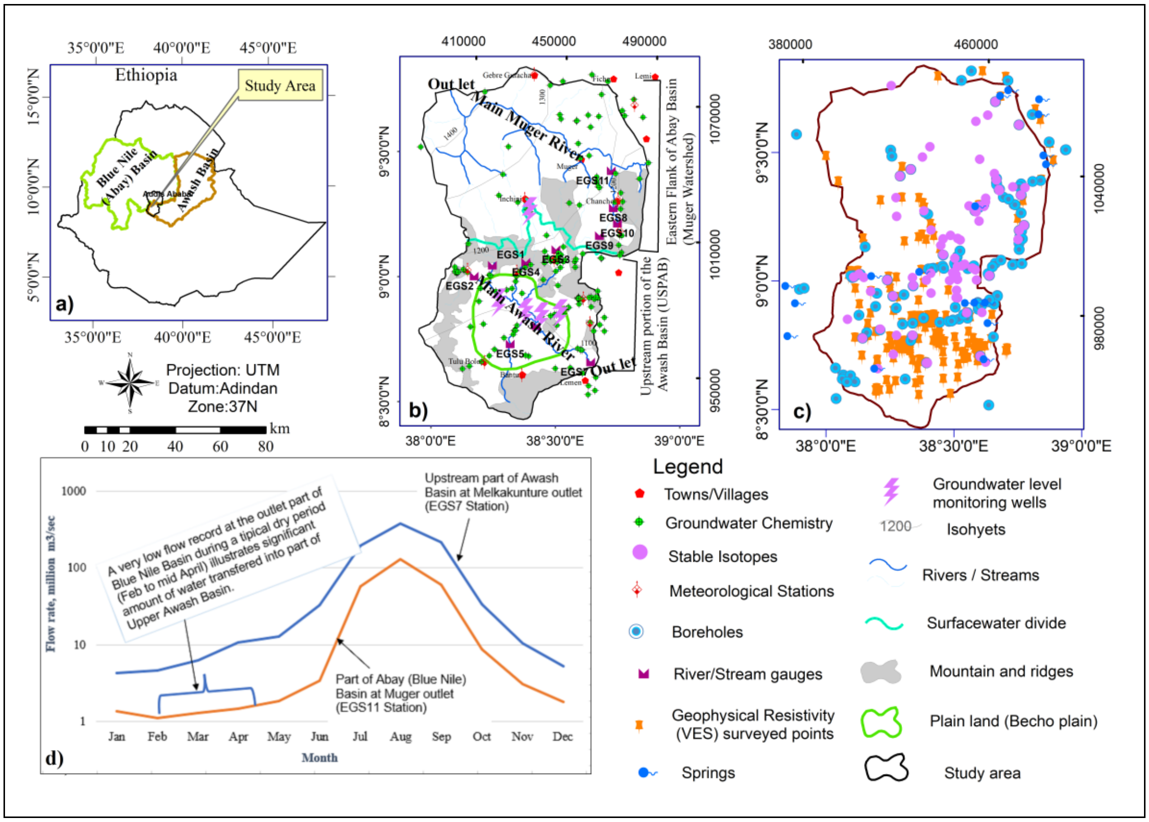

Figure 1.1 Study area and available data. a) Study area location, b) Meteorological, River / Stream gauge stations, and groundwater chemistry data c) Data related to water supply boreholes, springs, stable isotopes, and geophysical resistivity, and d) A long term (1981 to 2015) mean monthly flows from the two adjacent Upper Awash (Melkakunture station) and Blue Nile (Muger station) Basin outlets.

There is a clear relationship between the local weather and topography variations. According to the Isohytal and Theisen polygon estimation techniques, part of the Upper Awash Basin (PUAB) and part of the Blue Nile Basin (PBNB) receive an average of 1113 mm and 1326 mm of precipitation, respectively. The annual average temperature varies from 15.7 °C to 18.7 °C and 12.5 °C to 15.5 °C in the same sequence. There are two different rainy seasons. The spring rainy season, which occurs from April to May, and the summer rainy season, which extends from June to September. The two nearby watersheds' drainage networks were governed by a multitude of tectonic faults and fractures (Figure 1.1b).

The significant topographic variation of the area reveals different historical evolutionary mechanisms. Physiographically, the study area (part of the Upper Awash Basin, PUAB) is characterized by a broad, semi-circular valley plain in the middle, hilly ridges in the northwest, and volcanic centers on its eastern and southern borders. Conversely, Deep-cut gorges with flat-topped hills are typically prominent landscapes for the adjacent eastern flank of the middle Blue Nile Basin (Figure 1.2).

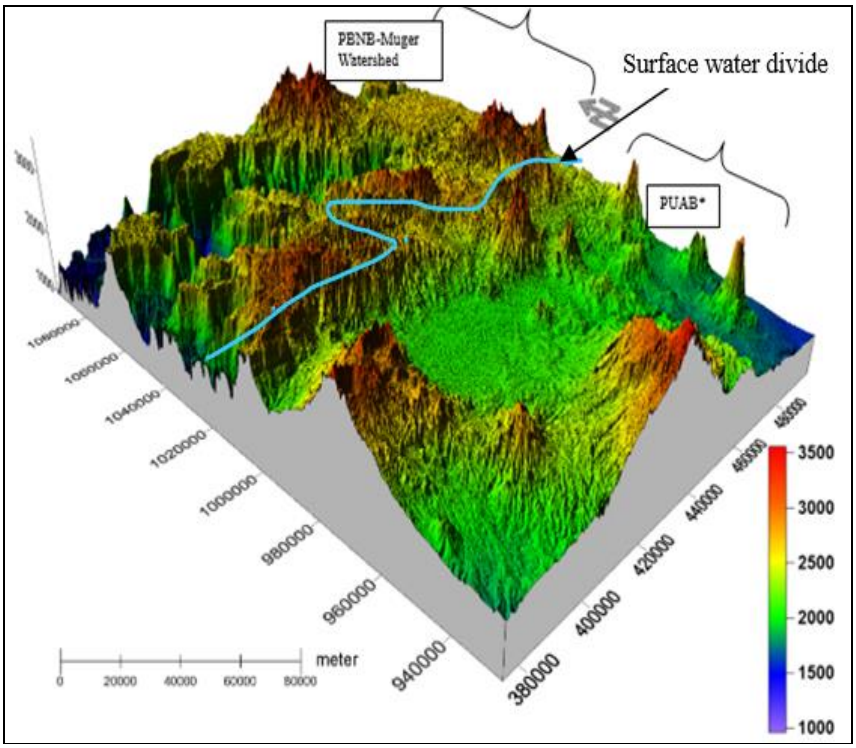

PUAB- Part of the Upper Awash Basin, PBNB- Part of the Blue Nile Basin

Figure 1.2 Study area physiographic setting

1.3 Statement of the problem

Various researchers have investigated the upper Awash Basin groundwater system, and most studies indicate that the main groundwater recharge zone is primarily from the plateau via existing geological structures and inter-basin groundwater transfer from adjacent sub-basins. Besides, the upper Awash basin's groundwater system and the anticipated research area are highly confined within the complex fault system, and knowledge from drilled and tested deep/shallow wells (WWDSE, 2008-2014) illustrates that different lithologic units characterize the geological setting of the research area. Due to the existing fault systems, their lateral and vertical setting vary from place to place, which requires due attention to characterize their hydraulic character together with their response to the over-pumping as well as recharge variability related to climate change for sustainable utilization.

High demand and extraction of groundwater in the area for multiple uses, including the implementation of irrigation using groundwater as a source in the central plain portion of the Upper Awash Basin, due to rapid urbanization and industrialization with enhanced population growth, necessitate area-specific scientific, detailed groundwater resource evaluation, which motivates the study and research work over there. To manage such a resource, detail investigation works like understanding the spatial and temporal distribution of groundwater, its dynamics, mechanisms, and rate of recharge, surface water and groundwater interactions with quantitative and qualitative determination, and the response of the aquifer to various stresses (Climate variability and excessive abstractions) is exceptionally important for sustainable utilization and management.

Furthermore, recent researches were carried out mainly for the upper Awash Basin, including the anticipated research area, relatively at a small scale, and most of the simulations were carried out for steady-state lamped single-layer aquifer systems rather than multiple layers of stress-based scenario simulations for resource management.

1.4 Objectives

1.4.1 General objective

The main objective of this study is to develop and apply a three-layer conceptual and numerical groundwater flow model of part of the Upper Awash Basin to characterize the groundwater system, quantify recharge and inter-aquifer fluxes, and evaluate groundwater response under different development scenarios.

1.4.2 Specific Objectives

The specific objectives include;

- To develop an area-specific hydrogeological conceptual model for part of the Upper Awash Basin by integrating geological, geophysical, hydrochemical, isotope, and hydraulic data.
- To construct a three-layer numerical groundwater flow model representing the major aquifer systems and hydraulic boundaries.
- To calibrate the model under steady-state conditions using observed groundwater heads and stream–aquifer interaction data.
- To quantify groundwater recharge, inter-aquifer fluxes, and water balance components.
- To evaluate groundwater system response under different abstraction and management scenarios, supporting sustainable groundwater use.

1.5 Research Questions/Hypothesis

1.5.1 Major research question

Can the stress-based groundwater flow simulation for a three-aquifer system be utilized sustainably for future management purposes?

1.5.2 Specific Research Questions

The following specific research questions are pointed out to meet the proposed objectives;

i) What are the hydrogeological characteristics and hydraulic connectivity of the three major aquifer systems in the part of the Upper Awash Basin?

ii) How does groundwater recharge vary spatially across the area under current climatic conditions?

iii) What is the contribution of rivers and inter-aquifer flow to the overall groundwater budget?

iv) How does the groundwater system respond to increased abstraction scenarios under steady-state assumptions?

v) Which aquifer units are most suitable for long-term groundwater development with minimal risk of depletion?

1.6 Significance of the study

Currently, large-scale mathematical simulation models with in-depth hydrogeological knowledge are increasingly used in groundwater management. For sustainable and efficient groundwater resource development and management, it is essential to thoroughly characterize the groundwater dynamics, including the understanding and quantification of groundwater transfer from the nearby watershed and the aquifers' response to the inherent climate variability in such high-demanding areas for various uses.

The Ministry of Water and Energy (MOWE), the nation's accountable public body, would benefit from the data and expertise this study will provide for the execution of groundwater resources management. Furthermore, the results of this area-specific research also maximize the outputs of earlier studies, may readily be used for sustainable exploitation of the groundwater, and initiate similar models to be done in different wellfields as a management tool.

2. LITERATURE REVIEW

Various geological and hydrogeological investigations have been carried out so far in the Awash and its adjacent sub-basins to determine mainly the litho-structural setup, aquifer characteristics and their distribution, source mechanism, and rate of recharge for different aquifer types, groundwater discharge zones, inter-basin groundwater transfer, and the overall groundwater dynamics of the area. Consequently, related articles, maps, and reports in the area have been reviewed.

The Ethiopian highland is divided into eastern and western provinces during the Cenozoic era of MER evolution, resulting in topographic uplift, graben formation, and a network of major faults striking West-East (W-E), North-South (N-S), Northeast-Southwest (NE-SW), and Northwest-Southeast (NW-SE). As a whole, Plateau and MER are the two intricate regions that control the overall groundwater flow system (Assefa, 1991; Abebe, 1995; Melaku et al., 1996; BCEOM, 2000).

As the study area is part of the Upper Awash and Blue Nile Basins, it has geologically evolved from three main phases, (i) the pre-sedimentation phase involving peneplanation of basement rocks, (ii) the sedimentation phase including deposition of thick Mesozoic sediments represented by repetitive marine transgression and regression, and (iii) post-sedimentation phase involving emplacement of extensive Tertiary to Quaternary bimodal volcanic rocks and associated sediments (Assefa, 1991; Tefera et al., 1996; Abebe et al., 1999; Wolela, 2008; Wolela, 2009; Gani and Abdelsalam, 2006; Gani et al., 2008).

The litho-structural and morphologic development of the study area was related to the two major episodes of extensional tectonics affecting the Horn of Africa during the Phanerozoic Eon. The earliest episode is marked by the deposition of a more than 1400m thick sedimentary sequence consisting of siliciclastic, evaporite, and calcareous rocks along the northwestern trending Mesozoic basin, commonly referred to as the Blue Nile Basin. These rocks comprise a complete cycle of transgressive and regressive environments of sedimentation in a Rift basin.

According to previous studies (Kazmin, 1979; Assefa, 1991; Gani et al., 2008), sedimentation started in the early Triassic (251 million years ago) and ended in the early Cretaceous period (145 Ma). After that, an enormous epirogenic uplift of Afro-Arabia took place after early Tertiary transgression from the southeast, and a classic continental flood basalt province was formed as a result of the decompression melting of a mantle plume, which produced massive amounts of basaltic magma in the lithosphere and caused the huge uplift. This abundant volcanic outpouring was taking place between 31 to 29 Ma (Pik et al., 1997).

The Trap Series of flood basalts of the Ethiopian plateau is the result of the uplifted crust fissuring under stress, which allowed massive amounts of basaltic magma to ascend. This event was followed by shield-volcano-building episodes from 23 Ma to 11 Ma. Again, in the southern part of the northwestern plateau, products of the shield volcanoes were followed by the fissural eruption and grouped under the Tarmaber-Megezez formation. They are made of lenticular, often zeolitized, alkali basalts with a large volume of tuffs, scoriaceous lava flows, and peralkaline rhyolites with a maximum thickness of 1,000 meters. In general, the geological setting of the area is represented by two major litho-stratigraphic units, namely the Mesozoic sedimentary rocks and Tertiary to Quaternary volcanic rocks, with minor superficial deposits.

It is mentioned that the sedimentary rocks were affected by predominantly NW-SE, and rarely by NE-SW trending normal faults with throws ranging from a few cm to tens of meters. The separation increases progressively up in the sequence to a maximum of 80 meters in the Upper Sandstone, and the fault zones range from a few cm to a few tens of meters (Abebe et al., 1998), and the sequences are cross-cut by N-S, NE-SW, and NW-SE trending fractures.

A common technique for assessing the groundwater resource is the geophysical vertical electrical sounding method, which is applied based on measuring the rock resistivity of the subsurface geologic units to describe the existence and distribution of permeable and impermeable layers (Singal & Gupta, 1999; Kovalevsky et al., 2004). Thus, the impact of porosity, water saturation, and clay content on geologic units is the key factor. The most crucial factor in geophysical electrical exploration for groundwater assessment is adequate electrical resistivity contrast, which provides the geophysical response of the subsurface geologic units. The number of layers, their thicknesses, and their resistivities are typically the results of vertical electrical soundings (VES) conducted on a horizontal or almost horizontally layered earth. Thus, evidence from the VES study was accompanied by information from available boreholes used to identify the spatial distribution of aquifer units. The basic principle behind the VES approach is the linear arrangement of four electrodes. two currents and two potentials. To reflect the average resistivity of the deeper geological formations, the electrode spacing is progressively extended during the survey to penetrate further into the subsurface.

Several deep wells were drilled and tested at different localities of the Upper Awash Basin to determine the groundwater dynamics, aquifer distribution, mechanism of recharge, and quality and quantity of groundwater resources (WWDSE, 2008-2014). Preliminary analysis of data from available deep wells within and surrounding the anticipated research area shows that the deep scoriaceous basaltic aquifer is a confined aquifer, with the confinement of the aquifer varying from 190m to 290m, which is verified at the different sites. Deep wells, having penetrated the lower scoriaceous basaltic formation, have a water level above the surface of the earth (overflowing wells) or less than five meters with a very high transmissivity (>1000 m^2/day). Geological and/or hydrogeological cross-sectional view based on information from the deep exploratory wells along the groundwater flow direction of the Upper Awash Basin illustrates that the scoriaceous basalt is exposed to the surface in the northern and northwestern parts of the Blue Nile Basin, and the downstream part of the Upper Awash Basin (locally known as Becho plain). It lies beneath the acidic units (rhyolite, ignimbrite, tuff), and rift basalt and superficial deposits of more than 250 meters. In general, at the western, southern, and eastern portions, the scoriaceous basalt is overlain by rhyolite, Rift ignimbrite, trachybasalt, tuff, Rift basalt, and alluvial deposits, with their thickness varying at places.

Major investigations carried out in the Awash Basin and its adjacent sub-basins of the Blue Nile Basin using hydrogeological field data analysis, construction of lithohydrostratigraphic correlation, major ion hydrochemistry, and environmental isotopes (Melaku, 1982; HALCROW-EVDSA, 1989; Kebede et al., 2005; Ayenew, 2007; Kebede et al., 2007; Ayenew, 2008; Demlie et al., 2008; WWDSE, 2008; Yitbarek et al., 2012; Azagegn et al, 2014; Azagegn, 2015; & Furi, 2011) provided that the occurrence and flow of groundwater from the plateau to the Rift floor is strongly controlled by the geological structures, type of lithology and geomorphological setup. On the other hand, the lithohydrostratigraphic correlation indicates that the permeable and porous scoriaceous deeper basaltic aquifer is extended laterally from the Blue Nile Plateau to the Awash River destination, Lake Abbe (Rift floor), and overlain by spatially varying thick ignimbrite, tuff, and rhyolite, as well as basaltic lithological formations.

Besides, evidence from isotopic signatures of water ($\delta^{18}O$, $\delta^{2}H$, ^{3}H, ^{14}C), major element geochemistry, and stable isotope of carbon ($\delta^{13}C$), together with construction of lithostratigraphic relationships from deep water supply wells reveals the inter-basin groundwater transfer from Blue Nile basin to upper Awash basin, which depends basically by the nature of the bounding faults (Kebede et al., 2007, Yitbarek et al., 2012; Azagegn et al., 2014). It is further noted that the recharge condition, groundwater flow, and aquifer parameters in the upper Awash basin are significantly influenced by the general bedding of the sedimentary formation underlying the volcanic units (WWDSE, 2008).

Despite high rainfall in the area, the most recent long-term flow data for the two nearby watersheds at the representative outlet stations show that the Muger station in the adjacent eastern flank of the Blue Nile Basin outlet records extremely low flow during the typical dry seasons (BCEOM, 2000). Meanwhile, a high flow is recorded at the PUAB's outlet (Melkakunture) station. Field observations at these stations during a typical dry period show that there is a strong flow at Melkakunture station, indicating a significant groundwater outflow from the eastern flank of the Blue Nile Basin to Awash Basin, and a low flow at Muger station, which is attributed to flow limited to river bed sediments and further to the underlying sandstone or limestone units (Figure 1.1d). It is further supported by the evidence that limestone and sandstone strata from parts of the Blue Nile Basin dip slightly into the Awash Basin (Kebede et al., 2007; Gani et al., 2008;

WWDSE, 2008; Yitbarek et al., 2012; Azagegn et al., 2014), which illustrates that the Awash Basin receives groundwater from a significant portion of the Blue Nile Basin.

The most recent investigation (Tadesse et al., 2023; Tadesse et al., 2024) was carried out to determine the link between aquifers and surface water and to identify the recharge zones of major aquifers in a section of the Upper Awash Basin. The study of groundwater-surface water interaction dynamics combines environmental tracers (^{222}Rn, δ^2H, $\delta^{18}O$, and EC), BFI, and lineament density to infer the exchange dynamics between surface water and groundwater. The results reveal that the primary effluent zones are located in the headwater regions of both basins, particularly along the surface water divide between sections of the Blue Nile and Upper Awash basins. Besides, the southern and southeastern periphery (PUAB outlet) is identified as the main regional groundwater discharge zone. Rivers and streams within the central plains of the Upper Awash Basin display limited or no interaction between groundwater and surface water.

Furthermore, the identification of recharge zones employs an integrated approach that incorporates lithohydrostratigraphic analysis, lineament density mapping, hydrogeochemical data, and stable isotopic data. Findings indicate that superficial deposits and Rift basalt aquifers are primarily replenished by modern precipitation and nearby streams or rivers through fractures. Meanwhile, highland and transitional regions emerge as key recharge zones for the regional confined scoriaceous basalt aquifer. Additionally, the results highlight groundwater flux originating from the adjacent eastern flank of the Blue Nile Basin. This comprehensive approach provides valuable insights into hydrological connectivity and supports effective water resource management strategies.

Due to a lack of relevant hydrogeological data, numerical groundwater flow modeling practices are rare in the country. However, few groundwater simulation models have been carried out for the investigation of groundwater dynamics in the Upper Awash Basin (Yitbarek et al., 2012; Azagegn, 2015), as a groundwater resource evaluation in Ada'a

Plain (WWDSE, 2009), Kombolcha-Kobo-Girana-Raya Valleys (WWDSE, 2010; ECDSWCO, 2016), and Akaki catchment (Ayenew et al., 2008; AAWSA, 2000).

Such single-layer numerical modeling works under steady-state conditions are excellent initiation for further activities in different basins or areas of the country, if relevant hydrogeological data is obtained. Despite possessing extensive knowledge of the region, large-scale, area-specific research, including groundwater flow simulation that considers a multi-quifer system, is critical for the sustainable use of the groundwater resource in such extremely demanding areas. Developing a strong hydrogeological conceptual model and understanding the groundwater flow system are key. This involves analyzing subsurface lithohydrostratigraphy, aquifer parameters, recharge/discharge areas, recharge rates, and aquifer-surface water interactions. Given the variability of volcanic aquifers, obtaining well-calibrated modeling results is vital for groundwater evaluation. These results guide optimal extraction rates to ensure sustainable use and minimize environmental impacts.

In general, characterization of various lithologic units with their hydraulic properties, along with the exploration of unknown groundwater sources across different subsurface lithologic formations, is critical in central Ethiopia. The high demand and extraction of groundwater, particularly to support water supply for Addis Ababa and its surrounding towns, alongside planned irrigation initiatives in the area, necessitate a comprehensive and scientifically detailed evaluation of groundwater resources. The rapid urbanization and industrialization, coupled with significant population growth, further emphasize the need for such studies. To effectively manage these resources, detailed investigations are essential. This includes understanding the spatial and temporal distribution of groundwater, assessing its dynamics, recharge mechanisms, and the interactions between surface water and groundwater. Evaluating both quantitative and qualitative aspects, as well as how aquifers respond to climatic extremes such as droughts and human-induced impacts like excessive abstraction, is paramount for sustainable use and management.

This large-scale (area-specific) research aims to provide detailed results that enhance the findings of previous studies through quantitative experimentation. The insights gained will be invaluable for groundwater development and management, promoting sustainable and environmentally sound water resource utilization practices. Considering future demands, it is important to quantify groundwater gains and losses within the central plain portion of the Upper Awash Basin. The practices derived from this study can be effectively applied to adjacent well fields, including Akaki, Legedadi-Legetafo, South Ayat-North Fanta, and Ada’a, in the future.

3. METHODOLOGY AND MATERIALS

For sustainable utilization of the groundwater resource, integrated scientific methodologies were employed to simulate a three-layer groundwater flow system under both steady and stress-based scenario conditions. This study incorporated pertinent secondary data from earlier studies, supplemented by additional field data (including sampling, testing, and mapping) to address data gaps. Major aquifers, their recharge area, and their link with surface water were defined using data from geology, litho-hydrostratigraphic concepts, hydrogeochemical, isotopic, and geophysical electrical surveys as supportive evidence.

3.1 Methods

3.1.1 Geology

Before conducting fieldwork, a comprehensive geological and structural characterization of the area was established by integrating existing geological maps of varying scales. This process involved several systematic steps.

- Gathering all available geological maps, reports, and datasets from various sources.
- Ensuring that all maps are compatible in scale.
- Dereferencing the maps to align with a common coordinate system.
- Review the geological attributes (such as lithology, structure, age, etc.) present on each map.
- Identifying and verifying geological contacts, faults, and lineaments.
- Merging geological data from multiple sources into a cohesive geological model.
- Applying geostatistical methods (such as Kriging or inverse distance weighting).
- Conducting quality checks to confirm that the harmonized map accurately represents the geological features.
- Detailing the methods employed for harmonization, including any assumptions made, sources of data, and limitations of the integrated map.

- Visualizing and finalizing the project by creating the final harmonized geological map, using appropriate color coding and symbols to depict the various geological units.

Ground checking (verification) was carried out using GPS based on a synchronized map with special emphasis on geological contacts and structures (lineaments, fractures, and faults) along predefined traverse routes and accessible sites. Lineament patterns of the area were extracted from the Digital Elevation Model (DEM) at a 30-meter resolution using Geomatica (Version 17) software, with some manual corrections. Lineament density zones were then created using these patterns as input features through a simple Kriging interpolation technique in the ArcGIS environment. This analysis was used to examine the role of geological structures in the groundwater flow system, including flow direction, relationships among aquifer units, aquifer-surface water links, and groundwater recharge in the area. After verification, spatial geological information was incorporated and calibrated against existing wells' lithological log data (60 lithologic logs) (WWDSE, 2008) to define the subsurface geometry (litho-structural setup). Additionally, a detailed geological map, along with various geological cross-sections, was prepared to understand the distinct geological setup of the area.

3.1.2 Hydro-meteorological study

Meteorological data from the past 22 to 30 years (Table 3.1), mainly precipitation and temperature, were collected from 15 stations (nine from part of the Upper Awash Basin and six from the nearby Muger watershed). Additionally, the Ministry of Water and Energy (MOWE) provided the most recent records, which ranged from 8 to 20 years, for the river or stream flow from 11-gauge stations (Seven stations from a portion of the Upper Awash Basin and four stations from the nearby Blue Nile Basin) (Figure 1.1b). In this study, the missing meteorological data were addressed using a normal ratio method, which adjusts rainfall estimates based on long-term averages from nearby stations. To fill short gaps in streamflow data, a linear interpolation technique was employed. Additionally, geostatistical methods such as kriging were applied to characterize the spatial distribution of both meteorological data and streamflow. These techniques effectively capture the physiographic variability of the basin, thereby enhancing the reliability of hydrological assessments. The meteorological and river flow data were primarily utilized to estimate the recharge rate and investigate the interaction between surface water and aquifer systems. Soil types, land use, and land cover data were also used from modified FAO land use/land cover and soil maps of Ethiopia (FAO, 1984).

Table 3.1 Meteorological stations and measured variables (Data source: NMA, 2020)

Sub-Basin	Stations name	Location		Recorded Year		Climate data				
		UTME	UTMN	From	to	P	T	RH	WS	SSH
PUAB (Melkakunture Watershed)	Adisalem	428211	997135	1990	2018	√	√	√	√	√
	Holeta	444752	1002284	1990	2012	√	√			
	Inchini	431816	1029227	1990	2018	√				
	Ginchi	406476	997957	1990	2015	√				
	Ambo	373101	992333	1990	2019	√	√			
	Sebeta	457742	985269	1990	2017	√	√	√	√	√
	Bantu-Liben	430498	951471	1990	2018	√	√			
	Boneya	460661	974417	1990	2019	√				
	Tulubolo	414028	957166	1990	2019	√	√			
PBNB (Muger Watershed)	Kachise	373073	1061872	1990	2017	√				
	Gebreguracha	435938	1084415	1990	2019	√				
	Debretsigie	480388	1070921	1990	2019	√				
	Entoto	470626	1003122	1990	2020	√	√			
	Suluta	473744	1015433	1990	2019	√	√			
	Chancho	473106	1028933	1991	2019	√	√			

N.B: P-Precipitation, T-Temperature, RH-Relative humidity, WS-Wind speed, SSH-Sunshine hours, and √ - symbol refers to available data

3.1.3 Geophysics

Evidence from geophysical electrical resistivity prospecting was added to the geological and hydrogeological description to support the spatial distribution of aquifer units. One of the most useful techniques for electrical prospecting is geophysical vertical electrical sounding, which uses the electrical characteristics (resistivity) of rock and soil units to identify aquifer zones. The fundamental principle behind the vertical electrical sounding (VES) approach is that a set of four electrodes, two currents, and two potentials are arranged in a linear configuration employing a Schlumberger array. During the survey, the electrode spacing is gradually increased to penetrate deeper into the subsurface to reflect the average resistivity of the deeper geological formations (Singal & Gupta, 1999; Kovalevsky et al., 2004).

The overall 188 VES data (120 secondary and 68 primary) were generated using the IRIS SYSCAL Junior resistivity instrument with a Schlumberger electrode array of electrode (AB/2) separation spread length of 1000m (Figure 1.1c). The instrument is powered by an internal rechargeable battery consisting of a transmitter, receiver, and booster all in one unit. With the use of Geosoft Oasis Montaj software, the data collected from the research area were georeferenced, processed, gridded using the least curvature technique, and smoothed using a 3X3 convolution filter to produce contoured resistivity maps. To determine the electrical resistivity variation of sub-surface materials, a straightforward mapping employing apparent resistivity (ρ_{app}) versus different electrode spacings (AB/2, 220, 330, 500, 750, and 1000) and the one-dimensional model of the whole data curves was also examined. To identify geological formation boundaries and geological structures, the spatially variable resistivity values were also connected with the lithological log data from the neighboring deep-water supply wells.

Errors in Vertical Electrical Sounding (VES) are a common challenge encountered in groundwater studies, but these issues can be systematically addressed through methodological rigor, cross-validation, and uncertainty quantification. Common sources of error in VES include electrode misplacement or poor contact, environmental noise (such as nearby power lines or moisture variability), and model non-uniqueness, where multiple subsurface configurations can yield similar resistivity curves. To mitigate these errors, the following strategies were employed: cross-referencing with borehole logs to validate layer depths and lithology, to gain complementary insights, and conducting repeat measurements to reduce random error and enhance confidence in results.

3.1.4 Hydrochemical and isotopes studies

Groundwater samples (21 in total) were carefully gathered in a clean, dry, and high-density polyethylene plastic bottle for laboratory chemistry analysis following extensive secondary data (103) gathered from several organizations (Total, 104 from wells and 20 from springs) (Figure 1.1b). Throughout the sampling operation, particular attention was given to different borehole depths, geological variations, and data gaps. A HI9811-5 meter (Hanna Instruments, USA) was used to measure water quality parameters such as temperature, pH, and electrical conductivity at the site during sample collection.

The major ion water chemistry analysis was carried out by the Ethiopian Construction Design and Supervision Works Corporation laboratory (ECDSWC). An electro-neutrality test was performed to ensure the accuracy of the chemical data, confirming that the sum of the cations and anions was nearly equal, as stipulated for reliable geochemical characterization and interpretation (Freeze & Cherry, 1979). Therefore, chemical data with errors of no more than 5% were taken into consideration for the geochemical characterization following a charge balance computation. In this work, water chemistry datasets were presented graphically using a trilinear (Piper, 1944) diagram (Aquachem version 4.0 software) to define the variation in hydrochemical patterns along the groundwater flow paths. Further presentation, analysis, and interpretation were made by clustering of these hydrochemical datasets using Agglomerative Hierarchical Clustering (AHC) of XLSTAT (Stat Soft Inc., 2008) to come up with different clusters, and the spatial distribution of different parameters was presented by maps with the help of the ArcGIS 10.8 tool.

Additionally, systematic in-situ measurements of ^{222}Rn (in Becquerels, Bq) were conducted on water samples from different reaches of the main rivers (Awash and Muger) and their tributaries. These measurements were taken during both the non-rainy season (from 14th to 28th March 2021) and the rainy season (from 14th to 31st August 2021), with particular attention given to the permeability of the underlying geological units and geological structures. A simple portable RAD7 radon detector fitted with a Big Bottle system (Durrige Company Inc., 2020) was used based on the principle of a liquid-gas membrane extraction module (Schmidt et al., 2008) that consists of hollow vinyl fibers that allow radon stripping from the sampled water with lower humidity (10-15%) to connect to a closed air loop.

The ^{222}Rn in air concentration, together with the temperature record into a software termed CAPTURE provided by the supplier of Durrige equipment to get the final mean

^{222}Rn in water for analysis. Measurement of radon from each 2.5-liter water sample was carried out for 2 hours in four cycles, with the first record being neglected and the average of the last three measurements taken as the mean ^{222}Rn value of the water sample. RAD7 allows for measurement of ^{222}Rn in water over a concentration range of 1PCi/L (37 Bq/m^3) to greater than 10,000 PCi/L, and the measured values in the field are within this range. Alongside, the measurement of Electrical Conductivity (EC) of rivers, streams, and groundwater was carried out as a supplement to the result of ^{222}Rn to determine mainly the surface water and groundwater interaction zones.

Figure 3.1 In-situ ^{222}Rn measurement at Awash River

In addition, a total of eighty-one (81) stable isotopic data ($\delta^{18}O$, δ^2H) (Figure 1.1c) from previous works were used as evidence for aquifer-surface water connectivity, recharge area, and recharge mechanism identification. It was mentioned in the previous works that stable isotopic ($\delta^{18}O$ and δ^2H) analysis was made using Liquid Water Isotope Analyzer equipment called Los Gatos Research DLT-100 laser instrument in the isotope hydrology laboratory of the School of Earth Sciences, Addis Ababa University.

3.1.5 Hydrogeology

After obtaining groundwater-related secondary data from multiple organizations, data gaps were determined. Following the acquisition of the available data, an inventory of the water sources in the study area, including boreholes and springs, was made. This was done in combination with in-situ verifications of the secondary data, which involved direct measurements of variables like coordinates, temperature, electrical conductivity, static water level, and, if feasible, the discharge of the borehole and spring flow.

Lithological log and pumping test data from existing water supply wells were used to understand and identify different aquifer layers with their hydraulic properties (hydraulic conductivity and transmissivity). The field technique is used to calculate aquifer hydraulic properties such as hydraulic conductivity, transmissivity, and storage properties. An aquifer pumping test is a commonly used in-situ technique to determine the hydraulic properties of water-bearing formations. It was undertaken by artificially creating pressure on the aquifer by continually pumping water from the borehole and monitoring variations in the pumped well's water level. From the change in hydraulic head, one can then estimate the hydraulic properties of the aquifer, such as transmissivity, hydraulic conductivity, and storativity. To investigate the transmissivity and hydraulic conductivity of the typical aquifer units, raw pumping test and recovery data (mostly of 72 hours) from all 34 water supply wells were collected and analyzed using Aquitest software (Aquitest version 3.5) (Waterloo Hydrogeologic Inc., 2002).

Only hydraulic conductivity and transmissivity are estimated using the available data because, without observation wells, it was difficult to determine storage values using analytical methods. Thus, the pumping test data is analyzed using the Cooper-Jacob time drawdown approach (Cooper & Jacob, 1946), and all of the recovered data from the water supply wells is analyzed using Theis's recovery technique (Theis, 1935). As a result, estimates of the area's transmissivity and hydraulic conductivity were made and used for subsequent studies. In addition, hydrogeological cross-sections were made to show the area's general litho-hydrostratigraphic architecture in four different directions, and the spatial distribution of such hydraulic properties was examined using the kriging interpolation technique (Geostatistical tool) in ArcGIS 10.8 software.

To study the temporal groundwater condition due to the variability of climate change and human impacts (excessive pumping), the generation of time-based water level and temperature data is critical. In this study, three locations, one at the plateau and two in the central plain portion of the Upper Awash Basin, were chosen to install data loggers for monitoring groundwater levels and temperature along the regional groundwater flow direction. It was done by considering the factors that can affect the distribution of groundwater monitoring sites. Even though the instruments at two of the boreholes in the plainland portion of the Upper Awash Basin failed, data were collected by reinstalling the instruments in those two boreholes. Representative wells (BHE30 from the plateau area, BHE20, and BHE28 from the portion of the Upper Awash Basin plain) were chosen along groundwater flow paths that are unaffected by pumping activity within and outside of the study area. Data loggers (SEBA-Troll 100 & 300) from SEBA-Hydrometry of Germany (http.//www.seba.de) were installed to monitor groundwater levels and temperature data under natural conditions. The BHE30 provided hourly monitored data for 14 months (April 2019 to June 2020). Besides, from BHE20 and BHE28, 14 months (July 2021 to April 2022) and 10 months (Jun 2016 to October 2017) data were collected. The water table fluctuation (WTF) technique was employed to estimate recharge rates based on the groundwater level data obtained from such wells.

3.1.6 Groundwater flow modeling

Understanding the groundwater system both spatially and temporally using integrated techniques is crucial, as existing intricate fault systems strongly control the study area's groundwater system. Before doing any groundwater numerical model, a hydrogeological conceptual model, which is typically developed using fundamental information from geological settings, stratigraphy, hydraulic properties of various geologic layers, piezometric levels, and water budget, serves as the foundation for the groundwater flow simulation (Anderson et al., 2015). Determining aquifer layers proved to be a difficult task due to the lateral and vertical variations of such volcanic terrain.

Nonetheless, using the most recent understanding and accessible hydraulic data, an attempt was made to classify various geologic formations into three major hydrogeologic units. Boundary conditions were thus established accordingly, and the numerical groundwater flow simulation and calibration were made using the visual MODFLOW flex package, based on the observed head data under steady conditions of a three-layer system.

Building the hydrogeological conceptual and numerical models of groundwater using raw GIS data objects is made possible by the robust capabilities provided by the visual MODFLOW flex program. There must be continuous layers simulating aquifers and aquitards across the model domain for the numerical simulation to be performed using the visual MODFLOW algorithm. As required by the MODFLOW numeric engine, a layer characteristics value is assigned to each layer. To determine an appropriate exploitation rate for the efficient and sustainable use of groundwater, a sensitivity analysis and model performance evaluation, along with several stress-based scenarios, were conducted.

In general, the overall groundwater flow modeling work begins by defining the problem through a review of previous data and establishing modeling objectives. Various methods were implemented to understand the groundwater flow system, leading to the development of a hydrogeological conceptual model. A grid was defined, and aquifer properties and boundary conditions were assigned for the numerical model construction. The model underwent steady-state calibration using head and flux, with results verified against observed data. Sensitivity analysis identified key aquifer parameters, followed by stress-based scenario simulation based on the steady state calibration results. Finally, the results were evaluated, and a modeling report was created. Figure 3.2 summarizes the research outline of this study.

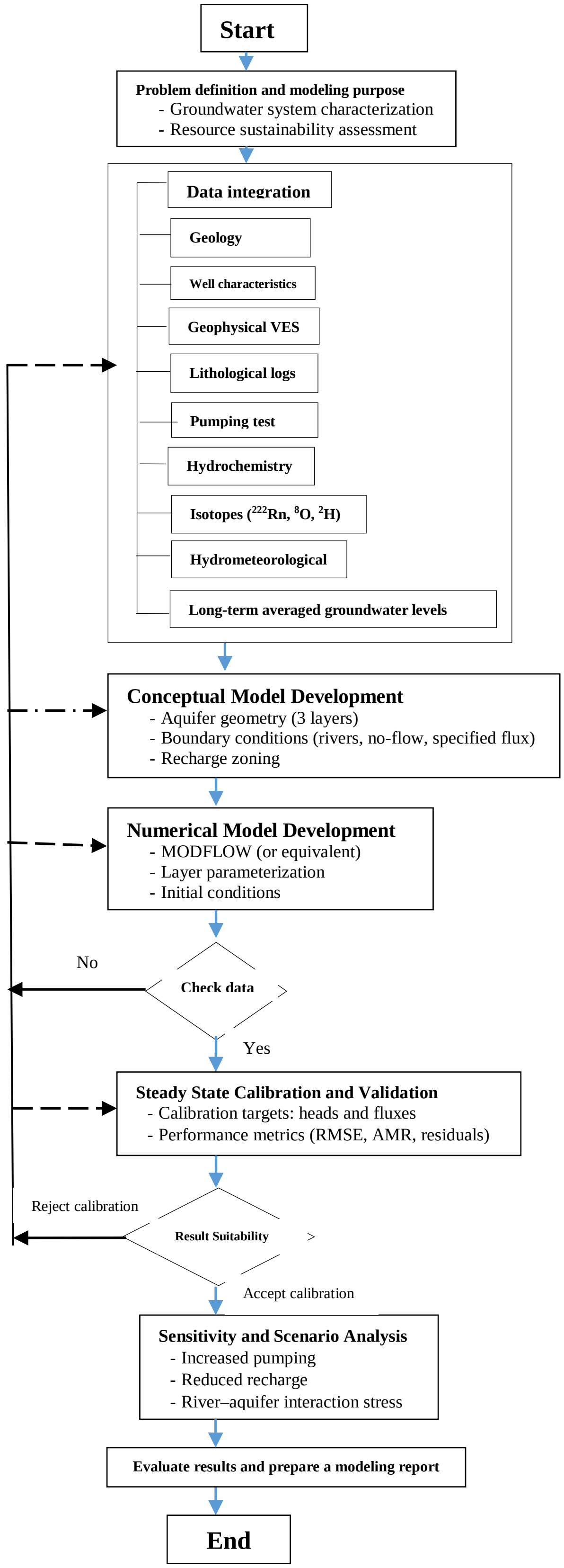

Figure 3.2 The overall research workflow

3.2 Materials

For the entire research period, different documents, equipment, and computer software were used at different stages to achieve the objective of the research. It was started by reviewing previous studies, like published/unpublished reports and any available office documents and maps, such as national as well as international research papers conducted in the same as well as different geologic settings relevant to the proposed research objectives. Primary as well as secondary data were processed and/or analyzed to generate and visualize the anticipated objective results using the following major scientific software such as;

- A computer code, RAP version 3.0.3, and Excel-based TIMESPLOT programs were used to separate surface runoff and Baseflow for the hydrograph separation recharge estimation method.
- The IRIS SYSCAL Junior resistivity field survey instrument and the Geosoft Oasis Montaj software to generate a contoured resistivity map.
- A RAD7 radon detector fitted with a Big Bottle system, along with CAPTURE software to measure and filter the concentration of ^{222}Rn in water, and a HI9811-5 meter (Hanna Instruments, USA) to measure in-situ water quality parameters such as temperature, pH, and electrical conductivity during sample collection.
- Aquitest version 3.5 and Aquachem version 4.0 for pumping test and hydro-chemical data analysis, respectively, and Statistica 10.0 for statistical data analysis
- ArcGIS 10.8 software and its extensions used to make different maps, for geostatistical analysis (Inverse Distance Weighting (IDW) and Kriging)
- AutoCAD-18 software to make different types of cross sections for conceptual hydrogeological development and presentation.
- Visual MODFLOW flex for data management, analysis, plotting, simulation, and visualization

4. RESULTS AND DISCUSSIONS

4.1 Hydrogeological understanding

4.1.1 Lithostratigraphy

The geological setting of the area is represented by two major litho-stratigraphic units, namely the Mesozoic sedimentary rocks and Tertiary to Quaternary volcanic rocks with minor volcano-clastic sediments, and superficial deposits. Geological cross-sections along different directions (AA′, BB′, CC′, and DD′) were created to realize the lithostratigraphic succession of the area based on information from existing boreholes' lithologic logs and knowledge of the overall geologic setup. Five different sedimentary rocks and eight volcanic rock units are observed in the study area (Figure 4.1), and their description from older to younger is as follows.

4.1.1.1 Mesozoic sedimentary rock units

Lower Sandstone

The lower sandstone is outcropped in the deep gorges of the Blue Nile River, where it is underlain unconformably by the basement rocks and overlain by the Shale unit. The unit is commonly sandstone intercalated with siltstone and mudstone, with occasional beds of conglomerate and shale, with a maximum thickness of 700m, presumably deposited in fluvial and deltaic environments. It is fine- to medium-grained, yellowish-pink in color, well-sorted, non-calcareous, cross-bedded quartz sandstone. The sandstone beds exposed in the Blue Nile River gorge show a slight dip in a nearly southeast direction.

Gypsum-Marl-Shale (Abbay Beds)

It occurs in the Blue Nile River gorge lying between the lower sandstone and the Antalo limestone. It consists of alternating beds of thick sandy limestone, calcareous sandstone, gypsum, and variegated shale. The total thickness of the Abbay beds reaches up to 580m, and its age is middle Jurassic (Kazmin, 1979).

Limestone unit (Antalo limestone)

The Antalo limestone unit, which is massive to fossiliferous and light to yellowish-grey in color, is exposed in the gorges of the Blue Nile and Muger Rivers. It is mostly composed of slightly fractured and jointed limestone that is intercalated with thin beds of shale and marl, as well as sporadic fine-grained sandstone bands. In the Blue Nile gorge, including Muger, the Adigrat Sandstone is overlain by shale and gypsum known as Goha Tsion Formation (Assefa, 1991). Goha-Tsion formation consists of interbedded sandstone, siltstone, mudstone, and shale in the lower part and alternating gypsum, dolomite, limestone, and shale in the upper part, with a thickness ranging from 450m to 600m, with a slight dipping in the southeast direction (1-2°). It has a gradational contact with the underlying and overlying lower sandstone and Antalo Limestone, respectively.

Upper sandstone (Amba-Aradam Sandstone)

The Amba-Aradam sandstone is widely known as the upper sandstone, which is outcropped in the Muger gorge and conformably overlies the Antalo limestone. It is dominantly composed of sandstone with thick beds of conglomerates, and thin beds of mudstone and shale, generally coarsening upward. The sandstone is grayish to pinkish-white in color and fine to coarse-grained in texture. Its thickness is in the range from 450 to 600m, and it shows a slight dip towards the south and southeast. In most parts of the basin, this unit outcrops below 2000 m.a.s.l.

The Mudstone unit is composed dominantly of mudstone with very thin beds of sandstone and shale. It outcrops in the Muger sub-basin underlying the volcanic rock units, and where it outcrops, its thickness reaches 110m, while a thickness of 216m is recorded from borehole lithologic logs.

4.1.1.2 Tertiary Volcanic Rock Units

In the northern and northwestern plateau parts of the study area, the volcanic rocks are subdivided into Ashangi and Aiba basalts, Alaji formation, and Tarmaber basalt. The Ashangi basalt represents the earliest fissural flood basalt volcanism, consisting of predominantly slightly alkaline basalts with inter-bedded pyroclastic, rare rhyolites commonly injected by dolerite sills and dykes. The upper part is more tuffaceous and contains interbedded lacustrine deposits with lignite seams. The Aiba basalts consist of massive transitional flood-basaltic flows, with intercalated agglomerate beds. The Alaji formation mainly consists of aphyric flood basalts associated with rhyolite, ignimbrites, and subordinate trachytes resting conformably on the Aiba Basalts, but in Muger Valley, it directly overlies the Mesozoic sediments. Accordingly, the following (from oldest to youngest) description pertains to the exposed volcanic rock units in the area.

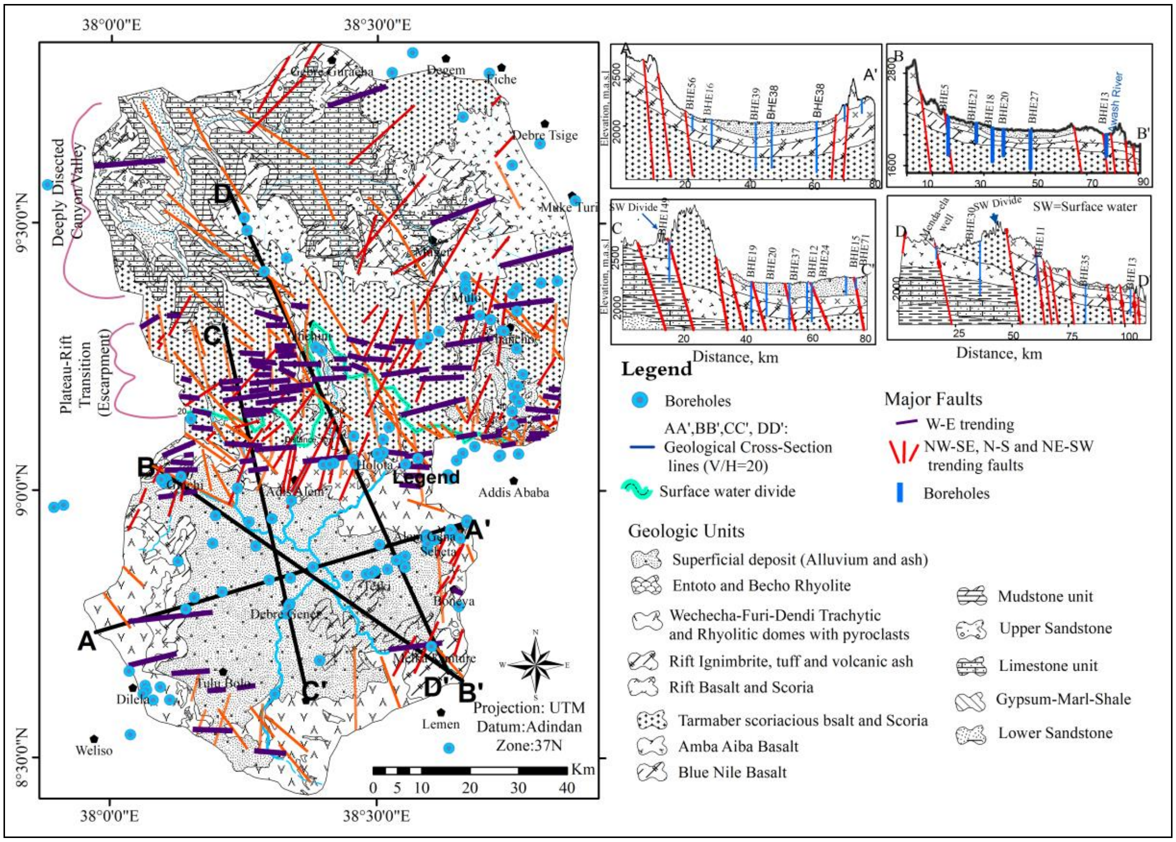

Figure 4.1 Geological map with different cross-sections

Blue Nile Basalt

This unit is thick basaltic flows and outcrops in the Blue Nile gorge, unconformably overlying the Mesozoic sediments, representing the earliest flood basalt volcanism in the area. It is alkaline basalt with columnar joints of wider spacing, forming a vertical cliff. In the hand specimen, it is massive and dark in color. The lower part of the interplanar spaces among columns is filled with secondary minerals (zeolites and clay).

Amba-Aiba Basalt

It is exposed in the same area overlying the Blue Nile basalt and is a flood basalt in thick flow with closely spaced columnar joints. In the hand specimen, it is aphanitic in texture and dark grey.

Tarmaber Basalt

It is the dominant unit exposed in the western and northern parts of the plateau and the Watershed divide of the Awash and Blue Nile River Basins. In the marginal Rift Valley part of the area, this unit is downthrown by the regional West-East running Ambo-Addis Ababa fault and overlain by younger ignimbrite (observed from lithology logs of existing boreholes). It consists mainly of scoriaceous lava flows, and in places, it is columnar olivine-bearing basalt as pockets within the scoriaceous components. The unit outcrops along the Rift margins and the Yerer Tulu Volcanic Lineament (YTVL) zones. It is directly overlying the Trap series volcanic rock units, which are highly weathered, fractured, and pinkish to grayish.

Rift Basalt

The rift basaltic unit is fine to coarse-grained basalt composed of olivine and plagioclase phenocrysts. In most parts of the outcropped area, it is a relatively thin lava flow overlying the ignimbrite. It is composed of vesicular basalt with minor trachytes, exposed along stream banks and beds in the Upper Awash basin and the southern part of the Muger sub-basin.

Rift Ignimbrite, Tuff, and Ash

The Ignimbrite unit is outcropped in most of the plain part and the periphery part of the Upper Awash Basin, composed of welded tuff (ignimbrite) and non-welded pyroclastic fall (Ash and tuff). It is grayish to white, and when welded, it exhibits flame textures and elongated rock fragments of various colors. Around the southeastern parts of the area, its thickness reaches up to 200m (Boreholes lithology data). The Rift Ash and Tuff unit is composed of tuff and ash, forming a relatively undulating topography in the flat plains, dotted with small isolated rhyolite/pumice domes, in the northwestern part of the Upper Awash basin.

Central Volcanic Units (Wechecha-Furi-Dendi Trachyte, and Rhyolitic units)

The central volcanic units are mainly trachytic lavas exposed at the Eastern and Western edges (locally named Wechecha, Furi, and Dendi) of the area, forming elevated ridges or mountain peaks. It is a grayish, fine to medium-grained trachyte with subordinate ash falls and ignimbrite. The Rhyolite and Trachyte domes form isolated silicic domes and associated tuffs along Rift margins and Rift shoulders.

Entoto and Becho Rhyolites

The Entoto ridge forms a watershed divide of the Blue Nile and Awash River Basins. The ridge forms a steep slope towards the Blue Nile Basin and a steep-to-gentle slope towards the Awash Basin. In a fresh hand specimen, it is grayish pink and reddish brown to yellowish grey when weathered. The rhyolites in the central plain portion of the Upper Awash Basin (Becho plain) form isolated cones.

Superficial (Alluvium, Ash, and weathered Tuff) deposit

It covers mainly the Tertiary Volcanics on the plateaus and central flat lands of the Upper Awash part, consisting of regolith, reddish-brown soils, and alluvium with thicknesses not more than 50 meters (Boreholes data). The Rift Ash and Tuff unit is composed of tuff and ash, forming a relatively undulating topography in the flat plains.

4.1.2 Tectonic structures

The study area, located within the central northwestern plateau and the western segment of the Main Ethiopian Rift (MER), exhibits structural development closely associated with the evolution of the East African Rift System (EARS). The geological history of the region is characterized by a sequential progression of processes: an initial phase of sedimentary deposition, wherein sediments accumulated in basins and preserved pre-tectonic environmental conditions, thereby establishing the foundation for subsequent structural and volcanic modifications; followed by rifting, marked by crustal extension that generated faults, grabens, and horsts, deepened basins, and facilitated continued sedimentation while creating pathways for magma ascent through lithospheric thinning; and ultimately, volcanic activity, during which magma intruded and erupted through rift-related fractures, producing basaltic, rhyolitic, and pyroclastic deposits that overlie or penetrate sedimentary sequences, signifying the transition from continental rifting toward potential ocean basin development. Hence, the Structural elements of the study area can be subdivided into primary and secondary structures. The former is intimately associated with a depositional history of sedimentary rocks and layering during volcanic eruption, and the latter relates to extensional tectonics responsible for Rift formation and volcanic activity.

The primary sedimentary layering in the Mesozoic units has been studied by differently oriented faults and basaltic dykes. The sedimentary rock units in the area invariably exhibit visible planar layers. laminations, bedding, and cross-bedding, which are acquired during the deposition of the sediments and presumably enhanced during diagenesis. These structural features are well marked by grain size, compositional, and color variations, and vary from one lithology to another, and also within the same lithology due to lateral and vertical facies change.

The main tectonic episode is associated with divergent geodynamic processes leading to the formation of the MER in the Cenozoic era. The rifting is manifested by narrow intercontinental discrete depressions, topographic uplift, and a network of faults that generally trend N-S, NE-SW, and NW-SE. In general, regional normal faults with different orientations, fractures, and joints with different densities are found in the study area (Figure 4.2). Four major fault feature types are recognized during the interpretation of satellite imagery lineament data. The widespread brittle deformation consisting of fractures and dislocations is also observed during the field survey.

NW-SE Fault System

The NW-SE fault system is the oldest, with an extended history, and affects all rock types in the northwestern part. They are crustal scale and served as a conduit for the extensive volcanic formation in the area, and their age may go up to the early Paleozoic, but they became reactivated later with the main tectonic event in the region. The faulted blocks are downthrown towards the NE in most cases, resulting in the formation of some graben and horst structures generally oriented NW-SE. The trend of the Wechecha volcanic belt can be associated with this fault system.

E-W Fault System

The E-W fault system, which is the upper boundary of the Ethiopian Rift margin, runs approximately E-W north of the Addis Ababa-Ambo road. It is the main fault system in the western plateau part and densely affects the Tarmaber basalt. Along the reactivated Yerer Tulu Volcanic Lineament (YTVL) zone, the E-W-oriented fault system has an impact on the volcanic rock units overlying the Mesozoic sediments. The development of a horst structure-oriented E-W is the result of the faulted blocks being downthrown towards the south in most cases and the horst of Mudstone formed by these faults are covered by early episodes of the Tertiary volcanic units in the eastern part, outcrops on the surface in the west-central part of the Muger sub-basin.

NE-SW Fault System

The NE-SW fault system runs parallel to the principal system of fissures in the Rift floor. This fault system densely affects the volcanic rocks, serves as a conduit to the younger eruption, and exhibits step-like block faults. The Mesozoic sedimentary and Tertiary volcanic rock units are thrown to lower levels by the SE fault system and are subsequently covered by Rift volcanic rock units.

N-S Fault System

The N-S fault system is the recent fault system that serves as a conduit for young volcanic.

Lineament density (LD)

The approach of using Digital Elevation Model (DEM)-derived lineament analysis, coupled with spatial interpolation techniques, pinpoints the lineament density distribution.

The study area is characterized by distinct geomorphology, litho-stratigraphy, and regional structural settings, which exhibit a varying trend to indicate the occurrence of variable hydrogeologic systems. Accordingly, lineament density (LD < 0.41 km/km^2) is relatively low in the central plain of the southern part and the extremely dissected northeastern and northwestern portions. Plateau and its environs are characterized by a relatively high LD between 0.96 and 3.0 km/km^2, which are very dense and interconnected. However, the outlet part of the southern section has an intermediate LD between 0.41 and 0.96 km /km^2 (Figure 4.2).

Lineaments that are primarily oriented NW-SE have an impact on most of the sedimentary units in the northern and northwestern parts, as well as the Trap series columnar and weathered basaltic units. Since the younger volcanic rock units that cover the Trap series Volcanics are primarily exposed at the flank of MER and YTVL zones, they are highly fractured and jointed, with main lineament orientations along the N-S, E-W, and NE-SW directions.

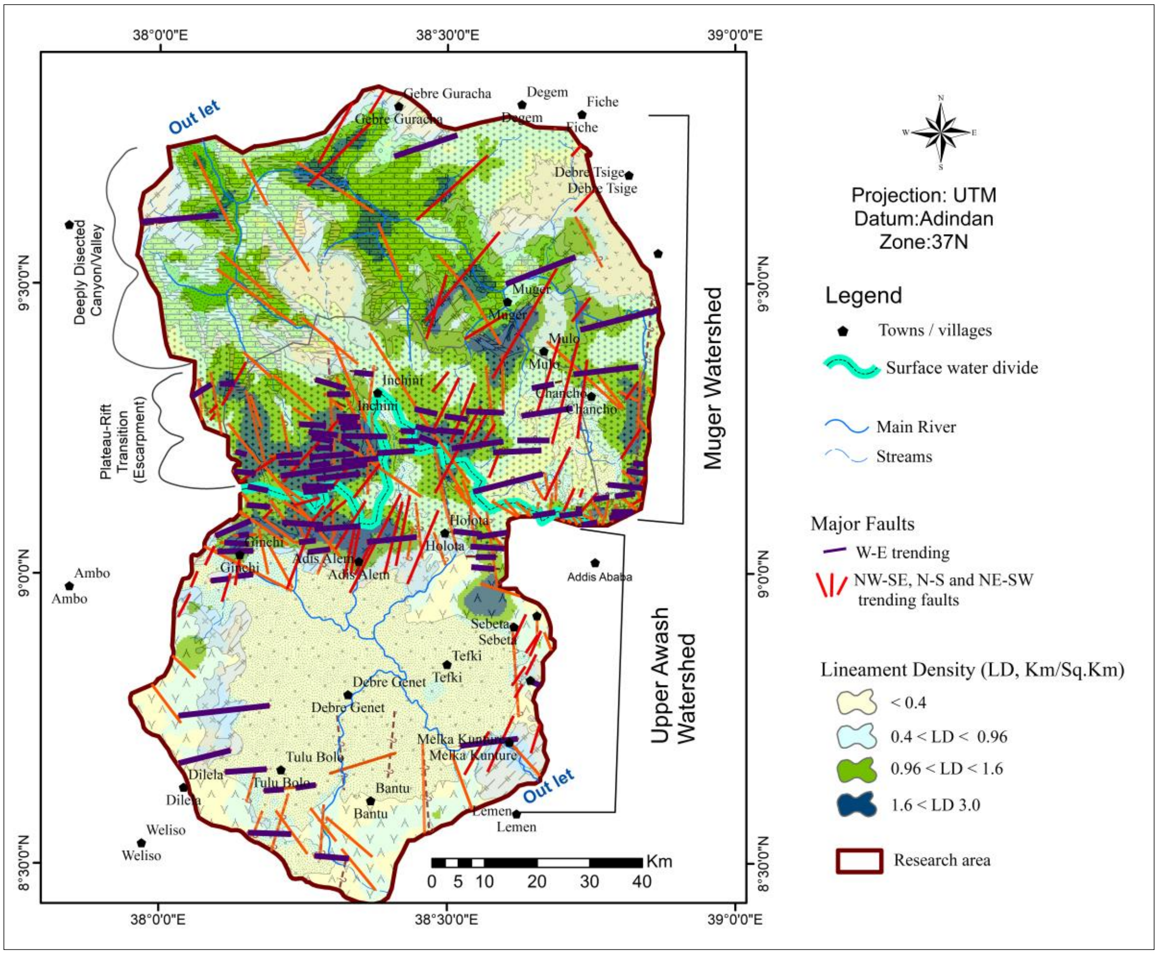

Figure 4.2 Lineament density

In general, faults play a crucial role in governing groundwater flow paths within the study area, particularly due to the area’s intricate volcanic geology and tectonic framework. Recent studies indicate that faults, such as those within the Yerer–Tulu-Volcanic Lineament-Zone and along the Main Ethiopian Rift margin, function as vertical conduits that facilitate deep infiltration of rainfall and surface water. Furthermore, these areas exhibit a high density of lineaments, which correlates with an increased potential for groundwater recharge, attributed to enhanced secondary porosity and permeability.

In addition, the presence of faults and horsts beneath volcanic strata creates hydrogeologic boundaries, segmenting the basin into distinct sub-aquifers. For instance, impermeable mudstone-capped horsts establish groundwater divides between the Upper Awash Basin and its adjacent areas, redirecting flow paths laterally. While groundwater contours typically align with surface topography at the catchment scale, regional fault systems can override local gradients, directing flow along favored structural orientations, such as NW–SE or E–W trends. Overlay analyses of baseflow separation, lineament density, and geological units demonstrate that regions situated near fault zones receive a disproportionately higher amount of recharge compared to those further away from these structural features.

4.2 Geophysical signatures

A total of 188 VES data collected using the IRIS SYSCAL Junior resistivity measuring instrument with a Schlumberger electrode array (AB/2) separation spread length of 1000m were used. To create contoured resistivity maps, the data gathered from the study area were georeferenced, processed, and gridded using the least curvature technique, then smoothed with a 3x3 convolution filter in Geosoft Oasis Montaj (Geosoft Inc., 2012b). A simple mapping using apparent resistivity (ρ_{app}) against various electrode spacings (AB/2, 220, 330, 500, 750, and 1000) and the one-dimensional model of the entire data curves was also investigated to ascertain the electrical resistivity variation of sub-surface materials.

It is challenging to determine an exact resistivity value for existing geologic units in the area, particularly in distinguishing between different volcanic units. However, factors such as porosity, fracturing, alteration, and thermal effects are used to differentiate their spatial distribution. Additionally, the spatial resistivity results were correlated with borehole short normal geophysical resistivity and lithological logs from nearby deep-water supply wells to identify the distribution of geologic units and structures (Figure 4.3).

For most sounding stations, additional data from the pseudo-electrical apparent resistivity (ρ_{app}) spreading across various electrode spacings (Figure 4.4) and the borehole resistivity logging result (Figure 4.3) provide supportive evidence that the subsurface is electrically heterogeneous over space. Based on lateral differences in formation resistivity, several vertical discontinuities have also been identified, revealing potentially significant geologic structures with different trends, such as NW-SE, W-E, NE-SW, and N-S (Figure 4.4, broken dark lines). The resulting images illustrate the resistivity variation, which is primarily found in the central southern portion, where it is high at shallow depths and relatively low at deeper depths. To determine the litho-hydro stratigraphic setting of the area, such variation is correlated with different depth lithology and borehole geophysical logs of water supply wells drilled and tested at different times (WWDSE, 2015 to 2022).

Low resistivity values detected at certain depths can be reliably attributed to the combination of pervious geological materials and thermal effects stemming from deep, encountered in water supply wells such as BHE23, which registers a temperature of 48°C, and BHE24 at 45°C. These resistivity patterns are intricately linked to a network of regional geological structures that shape the spatial distribution of diverse aquifer units within the area. In stark contrast, the zones exhibiting higher resistivity are characterized by the presence of dense, impervious acidic rock units that permeate various depths throughout the study area. These formations are manifestations of the acidic volcanic units. Furthermore, the subsurface can be effectively classified into a minimum of four distinct geoelectric layers, as illustrated in Figures 4.3 and 4.4.

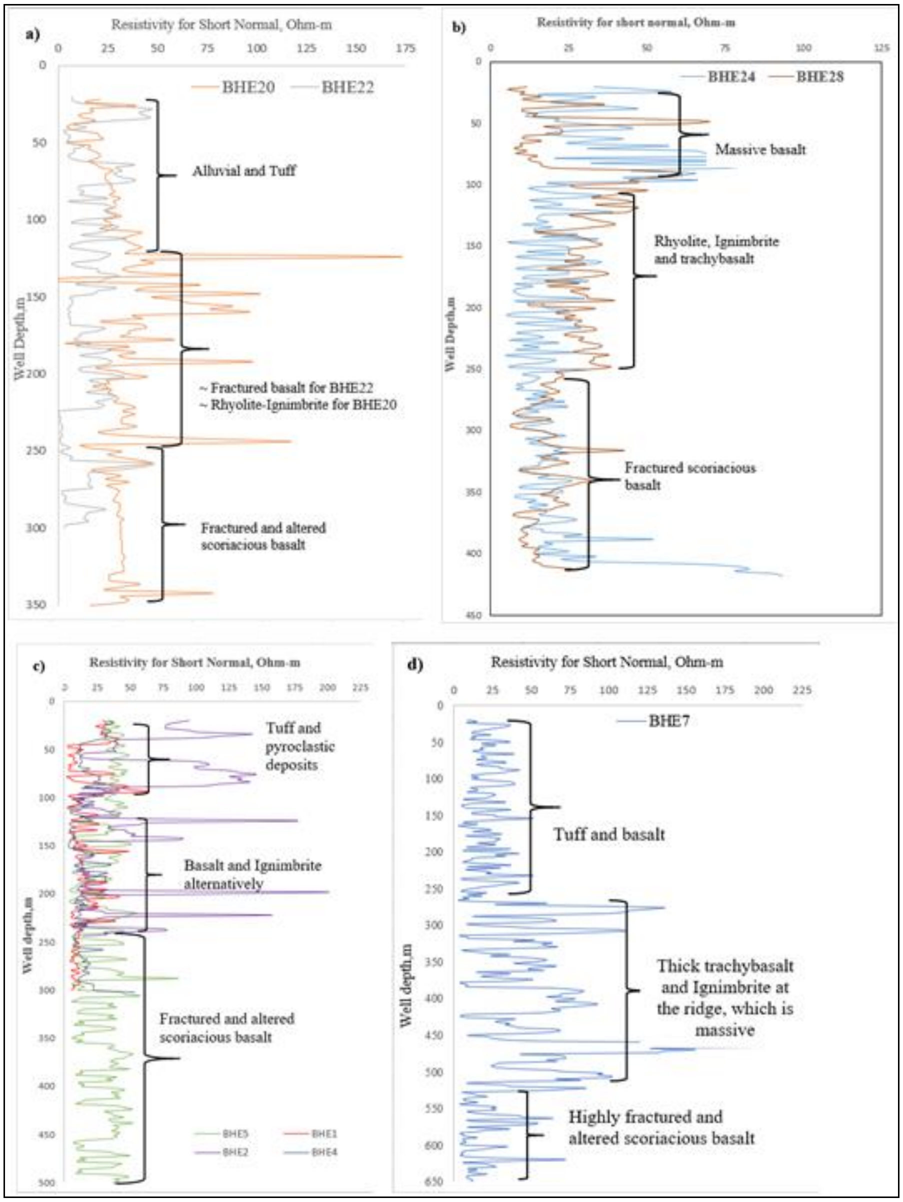

Figure 4.3 Depth against short normal geophysical resistivity well logging result of water supply wells from a) Central plain, b) Eastern, c) Western, and d) Escarpment (Data source: WWDSE, 2015 to 2022).

To enhance our understanding of these layers, efforts have been made to correlate them with lithology and borehole geophysical logs results obtained from existing water supply wells to create a more comprehensive depiction of the area's subsurface characteristics.

These are;

- The high resistive layer (ρ_{app} > 50 ohm-m), interpreted as acidic rock units (Ignimbrite, rhyolite, and trachyte) acts as an aquiclude.
- Moderate resistive layer (35 < ρ_{app} < 50 ohm-m), attributed to the Rift basaltic aquifer.
- Low to moderate resistive layer (20 < ρ_{app} < 35 ohm-m), which could be interpreted as the regional scoriaceous basaltic aquifer, covers most of the area, and
- A very low resistive layer ((ρ_{app} < 20 ohm-m), which is the response of alluvial and ash deposits for shallow spreads (i.e., mainly for AB/2. 220 m and 330 m) and highly fractured and/or altered due to the thermal effect for the regional scoriaceous basaltic aquifer for the stretched spreads (AB/2 > 500 m) covering mainly the central and southwestern parts of the area.

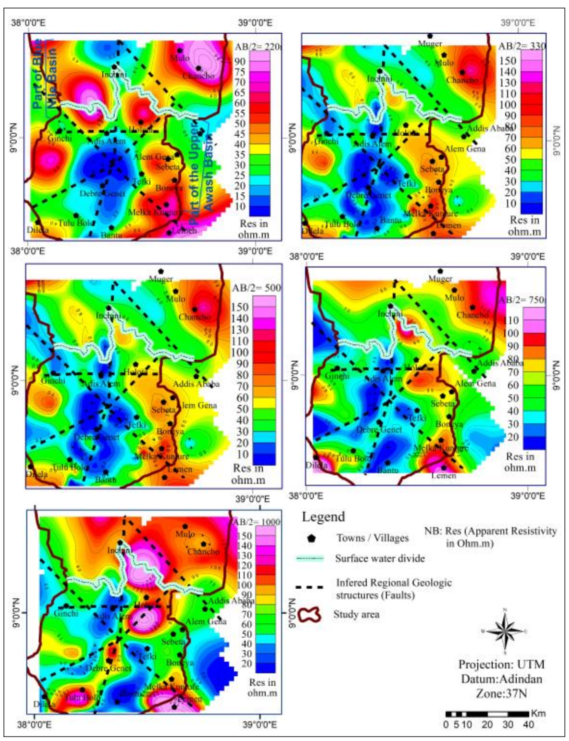

Figure 4.4 Spatial variation of pseudo-electrical apparent resistivity plan maps for different Schlumberger half electrode spreads (AB/2=220,330,500,750, and 1000) with a possible inferred regional geological fault of the area (Data source: WWDSE, 2017 to 2022)

4.3 Baseflow index as a hydrological signature

Baseflow, the minimum volume of stream flow over a specific period (Barlow et al., 2014), is continuous under specific conditions and enters a river channel via a delayed pathway within the hydrologic system (Meyboom, 1961; Fetter, 1994; Sloto & Crouse, 1996; Sophocleous, 2002; Combalicer et al., 2008). A practical way to compare the proportional contributions of groundwater to stream flow is through the BFI.

The main objective of this section is the determination of BFI with its spatial variation to complement the findings from other techniques for understanding aquifer-surface water interaction areas. Groundwater contribution is classified as high for BFI > 0.3 and low for BFI < 0.3, with the BFI typically falling between 0.4 and 0.8 (Stricker, 1983; Kunianisky, 1989). Tracing the boundary between Baseflow and surface runoff is challenging. However, the permeability of the geologic units and structures that a river flows through has a significant influence on the groundwater contribution to a river (Shaw, 1994).

Following the separation of hydrographs (Table 4.1), the mean annual BFI result reveals notable spatial variation in each flow recording station (Figure 4.1), which is consistent with the previous research outcomes of similar areas to consider for further steps (Azagegn, 2015; Berehanu et al., 2017; Ayenew et al., 2019).

Table 4.1 Mean annual Baseflow index (BFI) estimated for each station using Baseflow separation methods for a portion of the Upper Awash and the nearby Blue Nile Basins

ID	Local name	Longitude	Latitude	Altitude (m.a.s.l)	Area, Km^2	Daily Flow, m^3/sec	Annual Total flow, mm	Calculated mean annual baseflow index		BFI, Average	Annual baseflow, mm
								Using River Analysis Package (RAP) Technique	Using TIMESPLOT Technique		
EGS1	Upper Awash at wolonkomi	$38^{0}14^{'}54.05^{''}$	$9^{0}02^{'}30.99^{''}$	2132	60.0	0.82	403.2	0.49	0.54	0.51	206.86
EGS2	Upper Awash at Ginchi	$38^{0}10^{'}36.78^{''}$	$8^{0}59^{'}37.54^{''}$	2190	76.0	0.99	412.4	0.23	0.23	0.23	95.61
EGS3	Upper Awash at Holeta	$38^{0}30^{'}02.04^{''}$	$9^{0}06^{'}10.29^{''}$	2467	119.0	1.45	384.3	0.49	0.51	0.50	193.35
EGS4	Upper Awash at Addis Alem	$38^{0}22^{'}57.11^{''}$	$9^{0}03^{'}16.73^{''}$	2350	248.0	2.81	357.3	0.55	0.59	0.57	203.20
EGS5	Upper Awash at Asgori	$38^{0}22^{'}00.69^{''}$	$8^{0}48^{'}13.63^{''}$	2073	662.5	3.73	177.4	0.32	0.32	0.32	56.42
EGS6	Upper Awash at Bello	$38^{0}25^{'}13.81^{''}$	$8^{0}48^{'}13.94^{''}$	2053	2568.8	10.48	128.6	0.58	0.58	0.58	74.54
EGS7	Upper Awash at Melka kunture	$38^{0}38^{'}39.05^{''}$	$8^{0}39^{'}16.95^{''}$	2004	4456.0	29.17	206.4	0.49	0.50	0.49	102.16
EGS8	Muger at Roba	$38^{0}44^{'}05.65^{''}$	$9^{0}16^{'}06.79^{''}$	2554	30.0	0.34	177.8	0.49	0.51	0.50	206.86
EGS9	Muger at Gerbi	$38^{0}25^{'}10.76^{''}$	$9^{0}19^{'}56.01^{''}$	2624	65.0	0.95	394.2	0.52	0.51	0.51	95.61
EGS10	Muger at Sibilu	$38^{0}44^{'}44.49^{''}$	$9^{0}12^{'}16.26^{''}$	2551	375.0	6.63	843.2	0.43	0.49	0.46	203.20
EGS11	Muger at Muger	$38^{0}43^{'}52.34^{''}$	$9^{0}25^{'}04.76^{''}$	2547	489.0	9.76	464.6	0.46	0.51	0.49	56.42

*Note. **EGS1** represents. E-First word of the Author's name, GS1-Gauged station number*

The Baseflow contribution to streams for the majority of upstream stations (EGS1, EGS3, EGS4, EGS8, and EGS9) of both basins, located close to the rift border and surface water divide, has a high mean annual Baseflow index higher than 0.5. Accordingly, the streams in this area are recurrent because groundwater contributions dominate surface runoff. The fact that practically all of the streams in this area flow over the severely fractured volcanic rocks to contribute significantly to groundwater is the likely cause of the high BFI value.

BFI is relatively low for stations from the center part of the Upper Awash Basin (EGS2 and EGS5), due to the impermeable geologic units (ash and alluvium). Because of the fractured geologic units (Rift basalt and ignimbrite) together with NE-SW regional faults and lineaments, stations from relatively downstream areas of the Basins (EGS7, EGS10, and EGS11) have a moderate to high mean annual BFI between 0.35 and 0.5, indicating a significant groundwater contribution to the stream flow.

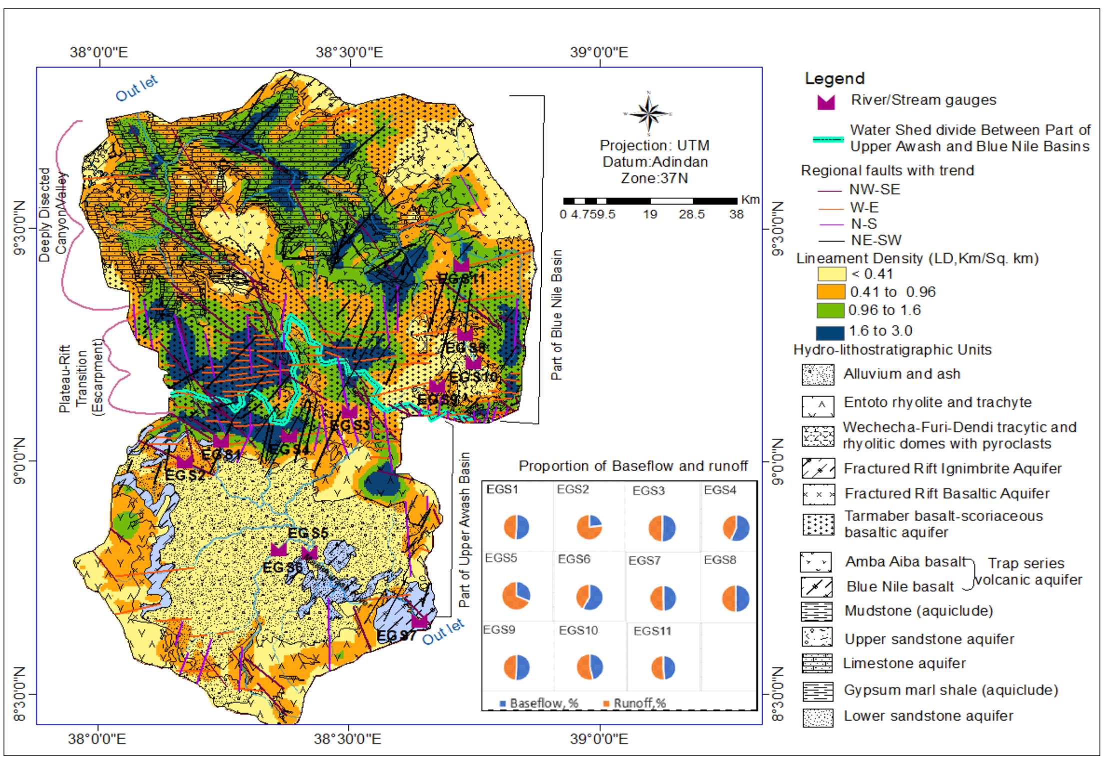

Fi

Figure 4.5 Groundwater contribution rates to rivers and streams in a pie chart, alongside their spatial distribution, geological setup, and lineament density

Correlating the Baseflow Index (BFI) with lineament density, particularly in structurally complex volcanic terrains like the study area, can substantially enhance our understanding of the aquifer-surface water relationship, as well as the delineation of recharge areas and their mechanisms. The lineament density (Figure 4.2) indicates that the escarpment and outlet zone of the PUAB exhibit high lineament density (LD ranging from 0.41 to 3.0 km/km^2), suggesting a favorable connection between the aquifer and surface water. In volcanic aquifers, a greater lineament density typically aligns with increased baseflow contributions, thereby making BFI a valuable proxy. Conversely, the central plain area of the Upper Awash Basin demonstrates relatively low BFI, low lineament density (LD < 0.41 km/km^2), indicating a weaker link between surface water and the aquifer.

4.4 Aquifer characteristics

4.4.1 Lithohydrostratigraphy

Geological units of the area were distinguished at depth using aquifer characteristics data from existing boreholes and geophysical study results. Since both the geology and hydraulic properties of the units are considered during characterization, the notable aquifers and confining (aquiclude) units were identified. Due to the similarity in hydrogeological properties, the lithologic logs from each water supply well were combined into hydrogeologic units to summarize the data.

The major aquifers associated with the Mesozoic Sedimentary rock units include a lower fine-grained sandstone aquifer with low primary and secondary porosity, except for some near-regional structures. The existence of an intercalated thick impervious marl unit at the lower portion of a limestone aquifer greatly affects its hydraulic conductivity, whereas the upper section is an excellent conduit at locations where it is exposed to the surface for direct recharge. The exception to this is that it is covered by layers of paleosol and impermeable mudstone, which prevent groundwater from entering from the aquifer units above it.

Except in some locations, where the principal porosity is covered by impervious thin mudstone and shale strata, which prevent direct recharge and groundwater transfer from the overlying aquifer (volcanic aquifer), the upper coarse-grained sandstone aquifer is the dominant sedimentary aquifer in the area. Springs that emerge from this unit close to lineaments and faults (Meragna, Jara-Midaworomo, Laganora-degem, Abote, and Salayish-ensaro springs) exhibit high discharge rates (up to 100 l/s). This aquifer also exhibits a little dip towards the south and southeast, just like the underlying limestone aquifer.

The lithologic log describes units as colluvial, alluvial, and ash, which are consolidated as superficial deposits (including alluvium and ash) forming the first upper-most aquifer. The second aquifer is characterized by a fractured rift basaltic system, consisting of various rock units, including weathered, vesicular, and fractured basalt. Acidic rock units, such as rhyolite, ignimbrite, and/or tuff, are classified together as a single hydro-stratigraphic unit, serving as an impermeable layer (aquiclude), which constitutes the third layer. Finally, the Tarmaber vesicular and scoriaceous basalt, often referred to as the scoriaceous basaltic aquifer, represents the fourth and most significant regional hydrogeologic unit. This unit is extensively distributed across the plateau, both at the surface water divide and at greater depths in the southern region. Hence, four principal hydrogeological units are recognized for parts of the Upper Awash groundwater system (Figure 4.5). These are. Superficial (mainly alluvial and ash) aquifers, fractured Rift basalt aquifers, acidic (Tuff, Ignimbrite, and rhyolite) acting as a confining unit, and fractured regional confined scoriaceous basalt aquifers. The lithologic and hydraulic characteristics of the identified hydrogeologic units are summarized in Table 4.2.

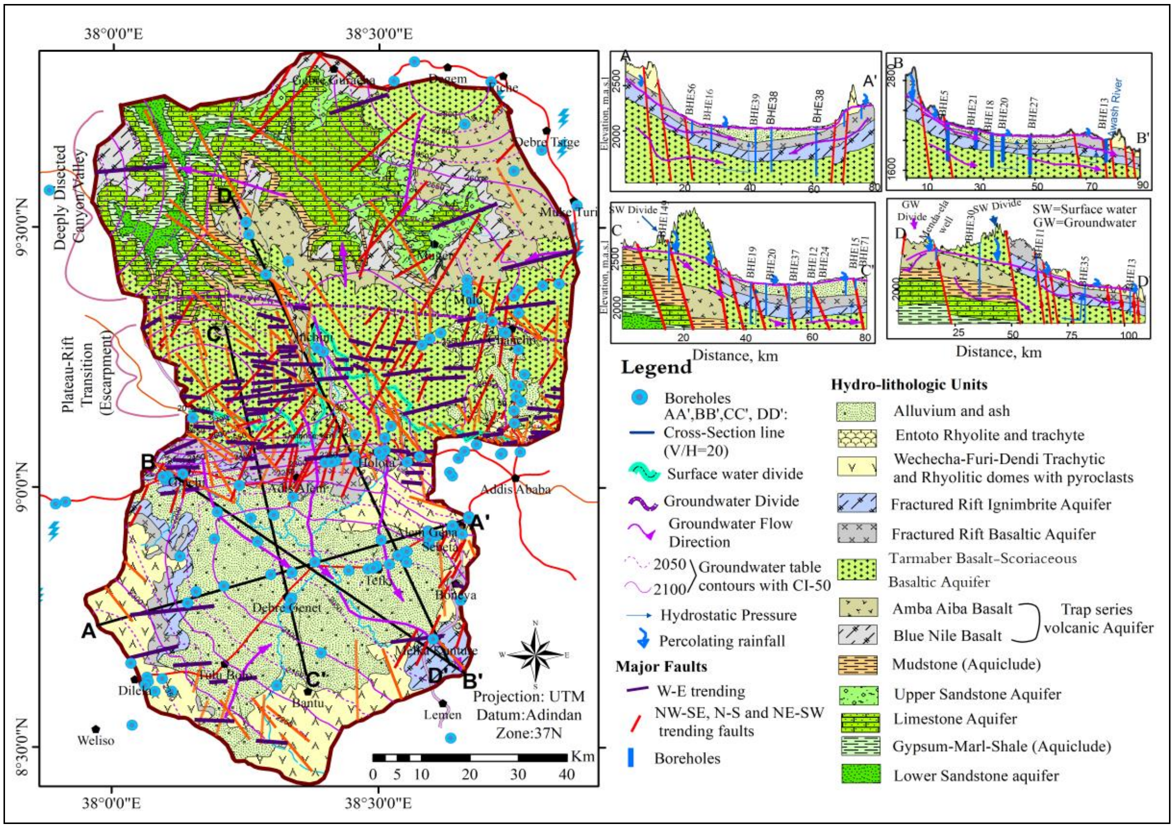

Figure 4.6 Hydrogeological maps of the area

4.4.2 Aquifer unit distribution

Superficial deposit aquifer is found mainly in the central part of the Upper Awash Basin, which has a small extent, shallow depth, and is composed of silty clay sediment of low permeability. It is recharged locally from rainfall and runoff and discharged into the upper basaltic aquifer. The alluvial aquifers do not form an independent aquifer, but it is interconnected with the upper basalt aquifer.

The fractured rift basalt aquifer is distributed in the northern and western periphery of the central plain part of the Upper Awash Basin and beneath the alluvial aquifer. It has a wide distribution with an average thickness of not more than 50m, forms an unconfined aquifer system, and is recharged locally where it outcrops and along faults and fractures. Most of the groundwater of this aquifer forms the Baseflow of the rivers in the upper Awash River system. In general, due to the similarity in hydraulic character of both superficial and fractured basalt aquifers, these two are treated as an unconfined aquifer for further simulation purposes.

The lithological logs of several water supply wells in the area and their environs revealed the presence of acidic volcanic units of variable thickness beneath the fractured rift basaltic aquifer. Such a unit is serving as an aquiclude (confining unit) in the majority of the study area. However, if the geologic structures (fault and lineament) affect it, it might be an aquifer in the northwestern and northern periphery (escarpment). It is a type of acidic volcanic unit that can be localized or regional. It includes pumice, ash, rhyolites, and ignimbrites sourced from the central volcanic of Menagesha, Furi, and Wechecha. It acts as a confining unit found between the upper unconfined and lower confined regional scoriaceous aquifers and is less fractured or faulted.

The regional basaltic aquifer, known as the Tarmaber basalt, is composed dominantly of scoriaceous basalt and Amba-Aiba basalt and occupies more than 95 % of the plateau and escarpments of the study area. Tarmaber and Amba-Aiba basalt formations are considered as one hydrogeological unit as per the analysis of pumping test data of water supply wells found in different areas, which have high transmissivity values and are hydraulically interconnected. Water supply wells drilled and tested at the central plain and the southeastern outlet (Melkakunture) parts penetrated the lower basalt aquifer at different depths. For instance, in the central part, the scoriaceous basalt was penetrated at 225 meters under the impermeable ignimbrite unit, and the groundwater level was raised to 2 meters. So many water supply wells were drilled and penetrated through such an aquifer. However, none of the boreholes fully penetrated this aquifer.

In general, analysis of the aquifer system in the area using evidence from geological and geophysical methods illustrates that the aquifer system of the area is a three-layer aquifer system composed of superficial deposits and fractured rift basaltic aquifers (treated as unconfined aquifer), aquiclude/confining unit (Ignimbrite, rhyolite, and trachyte), and the regional confined scoriaceous basaltic aquifer (confined aquifer) (Table 4.2).

Table 4.2 Summarized hydro-lithologic units (Data source: WEDSWS 2008 to 2017)

Hydrogeologic units	**Thickness range and estimated average thickness, m**	**Hydrogeologic characteristics**
Superficial (Alluvial and ash) aquifer (Layer-1)	5 to 80 (50)	☞ Characterized by about 50-meter thickness with low groundwater potential, recharged only from rivers, streams, and precipitation. ☞ It is commonly utilized for community water supply and is situated along major rivers and stream courses. ☞ Its yield varies from 0.5 to 4 l/s average of 1.5 l/s determined from daily community use using a hand pump, and its static water level varies from 5 to 21 meters below ground level. ☞ Obtaining representative pumping test data to evaluate its hydraulic properties is a challenging task. However, observations from the field and lithology logs of water supply boreholes indicate that it has high clay concentration, which leads to low permeability. ☞ It has between 88 and 488 mg/l of Total Dissolved Solids (TDS).
Weathered and fractured Rift basaltic aquifer (Layer-2)	50 to 180 (100)	☞ Distributed extensively in the USPAB as an unconfined with spatially varied thickness not more than 100 meters. ☞ Its average depth to groundwater level is 38.6 meters below the ground, transmissivity value in between 11 to 241 m^2/day, average of 76 m^2/day, discharge varies from 2 to 14.6 l/s with an average value of 5.2 l/s, and average TDS amount of about 237 mg/l. ☞ It is recharged locally through fractures where it outcrops and along primary porosities of the overlying superficial deposit aquifer.
Acidic volcanic unit (Layer-3)	60 to 150 [100]	☞ Based on their similarity in hydraulic behavior, it is the lumping of different lithologic units such as pyroclastic deposits, tuff, ignimbrite, trachyte, rhyolite, and pumice with thin intercalation of paleosol or sticky clay. ☞ It has a respective average depth to groundwater, discharge, and transmissivity of 56 meters, 3.9 l/s, and 17 m^2/day, and acts as a confining layer for the underlying regional scoriaceous basaltic aquifer.
Scoriaceous basaltic aquifer (Layer-4)		☞ The scoriaceous basaltic aquifer is the main fractured, pervious, and confined regional aquifer resulting from olivine-bearing scoriaceous lava, which favors strong groundwater storage and

Hydrogeologic units	Thickness range and estimated average thickness, m	Hydrogeologic characteristics
	>350 m	movement. ☞ Several water supply wells were drilled and tested, representing the scoriaceous basaltic aquifer, and none of them fully penetrated such an aquifer. Its thickness is more than 350 meters, and most of them are flowing (artesian). ☞ Its transmissivity value is between 18 to 2080 m^2/day average of 483 m^2/day. ☞ discharge varies from 9 to 98 l/s of average value 46 l/s, and TDS value in between 350 and 628 mg/l of average 468 mg/l.

4.4.3 Hydraulic properties of the aquifer

Knowledge of the hydrogeological characteristics of the rocks that make up the main aquifer systems is essential for the development and effective management of groundwater resources. The major hydraulic properties, such as piezometric head, transmissivity, hydraulic conductivity, storage coefficient, and aquifer thickness, are all spatially varied as a function of the geological and geomorphological settings, which need to be known to understand their spatial distribution. Only the hydraulic characteristics of the main aquifer units that correspond to a portion of the Upper Awash basin are discussed here because of data limitations.

This study attempts to use the interpolation technique based on the available measured data to fairly estimate the values in unmeasured points to analyze the spatial distribution of the hydraulic characteristics of the main aquifer units. Using the geostatistical analysis of ArcGIS 10.8, various maps illustrating the spatial variability were created based on the analysis of the available data for the corresponding parameters (ESRI, 2006).

4.4.3.1 Piezometric head distribution and flow direction

A groundwater table contour map is a graphical representation of the hydraulic gradient of the water table or potentiometric surface. Creating a groundwater table contour map is an important task in groundwater resource assessment and management, which involves plotting the elevation of the water table across an area and is used to interpret groundwater gradients, flow directions, fluxes, and velocities (Fetter, 2001; Woessner, 2020). Hence, from groundwater table contour lines, which are known as equipotential lines, the direction of groundwater flow perpendicular to such equipotential lines is directly constructed (Heath, 1983). Furthermore, it is important to understand the hydraulic link between the surface water and the aquifer system of the area.

In this study, the groundwater level or potentiometric maps for the unconfined aquifer and piezometric map for the confined aquifer are created using a one-time measurement of groundwater level data. To generate temporally (monthly/seasonally) varied groundwater level maps to visualize changes in equipotential lines and infer flow direction, properly monitored time-series head data is required, and it is difficult to address such notions in detail in this study. It is prepared by taking the difference between the topographic elevation and the depth-to-groundwater level, which gives the groundwater depth to the water level above the mean sea level (datum).

The present study considers head data from water wells with a depth of less than 150 meters (50 water supply wells), representing the unconfined aquifer system, and more than 250 meters (100 water supply wells), representing the area's deep confined aquifer system. A potentiometric surface for the unconfined and deep confined aquifers was generated independently using the Kriging interpolation technique applied to a set of regularly spaced boreholes with groundwater level point elevation in an ArcGIS environment.

Most of the time, the groundwater levels measured from boreholes drilled in several geologic formations show varying groundwater levels, indicating that faults connect the groundwater of different geologic units. Boreholes drilled through the unconfined aquifer (composed of alluvial, tuff, ash, and fractured basalt) have a depth to groundwater level 5.3 to 26.7 meters below ground level (m.b.g.l) or 2042 to 2350 m.a.s.l. whereas, from the regional deep confined aquifer (composed of highly fractured basalt and scoriaceous basalt), depth to a piezometric level ranges from mainly artesian conditions to a maximum of 45.9 m.b.g.l or 2001 m.a.s.l (at the southeastern outlet portion) to 2250 m.a.s.l at the edge of the escarpment. In light of this difficulty, an effort was made to create a groundwater level contour map (Figure 4.7a) for the unconfined aquifer and a piezometric level contour (Figure 4.7b) for the regional confined aquifer. The groundwater level contour maps illustrate similar groundwater flow directions towards the southeastern (outlet) part of the study area.

In general, the interpolated groundwater level contour map demonstrates a steep hydraulic gradient in the northern and northwestern parts and a gentle, wider, and very shallow gradient in the central and outlet parts of the model area. Even though the regional topographic gradient, local barriers, lithology, and geologic structures regulate the direction of the groundwater flow.

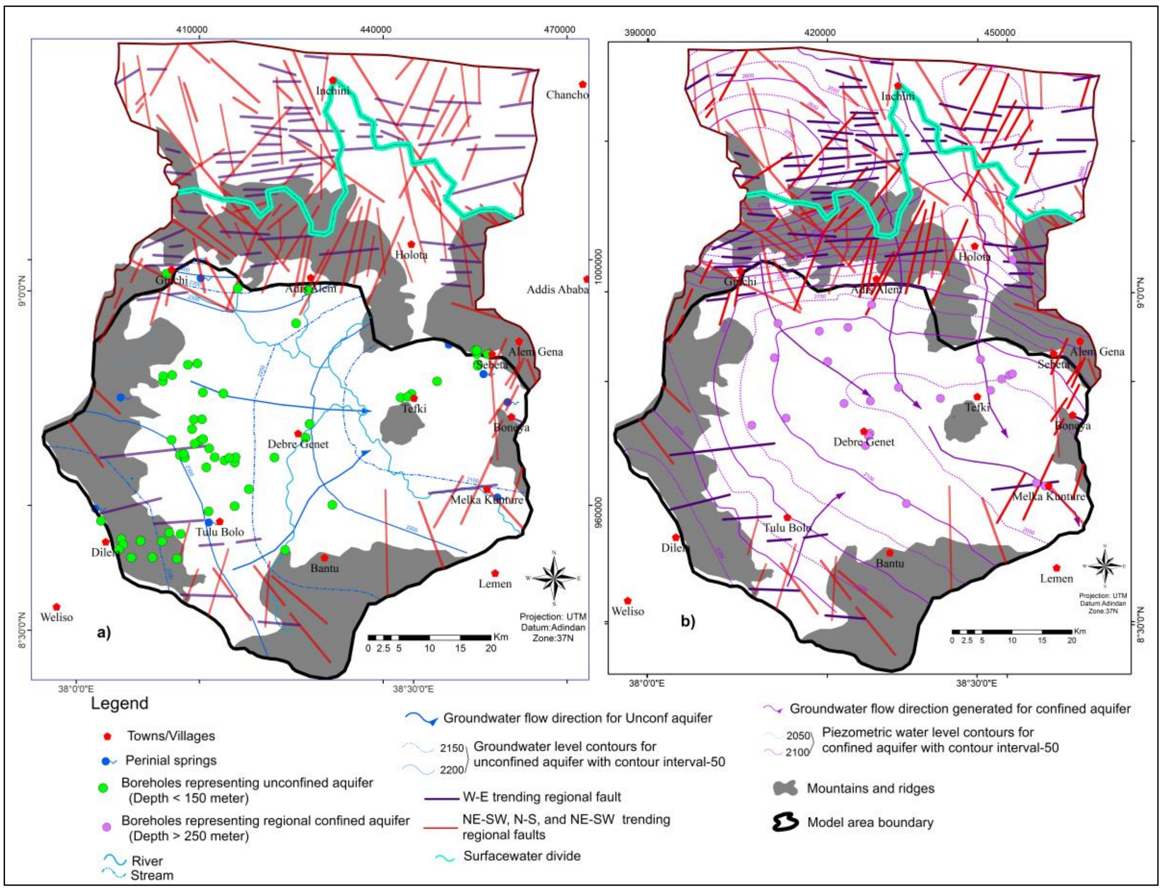

Figure 4.7 Groundwater level contour maps (m.a.s.l) with flow directions for a) Unconfined and b) Confined aquifer systems.

3.4.3.2 Transmissivity

Transmissivity is a crucial parameter in groundwater resource evaluation to determine the rate of groundwater flow, yield of wells, and the spread of contaminants in an aquifer (Driscoll, 1986). It is influenced by the thickness and permeability of the aquifer material and the viscosity and density of the groundwater. Knowledge of the transmissivity of the area helps in determining optimal well spacing and pumping rates. It is typically estimated through pumping tests, as pumping water from a well at a controlled rate and measuring water level changes in the pumping well and nearby observation wells (Freeze & Cherry, 1979).

All water supply wells (34 in #), raw pumping test and recovery data (72 hours) were gathered and analyzed using Aquifer Test Pro (Waterloo Hydrogeologic Inc., 2002) software version 3.5. Since the aquifer's storage term cannot be determined from single-well tests, the available data are only used to estimate hydraulic conductivity and transmissivity. It may be challenging to estimate storage values using analytical approaches in the absence of observation wells (Kruseman & De Ridder, 1990). The constant rate test's time drawdown and recovery data were used to compute the aquifer's transmissivity. As a result, the Cooper-Jacob time drawdown approach (Cooper & Jacob, 1946) is used to analyze pumping test data, and Theis's recovery technique (Theis, 1935) is used to analyze all of the water supply wells' recovered data. As a result, the transmissivity value for the unconfined and confined aquifers is in the range of 18 to 248 m^2/day and 5.4 to 2080 m^2/day, respectively.

4.4.3.3 Hydraulic conductivity

Hydraulic conductivity is a key component in many groundwater flow equations used to simulate the groundwater movement, predict water table changes, estimate well yields, and assess contaminant transport. Factors that control the hydraulic conductivity of the aquifer unit are grain size and its distribution, porosity, fluid properties (density, viscosity), fracturing, clay content, and degree of saturation. Accordingly, it varies significantly within an aquifer, both horizontally and vertically, with values from 10^{-8}

m/day for unfractured metamorphic rocks to 10^3 m/day for well-sorted gravels (Freeze & Cherry, 1979; Anderson & Woessner, 2015).

Measurement of hydraulic conductivity is challenging, primarily due to its vast range across different rock types. This variability can span several orders of magnitude, making it difficult to accurately characterize and compare different geological formations. This immense range presents significant challenges in measurement and interpretation. Even within a single rock type or formation, hydraulic conductivity can vary significantly due to factors like fractures, weathering, and local variations in composition. Measurements taken at different scales often yield different results due to the influence of larger-scale features like fractures and bedding planes. Different measurement methods can yield varying results for the same formation. It is a crucial notion in groundwater development and management, which is analyzed from properly conducted pumping test data.

The most common measurement techniques for hydraulic conductivity used in practice can be broadly categorized into field methods and laboratory methods. Each of these methods has specific applications and limitations. For instance, field methods generally provide more representative results for larger scales but can be more expensive and time-consuming. Laboratory methods offer more controlled conditions but may not capture the full complexity of in situ conditions. For this study, hydraulic conductivity for the two major aquifer types (unconfined and confined) is analyzed using one of the most widely used techniques of pumping test and recovery test data (from 34 water supply wells) and hydraulic conductivity values from previous works (WWDSE,2009; Azagegn, 2015).

The formula K = T/b, where *K* is hydraulic conductivity, *T* is transmissivity (m^2/day), and b is aquifer thickness (m), is commonly applied to confined aquifers. In practice, borehole screen length is often used to approximate b. However, accurate estimation of *K* is complicated by factors such as misaligned screen casing, inadequate gravel packing, and poor well development. These issues are further compounded in areas with multi-layered aquifer systems, where a single borehole may tap multiple water-bearing units due to screens installed across varying depths. In unconfined aquifers, saturated thickness fluctuates both spatially and temporally with changes in the water table, making the application of the formula more complex. It requires either site-specific saturated thickness measurements or representative averages for the area. In this study, hydraulic conductivity was calculated by deriving transmissivity from pumping and recovery test data, while the average saturated thicknesses were carefully validated using borehole geophysical logs correlated with screen intervals, ensuring accurate and location-specific estimates.

In this work, an effort was made to calculate the hydraulic conductivities of thirty-four (34) water supply wells, of which twenty-two (23) represent the confined aquifer (wells deeper than 250 m) and eleven (11) represent the unconfined aquifer (wells shallower than 150 m) using transmissivity data analyzed from pumping test and recovery data. In addition, seventeen (17) hydraulic conductivity values are obtained from previous works.

Based on the analysis of pumping and recovery test data, hydraulic conductivity in the range of 0.33 m/d to 17.9 m/d is obtained, which represents the confined aquifer system and for shallow to intermediate depth (Depth < 150 m) or unconfined aquifer shows the value in the range of 0.06 m/d to 1.76 m/d. Spatially distributed hydraulic conductivity zones were generated, mainly for unconfined (Figure 4.8a) and confined aquifer (Figure 4.8b) systems, using point (well site) hydraulic conductivity values as an input for geostatistical analysis of the kriging interpolation technique in the ArcGIS tool.

In volcanic terrains, the variability of hydraulic conductivity and transmissivity is influenced by several key factors, including the density of fractures, the stratigraphy of lava flow layers, and the heterogeneity of pyroclastic materials. Spatially distributed recharge values indicate a discernible trend in hydraulic conductivity, which generally increases towards the escarpment and the southeastern outlet region of the study area, moving away from the central plain.

This pronounced increase in hydraulic conductivity correlates with the presence of heavily fractured basaltic formations that are predominantly exposed in both the northwestern and southeastern margins of the model area. These regions exhibit a high degree of permeability due to the complex interplay of geological structures.

Additionally, fault zones within these volcanic landscapes often demonstrate significant anisotropy in hydraulic conductivity, meaning that conductivity is not uniform in all directions. Specifically, higher hydraulic conductivity is typically observed along the orientation of the fault strike, where fractures are preferentially aligned, facilitating enhanced fluid movement.

Hydraulic conductivity values derived from pumping and recovery test data in this study were found to be lower than those reported in the literature for similar volcanic aquifer systems. This discrepancy is attributed to the inherent fracture heterogeneity**,** eruption styles**,** and lithological variability that characterize volcanic terrains. Transitions between vesicular, aphanitic, and pyroclastic units create complex and unpredictable flow paths, resulting in significant differences in permeability and porosity across the area. A comparative review of literature values highlights this variability:

- Hawaiian basalt aquifers exhibit hydraulic conductivity values ranging from 1 to 2,500 m/day**,** with ±30 to 40% uncertainty due to fracture connectivity and test scale (Rotzoll et al., 2007).
- Northern Greece volcanic systems show hydraulic conductivity values between 0.19 and 216 m/day, influenced by facies transitions and limited borehole data (Rapti, 2025).
- In Ethiopia's Upper Blue Nile Basin**,** hydraulic conductivity ranges from 0.165 to 49 m/day**,** with ±25% uncertainty linked to weathering and interbedded sedimentary layers (Tafesse, 2019).

In contrast, this study reports K values of 0.06 to 1.76 m/day for the unconfined aquifer, and 0.33 to 17.9 m/day for the confined aquifer, with an estimated ±30% uncertainty. These values are considered reasonable for further analysis, given the geological complexity and data limitations. Incorporating uncertainty into hydraulic conductivity characterization is essential for improving model reliability and capturing the spatial variability inherent in volcanic aquifer systems.

Moreover, vertical faults in a plateau and escarpment have the potential to serve as extensive conduits for deep groundwater recharge, allowing for the migration of water from surface reservoirs to deeper aquifer systems. Considering the importance of these geological features, incorporating spatially distributed recharge values into groundwater modeling is crucial for achieving accurate and realistic simulations of groundwater flow dynamics in volcanic terrains. Such detailed modeling is essential for effective groundwater management and resource planning in these complex environments. Vertical hydraulic conductivities were approximated from their horizontal conductivity multiplied by 1% to 10% for further simulation (Freeze & Cherry, 1979; Anderson & Woessner, 2015).

4.4.3.4 Storage coefficients

Knowledge of the storage coefficients is critical for computing the available groundwater storage, estimating aquifer yields, delineating well fields, recharge estimation, and groundwater flow modeling, including contaminant transport modeling. Specific yield (S_y) and specific capacity (S_c) for unconfined aquifers and specific storage (S_s) and storativity (S) for confined aquifers are physical characteristics that characterize an aquifer's capacity to release groundwater from storage when the hydraulic head decreases. When evaluating groundwater resources, these characteristics are frequently ascertained by combining data from laboratory experiments and pumping tests (Freeze & Cherry, 1979).

The amount of water that gravity drainage releases from storage per unit aquifer surface area per unit groundwater table decline is known as the specific yield. It represents the drainable porosity of an unconfined aquifer and is mathematically expressed as $S_y = V_w/V_t$, where. V_w = volume of water drained by gravity, V_t = total volume of aquifer material. It is mainly governed by grain size distribution, pore size, and shape, pore connectivity of alluvial, and the degree of weathering or fracturing, with their connectivity in volcanic aquifers. The storage coefficient of an unconfined aquifer is approximately equal to the specific yield. Computation of the storage coefficient using analytical methods is difficult due to the absence of observation wells during pumping tests. In the study area, all pumping tests were carried out without an observation well water level record. However, the specific yield value obtained for unconfined aquifers using exploratory wells is in the range of 0.01 to 0.3 with an average of 0.15 (WWDSE, 2008). It is from a few unevenly distributed wells and does not represent the overall study area.

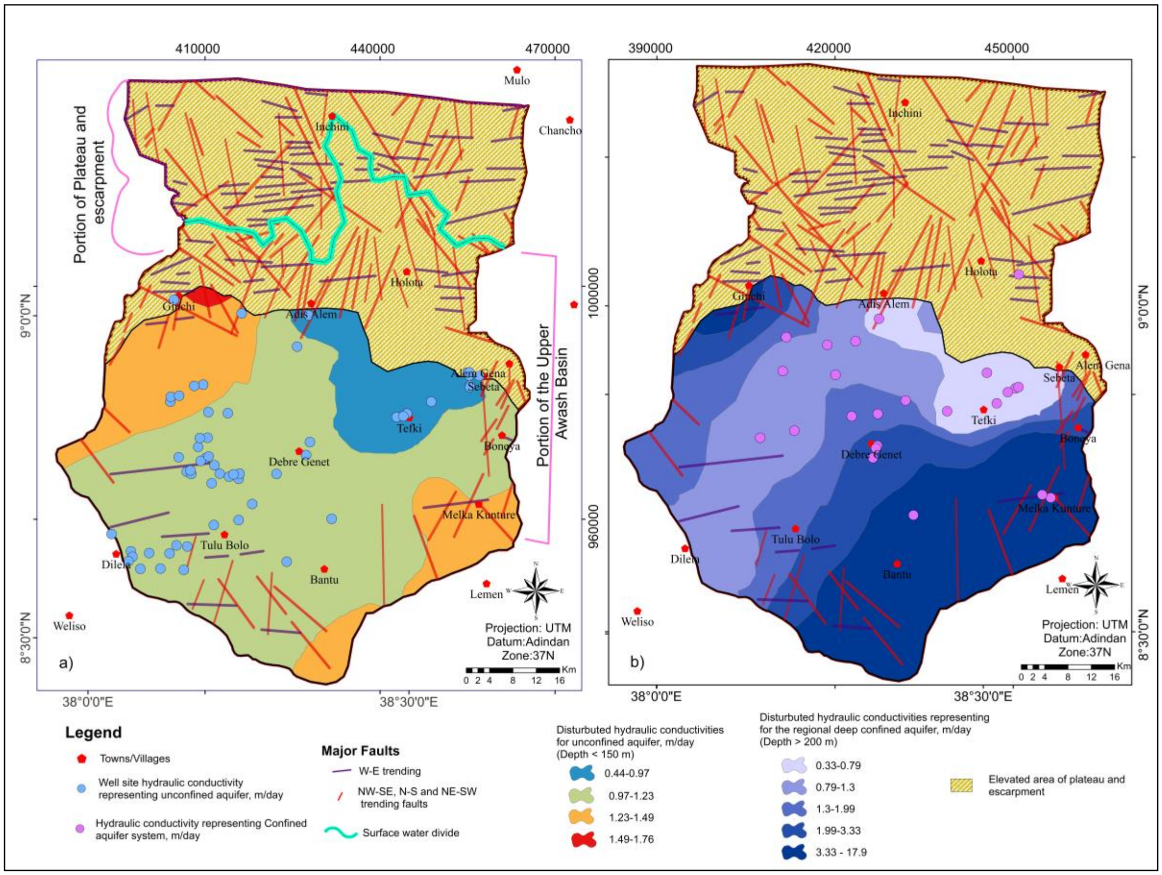

Figure 4.8 Distributed representative hydraulic conductivity zones generated for a) unconfined, and b) confined aquifer systems

Specific storage is the volume of water released from storage per unit volume of aquifer per unit decline in hydraulic head under confined conditions. It represents the capacity of an aquifer to release water through compression of the aquifer skeleton and expansion of water. This study uses the values of the following expression from the literature to calculate the storage coefficient, also known as the storativity, of the confined fractured scoriaceous basaltic aquifer.

$$S = Ss * b, \text{ where } Ss = \rho g (\alpha + n\beta)$$

Where S is a storativity or storage coefficient; S_s is specific storage; b-aquifer thickness (300 m); ρ is density of water (1000 kg/m^3); g is gravitational force (9.8 m/sec^2); α is aquifer compressibility (10^{-10} m^2/N); η is porosity (0.2); β is fluid compressibility ($4.4x10^{-10}$ m^2/N) (Freeze & Cherry, 1979). Hence, the confined aquifer's storage coefficient is 5.53 x 10^{-4}.

A review of previous works was made related to the analytical computation of storage coefficient for confined aquifer system using group pumping of two deep water supply wells with simultaneous water level monitoring in two observation wells for 3 days at Mojo wellfield for Adama town water supply project (MS consulting, 2023). The main reason for reviewing such results is that the hydrogeological and geological configuration is similar to that of the current study area. The method used to compute the storage coefficient is the Cooper-Jacob Straight-Line Method (Cooper & Jacob, 1946) with the following step-by-step computation. The principal data used for further analysis were pumping rate (Q), time-drawdown data from two observation wells, distances of observation wells from pumping well (r_1 and r_2), and drawdown measurements (s_1 and s_2), followed by computation of transmissivity, and time intercept where drawdown is zero (t_0).

Computation of the storage coefficient for the confined aquifer system was carried out using a synchronized group pumping test of two boreholes (named in the report, BH-20 & BH-21) pumped simultaneously and synchronized (started and ended at the same time) with two observation wells (BH-22 and BH-07).

Table 4.3 Pumped and observation wells data for storage coefficient computation (*Source: MS consulting, 2023*)

No	Group Pumped wells	Observation wells distance from pumped wells, m		Maximum drawdown recorded on observation wells after 72 hours of pumping, m		Discharge, L/s
		BH-22	BH-07	BH-22	BH-07	
1	BH-20	900	1367	1.66	0.42	95
2	BH-21	500	920			105.87

Since there was minimal drawdown on BH-07, only data from observation well BH-22 were utilized for additional analytical calculations (Table 4.3). BH-07 is geographically far from pumped wells; its negligible drawdown after 72 hours indicates limited hydraulic connectivity or influence under current test conditions. In contrast, BH-22, despite a minimal separation from the pumped wells, exhibited a more pronounced drawdown response, justifying its inclusion in the analysis. This decision aligns with best practices in aquifer test interpretation, which prioritize hydraulic relevance over spatial proximity (Kruseman & de Ridder, 1994; Domenico & Schwartz, 1998; Fetter, 2001). Thus, the transmissivity (T) of the confined aquifer system was calculated using the $T=2.303Q/4\pi\Delta S$ relation, yielding 1,389.8 m^2/day, and the change in drawdown per log cycle (ΔS) was determined from the drawdown vs. log time plot relation, which is 2.29m.

The formula $\log (r_{eq}) = (Q_1\log(r_1) + Q_2\log (r_2)) / (Q_1 + Q_2)$ is a well-established method for calculating the equivalent radial distance in dual-well pumping scenarios. This formula derives from the superposition principle applied to radial flow in confined aquifers. In this context, the equivalent distance between observation wells and multiple pumping wells is determined through a logarithmic weighted average based on radial distances and discharge rates (Driscoll, 1986; Kruseman and de Ridder, 1994; Domenico and Schwartz, 1998; Fetter, 2001), which preserves the analytical integrity of single-well solutions in dual-well scenarios. This approach is particularly relevant when applying analytical solutions such as Theis or Cooper-Jacob to systems with multiple pumping wells, and is widely accepted in hydrogeological practice for simplifying multi-well interference analysis. Accordingly, the equivalent distance (r_{eq}) between observation wells and pumped wells is computed and results in 682m.

Finally, the storage coefficient (S_c) is calculated using $S_c = 2.25\ T\ t_o/r_{eq}^2$, where S_c-is the storage coefficient (dimensionless), T is transmissivity (m^2/day), t_o- is the time intercept where drawdown is zero (days) from the drawdown vs log time plot relation (766.6 minutes or 0.53 days), and r_{eq}-is computed above. Thus, the storage coefficient (S_c) of the confined aquifer of the Mojo area, downstream outside of this study area, is 0.045.

In general, the lack of water level recording in observation wells during pumping tests makes it challenging to estimate storage coefficients using an analytical technique, not only in this study but throughout the country. Here, an attempt was made to calculate a storage coefficient, mainly for confined aquifer systems, by utilizing data from the literature as input into the empirical formula, resulting in 0.000553. In addition, a previously calculated storage coefficient using a pumping test with an observation well is 0.045, which represents this study area due to the similarity in hydrogeological characteristics.

When comparing the two sets of results, it becomes clear that the storage coefficient calculated using data from observation wells and pumping tests offers a more accurate representation of the study area than the value derived from the literature. This is largely because practical groundwater level data from a similar geological formation, the confined scoriaceous basalt aquifer, was utilized effectively. As a result, a storage coefficient value of 0.045 has been established for the confined aquifer system, which will be employed in subsequent groundwater flow simulations. However, the lack of sufficient point data has made it impossible to create a spatially distributed set of storage coefficient values, limiting the depth and precision of the modeling process.

4.5 Hydrogeochemical and Isotopic Signatures

4.5.1 Hydrogeochemical facies, Residual alkalinity (RA), and Ca^{2+} / Na^{+} ratio

The hydrochemical signature of groundwater in the study area is primarily governed by the aquifer's chemical composition and prevailing climatic conditions. Aquifer mineralogy determines the type of dissolved constituents through processes such as mineral dissolution, ion exchange, and extended water–rock interaction along deeper flow paths. Climatic factors, in turn, regulate the concentration and variability of these constituents via recharge and dilution, evapotranspiration, seasonal fluctuations in total dissolved solids, and temperature-driven chemical weathering. In essence, aquifer composition provides the source of ions, while climate dictates their concentration and temporal variability (Davis & De Wiest, 1966; Todd, 1980). Hydrogeochemical techniques, thus, shed light on the groundwater flow system by analyzing the variations in hydrochemical facies throughout the groundwater flow path. In this work, groundwater chemistry datasets (104 from wells and 20 from springs) were presented graphically using a trilinear (Piper, 1944) diagram to define the variation in hydrochemical patterns along the groundwater flow paths.

Accordingly, four distinct hydrogeochemical facies were identified (Figure 4.8a). mixed $CaHCO_3$/$CaMgHCO_3$, $CaNaHCO_3$, $NaCaHCO_3$, and $NaHCO_3$. The residual alkalinity (RA), which is the change amid the value of HCO_3 and Ca^{2+}+Mg^{2+}, the ratio of (Ca^{2+}+Mg^{2+}) and (Na^{+}+K^{+}), all in meq/l, and RA & Total dissolved solids (TDS) against the variation in groundwater types along the route are additional characteristics of aquifers' connectivity. As groundwater flows in a nearly NW to SE direction, its hydrochemical facies evolve from $CaHCO_3$ or $CaMgHCO_3$ to NaHCO3 water types, the Ca^{2+}/Na^{+} ratio gradually decreases, RA and TDS increase in general (Figure 3.8b, 3.8c, and 3.8d).

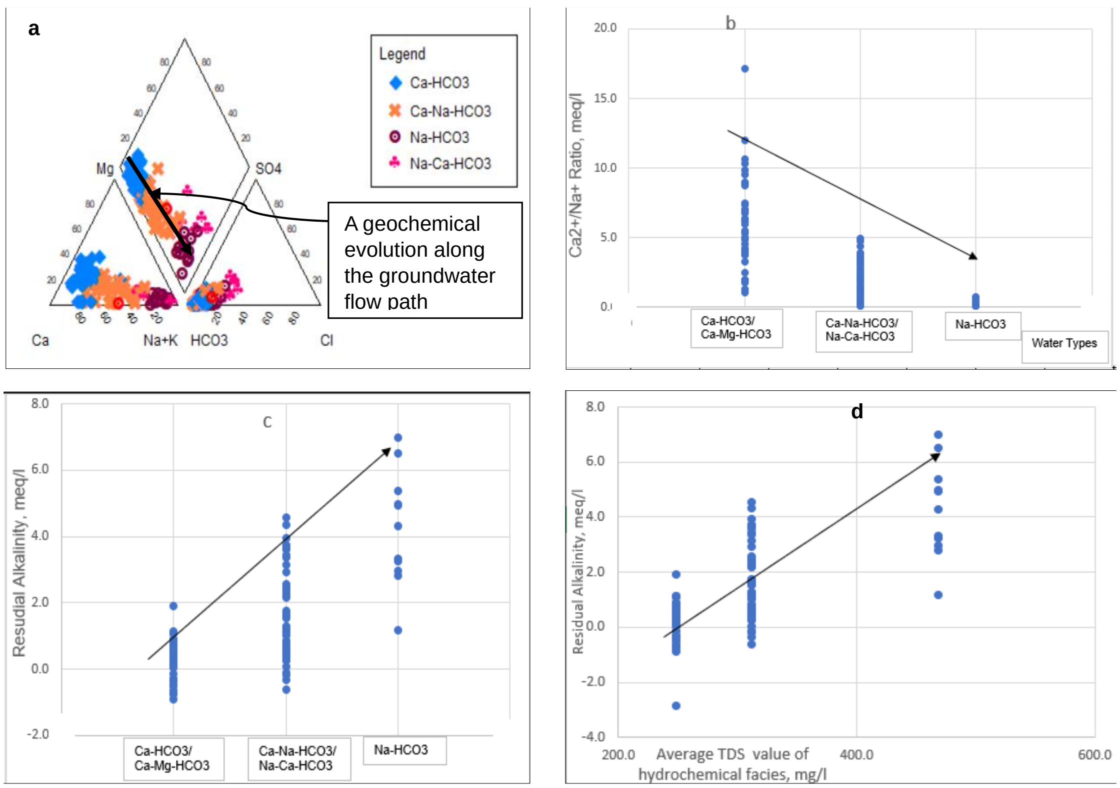

Figure 4.9 a) Trilinear diagram showing existing groundwater types, b) Ca2+/Na+ ratio vs. Water types, c) Residual Alkalinity (RA) vs. Water types, and d) RA vs average TDS of water types along the groundwater flow paths

Higher Ca^{2+}/Na^{+} ratios (>5), lower RA (<2.0), and TDS (<200 mg/l) are seen in the groundwater of the plateau and escarpment zones. Through dense fractures, meteoric water has recently entered the groundwater system in these regions, indicating that the waters are still in the preliminary phase of geochemical evolution (Figure 4.8a to d). Such results exemplify that the dominant portion constitutes a recharge area for the surrounding aquifers. Furthermore, in some deep boreholes and springs (Boreholes. BHE2, 126, 129, 136, 142, 143, 147, 148, 151, 152, 153, and springs. SPE6, 7, 15, 16, 18) in the same area, exceptionally high values of Ca^{2+}/Na^{+} ratio with relatively high TDS (TDS > 300 mg/l) and high RA (> 2.0) values were attained. This confirms that the recharge area for the deep regional groundwater system at USPAB extends beyond the surface water divide, validating the groundwater outflow from the eastern edge of the Abbay Basin to the Awash Basin.

4.5.2 Agglomerative Hierarchical Clustering (AHC)

Further analysis was made by clustering the groundwater hydrochemical dataset using Agglomerative Hierarchical Clustering (AHC) of XLSTAT (Stat Soft Inc., 2008) to come up with four clusters (Figure 4.9). Groundwater in Cluster-1 and Cluster-3 is nearly similar, characterized by an average TDS of about 289 and 295 mg/l, respectively. They are commonly signified by water types of mixed $CaHCO_3$ or $CaMgHCO_3$ (Cluster-1) and $CaNaHCO_3$ (Cluster-3) associated with water samples analyzed for shallow systems (springs and shallow wells) that fall dominantly in a plateau and transitional escarpment, circulating in the shallow aquifer system (upper basaltic and alluvial aquifers). Based on the groundwater evolution principle (Chebotarev, 1955; Hem, 1985; Edmunds et al., 2006), water in these clusters represents recently recharged water comprising a preliminary phase of geochemical evolution.

In the same region, shallow wells and springs that originate from the basaltic aquifer, influenced by small-scale faulting, are classified by specific water types. This highlights that plateaus and escarpments are recharge areas for the rift basaltic aquifers. On the other hand, shallow wells (BHE 50, 74, 75, 88, 90, 94, 97, 101, 106, 107, 115, 116, 117, and 125) drilled in alluvial and Rift basaltic aquifer (Depth < 150m) of central plain part of the southern portion have mainly $CaHCO_3$ water type of low RA and high Ca / Na ratio (2.3 to 6.2) signifies direct recharge from modern meteoric water.

The second cluster, represented by dilute chemistry of low average TDS concentration (about 165 mg/l) and mixed groundwater types ($NaCaHCO_3$) encountered partly in plateau (deep wells. 243 to 654 meters), transitional Rift margin zones (medium depth wells. 106 to 201 meters), and springs (SPE3,5,8,9, and 10) emanating along fault lines imply the groundwater in this zone are the result of cation exchange process for groundwater samples associated with ignimbrite and/or rhyolite geologic units. Most of them are situated in the transitional escarpment zone associated with a marginal fault system, which verifies that the transitional escarpment zone, accompanied by high fracture density bounding the plateau from the northern side, is also the recharge area for the fractured Rift basalt and Ignimbrite aquifer. A very low TDS value is attributed to the direct recharge from the meteoric water through the regionally interconnected faults.

Cluster-4 is characterized by hydrochemical facies of mineralized $NaHCO_3$ water type from deep wells (more than 336-meter depth) in plateau and transitional escarpment zones along local and regional faults, which include both cold and hot groundwater tapping dominantly from a highly fractured scoriaceous basalt aquifer have relatively high TDS of average concentration being 468 mg/l. Some deep wells with low TDS groundwater on the plateau and on the southern sides show intensive cation exchange in the scoriaceous aquifer units that replace the entire Ca^{2+} with Na^{+} at a clay layer interface, with a short residence time proving direct infiltration of rainwater into the deep aquifer system. Boreholes (BHE18-20,22-24,27,28,51,91,120,134) in this group are highly mineralized (TDS. 350 mg/l to 628 mg/l) artesian wells found mainly in the southern part, which could be an outcome of the groundwater evolution from $CaHCO_3$ to $NaHCO_3$ through $CaNaHCO_3$ and $NaCaHCO_3$ facies laterally through the regional flow route, proving the interconnection between the highland and part of the southern confined deep groundwater system.

Previous works carried out in Awash and the adjacent Blue Nile Basins support this outcome as well (Kebede et al., 2005; Ayenew et al., 2007; Yitbarek et al., 2012). Moreover, there are also a few mineralized water samples located mainly in the central southern part, characterized by $NaHCO_3Cl$ and $NaHCO_3SO_4$ water types from deep groundwater sources (TDS > 800 mg/l) also illustrates the availability of different aquifers and aquifer connectivity between highlands and escarpment zones.

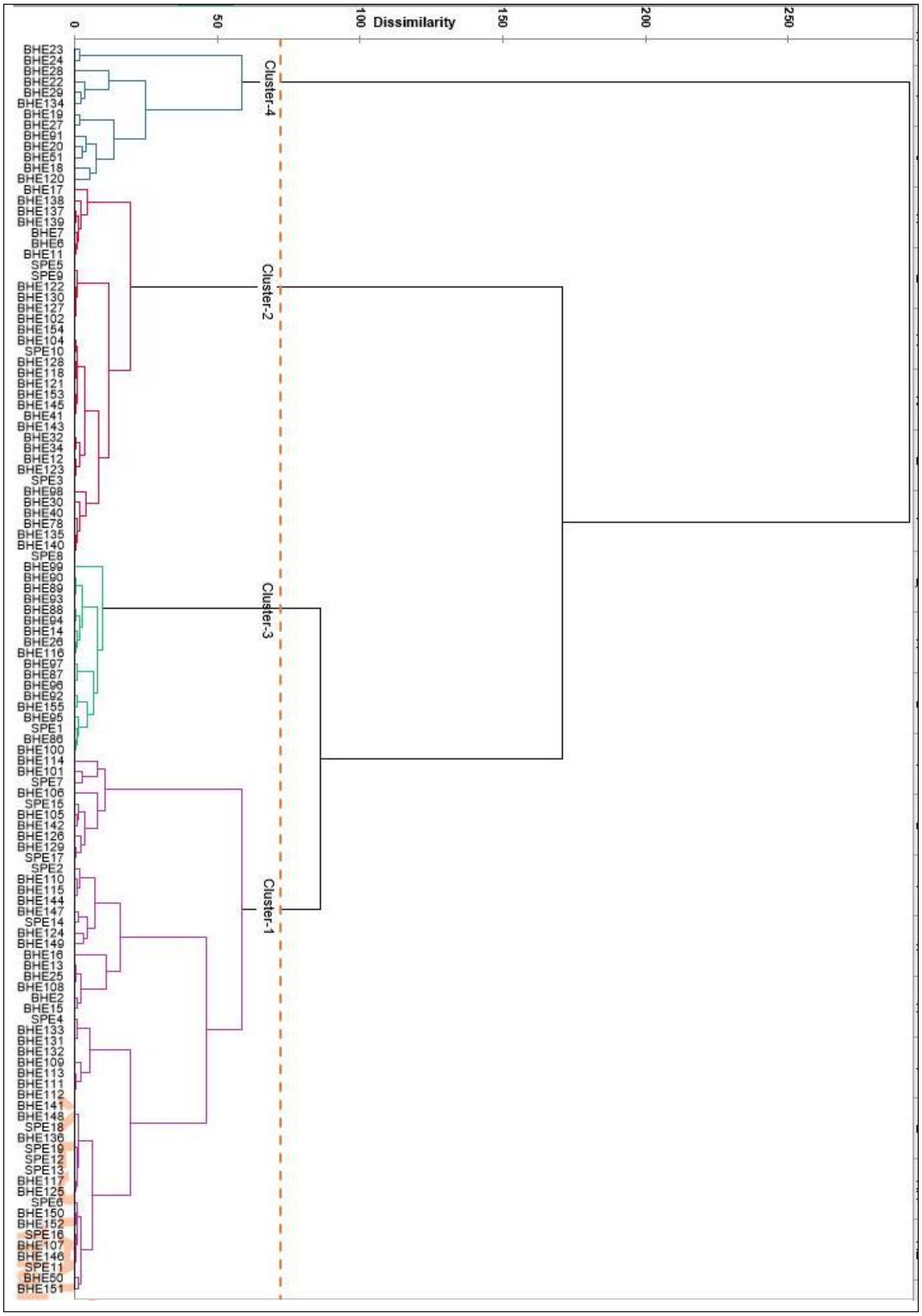

Figure 4.10 Agglomerative Hierarchical Clustering (AHC) dendrogram showing grouping of the hydro geochemical data

4.5.3 ^{222}Rn evidence

Environmental tracers of surface water and groundwater vary spatially along the groundwater flow direction in general and are primarily influenced by the surrounding rock or soil type, residence time, precipitation intensity, and temperature, all of which are associated with hydrogeochemical processes (Singh et al., 2011; Brindha et al., 2013). Among the methods recognized for determining groundwater and surface water connections, ^{222}Rn is the most prevailing unreactive tracer, formed through the ^{226}Ra to ^{238}U natural radioactive decay process with a short half-life (3.8 days) of higher concentration in groundwater (Ellins et al., 1990; Hamada & Komae, 1994; Clark & Fritz, 1997; IAEA, 2000; Cook, 2003; Hatch et al., 2006; Cartwright et al., 2011, Cartwright et al., 2014a; Fetter, 2018; Petermann et al., 2018). The low level of ^{222}Rn in the river indicates that the water is not from local or adjacent groundwater discharge. In contrast, the presence of the short-lived high ^{222}Rn in surface water consistently shows that groundwater is feeding the river within its measured reach (Cartwright et al., 2011).

Moreover, permeability conditions in the interface zone are crucial for mediation, and groundwater-surface water exchange may also have a significant effect on either side of the hydrological zone water quality (T´oth, 1963; Conant et al., 2019; Banks et al., 1995; Fetter, 2018). Thus, to preserve the existing water resources, it is important to know the exchange mechanisms and rate. In this section, an effort has been made to identify and characterize the groundwater-surface water interaction zones using results from a well-employed and proven environmental tracer, ^{222}Rn.

Of the 44 in situ ^{222}Rn measurements obtained during the non-rainy season, three came from boreholes, four from springs, and thirty-seven from various river or stream reaches. Similarly, during the rainy season, measurements were made at 15 distinct river or stream sections (Figure 4.11).

The ^{222}Rn measurement results reveal notable variations along the major rivers (a portion of the Upper Awash and Muger) and their tributaries during the course of the recording periods. As a whole, the river and streams ^{222}Rn values range from 17.1 to 1467 Bq/m^3

during the non-rainy season, while it is in the range from 2.7 to 468 Bq/m^3 in the rainy season.

According to qualitative classification, higher values, exceeding 400 Bq/m^3 for both wet and non-rainy seasons, were found mostly in the vicinity of the Upper Awash Basin's outlet sections and moderate to high (ranging from 100 to 400 Bq/m^3) along the escarpment between adjacent surface water divide zones. ^{222}Rn values were relatively low to very low (2.7 to 100 Bq/m^3) in the lowlands of the nearby Blue Nile Basin and the central plain part of the Upper Awash Basin (Figure 4.12).

The main reason for the very high ^{222}Rn values obtained (200 to 477 Bq/m^3 in the rainy season and 465 to 1467 Bq/m^3 in the non-rainy season) in the southern extreme portion of the main Upper Awash Basin is related to the regional groundwater discharge due to highly pervious basaltic geologic units resulting from regional geologic structures (faults and lineaments) (Figure 4.12). On the other hand, these results in this particular area demonstrate that it is the regional groundwater outlet zone with a relatively prolonged residence time.

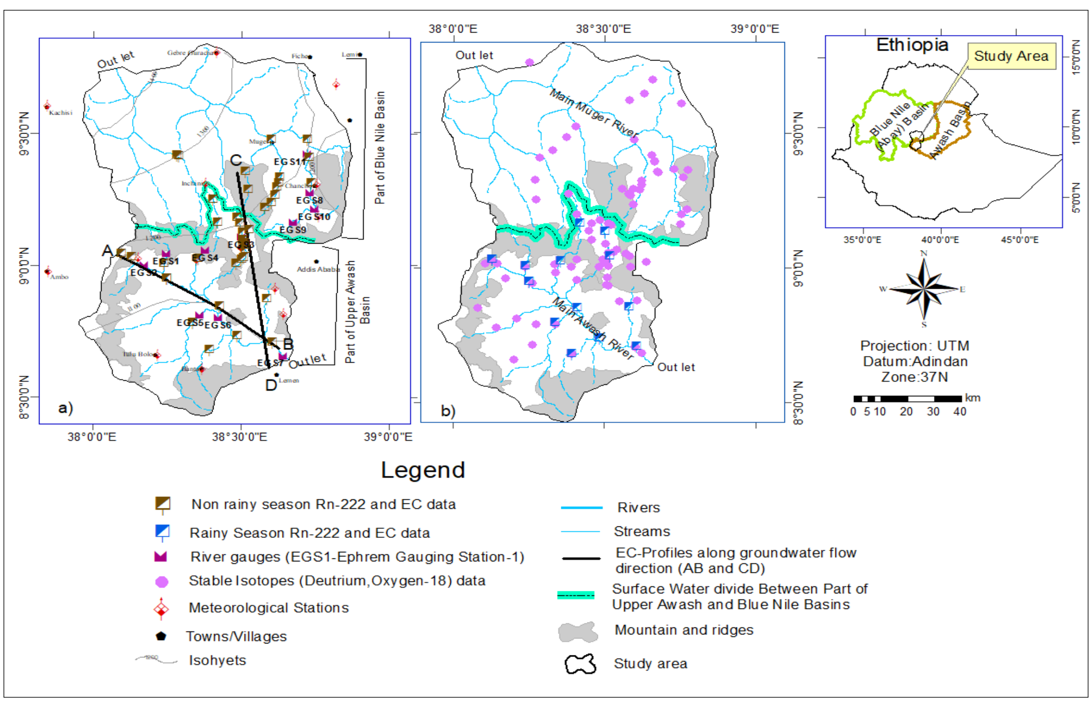

Figure 4.11 Map showing ^{222}Rn measured points during (a) non-rainy and (b) rainy seasons along with relevant data

Moderate to high values (100 to 200 Bq/m3 for the rainy season and 100 to 465 Bq/m3 for the non-rainy season) were measured from the upstream parts of basins, including the surface water divide, which is an area where existing streams flow over the highly fractured coriaceous basalt, Rift basaltic, and ignimbrite geologic units. The ^{222}Rn records subsequently make it evident that this area is identified as a local groundwater discharge zone, with a short residence time for the groundwater to dissolve and combine adequate ^{222}Rn.

The impervious geologic units (ash and silty-clay deposits) that cover the central flat land of the Upper Awash Basin have very low values below 100 Bq/m^3 in both rainy and non-rainy seasons. These units are largely unaffected by geologic structures with low lineament density coverage, which results in almost no or poor surface water-groundwater linking.

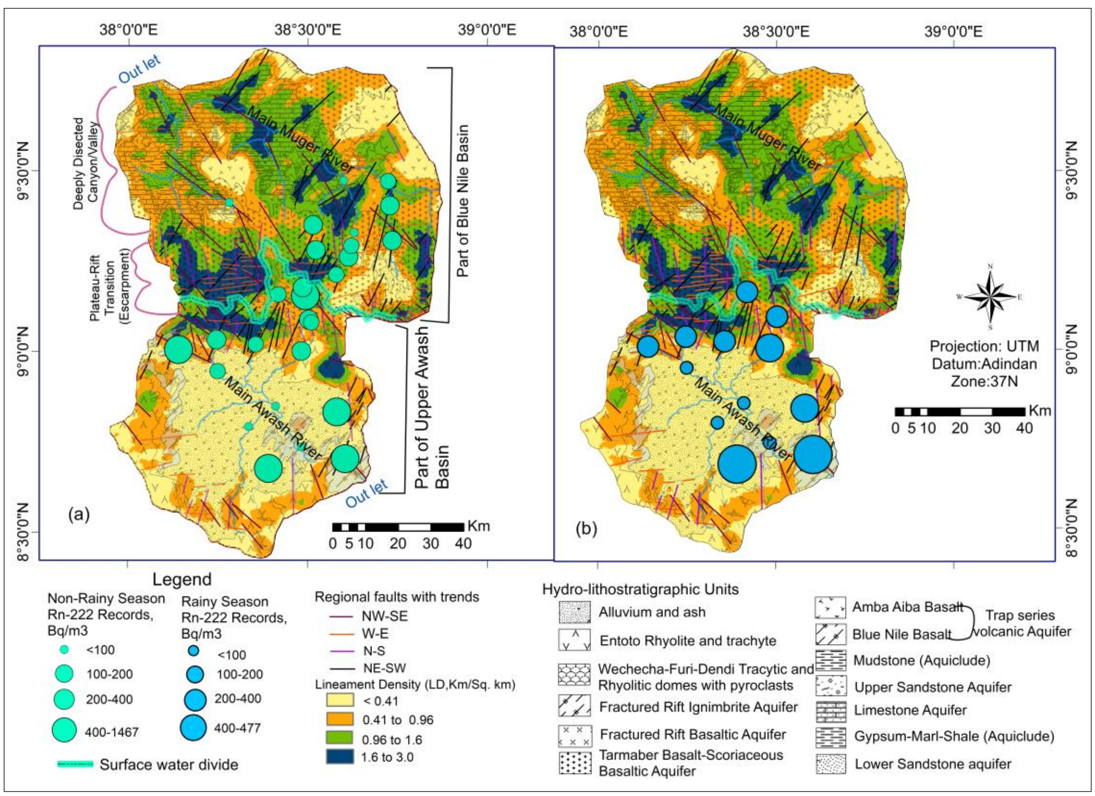

Figure 4.12 Categorized ^{222}Rn activity concentrations in rivers and streams during (a) non-rainy and (b) rainy seasons, accompanied by aquifer units and lineaments of the area.

Furthermore, the main Awash River and its tributaries flow over riverbed materials consisting of fractured rock units, such as ignimbrite and basalt in some areas, while in other areas, on clay to silty clay, as noted during fieldwork. This is demonstrated by the fact that floodwater inundates the central plain of the Upper Awash Basin for a considerable duration of time after the rainy season ends. Additionally, the high ^{222}Rn records from groundwater in existing boreholes and springs clearly show that groundwater contributes significantly to rivers and streams through weak zones.

4.5.4 Electrical Conductivity (EC) Evidence

To understand further the connection between aquifer units and surface water bodies, seasonal EC measurements of rivers, streams, and groundwater along the general groundwater flow direction were made in conjunction with the ^{222}Rn values. In summary, by measuring both electrical conductivity and radon levels seasonally along the groundwater flow direction, you can track the dynamic interactions between groundwater and surface water. This can help us to understand how groundwater contributes to surface water bodies, and how seasonal changes impact this relationship

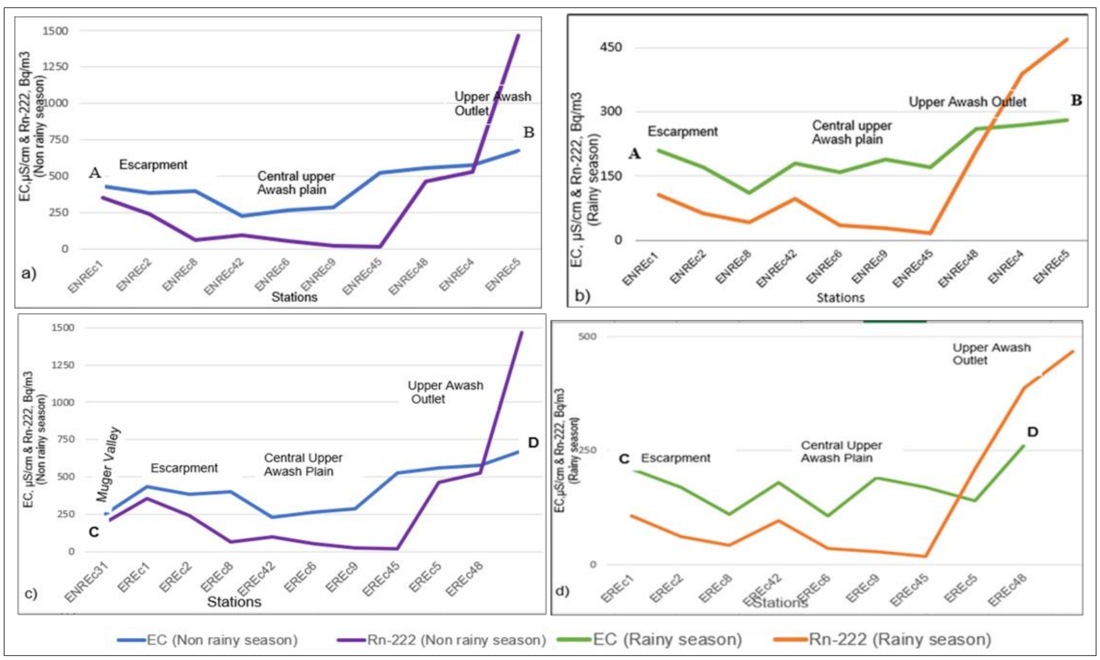

Figure 4.13 Seasonal EC and ^{222}Rn profiles in the parts of the Upper Awash and Blue Nile Rivers and streams along the groundwater flow direction

The result shows a clear variation as of ^{222}Rn. The EC of rivers and streams varies from 100 to 270 µS/cm in the rainy season and from 142 to 677 µS/cm in the non-rainy season. The study area outlet portions, part of the Upper Awash and Muger Watershed, have the highest and lowest electrical conductivity values, respectively. The low electrical conductivity at the Muger outlet station can be attributed to the significant dilution from tributaries, rainfall recharge, and rapid flow conditions, which reduce the concentration of dissolved ions.

Rivers and streams that flow from the plateau to the escarpment, including surface water divide areas, have EC values between 352 and 435 µS/cm during the non-rainy season, while parts of the Upper Awash outlet zones have EC values between 480 and 677 µS/cm. Rivers in the Muger valley and central plain of the Upper Awash have low values between 142 and 286 µS/cm (Figure 4.13). Rivers and streams exhibit EC values of 140 to 170 µS/cm near the surface water divide areas, below 120 µS/cm in the central plain part, and 180 to 270 µS/cm at the outlet section of the Upper Awash Basin during the wet season.

A substantial spatial variation along stream and river flows is observed based on the EC measurement. In light of this, the southern and southeast regions of the Upper Awash Basin have the highest values in both seasons, which are associated with the regional groundwater discharge to the main Awash River from the deeply faulted volcanic rocks. Due to impermeable sediment units, the stations in Muger Valley and the middle flat terrain of the Upper Awash had the lowest values, indicating a weak aquifer-surface water link, and this result is primarily consistent with the findings of an earlier study (Azagegn, 2015). For streams running in the surface water divide area, the corresponding intermediate values of 140 to 180 µS/cm and 285 to 435 µS/cm were observed throughout rainy and non-rainy seasons, further demonstrating that groundwater is discharging into streams through pervious geologic units of ignimbrite and basalt.

4.5.5 Stable isotopes ($\delta^{18}O$, δ^2H)

Stable isotope data of water were employed to support the hydrogeological and hydrogeochemical results, which are displayed as a scatter plot to illustrate the recharge area of aquifer systems. Using data from the IAEA-Addis Ababa station database, the weighted average monthly $\delta^{18}O$ and δ^2H values for the research area's representative long-term (1961 to 2022) monitoring are. summer rain. -1.2 ‰ & +4.3 ‰, and spring rain. +0.7 ‰ & +17.1 ‰. Numerous isotopic signatures ($\delta^{18}O$ and δ^2H) from various water sources associated with the area for which samples were gathered are displayed in Figures 4.14a & 4.14b. The generated LMWL and LEL are in line with earlier theories regarding the Awash Basin (Craig et al., 2005; Kebede & Travi, 2012). The isotopic composition of the area's shallow groundwater varies significantly between -3.13 ‰ to -0.61 ‰ with an average of -1.34 ‰ in $\delta^{18}O$ and -11.0 ‰ to 4.8 ‰ with an average of -3.01 ‰ in δ^2H, while the deep groundwater varies between -5.39 ‰ to -2.33 ‰ with an average of -3.9 ‰ in $\delta^{18}O$ and -29.2 ‰ to -9.53 ‰ with an average of -18.2 ‰ in δ^2H.

Water samples from low-yield springs and shallow sources (Depth < 150 meters) have isotopic signals that are enriched, whereas the deeper source (Depth > 300 meters) groundwater is significantly depleted (Figure 4.14a & 4.14b). For shallow groundwater, mainly for the southern portion, the enrichment with a high mean value (13.3) of deuterium excess related to the LMWL d-excess of 11.37 exemplifies recharge from fractionated summer rain and/or streams (Clark & Fritz, 1997), as most shallow boreholes in the central southern plain are situated near streams.

Most deep wells intercept the deep regional aquifer, and its isotopic signals ($\delta^{18}O$ and δ^2H) reveal a low mean value of deuterium excess (around 11), which is significantly depleted regarding the summer rain. The result indicates that the deeper regional aquifer system, especially for the southern section, receives its primary recharge from heavy summer rain that falls on the highland/plateau area during cooler weather. It further implies a lengthy residence time for subsurface recharge via deep circulation into a deep scoriaceous regional aquifer. Similar isotopic compositions between the deep aquifer system with some cold and thermal high-yield springs that primarily emerged at the interface between ignimbrite and basaltic rock indicate subsurface recharging from the plateau (Figure 4.14a).

The results also confirm the litho-hydro stratigraphic relationships outlined and discussed in section 3.5.1. In contrast, the deeper aquifer in the region shows notable isotopic depletion in δ^2H and $\delta^{18}O$, consistent with earlier findings (Kebede et al., 2007; Ayenew et al., 2007; Rango et al., 2010; Yitbarek et al., 2012; Azagegn et al., 2014) and suggests that the plateau and PUAB regionally confined groundwater system is connected hydraulically via a network of interconnected fault networks.

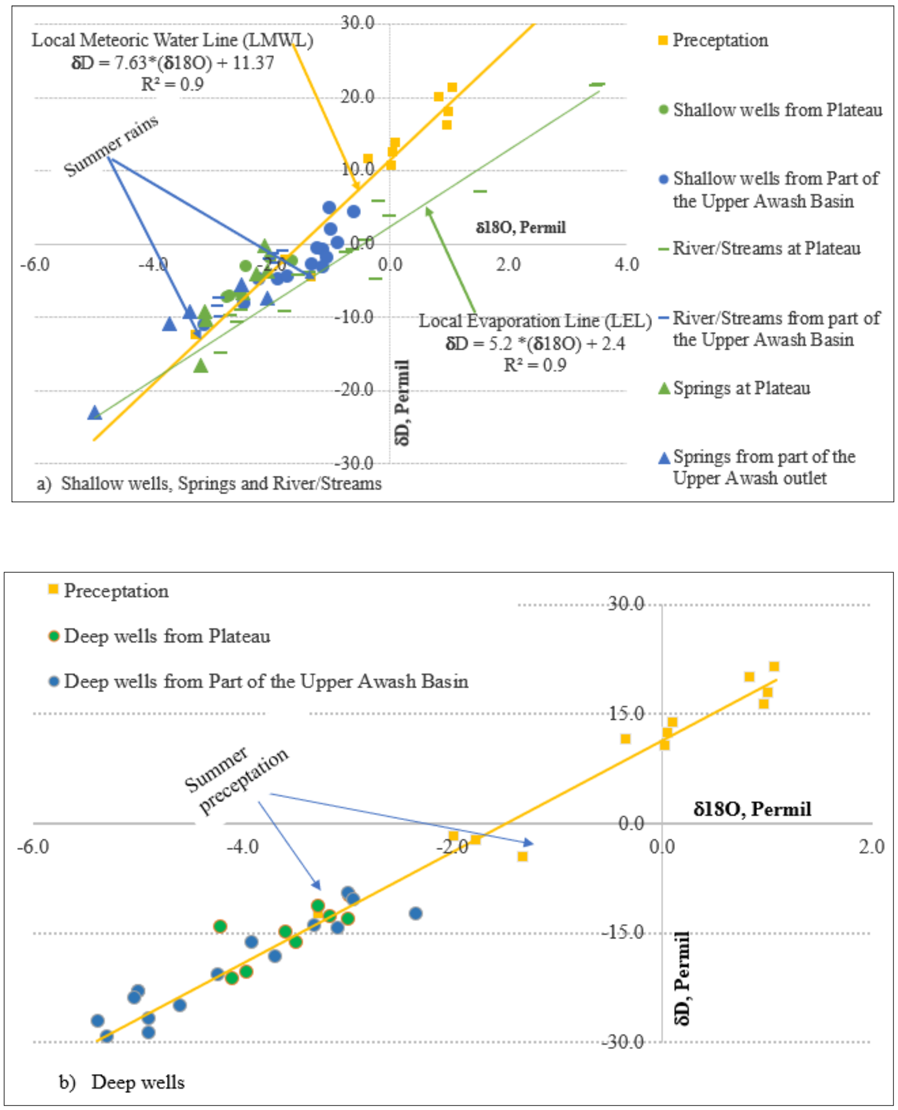

Figure 4.14 δ^2H against $\delta^{18}O$ scatter plot for signals of a) shallow wells, springs, and surface water; and b) deep aquifer with the LMWL and Local Evaporation Line (LEL) for the Plateau, escarpment, and southern part of the area

4.6 Recharge estimation

Groundwater recharge is the process by which water moves downward from the surface to replenish the groundwater table, either through direct contact or percolation. This process is essential for the hydrological cycle, supporting the long-term sustainability of groundwater resources. Recharged water can be extracted for various uses or contribute to the river and stream flow. Factors influencing recharge rates include lithology, geological structure, rainfall intensity, urbanization, vegetation, and climate (De Vries & Simmers, 2002; Yeh et al., 2016).

Nowadays, groundwater recharge estimation in groundwater resource valuation has moved from a basic problem to a fundamental one. It is practically a difficult task due to the uncertainties and assumptions associated with different methods of analysis that differ in the type of recharge, space, and time scales represented (Simmers, 1988; Lerner et al., 1990; Scanlon et al., 2002; Nimmo et al., 2005; Scanlon et al., 2006; Healy, 2010). Recharge estimation requires a good conceptual hydrogeological model, and the accuracy of the recharge estimate depends largely on the correlation of the conceptual model to the actual physical model (Lerner et al., 1990).

Developing an accurate conceptual model of the study area, considering the local climate, hydrological, and hydrogeological conditions, is crucial for reliable recharge estimation. If the conceptual model is incorrect or oversimplified, it can lead to inaccurate estimates. Various methods and techniques are available to estimate groundwater recharge, but the selection and application of these methods require careful consideration of the area. Referring to the current state of science, it is extremely tough to assess the accuracy of any method, and the usage of multiple estimation methods is beneficial, as any single method is vulnerable to sources of error that may be recognized and corrected with results from other methods (Healy & Cook, 2002; De Vries & Simmers, 2002).

Since recharge takes place below the surface, it is frequently challenging to measure directly. Thus, indirect estimate techniques are commonly employed. In conclusion, using a variety of approaches to estimate groundwater recharge is a practical approach that considers the uncertainties and constraints included in each technique (Lerner et al., 1990; Scanlon et al., 2002).

In this study, attempts were made to estimate and evaluate the recharge rates with previous results for the two (unconfined and confined) aquifer systems using a diversified approach, including Water Balance, Water Table Fluctuation (WTF), Baseflow Separation (BFS), and Darcian methods, including valuation of groundwater inflow from the adjacent Blue Nile sub-basin (Muger Watershed).

4.6.1 Baseflow separation method

Baseflow separation differentiates between Baseflow and surface runoff components in a streamflow hydrograph. Baseflow represents the portion of streamflow that is sustained by groundwater discharge, which is typically characterized by a more stable and slowly varying flow component, as it is influenced by the long-term storage and release of water from aquifers. Surface runoff refers to the direct contribution of precipitation or other surface water inputs to streamflow.

By analyzing both short-term and long-term hydrographs, it is possible to determine the groundwater component or Baseflow (Arnold & Allen,1999; Woessner, 2020), which can further serve as an estimate of recharge. Baseflow index (BFI) is the ratio of long-term mean baseflow to total streamflow, which reflects the contribution of groundwater discharge to streamflow, serving as a proxy for recharge inferred by assuming that baseflow originates from groundwater that was previously recharged, and the method assumes steady-state conditions, where recharge equals discharge over long time scales. There is also the assumption that losses from the gauged watershed due to underflow, groundwater evapotranspiration, and abstraction are minimal and can be neglected (Riser et al., 2005).

The study area is heterogeneous, and its recharge and discharge paths are non-linear and anisotropic, which affects the baseflow character. Applying BFI for recharge estimation in this area indeed requires careful consideration. Calibration to local conditions, such as lithology, lineament density, and aquifer connectivity, along with validation using independent methods, is quite important. The accuracy of the separation results depends on the quality and availability of streamflow data, the hydrological characteristics of the watershed, and the specific method used. Overall, hydrograph separation methods play a crucial role in understanding the hydrological processes within a watershed and provide valuable information for water resources management, flood prediction, and environmental assessments.

So far, several Baseflow separation techniques have been developed and used by different researchers. out of which, the River Analysis Package (RAP) (Stewardson & Marsh, 2003) and a TIMESPLOT Recursive Digital Filter (RDF) (Brodie & Hosteler, 2005) were used in this study to quantify the recharge.

The River Analysis Package (RAP) software was used in estimating the average annual Baseflow index. It contains the Time Series Analysis (TSA) component to help researchers tackle various river management projects (Stewardson & Marsh, 2003). TSA analyses use daily time series flow data to generate summary statistics over time. The program was developed with a graphical user interface that allows users to interactively investigate time series data and undertake the Lyn-Hollick filter expression (Lyne & Hollick, 1979) to calculate the Baseflow component of the hydrograph in RAP with an α (alpha) value of 0.975.

The TIMESPLOT recursive digital filter, which is a routine tool for signal analysis and processing, is used to remove the high-frequency quick-flow signal to derive the low-frequency Baseflow signal (Lyne & Hollick, 1979; Nathan & McMahon, 1990; Brodie & Hosteler,2005). The filtering method uses a numerical algorithm for the separation of stream hydrographs, and the filter is generally run multiple times through a dataset. Such a filter is simple and robust, but the results are very sensitive to the Baseflow filter parameter alpha (α), which needs calibration using daily discharge data empirically for each station before the results can be considered numerically valid. To perform the filter, the expression mentioned in (Brodie & Hosteler,2005) was used.

$$q_{f(i)} = \begin{cases} \alpha q_{f(i-1)} + (1+\alpha)/2 \left(q_{(i)} - q_{(i-1)} \right) & \text{for } q_{f(i)} > 0 \quad \text{Otherwise} \\ 0 & \end{cases} \quad (1)$$

$$q_{b(i)} = q_{(i)} - q_{f(i)} \quad (2)$$

Where; $q_{f(i)}$-is the quick flow response at the i^{th} sampling instant, $q_{f(i-1)}$ is the quick filtered flow for the previous sampling instant to i, $q_{(i)}$ is the original streamflow at the i^{th} sampling instant, $q_{(i-1)}$ is the original streamflow for the previous sampling instant to i, $q_{b(i)}$ is the Baseflow at the i^{th} sampling instant, and is the filter parameter that enables the shape of the separation to be altered.

The recursive digital filter calculates the Baseflow for each interval (day-i) using information about the flow on day-i, day i-1, and parameter values. The Baseflow index, which is the long-term ratio of Baseflow to total stream flow, is commonly generated from this analysis.

Both methods (RAP and TIMESPLOT) need daily river/stream flow data as input for analysis. Records from 11 stations (7 stations from part of the Upper Awash Basin and 4 stations from the adjacent Blue Nile Basin) (Figure 1.1b), having the latest records ranging from 8 to 20 years, were collected from the Ministry of Water and Energy Authority to evaluate the Baseflow index for the recharge estimation.

In this study, the mean annual BFI is analyzed using the RAP technique for α values of 0.93, 0.95, 0.975, 0.98, and 0.99. We used a mean annual BFI for $\alpha = 0.975$ from the RAP technique and for $\alpha = 0.989$ from the TIMESPLOT generated for each station. The mean annual recharge values from two methods are generated using a long time series of daily flow data for PUAB and PBNB stations. Finally, the recharge computed using BFI ($R = BFI^* Q_{total}/Area$) is aligned with the lineament density and local geology of each station. It shows that high BFI values from stations at the escarpment (EGS1, EGS3, EGS4), the Outlet part of UAB (EGS7), and from the plateau (EGS8 to EGS11) are aligned with high lineament density ($LD > 0.4\ km/km^2$) and fractured basaltic unit. Furthermore, the mean annual recharge computed from this method is validated with the results of independent methods, like WTF and Darcy's approach, for further simulation purposes.

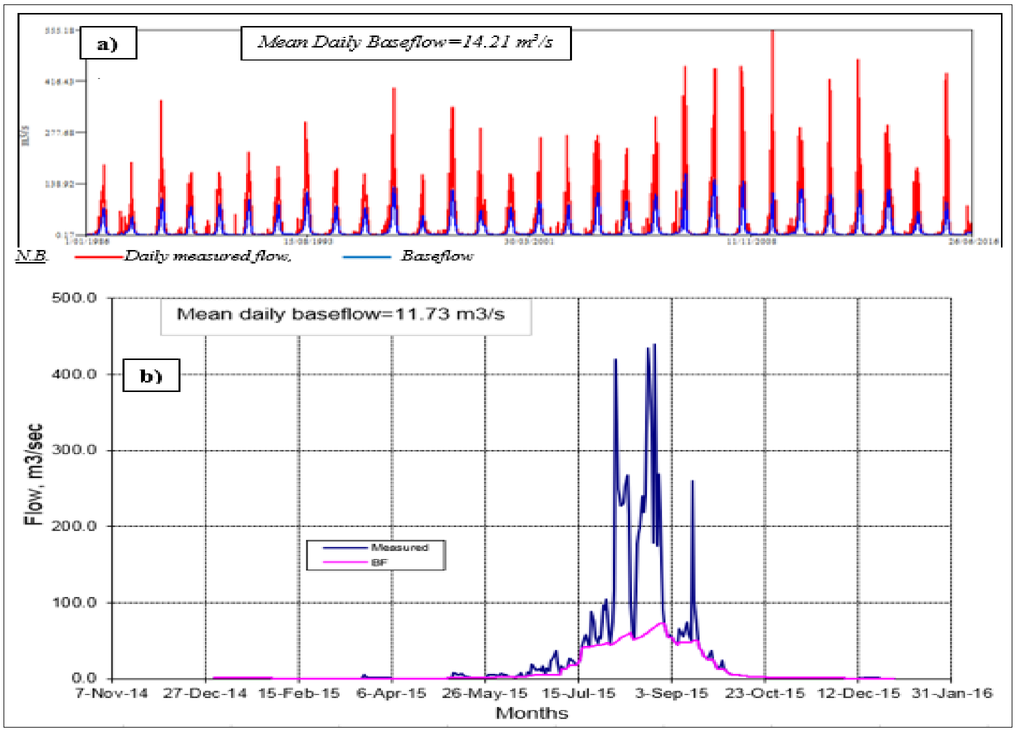

Figure 4.15 The resulting sample graph after a) RAP and b) TIMESPLOT analysis specifically for the Part of the Upper Awash Basin (PUAB) outlet station (Melka-kunture station-EGS7)

The sample Baseflow separation graphs (Figure 4.15a and 4.15b) after RAP and TIMESPLOT analysis for PUAB station (EGS7) found in the outlet part and Baseflow or recharge rates obtained for different gauged streams from the two adjacent Watersheds are given in Table 4.4. The analysis of Baseflow separation using RAP and TIMESPLOT graphs is included in Appendix-8 and Appendix-9.

The weighted mean annual recharge rate, representative of the sub-basins, was obtained from the Baseflows of the gauged streams weighted with their respective catchment areas. As the station at the outlets PUAB (EGS7) and PBNB (EGS11) incorporate all the aforementioned catchments, instead of averaging, it is logical and better to consider the recharge values at EGS7 (102.2 mm/y or 455.3MCM/y) and EGS11 (56.4 mm/y or 150.8 MCM/y) are the sub-basins' mean annual recharge amounts (Table 4.4). Thus, the estimated mean annual recharge from Baseflow separation using RAP and TIMESPLOT techniques for PUAB and Blue Nile Basins is 9.2 % and 4.2 %, respectively, of the mean annual precipitation.

Table 4.4 Estimated mean annual recharge rate obtained using hydrograph separation using RAP and TIMESPLOT techniques for part of the Upper Awash and its adjacent Blue Nile Basins

ID	Station name	Longitude	Latitude	Altitude (m.a.s.l)	Available data record		Area, Km^2	Daily Flow, m^3/sec	Annual Total flow,mm	mean annual BFI using River Analysis Package (RAP) Technique	mean annual BFI using TIMESPLOT Technique	BFI, Average	Annual recharge, mm	Weighted mean recharge,mm/yr	Weighted Base flow, MCM/yr
EGS1	Upper Awash at wolonkomi	$38^{0}14'54.05''$	$9^{0}02'30.99''$	2132	4/9/1997	24/12/2005	60.0	0.82	403.2	0.49	0.54	0.52	207.62	2.8	0.2
EGS2	Upper Awash at Ginchi	$38^{0}10'36.78''$	$8^{0}59'37.54''$	2190	1/1/1996	30/12/2010	76.0	0.99	412.4	0.23	0.23	0.23	94.84	1.6	0.1
EGS3	Upper Awash at Holeta	$38^{0}30'02.04''$	$9^{0}06'10.29''$	2467	1/1/1994	30/12/2009	119.0	1.45	384.3	0.49	0.51	0.50	192.15	5.1	0.6
EGS4	Upper Awash at Addis Alem	$38^{0}22'57.11''$	$9^{0}03'16.73''$	2350	1/1/1994	30/12/2012	248.0	2.81	357.3	0.55	0.59	0.57	203.68	11.3	2.8
EGS5	Upper Awash at Asgori	$38^{0}22'00.69''$	$8^{0}48'13.63''$	2073	1/1/1996	9/12/2014	662.5	3.73	177.4	0.32	0.32	0.32	56.75	8.4	5.6
EGS6	Upper Awash at Bello	$38^{0}25'13.81''$	$8^{0}48'13.94''$	2053	1/1/2004	28/4/2015	2568.8	10.48	128.6	0.58	0.58	0.58	74.59	43.0	110.5
EGS7	Upper Awash at Melka kunture	$38^{0}38'39.05''$	$8^{0}39'16.95''$	2004	1/1/1986	26/6/2016	4456.0	29.17	206.4	0.49	0.50	0.50	102.18	102.2	455.3
Total Recharge for parts of the Upper Awash Basin in the study area (Watershed total area=4456.0 km^2)															
EGS8	Muger at Roba	$38^{0}44'05.65''$	$9^{0}16'06.79''$	2554	1/1/1989	31/12/2011	30.00	0.34	177.77	0.49	0.51	0.50	102.16	6.27	0.3
EGS9	Muger at Gerbi	$38^{0}25'10.76''$	$9^{0}19'56.01''$	2624	10/26/1989	26/4/2010	65.00	0.95	394.20	0.52	0.51	0.51	95.61	12.7	2.0
EGS10	Muger at Sibilu	$38^{0}44'44.49''$	$9^{0}12'16.26''$	2551	1/1/2003	8/1/2011	375.00	6.63	843.19	0.43	0.49	0.46	203.20	155.8	119.5
EGS11	Muger at Muger	$38^{0}43'52.34''$	$9^{0}25'04.76''$	2547	1/1/2003	29/12/2011	489.00	9.76	464.59	0.46	0.51	0.49	56.42	56.4	150.8
Total Recharge for parts of the Blue Nile Basin in the study area (Watershed total area=489.0 km^2)															

Note. ***EGS1*** *represents. E-First word of the Author's name, GS1-Gauged station- number*

4.6.2 Water balance method

The water balance method, initially developed in the 1940s, was later refined based on water accounting principles. This approach accounts for the inflows into the system, the outflows, and changes in storage, including groundwater and water present in soil, ponds, and vegetation, during the specified period (Thornthwaite, 1948; Thornthwaite & Mather, 1957). The universal concept of mass conservation of water implies that the water balance method is applied over any space and time scale (Healy et al., 2010), which is good after the conceptualization of hydrologic systems at all scales.

In recharge estimation, understanding the hydrological system of the area is critical as evaporation and infiltration are major elements in hydrologic water balance analysis, for which some amount of the infiltrated water added to the groundwater reservoir through recharge is critically dependent on the geological structure as well as the nature of the geologic material. So, the estimation of groundwater recharge involves handling the surface and subsurface phenomena interactions, which include the knowledge of the geological nature of the area, soil characteristics, land use, and land cover conditions, as well as the topography and slope. In addition to that, the study of climatic characteristics (Temperature, Relative humidity, wind speed, and sunshine hours) is vital to estimating the water balance components. Except for surface runoff in a well-defined geometric boundary, variables included in a general water balance equation cannot be directly evaluated but estimated using different approaches (Jr & Lewis, 2003).

As the area includes part of the Upper Awash and the adjacent left flank of the middle Blue Nile Basins, which are hydraulically connected systems thought by different researchers (Kebede et al., 2007; WWDSE, 2008; Yitbarek et al., 2012; Azagegn et al., 2014), the inflow components include groundwater flux from the portion of Blue Nile Basin in addition to precipitation. The outflow components include the actual evapotranspiration (AET), runoff, groundwater outflow, and groundwater withdrawal by pumping. Considering the above inflow and outflow components, the general groundwater balance equation to estimate recharge in the area for a given time is given as.

$$\boxed{R = (P+G_{wi}) - (AET + Ro + G_{wo} + A)}$$

Where. R-is annual recharge (mm), P-is mean annual precipitation (mm), AET-is mean annual actual evapotranspiration (mm), R_o-is mean annual runoff (mm), G_{wi}-is groundwater inflow from the adjacent sub-basin (mm), G_{wo}-is groundwater outflow (mm), and A-is annual abstraction of groundwater using pumping (mm).

Before recharge estimation, values for precipitation, potential evapotranspiration (PET), actual evapotranspiration (AET), runoff (Ro), and annual abstraction (A) were quantified. The areal precipitation of the area was calculated using the Isohytal and Theisen polygon methods. The areal precipitation of the area using the Isohytal and Theisen polygon methods estimates that the yearly average precipitation for the PUAB is 1113 millimeters, while the Abbay Basin portion experiences 1326 millimeters.

The mean monthly potential evapotranspiration (PET) is computed using the Thornthwaite equation along with long-term meteorological data from different stations. So, the average value from the Thornthwaite formula is used for the computation of AET.

Table 4.5 Mean PET values (mm) obtained from the Thornthwaite approach

Area	Jan	Feb	Mar	Apr	May	June	Jul	Aug	Sep	Oct	Nov	Dec	Annual
PUAB	54.9	65.8	71.0	74.6	77.8	73.4	65.9	63.3	60.2	56.3	53.2	62.8	779.3
PBNB	42.7	47.6	54.1	55.4	56.7	51.4	46.1	43.0	43.1	40.3	38.5	37.4	556.2

N.B. *PUAB- Part of the Upper Awash Basin, PBNB- Part of the Blue Nile Basin*

Actual evapotranspiration (AET) is the major water balance component of water evaporated back to the atmosphere from the soil and vegetation under the prevailing soil, water, and atmospheric conditions. There are various methods of AET computation, among which the Turc and the Soil Moisture Deficit (SMD) empirical methods were used. The Turc method (Turc,1961) is an empirical equation that uses only air temperature and precipitation as input and is simple to implement. It assumes vegetation is well watered, making it more suitable for humid regions, and estimates the mean monthly AET based on measurements of maximum and minimum air temperature and precipitation using the equation.

$$\boxed{AET= P /(1.9 +(P/300+25T+0.05T^3)^2)^{0.5}}$$

Where AET is the mean annual actual evapotranspiration (mm), P is the mean annual precipitation (mm), and T is the mean annual air temperature (˚C).

Table 4.6 AET values (mm) computed using the Turc method

Area	Mean annual precipitation, mm	Mean annual Temprature, ^{o}c	AET, mm
PUAB	1113	17.23	602.8
PBNB	1326	14.2	624.5

Additionally, the AET value of the area was computed using a soil moisture deficit (SMD) method. It is a physically-based approach that accounts for soil moisture availability, root depth, evapotranspiration demand, and is more responsive to seasonal variability, land cover, and soil properties. It requires detailed input data but offers greater realization in water-limited environments. In principle, the value of soil moisture deficit and AET varies with soil type and vegetation (Shaw, 1994). For this purpose, classification of the area using land use /land cover, soil type, and vegetation with varying root depths (Figure 4.16) covering the area is important for SMD. The combination of land use/land cover and soils with the proportion of area coverage has been recognized from the latest 2020 version FAO land use/land cover and soil maps of Ethiopia.

The vegetation covering the area is forests, perennial crops, dense and open woodlands, bush and grasslands, and cultivated lands. Perennial crops, forests, and woodlands are categorized together, and cultivated areas are those areas that are used for shifting cultivation (50% cultivated and 50% covered with grasses for grazing), and hence 50% grouped as grassland and 50% as cultivated lands. Accordingly, grassland covers about 13.86%. The remaining 37.05% of the area is dominantly cultivated, mostly with maize and sorghum crops. Cultivated lands with cereals, grass, and forest were characterized by root constants. 75 mm, 150 mm, and 250 mm, respectively (Shaw, 1994).

Thus, the area is classified into three land use/land cover units and vegetation with varying root depths. Accordingly, the AET of the area is calculated using the Thornthwaite and Mather standard SMD method based on the monthly mean precipitation and mean monthly PET. The AET values calculated for each land cover unit (root constants) were weighted with the proportion of their aerial coverage to get the mean AET values of the sub-basins from the SMD method (Table 4.7).

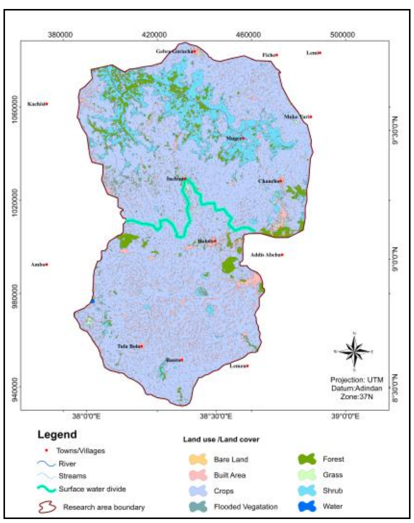

Figure 4.16 Land use/land cover map (Modified from FAO, 2020)

Table 4.7 AET values in mm computed using the soil moisture deficit (SMD) method

Area	Jan	Feb	Mar	Apr	May	June	Jul	Aug	Sep	Oct	Nov	Dec	Annual
PUAB	28	39	67	80	88	96	82	88	94	97	54	33	845.1
PBNB	42	30	52	55	57	51	46	43	43	40	39	37	536.2

While both the Turc and SMD methods have merit, the SMD approach is generally more reliable across diverse landscapes due to its physically-based nature and sensitivity to local hydrological conditions. In PUAB, SMD effectively accounts for urban hydrology and limited infiltration, whereas in PBNB, it reflects the interplay between vegetation, elevation, and cooler climate. The Turc method, though useful in forested and humid zones like PBNB, may oversimplify AET dynamics in more complex or water-limited settings.

Finally, AET values computed using the Turc and SMD methods for the area were averaged for subsequent use (Table 4.8).

Table 4.8 Mean annual AET (mm) of the area

Area	Turc Method	SMB method	Average
PUAB	602.8	845.1	723.9
PBNB	624.5	536.2	580.3

The most notable difference is observed in the actual evapotranspiration (AET) calculated using soil moisture deficit (SMB) as compared to the Turc method (Table 4.8). The average AET values derived from these two methods indicate that the PUAB region has higher AET values than the PBNB basin. The PUAB area features extensive built-up regions and impervious surfaces, which can indirectly influence local microclimates and runoff patterns. In contrast, the PBNB basin is primarily covered by natural vegetation and forests, which enhance interception and transpiration and promote infiltration. These differences in surface and vegetative cover likely explain the variation in AET observed between the two regions.

Runoff (R_o)

Hydrograph separation techniques using RAP and TIMESPLOT were used to determine the mean annual volume of runoff since the study area, parts of the Upper Awash and Blue Nile Basin, have had daily river discharge data available at their respective outlet stations, EGS7 and EGS11. After analysis utilizing such methods, the estimated mean annual runoff for the outlet portions of the Upper Awash and Blue Nile Basins is 103.2 mm and 416.7 mm, respectively (Table 4.9).

Table 4.9 Estimated mean annual runoff obtained using the Baseflow separation techniques for part of the Upper Awash and its adjacent Blue Nile Basins.

ID	Station	Longitude	Latitude	Altitude (m.a.s.l)	Available data record		Area, Km^2	Runoff index	Daily Flow, m^3/sec	Weighted mean,mm/yr	runoff, MCM/yr
EGS1	Upper Awash at wolonkomi	$38^{0}14'54.05''$	$9^{0}02'30.99''$	2132	4/9/1997	24/12/2005	60.0	0.48	0.77	2.6	11.6
EGS2	Upper Awash at Ginchi	$38^{0}10'36.78''$	$8^{0}59'37.54''$	2190	1/1/1996	30/12/2010	76.0	0.77	0.99	5.4	24.1
EGS3	Upper Awash at Holeta	$38^{0}30'02.04''$	$9^{0}06'10.29''$	2467	1/1/1994	30/12/2009	119.0	0.50	1.45	5.1	22.9
EGS4	Upper Awash at Addis Alem	$38^{0}22'57.11''$	$9^{0}03'16.73''$	2350	1/1/1994	30/12/2012	248.0	0.43	2.81	8.6	38.1
EGS5	Upper Awash at Asgori	$38^{0}22'00.69''$	$8^{0}48'13.63''$	2073	1/1/1996	9/12/2014	662.5	0.68	3.73	17.9	79.9
EGS6	Upper Awash at Bello	$38^{0}25'13.81''$	$8^{0}48'13.94''$	2053	1/1/2004	28/4/2015	84.0	0.42	10.48	31.1	138.7
EGS7	Upper Awash at Melka kunture	$38^{0}38'39.05''$	$8^{0}39'16.95''$	2004	1/1/1986	26/6/2016	4456.0	0.50	29.17	103.2	459.9
Total runoff for parts of the Upper Awash Basin (Total area=4456.0 km^2)											
EGS8	Muger at Roba	$38^{0}44'05.65''$	$9^{0}16'06.79''$	2554	1/1/1989	31/12/2011	30.0	0.50	0.77	24.7	12.1
EGS9	Muger at Gerbi	$38^{0}25'10.76''$	$9^{0}19'56.01''$	2624	10/26/1989	26/4/2010	65.0	0.49	0.95	30.0	14.7
EGS10	Muger at Sibilu	$38^{0}44'44.49''$	$9^{0}12'16.26''$	2551	1/1/2003	8/1/2011	375.0	0.54	6.63	230.9	112.9
EGS11	Muger at Muger	$38^{0}43'52.34''$	$9^{0}25'04.76''$	2547	1/1/2003	29/12/2011	489.0	0.51	12.67	416.7	203.8
Total runoff for parts of the Blue Nile Basin (Total area=489.0 km^2)											

Abstraction (A)

In the research area located within a portion of the Upper Awash Basin, there are 135 water supply wells. These wells serve a crucial purpose, providing water for various needs including irrigation, industrial operations, and residential consumption. The limited experience in the country with monitoring groundwater quality, quantity, and levels has made it difficult to accurately estimate and measure groundwater extraction from aquifer systems. As a result of this limitation, the annual withdrawal of water from the groundwater source through 116 supply wells (located within the boundary) has been estimated (Table 4.10) based on discussions about the daily extraction of groundwater from municipal and rural water supplies, along with information from individuals and organizations.

Table 4.10 Estimated current groundwater abstraction from a PUAB

No.	Type of wells	Depth,m	Average discharge, L/s	Number of wells	Daily Consumption (Litre) by 14 hours pumping, L/14 hrs	Annual consumption, Mm^3	Annual consumption, mm
1	Shallow wells	< 150 m	5.2	56	14,676,480.0	5.36	5.25
2	Medium depth wells	Between 150 and 250	3.9	36	7,076,160.0	2.58	
3	Deep wells	> 250m	35	24	42,336,000.0	15.45	
			Total	116	64,088,640.0	23.39	

Recharge (R)

By considering the computed inflow and outflow components, the groundwater recharge of the area was calculated using the water balance expression shown in Table 4.11.

Table 4.11 Annual recharge computed using the water balance approach

Area	Rainfall, mm	AET, mm	Ro, mm	A, mm	Area, Km^2	R, mm	R, Mm^3
PUAB	1112.7	723.9	103.2	5.25	4456	280.4	1249.2
PBNB	1325.7	580.3	416.7	Negligible	1085	328.68	356.6

Groundwater inflow (G_{Wi})

The study area includes part of the Upper Awash Basin and the adjacent left flank of the Blue Nile Basin, known as the Muger Watershed. Numerous studies have established the understanding that the two adjacent Watersheds exhibit hydraulic connectivity, as indicated by a range of evidence gathered mainly from geological, hydrogeochemical, and isotope analysis techniques (Kebede et al., 2007; WWDSE, 2008; Yitbarek et al., 2012; Azagegn et al., 2014; Berhanu et al., 2017). Accordingly, groundwater circulation in the study area is strongly influenced by the local geomorphic framework and the subsurface arrangement of permeable and impermeable lithologic units. These factors govern both the vertical extent and horizontal flow patterns of groundwater movement. In particular, the presence of an East-West-oriented horst structure in the Muger sub-Basin, composed predominantly of impermeable mudstone, plays a critical role in shaping aquifer geometry and hydraulic connectivity.

This mudstone horst lies beneath the overlying Tertiary volcanic formations, which host the area's primary aquifers. Due to its low permeability, the mudstone acts as a hydraulic barrier**,** segmenting the aquifer system into two distinct groundwater sub-basins: the Muger sub-basin to the north and the Upper Awash sub-basin to the south. This structural control disrupts the continuity of groundwater flow and contributes to asymmetric recharge and discharge patterns across the region. Importantly, in the northern and northwestern escarpment zones**,** the surface water divides do not align with groundwater divides**.** This mismatch arises from subsurface heterogeneity and the influence of buried structural features, such as faults and lithologic contacts, which redirect groundwater flow independently of topographic gradients. As a result, groundwater may cross surface watershed boundaries, complicating basin-scale water budgeting and resource management. Understanding these structural and geomorphic controls is essential for delineating aquifer extents, predicting flow paths, and designing sustainable groundwater development strategies in the Upper Awash Basin.

Moreover, the recharge zones within the Muger (1,770 km²) sub-basin contribute significant groundwater flux to the Upper Awash groundwater basin. These zones are structurally connected through fault-controlled flow paths and permeable volcanic formations, enabling inter-basin groundwater transfer. To quantify this contribution in this study, the total volumetric recharge from the Muger sub-basin is first estimated using mean annual recharge rates and total sub-basin area. The groundwater outflow to the Upper Awash basin is then calculated as the difference between total recharge in the Muger sub-basin and the recharge retained within the contributing areas. This approach assumes that the flux from the contributing zones is proportional to their spatial extent and recharge intensity.

Mathematically, the groundwater outflow from the Muger sub-Basin is expressed as:

$$Q_{outflow}=A_{contiributing} * R_{mean}$$

Where: $Q_{outflow}$ = groundwater flux to Upper Awash (mm/year), $A_{contributing}$ = area of contributing recharge zone (km²), and R_{mean} = mean annual recharge rate (mm/year)

This method provides a spatially explicit and geologically validated estimate of inter-basin groundwater transfer, supporting the conceptual model of regional aquifer connectivity and informing sustainable resource management strategies. Recharge to the Muger and Upper Awash sub-basins has been determined using the water balance approach, with the results presented in Table 4.11. Based on the justifications discussed above and this study, the recharge area of 1,059 km² in the Muger sub-basin contributes groundwater flux to the Upper Awash groundwater basin. Consequently, the total volumetric recharge to the Muger groundwater sub-basin is calculated as the difference between the total volumetric recharge into the Muger sub-basin and the volumetric recharge from the areas that contribute to it. This groundwater outflow from the Muger sub-basin is estimated by considering the size of its recharge area, which contributes to groundwater flux in the Upper Awash basin, as a factor of the mean annual recharge of the Muger sub-basin. Therefore, the groundwater flux from the portion of the Blue Nile Basin (Muger Watershed) was computed, and the result is shown in Table 4.12.

Table 4.12 Annual groundwater flux to the Upper Awash groundwater system after the water balance approach

Area	Contributing area, Km^2	Recharge, mm	Groundwater flux to PUAB, mm	Groundwater flux to PUAB, Mm^3
PBNB	1059	328.7	320.8	348.1

Due to the groundwater flux from the adjacent sub-basin, the volumetric recharge for part of the Upper Awash Basin was finally computed in Table 4.13.

Table 4.13 Computed annual recharge and the water balance for part of the Upper Awash Basin using the water balance method

<table>
<tr><td>Watershed</td><td>RF, mm</td><td>AET, mm</td><td>R_o, mm</td><td>A, mm</td><td>Area, Km^2</td><td>R, mm</td><td>R, Mm^3</td></tr>
<tr><td>PUAB</td><td>1112.7</td><td>723.9</td><td>103.2</td><td>5.25</td><td>4456</td><td>280.4</td><td>1249.2</td></tr>
<tr><td colspan="6">Groundwater flux from the adjacent sub-basin</td><td>320.8</td><td>348.1</td></tr>
<tr><td colspan="6">Total recharge</td><td>601.2</td><td>1597.3</td></tr>
<tr><td colspan="8">Water balance for PUAB</td></tr>
<tr><td>Watershed</td><td>RF, mm</td><td>Gi, mm</td><td>AET, mm</td><td>Ro, mm</td><td>A, mm</td><td colspan="2">Go, mm</td></tr>
<tr><td>PUAB (4456 Km^2)</td><td>1112.7</td><td>320.8</td><td>723.9</td><td>103.2</td><td>5.25</td><td colspan="2">601.2</td></tr>
</table>

Where:

RF = rainfall (mm), AET=actual evapotranspiration (mm), Gi= Groundwater inflow to PUAB from the adjacent Muger Watershed (mm), Ro=Runoff (mm), A=Abstraction (mm), and Go=Groundwater outflow from PUAB (mm)

4.6.3 Water Table Fluctuation (WTF) Method

Techniques that measure groundwater levels over time and across different locations are among the most widely used methods for determining recharge. The WTF practice has been developed and refined since the early 1920s (Meinzer, 1923; Meinzer & Stearns, 1929; Rasmussen & Andreasen, 1959; Gerhart, 1986; Charles & William, 2001; Delin et al., 2007).

This method examines variations in groundwater level over time to estimate recharge for unconfined aquifers using the assumption that the amount of available water in a column of unit surface area is equal to specific yield times the height of water in the column, which is straightforward to apply based on the idea that increases in groundwater level in unconfined aquifer is caused by recharge water arriving at the water table (Healy & Cook, 2002). Water level measurements from wells are the principal source of information used to assess annual and long-term variations in groundwater storage and monitor the effectiveness of groundwater management.

In this study, three locations, one at the plateau and two in the central plain portion of the Upper Awash Basin, were chosen to install data loggers for monitoring groundwater levels and temperature along the regional groundwater flow direction. It was done by considering the factors affecting groundwater monitoring site distribution (Figure 1.1b). Even though the instruments at two of the boreholes in the plainland portion of the Upper Awash Basin failed, data were still collected by reinstalling the instruments in those two boreholes. Representative wells, BHE30 from the plateau area, BHE20, and BHE28 from the portion of the Upper Awash Basin plain, were chosen along groundwater flow paths that are unaffected by pumping activity within and outside of the study area.

Data loggers (SEBA-Troll 100 & 300) from SEBA-Hydrometrie of Germany (http.//www.seba.de) were installed to monitor groundwater levels and temperature data under natural conditions. Borehole BHE28 provided data for 10 months, while BHE30 and BHE20 provided hourly monitored data for 14 months each. The groundwater level data from these wells were used to estimate recharge rates using the WTF approach.

To determine the recharge, Δh is set to be equal to the difference between the peak of the rise and the low point of the extrapolated antecedent recession curve at the time of peak. The WTF method has some limitations, and recharge rates may vary substantially within the watershed due to the differences in elevation, geology, land surface slope, vegetation, and other factors. Data from multiple wells should be used to ensure that recharge estimates are representative of the catchment as a whole, and the main uncertainties that affect the recharge estimate are the difficulty in estimating specific yield and the frequency of water level measurement.

In general, the study area of 4,456 km² has insufficient monitoring, with only five data loggers installed. Two loggers from part of the Upper Awash Basin were lost and relocated to three new sites: one on the plateau and two in the central plain PUAB. These loggers will track groundwater levels and temperature. While the data offers some insights into seasonal fluctuations, it is not comprehensive enough to represent the entire area and will guide future monitoring efforts. The application of the WTF method in a fractured aquifer requires some special attention (Healy & Cook, 2002), and related to the specific yield of a volcanic aquifer, it varies significantly based on the type of volcanic rock, its structure, and the extent of fracturing and weathering. According to the literature, the general range for the specific yield of volcanic rock aquifers is 0.02-0.15 (Freeze and Cherry, 1979; Domenico and Schwartz, 1998; Rivera, 2014). In this particular study area, analysis of pumping test data was conducted for the aquifer units of three monitored wells, which feature fractured and highly fractured basaltic aquifers. As a result, a specific yield value of 0.1 is assigned for slightly fractured basaltic and 0.15 for highly fractured Basalt and alluvial aquifer wells, and then the recharge rate is computed using the following expression;

$$R = S_y(\Delta h/\Delta t)$$

Where; R-is the recharge rate (mm/y), S_y is the specific yield, and Δh-is the change in water table height over the time interval, Δt.

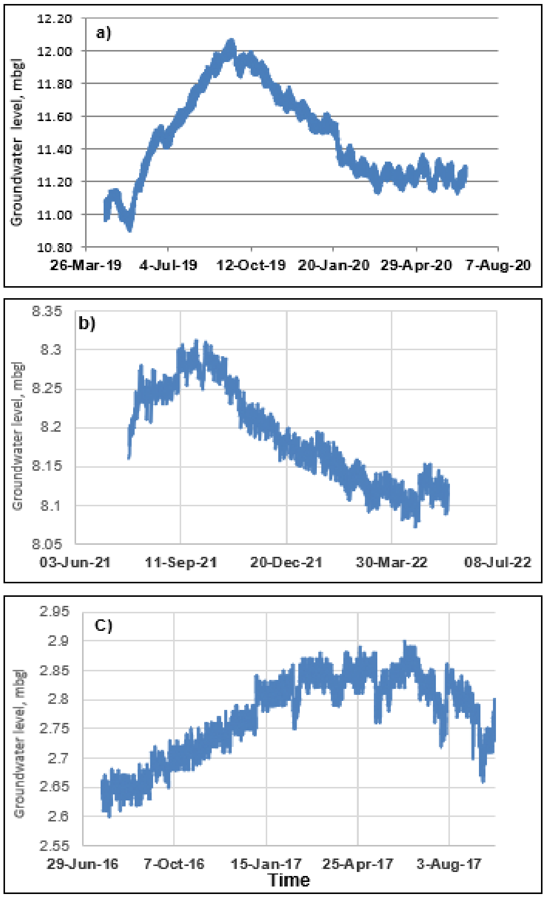

Figure 4.17 Monitored groundwater level record using data logger at a) BHE30 from the plateau, b) (BHE20), & C) BHE28 from the central plain part of the Upper Awash Basin

Based on the groundwater level monitoring of wells (BHE30, BHE20, and BHE28) at the plateau and central plain portion of the Upper Awash Basin, the recorded groundwater level obtained from the data loggers (Figures 4.17a, 4.17b, and 4.17c) and the estimated recharge rates is as follows (Table 4.14).

Table 4.14 Estimated recharge rate of the plateau and plain PUAB

Groundwater level monitored wells	Minimum groundwater level (hmin), m.b.g.l	Maximum groundwater level (hmax), m.b.g.l	Change in groundwater level flucutation (Δh),m	Specific yield (Sy)	Recharge , mm/year	Aquifer type
BHE30	11.12	12.07	0.95	0.1	95	Fractured basalt
BHE20	8.07	8.31	0.24	0.15	36	Highly fractured basalt and fine sand
BHE28	2.6	2.9	0.3	0.15	45	Highly fractured basalt and coarse sand

Hence, an average annual recharge value of 95 mm was estimated for the plateau area, while a mean value of 40.5 mm was estimated from the records for the PUAB. It is 8.5 and 3.6 % of the total mean annual precipitation for the plateau and the central plain, PUAB, respectively.

4.6.4 Darcian approach

The Darcy method has been used since 1937, with the assumption that groundwater flow is horizontal in aquifers and vertical in aquitards (Fetter, C.W., 2018; Zhao, M., & Zhang, L., 2021). The Darcy flux approach states that the volumetric flux through a vertical cross-section of an aquifer is equated to the recharge rate times the surface area that contributes to flow through aquitards (Singh, K.P., & Kumar, P., 2020; Bohle, J. K., & Denver, J.M., 2022). It can be used to compute the flow rate through a cross-sectional area of the aquifer by summing up flow rates through individual stream tubes.

The groundwater flow rate through a stream tube at a selected cross-section can be computed by considering the discrete difference in the hydraulic head for two successive contour lines, the stream tube's width, and the aquifer's thickness. The method's accuracy relies on both the accuracy of hydraulic conductivity values and their spatial variability (Nimmo et al., 2005; Morris, J.T., & Bartels, E., 2023). This method assumes that the hydraulic gradient is uniform between the tensiometers and that all the water that infiltrates to the depth of the tensiometers becomes recharge or groundwater flux; it does not consider water that is subsequently lost from the unsaturated zone, such as by evapotranspiration. Although Darcy’s law was originally derived for flow through porous media, its application to fractured aquifers is justified in this study through the equivalent porous medium (EPM) assumption. This approach treats the fractured system as a continuum with effective hydrogeologic properties, such as hydraulic conductivity (K) and specific storage (Ss), that represent the bulk behavior of the fractured matrix. The validity of this assumption is supported by consistent drawdown responses across 34 representative wells and the spatial coherence of transmissivity values derived from pumping tests. Given the scale of analysis and the density of fractures, the aquifer behaves as a porous medium, allowing the application of Darcy's principles for recharge estimation and flow analysis. This methodology aligns with established hydrogeological practice and is supported by foundational literature (Bear, 1972; Zhang and Schwartz, 1995; Neuman, 2005).

This method has not been widely used in the country due to the complex geological setting, characterized by an uneven distribution of transmissivities and hydraulic conductivities, and a lack of sufficient monitoring wells. However, the application of the method appears to be justified for this study area of aquifers. While there is a reasonable variation in transmissivity, representing the major aquifers, a reliable average can be determined from pumping tests carried out for several representative wells (34 in number).

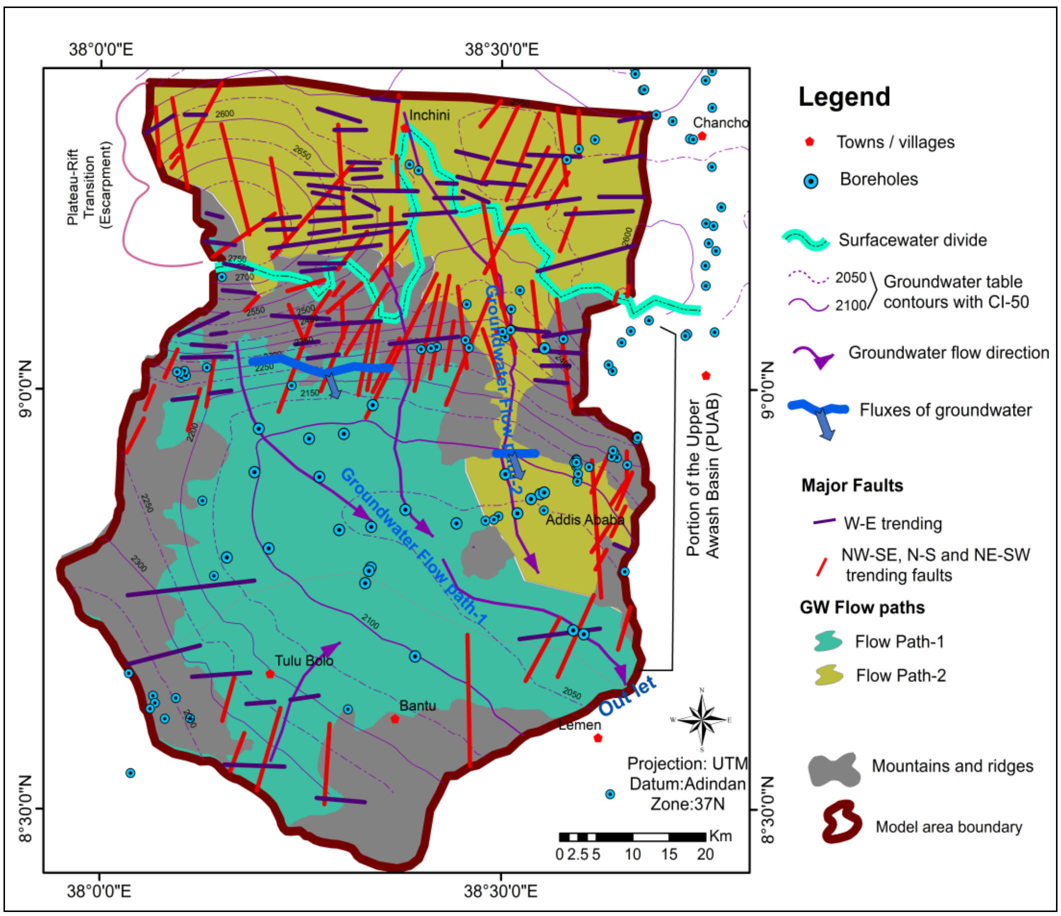

Figure 4.18 Groundwater flow system (Contour in meters above sea level) for confined aquifer system of the area

Several groundwater levels recorded in wells with a reasonable distribution over the study area allow the preparation of groundwater level contour maps (Figure 4.18). It is easy to apply if information on large-scale effective hydraulic conductivity and hydraulic gradient is available, assuming a steady flow of no water extraction through a cross-section of an unconfined or confined aquifer. The groundwater level elevation contour map (Figure 4.18) is used to determine the flow gradient (i) and flow length (L). The term flow length refers to the distance along the flow path. In the context of Darcy's approach to estimating recharge, the relevant dimension is the width perpendicular to the flow, which defines the cross-sectional area through which the flow occurs. However, the transmissivity (T) value of an aquifer is computed from the pumping test and recovery data measured in 34 spatially distributed boreholes.

The recharge estimation formula $R=T \cdot i \cdot L \cdot 365$ is derived from Darcy's law, adapted for annual groundwater flux across a defined flow section. This formulation is commonly used in regional hydrogeological assessments (Fetter, 2001; Domenico & Schwartz, 1998), where: R is the annual recharge rate (m^3/year), T is transmissivity (m^2/day), i is the hydraulic gradient(dimensionless), L is the flow width perpendicular to the direction of groundwater flow (m), and 365 converts daily flux to annual volume. The recharge volume expression, used to estimate annual lateral inflow through a vertical section, is derived from Darcy's Law:

- Darcy's law gives specific discharge: $q=K \cdot i$, where K is hydraulic conductivity
- Transmissivity is defined as $T=K \cdot b$, with b-is being the aquifer thickness.
- Total recharge volume over a year is: $Q=q \cdot A \cdot t$, where $A=b \cdot L$ and t= 365 days.
- Substituting and simplifying gives: $Q=T \cdot I \cdot L \cdot 365$

The parameter L is measured from the groundwater contour map (Figure 4.18) by identifying the segment of the flow boundary that intersects equipotential lines at approximately right angles. This segment represents the effective cross-sectional width through which groundwater flow occurs. In this study, L was delineated by tracing the length of the contour-perpendicular boundary across the modeled aquifer zone, ensuring alignment with the dominant flow direction inferred from the potentiometric surface.

Hence, the recharge rates for unconfined and deep confined aquifer systems were computed for the area of interest, i.e. portion of the Upper Awash Basin. Furthermore, representative boreholes for unconfined and confined aquifers along the two flow paths were carefully selected to estimate transmissivity from pumping-test data and to compute the annual recharge rate of the existing aquifer system using the groundwater-level contour map (Tables 4.15 and 4.16).

Table 4.15 Groundwater flux from the northwestern side (Flow path 1, an area of 2308 Km^2)

No.	Aquifer Type	T, m^2/day	i	L, m	R, m^3/day	R, Mm^3/Yr	R, mm/year
1	Unconfined aquifer system (Data from BHE64, 78, 124,125, 131)	64.4	0.004	68,221.0	17,579.2	6.4	2.8
2	Deep confined aquifer system (Data from BHE1, 3,5, 18,19, 20, and 22)	416	0.006	68,221.0	170,279.6	62.2	26.9
					Total	68.6	29.7

Table 4.16 Groundwater flux from the northern side (Flow path 2, an area of 2018.6 Km^2)

No.	Aquifer Type	T, m^2/day	i	L, m	R, m^3/day	R, Mm^3/Yr	R, mm/year
1	Unconfined aquifer system (Data: BHE 60,84,86,87)	92.03	0.003	81,961.0	22,628.6	8.3	4.1
2	Deep aquifer system (Data: BHE28,29,32,36,47,48,50)	819	0.006	81,961.0	402,756.4	147.0	72.8
					Total	155.3	76.9

Table 4.17 Summary of estimated recharge rates for each aquifer unit

No.	Aquifer Type	R, Mm^3/year	R, mm/y
1	Unconfined aquifer system	14.7	6.9
2	Deep aquifer system	282.3	99.8
	Total	296.9	106.6

Using Darcian flux computation, the overall recharge rate for a PUAB groundwater flow system is about 106.6 mm/y or 296.9 Mm^3/year, about 9.6 % of the annual precipitation (Table 4.17).

The rationale for employing the same groundwater-flow length and direction for both confined and unconfined aquifers within Darcy's framework for recharge estimation in interconnected systems, such as parts of the Blue Nile and Upper Awash basins, is grounded in both conceptual clarity and practical modeling considerations.

Conceptually, interconnected systems demonstrate continuity across aquifer boundaries, as groundwater flow is influenced by hydraulic gradients and structural features rather than lithological divides. In the case of the Blue Nile and Upper Awash basins, this is exemplified by inter-basin groundwater transfer, particularly through NW-SE trending fault zones and volcanic lineaments. Furthermore, at a regional level, groundwater flow typically aligns with topographic gradients and structural characteristics. This alignment supports the idea of a consistent flow direction across different aquifer types. Notably, recharge zones in the Blue Nile, such as the Mugher and Jema sub-basins, significantly contribute to the Upper Awash system, accounting for up to 37% of its annual recharge (Azagegn et al., 2014; Berhanu et al., 2017). To simplify recharge calculations in complex terrains, adopting uniform flow directions and lengths across aquifer types is essential, as it does not drastically compromise accuracy and aids in integrating various recharge estimation methods.

From a technical perspective, both confined and unconfined aquifers respond to regional hydraulic gradients despite their differing flow mechanisms, pressure-driven versus gravity-driven. In volcanic areas like this study area, it is reasonable to assume unified flow patterns since these aquifers often share recharge sources and structural influences. As mentioned before, a W-E trending impermeable mudstone horst serves as a groundwater divide but simultaneously facilitates flow from part of the Blue Nile to the Upper Awash. The orientation of faults and lineament density also plays a critical role in determining groundwater flow paths, frequently outweighing the confinement status of the aquifers. Supporting these assertions, isotopic and hydrochemical evidence indicates that waters with $\delta^{18}O$ and δD depletion, along with high total dissolved solids and $NaHCO_3$ signatures, provide insights into the lateral flow from the Blue Nile to the Upper Awash. Such signatures are consistent across different aquifer types, further reinforcing the assumption of a shared flow direction and length.

Strategically, adopting the same flow length and direction facilitates coherence in modeling across sub-basins, enhances the integration of recharge estimates from various methods, and aligns with the observed inter-basin flow dynamics and structural geology. This approach ultimately strengthens the understanding of groundwater interactions within the interconnected basins.

The dynamics of confined volcanic aquifers exhibit a greater hydraulic gradient compared to unconfined aquifers, a phenomenon that can be attributed to several geological, hydrodynamic, and structural factors. In confined systems, such as those found in the study area, aquifers are encased by low-permeability layers known as aquitards, which create pressure by trapping water. This pressure is aggravated by recharge from highland areas, leading to artesian pressures that increase the hydraulic head. Consequently, the pressure differential results in a steeper hydraulic gradient over shorter distances compared to the gravity-driven flow characteristic of unconfined aquifers.

The geological structure of volcanic terrains further contributes to this phenomenon. Confined aquifers typically exist beneath the impermeable caps of thick massive basalt or ignimbrite layers, which limit vertical water movement. Faults and fractures serve as conduits, channeling water both vertically and laterally, thus concentrating gradients along narrow pathways. Notably, the NW-SE trending faults that intersect the Blue Nile and Upper Awash basins augment the buildup of hydraulic head in these confined areas.

Moreover, the localization of recharge in regions such as the Muger sub-basin delivers water to confined layers that struggle to dissipate it due to their low vertical permeability. This results in concentrated head accumulation, thereby steepening the gradient. The contrast in lithology also plays a crucial role: confined aquifers composed of high-hydraulic-conductivity materials like fractured scoriaceous basalts are often overlain by low-permeability units. This considerable difference in permeability enhances head disparities over short distances, further steepening the gradient.

According to Darcy's Law, which defines the flow concerning the hydraulic gradient, the gradient in confined aquifers tends to be greater due to the pressure buildup. Even with moderate hydraulic conductivity, the steep gradients can drive substantial flow. In the context of the left flank of the Blue Nile and Upper Awash system, recharge from the Blue Nile enters confined aquifers located beneath structural highs, facilitating inter-basin flow through fault-controlled pathways. In contrast, unconfined aquifers in the Upper Awash experience gentler gradients, attributed to their open connection with the water table and atmospheric pressure.

In the context of groundwater flow within interconnected volcanic aquifer systems, the relationship between transmissivity and hydraulic gradient can appear surprising. According to Darcy's Law, groundwater flow is characterized by the equation $Q = -T * (dh/dl)$, where discharge (Q) is influenced by transmissivity (T) and the hydraulic gradient. Typically, one might associate higher transmissivity with a lower hydraulic gradient, given that a more transmissive aquifer can move water more freely. However, in these complex volcanic terrains, several factors lead to an opposite observation where greater hydraulic gradients are evident in areas of high transmissivity.

Initially, the recharge-driven gradients in area like Muger sub-basins demonstrate that intense recharge from fractured highlands generates steep gradients, indicating that the gradient reflects energy input from recharge rather than merely the resistance of the aquifer itself. Additionally, inter-basin transfers contribute to this phenomenon; the Upper Awash receives groundwater from the Blue Nile, where high transmissivity zones necessitate a driving gradient to maintain inter-basin flow. Structural features such as faults and lineaments also play a crucial role by channeling groundwater flow and creating localized high gradients within transmissive zones. These structures can act as hydraulic ramps, facilitating rapid flow across basin boundaries. In confined aquifer systems, even with high transmissivity, artesian pressure from upgradient recharge areas maintains high hydraulic gradients.

Overall, in interconnected aquifer systems, transmissivity can be viewed as the capacity of the aquifer to move large volumes of water, while the hydraulic gradient serves as the driving force, ensuring directional flow, especially across divides. Therefore, in the context of the Blue Nile and Upper Awash basins, the existence of high hydraulic gradients in zones of high transmissivity is not contradictory but vital for sustaining regional groundwater fluxes and facilitating effective recharge propagation.

4.6.5 Comparison of results

Comparing recharge rates estimated by different methods is not straightforward, as each method may have its strengths, limitations, and uncertainties, which require a systematic approach to ensure a fair and meaningful comparison. It is crucial to carefully analyze and interpret the recharge rates by considering each method’s underlying principles, data availability, specific objectives, and conceptualization of the groundwater flow system. These factors will ensure that the selected method provides meaningful and better recharge rates for further investigation.

The hydrogeological conceptualization of the area is that aquifers of the study area receive most of their recharge from the northern, northwestern, and western parts. The findings of earlier studies (Kebede et al., 2007; Ayenew et al., 2008; WWDSE, 2008; Yitbarek et al., 2012; Azagegn et al., 2014) using lithohydrostratigraphy, groundwater hydrochemical, and isotopic evidence also illustrated that the primary sources of recharge for the unconfined aquifer system (superficial deposit and Rift Basalt units) are modern precipitation, nearby streams or rivers through fractures, and sub-surface inflow from the plateau or escarpment. It was also verified that the plateau and transitional escarpment, as well as the region beyond the plateau, serve as the main recharge areas for the regional confined scoriaceous basaltic aquifer.

To quantify the reliable recharge rate of the area for further investigation, a comparison of study results with one another plus with previous studies was carried out. A variety of recharge estimation techniques, such as Baseflow separation, water balance, groundwater level fluctuation, and Darcian methods, were applied, considering their applicability in humid hydrogeological systems and the different input data they utilize.

Previous recharge estimations conducted by various researchers (WWDSE, 2008; Yitbarek, 2009; Azagegn, 2015; Nuramo, 2016; Berehanu et al., 2017) indicate a significant variation in recharge rates for different areas within the Upper Awash and Blue Nile Basins. The recharge rates range from 18.4 to 319 mm/y, and from 90 to 239 mm/y for parts of the Upper Awash and Blue Nile Basins, respectively (Table 4.18).

Table 4.18 Summary of previously estimated recharge rates for similar areas, including the research area (mm)

No.	Location	Computed annual recharge		Methods	Reference
		mm	Mm^3		
1.	Melkakuture Watershed	81.4	362.7	Baseflow separation	Nuramo, 2016
		319.5	1423.7	Water balance	
		142.0	632.8	Water balance model (WATBAL)	WWDSE,2008
		82.5	369.2	HBV rainfall-runoff model	WWDSE,2016
		18.4	173.0	Baseflow separation	Yitbarek,2009
	Muger watershed	90.0	44.8	GWT Fluctuation	
2.	Ombole watershed	131.0	1002.9	Water balance	Azagege, 2015
		135.0	1033.6	Chloride mass balance	
		103.0	788.6	Baseflow separation	
	Muger watershed	125.0	62.3	Water balance	
		148.0	73.7	Chloride mass balance	
		158.0	78.7	Baseflow separation	
3.	Ombole watershed	135.0	1033.5	Chloride mass balance	Berhanu, 2017
		91.3	698.6	Baseflow separation	
		157.0	1201.9	1D-Hydrus	
	Muger watershed	239.0	119.1	1D-Hydrus	

The current results also show a wide range in the order of 40.5 to 601.2 mm/y and 56.4 to 328.7 mm/y for a PUAB and PBNB, respectively (Table 4.19).

Table 4.19 Current estimated recharge rates utilizing four different approaches

No.	Areas	Computed annual recharge		Methods
		mm	Mm^3	
1	A portion of the Upper Awash Basin (4456 Km^2)	40.5	139.3	Water table fluctuation (WTF)
		106.6	296.9	Darcian computation
		102.2	455.3	Hydrograph separation
		601.2	1597.3	Water balance
2	A portion of the Blue Nile Basin (489 Km^2)	95	46.5	Water table fluctuation (WTF)
		328.7	356.6	Water balance
		56.4	150.8	Hydrograph separation

The range of recharge rates observed in this study aligns with findings from previous research conducted in the area (Table 4.18). However, differences in recharge rates can be attributed to the principles behind each technique, variations in data usage, and inherent uncertainties. To establish a reliable recharge rate for the study area, a comprehensive analysis and interpretation of the results are necessary, considering the context, data availability, and the specific objectives of the recharge assessment.

Baseflow, which is the portion of stream flow that is typically attributed to groundwater discharge, can occasionally be used as an approximation of recharge when underflow, evapotranspiration, and other groundwater losses from the watershed are assumed to be negligible. However, some authors (Chen & Lee, 2005; Riser et al., 2005) argue that Baseflow is not an exact recharge. For this study, this method computed a recharge rate of 102.2 mm/y or 455.3 MCM/year (9.2 % of the yearly precipitation) for PUAB. To use this result as a representative of the entire aquifer system for further simulation works, the regional underlying confined aquifer is a critical drawback of the other three methods.

Although the water balance approach is a useful tool for calculating recharge in the area, it has considerable drawbacks. It is an indirect estimate, which introduces additional sources of uncertainty and potential computational errors by accounting for the differences between the input and output components of the water balance expressions. Reliable data on evaporation, precipitation, soil properties, and other hydrological factors might be hard to come by, which can lead to a rough estimation of recharge. Using data from six and four widely scattered meteorological stations in the area, the final computation yielded results for a PUAB and PBNB, respectively, 601.2 mm/y and 328.7 mm/y. These higher values represent potential rather than net recharge rate on an annual basis when compared to the other three methods.

The WTF method is quite simple, as no assumptions are made on the mechanism by which water reaches the groundwater. The main disadvantages are related to its applicability to only unconfined aquifers, and difficulties arise in obtaining a specific yield value for specific aquifer types. Of the four methods used in this study, the WTF method generally estimated the lower recharge rates for both portions (40.5 mm/y for

PUAB and 95 mm/y for a PBNB), representing gross recharge on an annual basis. It is a better result mainly for the delineated unconfined aquifer in the central plain PUAB with an area of 3440 km^2. The recharge rate estimated using the Darcian approach is often considered better than other methods due to its focus on localized measurements and the specific characteristics of the study area. The choice of method for estimating recharge in unconfined aquifers often favors the Water Table Fluctuation (WTF) method over Darcian flow, despite the latter's theoretical strength. The WTF method is preferred due to its practical application, as unconfined aquifers feature a free water table that responds directly to recharge events. WTF effectively captures these local fluctuations, making it suitable for settings where water levels can be directly observed. In contrast, confined aquifers do not show similar fluctuations due to pressure, limiting the applicability of the WTF method. While Darcy's Law is universally applicable, it is more theoretical. For interconnected aquifer systems in the Upper Awash and Blue Nile Basins, the WTF method is favored for estimating recharge in shallow unconfined aquifers, while Darcy-based modeling is used for confined volcanic aquifers due to significant structural controls and pressure gradients.

The key reasons why Darcy's method is better than the three are;

- The Darcy method allows for determining recharge rates at specific measurement points or small areas, providing a more accurate assessment of spatial variations in recharge.
- It relies on direct measurements of hydraulic conductivity and hydraulic gradients, which can yield precise and relevant data about how water moves through the subsurface.
- The method considers the unique characteristics of the study area, such as soil properties and geological features, leading to more tailored and applicable recharge estimates.
- Combined with other methods, like the water table fluctuation (WTF) method, it enhances understanding of groundwater recharge processes, offering a more comprehensive perspective.

- The Darcy method provides valuable insights into the vertical flux of water through the unsaturated zone, which is critical for understanding how recharge occurs through surface water and groundwater interactions.

Overall, these factors contribute to the effectiveness of the Darcian approach in estimating recharge rates, making it a preferred choice in hydrogeological studies.

Generally, the WTF approach often considers both specific yield and groundwater level when estimating recharge; it is reasonable to use the recharge rate from such a method for an unconfined aquifer rather than the other three techniques. An attempt was made to use the result of the WTF in conjunction with the Darcian technique to provide a more comprehensive result by considering the available unconfined and confined aquifer systems.

4.7 Summarized discussion

The overall results of the investigation are discussed in this section using converging evidence from multiple techniques such as geological, hydrogeological, hydrological (Baseflow separation), hydrogeochemical, and environmental isotopes (stable isotopes and ^{222}Rn). The groundwater flow system of the area is conceptualized and underlines the hydro lithostratigraphy, aquifer-surface water interaction, and aquifer's recharge area identification with the valuation of recharge.

4.7.1 Lithohydrostratigraphy

Lineaments predominantly oriented NW-SE influence most of the sedimentary units in the northern and northwestern regions, as well as the Trap series columnar and weathered basaltic formations. The younger volcanic rock units overlaying the Trap series Volcanic, primarily found along the flanks of the MER and YTVL zones, are notably fractured and jointed, with predominant lineament orientations in the N-S, E-W, and NE-SW directions. The W-S oriented fault system in the region is depicted as the cause for the degradation of the regional confined scoriaceous basaltic aquifer. Additionally, the NW-SE, NE-SW, and N-S directed regional tectonic structures play a critical role in facilitating the flow of recharged water from the Plateau to the southern groundwater system.

The geo-structural characterization of the area was undertaken by harmonizing geological maps of varying scales with ground verification and calibration through existing borehole lithologic logs. Furthermore, utilizing data from pumping and recovery tests, an attempt was made to identify aquifer units and their hydraulic properties. Hydrogeological cross-sections were developed to illustrate the overall lithohydrostratigraphic architecture effectively.

The lithologic logs were systematically integrated to establish distinct hydrogeologic units, given the comparable hydrogeological properties observed across the various water supply wells. This analysis identified four primary hydrogeologic units, each exhibiting unique characteristics and reaching a depth of 600 meters. These units provide critical insights into the subsurface geology and hydrology, facilitating a better understanding of the aquifer systems and their potential for sustainable water supply management.

The hydrogeological setting of the area is characterized by several distinct types of litho-hydrostratigraphic units. First, there is the superficial deposit aquifer composed of alluvial and volcanic ash deposits, which include various units such as colluvial sediments, alluvium, and ashfall. Beneath these layers, one can find the fractured Rift basaltic aquifer, which includes a series of rock units that incorporate weathered, vesicular, and fractured basalt. In addition to these productive aquifers, there exists a layer of impermeable acidic rock units mostly found beneath it, including rhyolite, ignimbrite, and tuff, which collectively function as a confining unit. This impermeable layer restricts groundwater movement and creates pressure for the underlying aquifer. The most significant regional hydrogeologic unit is the Tarmaber vesicular and scoriaceous basalt, commonly referred to as the scoriaceous basaltic aquifer. This aquifer is extensively distributed in the plateau, and at greater depths, particularly in the central plain part and southeastern outlet zones. Due to its stratigraphic relationships and the underlying geological framework, the scoriaceous basaltic unit plays a crucial role in facilitating the dynamics of regional groundwater flow, acting as a key conduit for the regional groundwater movement from the plateau to the model area and further outwards into the adjacent groundwater system.

4.7.2 Groundwater-surface water interaction

Characterization of the groundwater-surface water interaction zones involved by integrating the findings from ^{222}Rn, EC, and BFI, accompanied by the geological configuration.

The combined results of environmental tracers (^{222}Rn, δ^2H, $\delta^{18}O$, and EC), BFI, and lineament density are used to determine the inferred exchange between surface water and groundwater in the map shown in Figure 4.19. Thus, the primary effluent stretches are.

- Headwater portions of both basins, including regions that fall along the surface water divide between portions of the Blue Nile and Upper Awash basins, which are distinguished by a) ^{222}Rn: 100 to 200 Bq/m^3 for rainy seasons and 100 to 465 Bq/m^3 for non-rainy seasons. b) EC: Between 140 and 170 µS/cm during wet seasons and between 352 and 435 µS/cm during non-rainy seasons. c) δ^2H and $\delta^{18}O$: The isotopic signature of shallow wells, rivers, streams, and springs is comparable (Figure 4.19). d) BFI. BFI > 0.5, and e) high lineament density zone (0.96 to 3.0 km/km^2).
- Southern and southeastern (outlet PUAB) periphery is recognized as the regional groundwater outlet zone with a) ^{222}Rn: 200 to 477 Bq/m3 and 465 to 1467 Bq/m^3 for rainy and non-rainy seasons, respectively, b) EC: 180 to 270 µS/cm for rainy and 480 to 677 µS/cm for non-rainy seasons, c) BFI: 0.35 < BFI < 0.5 d) moderate to high lineament density zone (0.41 to 0.96 km/km^2).
- The rivers and streams in the central plain area of the Upper Awash Basin exhibit relatively low Baseflow index (BFI < 0.35), low ^{222}Rn levels (< 100 Bq/m^3), and low electrical conductivity (EC < 142 µS/cm) in both seasons. Additionally, the low lineament density in the region suggests minimal or no connection between groundwater and surface water, except for the EGS6, which has a BFI value of 0.58. One possible explanation for the high BFI, given that the station is located in a plain area, is that its connectivity with the major NE-SW trending fault

system (Yerer-Tulu-Welel Lineament zone) running along this station might feed the regional groundwater.

During a typical dry period, the main river in the central plain area is almost dry. In contrast, during the rainy season (from July to the end of September), the region experiences significant flooding, resulting in prolonged waterlogged conditions. During fieldwork in the dry season, we observed substantial water flow in the streams at the escarpment, particularly in the Holeta, Addis-Alem, Wolonkomi, and Ginchi areas. However, in the central plain section, almost no flow, which shows the water had seeped into the deeper groundwater system at the foot of the escarpment. Meanwhile, at the outlet section in Melkakunture, the water flow was significantly higher. It is supported by the result of ^{222}Rn measurements, which indicate high values during the typical dry season at both the escarpment and the outlet. In addition to that, the recorded flows in the upstream sections show high values during the dry period (Table 4.20). Due to the absence of data and the challenging, highly dissected topography, it is not feasible to fully characterize the lower reaches of part of the Blue Nile River and its tributaries.

Table 4.20: Monthly flow rate at different stations (L/s/Km^2)

No.	Station Name	1	2	3	4	5	6	7	8	9	10	11	12	Sub-catchment area, km2
1	Holeta R @ Holeta (EGS3)	3.18	2.69	2.64	3.51	3.14	4.69	28.59	50.74	26.23	8.49	5.05	4.09	119
2	Berga @ Adisalem (EGS4)	4.56	4.33	4.04	4.14	4.07	7.72	41.81	69.23	39.00	14.65	10.32	6.55	248
3	Teji @ Ginchi (EGS2)	0.22	0.17	0.23	1.18	1.99	4.06	17.61	23.55	12.05	1.74	0.46	0.27	662.5
4	Awash @ Awash Bello (EGS6)	0.12	0.09	0.11	0.46	0.60	3.05	10.53	15.38	12.05	2.73	0.58	0.23	2568.8
5	Awash @ MK (EGS7)	0.38	0.31	0.51	0.92	1.44	3.86	19.83	38.85	21.99	2.68	0.75	0.47	4456

N.B.: Numbers 1 to 12 represent months (January to December)

In general, the plateau's aquifer system is hydraulically connected to the outlet portion aquifer system for PUAB through the regional geological structures, as evidenced by records of higher seasonal values of ^{222}Rn and EC, and high BFI found in various river or stream reaches of the area. Furthermore, most isotopic (δ^{18}O, δ^{2}H) data from deep water sources in a plateau, escarpment, and a portion of the Upper Awash show similarly highly depleted signatures related to Addis Ababa summer rain, indicating that the aquifer systems have similar origins (plateau and escarpment area) and hydraulic connectivity due to the presence of regional fault systems that trend north-south and northwest-southeast, which transfer plateau-type water into the Upper Awash Basin's aquifer system. In conclusion, the findings from ^{222}Rn and BFI were enhanced by incorporating data from geology, EC, and stable isotopes (δ^{18}O, δ^{2}H) to provide a more comprehensive characterization of the zones where groundwater and surface water interact.

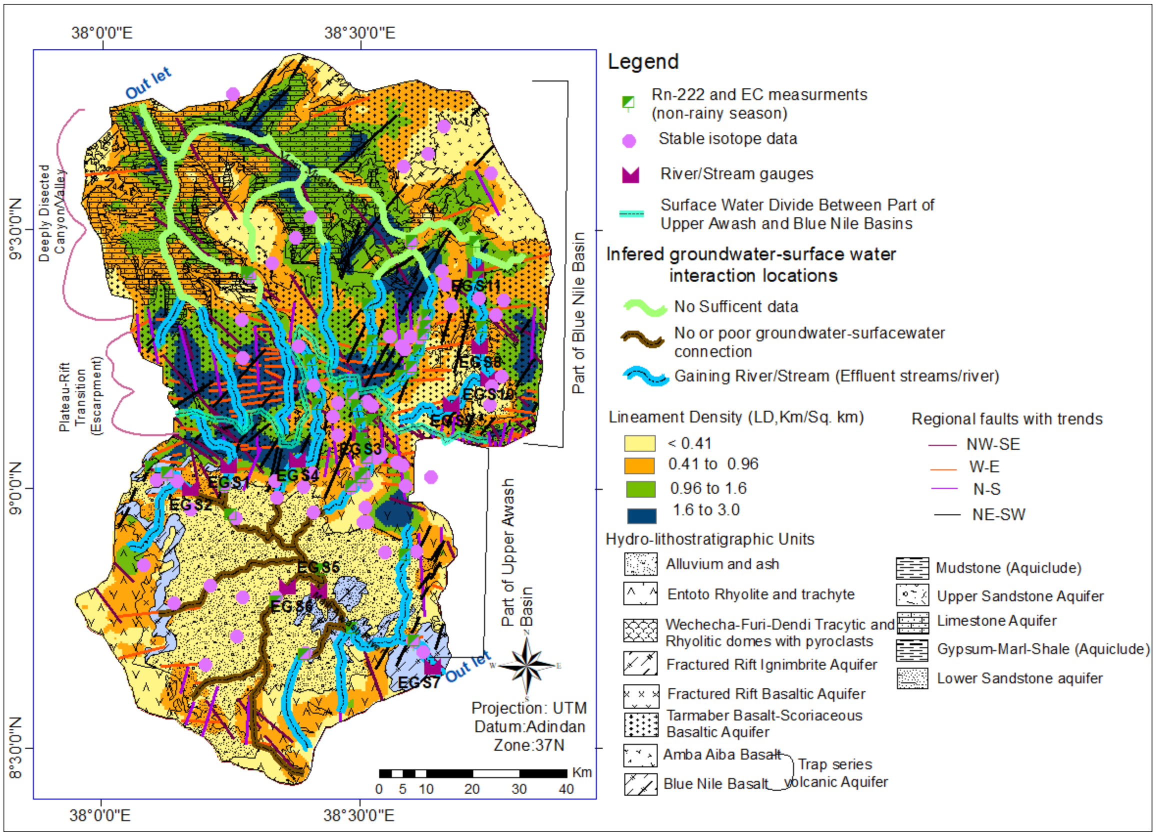

Figure 4.19 Inferred stream segments of the groundwater-surface water interaction zones of the area

4.7.3 Aquifers recharge area identification and recharge rate estimation

4.7.3.1 Recharge area identified for available aquifers

Figure 4.20 provides an illustrative summary of the recharging zones based on the combined hydrochemical and stable isotopic signatures of groundwater, in conjunction with the geostructural distribution. The main recharge zones for the major unconfined and deep, confined regional aquifer systems are described here.

- Unconfined aquifer (depth less than 150 meters; consists of superficial deposit and Rift basalt) is recharged mainly from modern precipitation and existing rivers/streams. Water samples from such aquifer have mixed $CaHCO_3$ and $CaMgHCO_3$ water types, low average TDS (<200 mg/l), high Ca^{2+}/Na^{+} ratio (> 5) ratio, lower Residual Alkalinity (< 2.0), isotopically enriched signal (mean value for $\delta^{18}O$ > -2.0 ‰ and $\delta^{2}H$ > -5.0 ‰), and high deuterium excess (13.3).

- The acidic rock units (mainly consisting of rhyolite, ignimbrite, and trachyte) are situated between the unconfined and deep confined aquifers, vary in thickness based on the influence of faults, and stretch horizontally to the southern portion's outflow. In general, it is a confining unit acting as an aquiclude/aquifuge.

- Recharge area for the deep regional confined aquifer (artesian scoriaceous basalt) system with a thickness of more than 350 meters is mainly the headwater parts (Plateau and transitional escarpment) and beyond it, which is characterized by. high lineament zone (0.96 to 3.0 km/km^2), groundwater samples from deep wells throughout the study area show highly concentrated $NaHCO_3$ or $NaHCO_3Cl$ water types, high TDS (> 468 mg/l), low Ca^{2+}/Na^{+} (<1) ratio, higher Residual Alkalinity (> 2.0), depleted isotopic signature (< -3.0 ‰ for $\delta^{18}O$, < -9.0 ‰ for $\delta^{2}H$), low d-excess (nearly 11) related to the LMWL.

As illustrated from different graphical descriptions of the groundwater hydrochemical and isotopic data, the plateau, including the surface water divide areas, has relatively dilute hydrochemistry associated with moderate to high fracture zones, categorized as a recharge area for the surrounding aquifer, which progressively evolved to the mineralized hydrochemical composition with groundwater flow routes into its outlet. Additionally, plateau and/or transitional escarpment areas of having high lineament distribution are recognized as a recharge zone primarily for the regional fractured confined scoriaceous basalt aquifer. High RA, high TDS, and NaHCO3 water types from the plateau and USPAB deep wells signify the groundwater outflow from the eastern flank of the Blue Nile Basin to the nearby Basin. The hydrochemical data of shallow boreholes and low-yield cold springs distributed throughout the area show very low RA (RA < 1.0) and isotopically enriched waters, which indicates that shallow groundwater systems receive direct recharging from meteoric water.

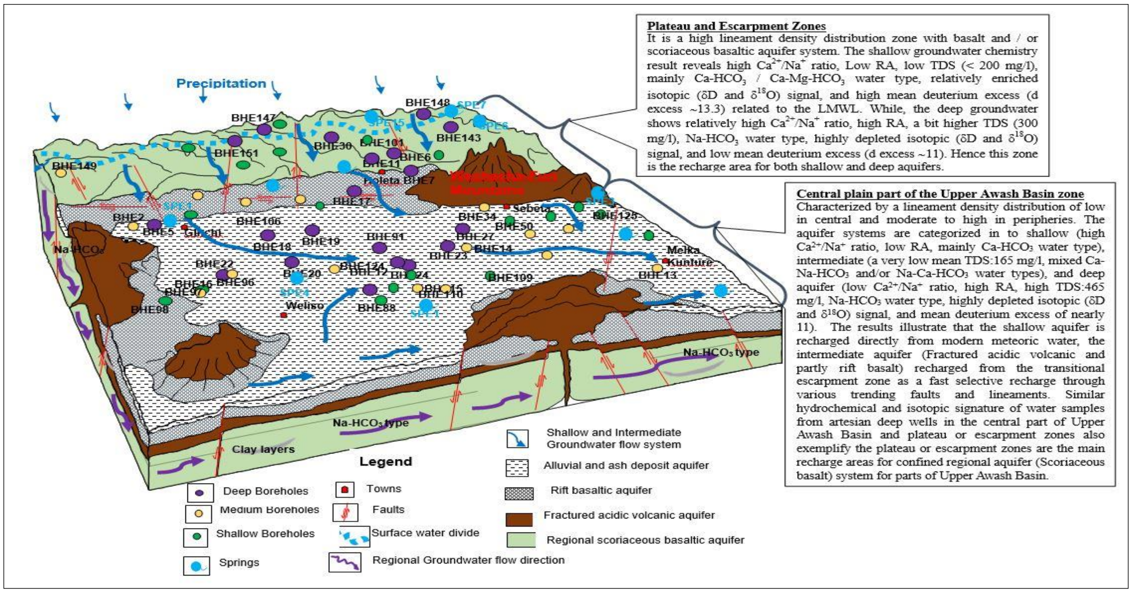

Figure 4.20 Study area Schematic hydro geochemical evolution conceptual model of the groundwater flow system (not to scale)

4.7.3.2 Groundwater recharge rate

Recharge for PUAB is computed using the principle of groundwater budget, which is defined as the total volume of water entering and exiting an aquifer. In a balanced groundwater system, particularly before development, the amount of water replenishing the system equals the amount being discharged over time. The water storage capacity either remains constant or fluctuates around an average level due to annual or longer-term variations (Fetter, 2001; Healy & Sophocleous, 2004; Wetzel & Newell, 2006; Duncan, 2017).

The recharge for PUAB is calculated using the groundwater budget principle; the water replenishing the system is equal to the water being discharged over time. In general, the groundwater that flows into the central plain of the Upper Awash Basin (the area we are focusing on: Model area boundary) comes from the northwest and northern plateau, and this is called subsurface inflow. This water eventually moves southeast to exit the system (Figure 4.7). The groundwater that reaches the southeastern outlet zone comes from seepage due to runoff and direct rainfall on the fractured basaltic and surface deposits, along with subsurface inflow from the northern, northwest, and southwestern parts of the plateau and escarpment.

The groundwater flow (recharge) for both unconfined and confined aquifers is 106.6 mm per year. This figure comes from Darcy's method, used in a section of the Upper Awash Basin (Table 4.18). The value includes water from runoff, direct rainfall on the unconfined aquifer, and water flowing into both aquifers from sub-surface inflow. After determining the total recharge amount of 106.6 mm per year, it is difficult to figure out how much is for the unconfined aquifer and how much is for the confined aquifer.

An attempt was made to classify the groundwater recharge based on the area of interest (referred to as the Model area) and the extent of the flux or subsurface inflow zone located on the escarpment and plateau. The recharge was estimated using the Water Table Fluctuation (WTF) method (Section 4.6.4), which is best suited for unconfined aquifer. For the central plain land area to be modeled, this method yielded a recharge estimate of 40.5 mm/year, factoring in seepage recharge from runoff and direct precipitation, based on an area coverage of 3,440 km^2.

Additionally, the value computed using Darcy’s method, which also incorporates subsurface inflow to the unconfined aquifer, amounted to 6.9 mm/year (Table 4.18). Therefore, the total recharge rate for the unconfined aquifer is 47.4 mm/year, consisting of 40.5 mm/year from the WTF method and 6.9 mm/year from subsurface inflow.

The remaining amount of groundwater recharge calculated is 59.23 mm/year, which accounts for the subsurface regional groundwater inflow from the plateau and/or escarpment to the confined aquifer system. Numerical groundwater modeling will further verify and validate the conceptual and analytical groundwater budget computed for the PUAB aquifer system (Table 4.21).

Table 4. 20 Computed mean annual groundwater budget for PUAB

No.	Groundwater Inflow Components to the central plain part of the Upper Awash Basin	Inflow			Outflow		
		mm/year	m^3/day	MCM/yr	Mm/yr	m^3/day	MCM/year
1	Recharge from runoff seepage (at the foot of the escarpment, and through stream channels) and direct precipitation on the alluvial plain) computed using WTF method (Area: 3440 km^2)	40.5	381,698.73	139.3			
2	Recharge from draining the northwestern and northern plateau & Escarpment as a regional subsurface inflow for unconfined aquifer system (Area: 2552 km^2)	6.9	48,243.28	17.6			
3	Recharge from draining the northwestern and northern plateau & Escarpment as a regional subsurface inflow for confined aquifer system (Area: 2552 km^2)	59.23	414,123.13	151.2			
Total budget for central plain part of the Upper Awash Basin groundwater system estimated by Darcy's method.		106.6	844,065.14	308.1	106.6	844,065.14	308.1

Point recharge rates estimated using the WTF method from this study (3 boreholes) and previous works (3 boreholes) within and surrounding the area were used as input for the kriging interpolation technique in the ArcGIS tool to create the area's spatially distributed recharge rate for the unconfined aquifer. Based on the areal distribution map (Figure 4.21), the amount of groundwater recharge varies among locations, which ranges from 30 to 55 mm/y for the central plain land portion, 55 to 75 mm/y for the Rift marginal areas (escarpments), southwestern, northwestern and 45 to 55 mm/y for the outlet part of the area. The high fracture zone (high lineament density) of several major faults trending W-E, NW-SE, and N-S creates highly porous rock units with higher recharge on the northern, northwestern, and western sides.

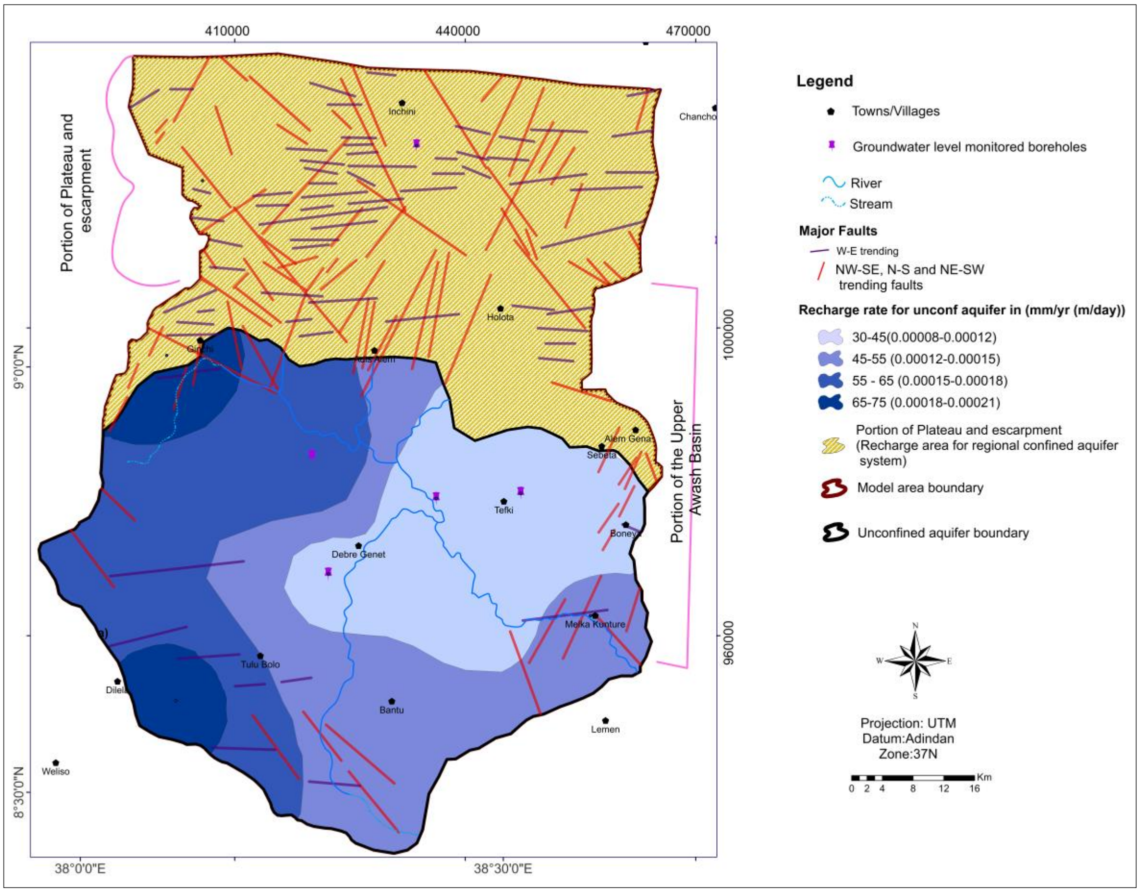

Figure 4.21 Spatially distributed recharge rate for unconfined aquifer (PUAB)

4.8 Hydrogeological conceptual model of the area

A conceptual model of a groundwater system is a crucial tool, offering qualitative knowledge that serves as the foundation for further quantitative assessment. It is an evolving representation that should be improved as new information becomes available and knowledge of the system grows. Diagrams, cross-sections, and maps are used to visually portray the key elements and functions of the groundwater system (Woessner and Poeter, 2020). To bridge the gap between the groundwater system and the real-world system, a well-constructed and simplified conceptual model is a decisive component of the groundwater modeling process.

Conceptual hydrogeological models help to simplify the understanding of main groundwater components, such as the recharge, flow mechanism, aquifer system, and other geological elements influencing groundwater movement, in such complicated hydrogeological settings. The model includes and reflects the hydrostratigraphy, geological and hydrogeological properties, aquifer hydraulic parameters, boundary conditions, and recharge sources.

The model area, delineated as part of the Upper Awash Basin (Figure 4.22), is found totally in the Western Rift margin, which is bordered to the north and west by the northwestern plateau and escarpment, and to the south by notable volcanic centers that border the upper Gibe basin. It has a relief of 426 meters and an altitude in the range of 2056 to 2483 meters above sea level and is known as a vast plain surrounded by an escarpment, and often has a semi-circular geometry. The drainage system of the area belongs to the upper Awash basin, which originates from the escarpment associated with the northwestern plateau, with a wide development of streams, gullies, and rills that converge in the central part of the model area towards the main Awash channel. Geomorphologically, it constitutes mainly the northern and northwestern escarpment, mountain peaks along the Watershed, and the Western and Southwestern elevated marginal edge of the Dendi and Wonchi caldera.

Both Quaternary superficial deposits and Cenozoic volcanics cover the area, with the latter being a bi-modal volcanic rock, which originates from both fissural and central volcanic eruptions. The dominant geological units found in the model area include pre-Rift (basalt of Amba-Aiba & Tarmaber), syn-Rift (basalt, scoria, ignimbrite, tuff, and ash), and post-Rift (trachyte and rhyolite) with a thin layer of superficial deposits (alluvium and ash).

Most of the geological structures (normal faults, fractures, and joints) trending mainly W-E, NW-SE, N-S, and NE-SW resulted from the evolution of the MER and the older Yerer Tulu Volcanic Lineament (YTVL) zone. The highly faulted and fractured northern and northwestern margins, which are mountainous volcanic rocks, have an area of about 2552 km^2 (42.6%), and the central plain portion of the Upper Awash Basin is about 3440 km^2 (57.4%).

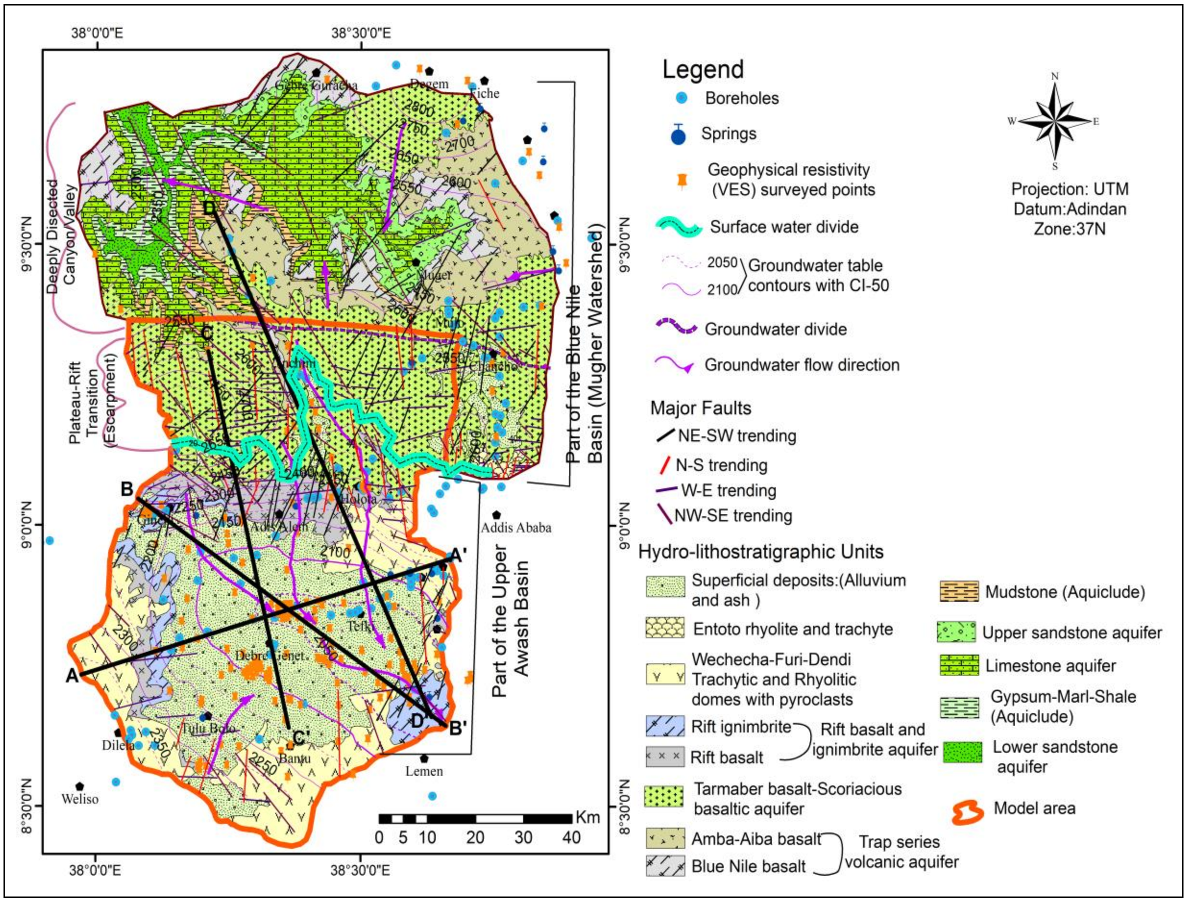

Figure 4.22 Hydrogeological maps of the area, including the anticipated model area

The lithological stratigraphy and tectonics of the plateau and western margin of the MER govern the general hydrogeological setup of the area. Hence, the general bedding of the sedimentary formation underlying the volcanic unit in the northwestern part, the tectonic condition, and the hydraulic properties of the various volcanic units that outcrop in the area highly control the overall groundwater system (recharge mechanism, groundwater flow, and aquifer parameters) of the area.

Analysis and investigation of information from geology, geophysics, and hydrogeology, incorporated with evidence from groundwater geochemistry, isotopes, and different depth boreholes, have revealed the general aquifer configuration, properties, recharge, and discharge mechanisms of the area. Accordingly, the hydrogeological cross-sections (Figures 4.23a-d) were built along a northwest to southeast (Line BB', CC', DD') and across nearly west to east (Line AA') the groundwater flow direction to understand the general configuration of the groundwater flow system.

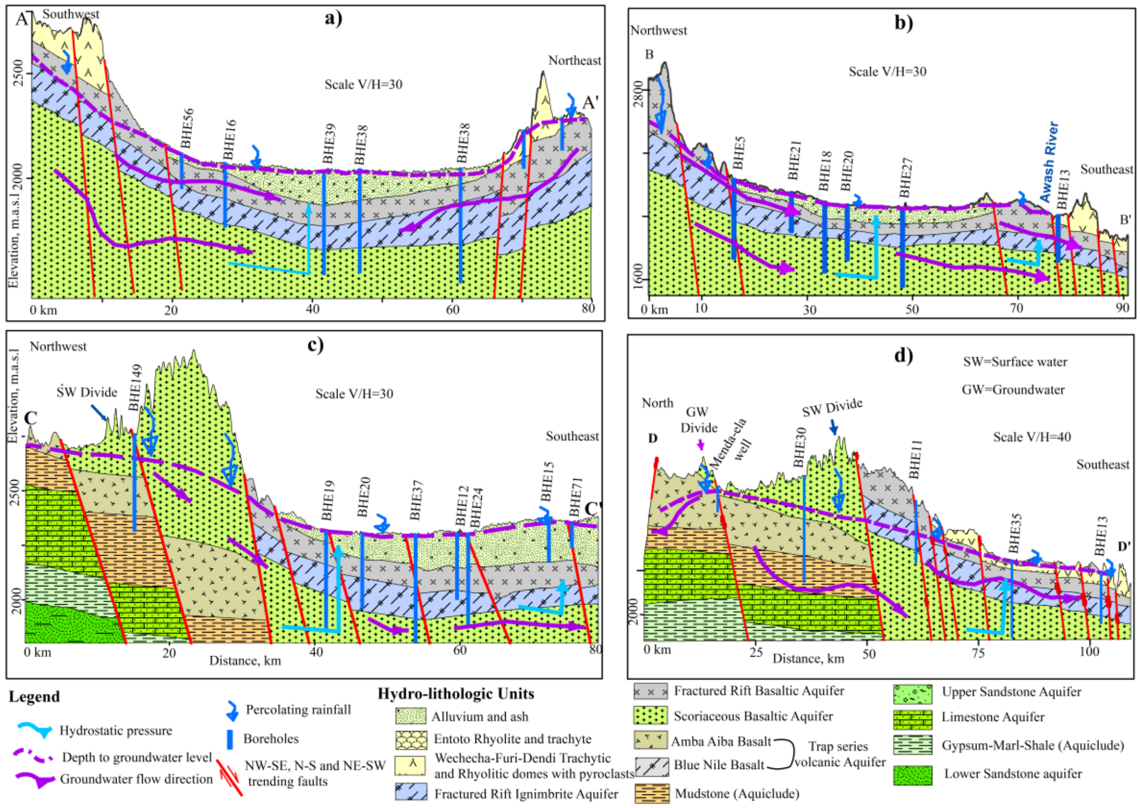

Figure 4.23 Hydrogeological Cross-sections across(a) and along (b), c), d)) the groundwater flow directions

Litho-stratigraphy of the area was identified using knowledge from geological mapping, lithology logs of existing boreholes, and geophysical vertical electrical sounding (VES) results. Major aquifers and confining (aquiclude) units were revealed after pumping and recovery test data analysis for aquifer characterization. Hence, four principal hydrogeological units are recognized for parts of the Upper Awash groundwater system. These are; Superficial (mainly alluvial and ash) aquifers, fractured Rift basalt aquifers, acidic (Tuff, Ignimbrite, and rhyolite) acting as a confining aquiclude, and fractured regional confined scoriaceous basalt aquifer.

The area's geological, hydrochemical, and isotopic evidence illustrates that the water source for the unconfined aquifer (superficial deposits and Rift basalts) is from meteoric water and nearby streams/rivers through fractures. Furthermore, the integrated results from deep sourced water from a portion of the Upper Awash Basin and plateau or escarpment show similar character indicating that the aquifer systems have similar origins (plateau and escarpment area) and hydraulic connectivity due to the presence of regional fault systems that trend north-south and northwest-southeast, which transfer plateau-type water into the Upper Awash Basin's aquifer system.

Nearly similar groundwater flow directions from the northern, northwestern, and southwest parts of the area towards the southeast (outlet) portion are depicted from the generated groundwater level contour map for unconfined and a piezometric level contour for the regional confined aquifers. It is also shown that the area has a gentle, wider, and extremely shallow hydraulic gradient in the central and outlet sections and a steep one in the northwestern and northern portions even though the regional topographic gradient, local barriers, lithology, and geologic structures regulate the direction of the groundwater flow system. In general, the groundwater flow within the area is dominantly from northwest and north to the southeast and minor from the southwest through the central plain part of the area and outflows locally into Awash River in the southeastern parts. The main recharge mechanisms are sub-surface inflow from the plateau and escarpment basaltic and scoriaceous basaltic volcanic rocks along the regional faults (NW-SE, N-S, W-E, and N-S trending), infiltration of runoff and rainfall in the plain.

Regarding the interaction between the groundwater and surface water, the geological information and the combined results (^{222}Rn, EC, and BFI) show that the primary discharge zone of the area is the southeastern downstream portion of the main Awash River. The local groundwater discharge zones in the upstream areas of the two adjacent sub-basins, including sections along the surface water divide, are primarily caused by highly faulted volcanic rock units. In contrast, the central plain area of the Upper Awash Basin, due to the presence of impervious superficial layers such as alluvial deposits, tuff, and ash, shows a relatively weak connection between the groundwater and surface water systems.

MODFLOW plays a significant role in testing the conceptual model of a given area by serving as a powerful numerical tool for simulating groundwater flow under specific hydrogeological conditions. Once the conceptual framework, comprising aquifer geometry, recharge zones, and boundary conditions, is translated into a MODFLOW grid, the model can evaluate whether the assumed flow paths, hydraulic properties, and recharge mechanisms produce results that correspond with observed data. By calibrating the model against measured parameter values, MODFLOW helps identify discrepancies within the conceptual model. Additionally, sensitivity analysis and scenario testing allow for the refinement of key parameters, ensuring that the model accurately represents current conditions and can predict system behavior under future stressors, such as drought or increased extraction.

5. GROUNDWATER FLOW MODELING

5.1 Overview and Goal

Over the past thirty years, groundwater modeling has evolved from a specialized and limited tool to a sophisticated and widely applied method for managing groundwater resources by solving the partial differential equations that characterize groundwater flow systems (Anderson & Woessner, 1992; Mandle, 2002). Groundwater modeling is one of the management tools for understanding complex groundwater systems and helping decision-makers manage water resources by studying the effects of pumping on groundwater levels, spring flows, groundwater flow direction, and the effects of climate change on groundwater resources (Franke & Reilly,1987; Harbaugh & McDonald, 1996). Stress-based simulations also play a crucial role in tackling time-dependent challenges in hydrogeology. They are particularly important for understanding the dynamics of groundwater-level fluctuations and the multifaceted impacts of climate change. By providing insights into these critical issues, stress-based scenario simulations serve as an indispensable tool for sustainable water resource management. They enable effective long-term planning, helping stakeholders navigate the complexities of climate change and the growing demands on our water supplies. This approach not only assists in preserving precious water resources but also supports strategic decision-making that is essential for future resilience against environmental changes. The concept of stress-based scenario simulations in groundwater modeling (Lubczynski & Gurwin, 2005) provides a practical approach under certain conditions. This method can be highly effective for addressing various groundwater management issues, especially in heavily stressed aquifers where human activities have a significant impact.

To effectively utilize groundwater models, one must have a solid understanding of hydrogeological principles, perform careful data analysis, and communicate results and their implications. A well-calibrated model based on high-quality data and a solid understanding of hydrogeology provides the best foundation for reliable predictions of future groundwater conditions and responses to management actions.

Numerical models of groundwater flow are valuable techniques in hydrogeological studies across various countries. Unfortunately, this method is rarely used in Ethiopia due to limited relevant hydrogeological information. Recently, groundwater simulations have been conducted to study groundwater dynamics in the Upper Awash Basin (Yitbarek et al., 2012; Azagegn et al., 2014). These simulations also focus on groundwater resource evaluation in the Ada'a plain and Raya Valley (WWDSE, 2009; WWDSE, 2010), as well as in the Akaki catchment area (AAWSA, 2000; Ayenew et al., 2008). Because of the significant groundwater potential and the inherent variability of volcanic aquifers found in the area, specifically within the Upper Awash basin, an effort was made to develop a hydrogeological model that is tailored to the unique characteristics of the area.

In this study, a scientifically grounded groundwater flow model was developed using Visual MODFLOW Flex, incorporating a three-layer system: an unconfined aquifer, a confining unit**,** and a confined aquifer. This conceptual framework of the present study area is supported by regional geological understanding and local geology, correlated with the lithological logs of existing water supply wells. Specifically, acidic volcanic rocks, including tuff**,** ignimbrite**,** trachyte**,** and rhyolite, commonly act as confining layers, separating shallow unconfined zones from deeper confined aquifers.

Visual MODFLOW Flex enables precise definition of layer-specific properties, including hydraulic conductivity, storage parameters, and boundary conditions**.** In this model, the confining unit is represented as an impermeable layer**,** simplifying its role while effectively simulating its function in restricting vertical flow and creating artesian conditions. This representation is justified by field evidence that most deep-water supply wells drilled into the confined aquifer exhibit artesian behavior, confirming the presence of significant vertical hydraulic separation. By adopting this layered structure, the model supports realistic simulation of groundwater dynamics**,** interlayer interactions, and management scenarios, providing a robust foundation for predictive analysis and sustainable resource planning.

This model seeks to accurately represent the complex interactions and dynamics of subsurface water systems, highlighting the various geological features and hydrological processes that impact groundwater availability and movement within this volcanic landscape. To evaluate its potential and usability, simulations were first conducted under steady-state conditions, followed by a stress-based scenario analysis for resource management.

The original objective was to develop a fully stress-based scenario groundwater flow model to simulate aquifer dynamics over time. However, due to limitations in the availability of continuous time-series groundwater level monitoring data, a revised approach was adopted. This involved first calibrating a steady-state model and subsequently conducting simulations under different scenarios to evaluate aquifer responses under various stress conditions. To address this, a methodologically sound alternative was implemented:

- Develop a well-calibrated steady-state model to establish a reliable baseline.
- Use synthetic or estimated time-series inputs to simulate different scenarios.
- Evaluate system behavior under stress conditions such as drought, increased pumping, and artificial recharge for 30 years

The adopted methodology is scientifically justified for the following reasons:

- Avoids unreliable calibration from sparse time-series data
- Ensures hydraulic parameters are well-constrained before introducing temporal variability
- Enables exploration of multiple future conditions without requiring complete historical datasets
- Provides actionable insights for groundwater management under uncertainty

This approach is consistent with practices in regions facing similar data limitations:

- Applied in semi-arid and fractured aquifer systems (Gossel et al., 2007; Rosi and Gattinoni, 2013).
- Successfully implemented in East Africa and South Asia (Tadesse and Alemayehu, 2023; World Bank, 2021).
- Used to inform groundwater policy and infrastructure development

The groundwater flow model developed in this study, which uses a finer grid size, can serve as a valuable management tool and a reference for future simulation studies in nearby wellfields aimed at the sustainable use of groundwater resources.

5.2 Theories

Groundwater modeling is a complex area of study that requires a solid understanding of hydrogeology, mathematics, and computational methods. A well-developed groundwater model can serve as a valuable tool for decision-making in water resource management and environmental protection. Groundwater models are inherently uncertain due to the hidden nature of subsurface systems. Most uncertainties arise from limited direct observations, geological complexity, point-based measurements, temporal variability, measurement errors, and parameter estimations (Beven, 2001). Furthermore, the dynamic character of groundwater systems emphasizes the necessity of constant monitoring, study, and flexible management strategies. While this dynamism adds complexity, it also makes the field of hydrogeology attractive and crucial for sustainable water resource management. Despite these limitations, it's important to recognize that understanding of subsurface systems has improved significantly over the past decades.

Groundwater models can be used to predict future conditions and to understand complex subsurface processes. The decision to use predictive or generic modeling approaches depends on the specific objectives of the study, the available data, and the understanding of the system being investigated (Anderson & Woessner, 1992). Integrating both approaches often leads to a thorough understanding and effective management of groundwater resources.

Modeling begins with creating a conceptual framework of the hydrogeologic system, followed by applying Darcy’s law to address specific challenges. Furthermore, a numerical simulation is conducted to analyze various scenarios to enhance our ability to manage the groundwater resource. Mathematical relationships that describe groundwater flow are essential for developing quantitative models of groundwater systems. By combining Darcy’s law with the continuity equation, which represents mass conservation (mass inflow equals mass outflow plus changes in storage), we can create universal equations to characterize groundwater flow under different conditions. Groundwater flow equations are often called governing equations because they describe the factors that control groundwater flow. These equations are based on Darcy’s law and the continuity equation, which ensures the conservation of mass in water. Under steady-state flow conditions, the mass of water in a system remains constant; in other words, inflow equals outflow, and the hydraulic heads, gradients, and flow rates do not change over time. Whereas, when the flow is stress-based scenario , the mass of water varies with time, inflow doesn't equal outflow, and heads, gradients, and flow rates vary with time (Woessner & Poeter, 2020).

The law of conservation of mass for flow through a saturated porous medium requires that the flux of fluid mass into the system equals the flux of fluid mass out of the volume plus the change in mass stored within the volume (McDonald & Harbaugh, 1988; Anderson & Woessner, 1992). Darcy's law is represented by the specific discharge (q) and the mass flux is represented by ρq (i.e., mass flux = qq), where Mass flux-mass of water passing through a unit area per unit time (kg/m^{3D}), ρ-density of water (kg/m^3), and q-specific discharge (m/day).

In most cases, the mass flux will not be one-dimensional along the x-direction. Instead, it will occur in an arbitrary direction, with components in the x, y, and z directions. Therefore, it is essential to account for the change in mass flux across the system in all three dimensions.

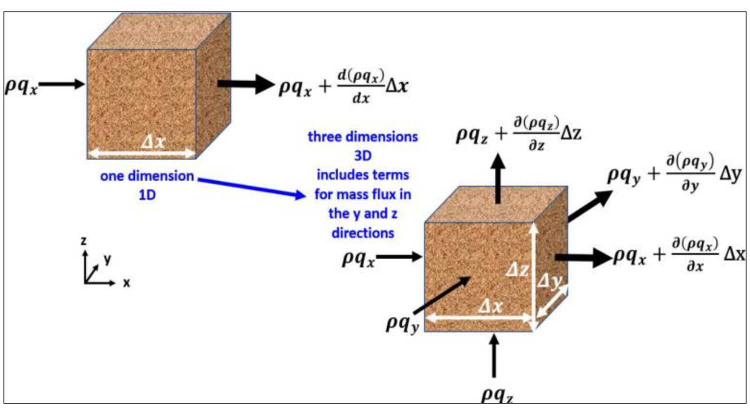

Figure 5.1 Schematic representation for confined aquifer condition showing three-dimensional mass influx and outflux ($\rho q x$) and addition or loss of mass flux in the outflow ($+\partial/\partial x(\rho q_x)\ \Delta x$) (Woessner & Poeter, 2020)

Darcy's Law governs groundwater flow modeling by describing how groundwater moves through porous media. This fundamental principle in hydrogeology is essential for understanding and modeling groundwater flow (Anderson & Woessner, 2015). Mass flux into the system is determined by the product of specific discharge and fluid density. When the head decreases, water is released from the porous medium, increasing mass flux, as shown in Figure 5.1. Note that flux is measured in velocity units (m/day) since it represents flow rate (m^3/day) divided by flow area (m^2).

The fluxes in and out of the system and the change in storage are the fundamental groundwater balance to determine the governing equations. i.e., the difference between mass flux in and mass flux out equals the change in storage.

Mass flux in = ρq_x (For one dimension) (1)

Mass flux out = $\rho q_x + \Delta(\rho q_x/\Delta x)\Delta x$ (For one dimension) (2)

The mass flow rate is obtained by multiplying the fluxes by the cross-sectional area of the system that they pass through (for three-dimensional flow in the x-direction, the area is $\Delta y \Delta z$) as shown below.

Mass flow in x-direction=$q_x \rho A_x = q_x \rho d_y d_z$

Mass flow in y-direction=$q_y \rho A_y = q_y \rho d_x d_z$

Mass flow in z-direction=$q_z \rho A_z = q_z \rho d_x d_y$

The respective total mass inflow and outflow in the x, y, and z direction in and/or from the system is presented by: $qx\rho\Delta y\Delta z + q_y\rho\Delta x\Delta z + q_z\rho\Delta x\Delta y$ (3)

$(q_x\rho + \delta q_x/\delta_x(\rho d_x)\, d_y d_z) + (q_y\rho + \delta q_y/\delta_y(\rho d_y)\, d_x d_z) + (q_z\rho + \delta q_z/\delta_z(\rho d_z)\, d_x d_y)$ (4)

The change of storage can be expressed as $-\delta V_w/\delta_t$, where the negative sign indicates that outflow is greater than inflow, which is represented by specific storage (S_s). It is defined as the amount of water released from the storage (aquifer) divided by the unit total volume of the aquifer per unit change in head, as shown below.

$S_s = \delta V_w/V_t\ (-\delta h)$

Where, V_t-is the total volume ($d_x d_y d_z$) in m^3; $-\delta h$ negative means the water release from the storage. Thus, the rate of change in storage is presented as

$$\delta V_w/\delta t = -S_s(\delta h/\delta t)\, d_x d_y d_z \qquad (5)$$

Thus, substitute expressions (2), (3), and (5) accordingly into the mass balance equation (i.e. total mass inflow minus mass outflow equals the change in storage) by assuming the density is constant and adding the volumetric flux (N), which describes the source/sink of water and after mathematical simplification, the equation becomes;

$$(\delta q_x/\delta_x + \delta q_y/\delta_y + \delta q_z/\delta_z)\, d_x d_y d_z + N d_x d_y d_z = -S_s(\delta h/\delta t)\, d_x d_y d_z \qquad (6)$$

By removing ($d_x d_y d_z$) from both sides of expression (6), the new expression becomes

$$(\delta q_x/\delta_x + \delta q_y/\delta_y + \delta q_z/\delta_z) + N = -S_s(\delta h/\delta t) \qquad (7)$$

Again, by utilizing Darcy's law, the Darcy flux in the x, y, and z directions is shown as

$$\text{i.e.} \quad q_x = -k_x \delta h/\delta x,\ q_y = -k_y \delta h/\delta y,\ q_z = -k_z \delta h/\delta z \qquad (8)$$

Therefore, after substituting expression (8) into (7), a three-dimensional, confined, stress-based scenario , anisotropic, and heterogeneous condition of the groundwater flow process (Bear, 1979; McDonald & Harbaugh, 1988; Woessner & Poeter, 2020) is presented as;

$$\boldsymbol{\partial/\partial_x (K_x\, \partial h/\partial_x) + \partial/\partial_y (K_y\, \partial h/\partial_y) + \partial/\partial_z (K_z\, \partial h/\partial_z) \pm W = -S_s\, \partial h/\partial t} \qquad (9)$$

and the groundwater flow equation at steady state conditions with heterogeneous and anisotropic conditions is presented as

$$\boldsymbol{\partial/\partial_x (K_x\, \partial h/\partial_x) + \partial/\partial_y (K_y\, \partial h/\partial_y) + \partial/\partial_z (K_z\, \partial h/\partial_z) \pm W = 0} \qquad (10)$$

Where; K_x, K_y, and K_z are the values of hydraulic conductivity along the x, y and z directions (m/day), h- is the potentiometric head (m), W- is a volumetric flux per unit volume representing sources and/or sinks of water, where negative values are extractions, and positive values are injections (1/day), S_S- is the specific storage of the porous material (1/m), and t- is time (day).

In an unconfined aquifer system, the flow equations are nonlinear because the transmissivity of the aquifer is dependent on the saturated thickness, which varies in the direction of flow due to the sloping water table. In such a system, the water table slopes, causing the flow to be parallel to it, and the saturated thickness decreases in the direction of flow. If the slope of the water table is small, Darcy's Law can be utilized to formulate governing equations by applying the approximate gradient ($-dh/dx$) instead of the true gradient ($-dh/d$L), under the assumption that flow is horizontal, meaning there are no vertical flow components.

By expressing the flow area as the product of the water table's height and the system's unit width in the y-direction, the flow is represented in equation (11).

$$q = -(K dh/dx)\, h\Delta y \qquad (11)$$

When the bottom of the unconfined aquifer is used as the reference point, the hydraulic head defines the saturated thickness. To incorporate this relationship into the flow equation, equation 9 is modified such that the aquifer thickness, b, is replaced with h, with the varying value of h included within the derivative. Additionally, to accurately depict unconfined flow, the specific yield (S_y) is employed as the aquifer's storativity.

Therefore, the conditions of unconfined, three-dimensional, stress-based scenario , anisotropic, and heterogeneous groundwater flow are represented by.

$$\partial/\partial_x K_x (h\, \partial h/\partial_x) + \partial/\partial_y K_y (h\, \partial h/\partial_y) + \partial/\partial_z K_z (h\, \partial h/\partial_z) \pm W = S_y\, \partial h/\partial t \qquad (12)$$

In groundwater modeling, simulations typically involve solving such partial differential equations through numerical methods such as the Finite Difference Method (FDM) or the Finite Element Method (FEM) (Anderson & Woessner, 1992; Fetter C.W., 2001). A widely used groundwater modeling program, known as MODFLOW, utilizes a finite-difference approach by partitioning the model domain into regular rectangular grids, referred to as blocks or cells. Measurements such as head, drawdown, and concentration are calculated at the nodes within these grids. In contrast, the program FEEFLOW employs a finite element model (FEM) that uses interpolation at the points where irregular polygons, typically in the form of triangles or tetrahedral, intersect.

Accordingly, the study area is discretized into finite difference regular block-centered rectangular grids for numerical simulation, which is conducted using Visual MODFLOW Flex (Waterloo Hydrogeologic Inc., 2011; www.waterloohydrogeologic.com).

Visual MODFLOW Flex is a powerful and user-friendly advanced software package for groundwater modeling, and it is widely utilized in both industry and academia. It offers extensive features that build upon the previous MODFLOW packages, including.

- Integrates pre-processing, simulation, and post-processing within a single interface
- Compatible with various MODFLOW versions and associated programs
- Facilitates the creation of conceptual models before numerical model development
- Enables the import of GIS data for conceptual model construction
- Supports both structured grids and unstructured grids
- Features automated parameter estimation through PEST integration
- Offers 3D and 3D visualization of model inputs and results
- Includes animation capabilities for stress-based scenario simulations
- Allows for the creation and comparison of multiple stress-based scenario model scenarios
- Supports a variety of file formats for data import
- Capable of exporting to common GIS and database formats.

Visual MODFLOW Flex was chosen for this study due to its user-friendly interface and strong visualization capabilities. It effectively simulates unconfined, leaky, and confined aquifer systems. A three-dimensional groundwater flow model was developed for steady and stress-based scenario conditions for three layers: unconfined, aquiclude, and confined, by setting boundary and initial conditions and calibrating each layer based on the conceptual hydrogeological model discussed earlier (Section 4.8).

5.3 Steady-State Numerical Model

5.3.1 Structure of the model

In this study, the characterization of layers (aquifer layers and confining unit) was based not only on their average thickness but also on their hydraulic properties, derived from a comprehensive evaluation of subsurface data. Specifically, lithological logs from 60 water supply wells and pumping and recovery test results from 34 wells were analyzed to define the hydraulic behavior of each layer (Sections 3.1.1 and 3.1.5). Further, the specific characteristics of each layer were discussed in detail using available field data and summarized under the results and discussion section (Table 4.8), which provides a consolidated view of the aquifer system's vertical structure and hydraulic heterogeneity, supporting the assignment of realistic parameters in the groundwater flow model. The regional confined scoriaceous basalt aquifer is not fully penetrated by the 654-meter and 550-meter deep boreholes located at the escarpment and in the central plain part of the Upper Awash Basin, respectively. Accordingly, the thickness of the confined aquifer beneath the confining layer is considered to be 350 meters (Table 5.1).

In general, the three-dimensional structure of the study area's aquifers includes an unconfined aquifer (comprised of superficial deposits and rift basalt), an aquiclude (consisting of rhyolite, ignimbrite, and trachyte), and a confined aquifer (highly fractured regional scoriaceous basalt). This model is constructed with three layers that are primarily recharged through direct infiltration of precipitation, seepage from river or stream channels, and subsurface regional inflow from the northern and northwestern sections.

Table 5.1 Model layers with their characteristics

Model Layer	Geologic unit	Aquifer type	Estimated average thickness, m
1	Superficial deposits (silty clay, sand, boulder, and pumice) and the fractured Rift basaltic unit	Unconfined	150
2	Acidic volcanic unit (Lumping of different lithologic units such as pyroclastic deposits, tuff, ignimbrite, trachyte, and rhyolite with thin intercalation of paleosol or sticky clay.	Confining unit (Impermeable)	100
3	The scoriaceous basaltic unit resulted from scoriaceous lava	Confined (Artesian)	350

The study area covers 5,992 square kilometers (km^2), including the elevated ridges like plateaus and escarpments surrounding the model area. The model domain itself is about 3,440 km^2 and measures about 43 km in width and 78 km in length. It uses a grid with a spacing of 500m *500m, consisting of 221 rows and 172 columns. This creates a total of 113,825 active cells or nodes in each of the two aquifer layers of the model, while outside this area, there are 91,705 inactive cells.

Ministry of Water and Energy (MOWE), together with the Ministry of Irrigation and Lowlands (MOIL), has planned to use groundwater as a source for irrigation development in the area beginning in 2026, which puts stress on the groundwater of the area. For this reason, A steady-state simulation was created to represent average aquifer conditions (data used to calibrate or represent average aquifer conditions) in 2025. The steady-state groundwater model is used to analyze the water budget, hydraulic properties, boundary conditions, and model calibration. The results of the calibrated steady-state model are used as the foundation for stress-based simulations and sensitivity analysis. To examine the model's ability to replicate aquifer responses over 30 years (January 1, 2026, to December 31, 2055), the model's framework is applied to a sensitivity analysis and a pumping scenario utilizing monthly time steps.

5.3.2 Boundary conditions

Boundary conditions play a pivotal role in groundwater flow modeling by clearly defining how the modeled area interacts with its surrounding environment. These conditions can be categorized into physical and hydraulic boundaries, each serving to shape the behavior of groundwater as it flows through various geological formations. Accurate designation of these boundary conditions is indispensable for effectively capturing the dynamics of the groundwater system and its reactions to external stresses over time (Anderson & Woessner, 2015).

To appropriately define these boundaries, a comprehensive understanding of the hydrogeological system, the available data, and the specific objectives of the modeling effort is essential. As the modeling process unfolds, it is crucial to continually refine and adjust the boundary conditions based on ongoing insights gained during model development and calibration. Another key aspect to consider is temporal discretization, which involves structuring time-varying boundary conditions to reflect changes accurately over the designated simulation period. In stress-based scenario modeling scenarios, the overall timeframe is segmented into distinct stress periods and smaller time steps, allowing for a more detailed analysis of groundwater flow dynamics.

In groundwater numerical models, three primary boundary conditions are employed to delineate how groundwater enters and exits the model domain (McDonald & Harbaugh, 1988; Anderson & Woessner, 1992; Woessner & Poeter, 2020). Each type plays a specific role in ensuring that the model accurately represents real-world conditions and variability, thereby enhancing the reliability of the model's predictions.

The first type of boundary condition is the specified head boundary, also known as Dirichlet conditions. This type of boundary can be applied to scenarios where the water level remains constant throughout the simulation or when specific water levels are known. It is often used for areas where geological layers outcrop or at model edges adjacent to large bodies of water, such as lakes and oceans. However, this model domain does not include any such water bodies or specify a constant head boundary.

The second type of boundary condition is known as the specified flux (Neumann condition). In this case, a known flow rate is applied across the boundary, which may be zero (indicating a no-flow boundary) or a specific value. This type of boundary is commonly used for water divides in both surface and groundwater contexts, as well as for impermeable geological formations. It is also applied to represent water entering the system from precipitation (direct recharge), which can vary spatially and temporally, and is typically implemented for the uppermost active layer. In the model area, a no-flow boundary is represented by the Dendi volcanic, comprised mainly of pyroclastics such as tuff and ash, located in the west, as well as the Gurage highlands to the southwest, due to their low hydraulic conductivity. Similarly, the predominantly impermeable trachytic geological formations of lava domes and volcanic shields, including Wochecha, Menagesha, and Furi, create a no-flow boundary along the northeastern and eastern sides of the model area.

The head-dependent flux (Cauchy or Mixed) boundary is the standard formulation of the General Head Boundary (GHB) in MODFLOW, representing the third type of boundary condition. This boundary condition simulates the movement of water into or out of the model domain, relying on the difference between a reference head and the head computed by the model. It is commonly used for rivers, their tributaries, drains, springs, or general head boundaries. For example, when the model-calculated head exceeds the boundary head, the drain boundary condition permits only the removal of water from the system. In cases of surface water-aquifer interaction, seepage is contingent upon the river stage and the aquifer head. Based on the available observed head data, along with evidence from

^{222}Rn, electrical conductivity (EC), and isotopic analysis, the GHB is positioned in the southeast section of the current model domain (Sections 4.4.3.1, 4.5.3, 4.5.4, and 4.5.5).

5.3.2.1 No flow boundary

The western boundary of the Woliso-Ambo mountain range, which includes Mount Dendi, and the southwest part of the model domain, which borders Gurage Mountain, are generally designated as no-flow boundaries. Acidic volcanic centers such as Menagesha, Wechecha, and Furi play a critical role in shaping regional groundwater flow. These centers and ridges are primarily composed of acidic volcanic rocks**,** notably trachyte, ignimbrite, and rhyolite. These rocks are: Silica-rich, fine-grained, and often densely welded. They are characterized by low primary porosity and limited fracture connectivity, exhibit a very low hydraulic conductivity, even at depth, due to minimal secondary permeability development. This makes them effectively impermeable and suitable for representing no-flow boundaries in both unconfined and confined aquifer layers.

While some volcanic units may show increased permeability due to weathering or fracturing near the surface, deep-seated acidic centers tend to remain hydraulically tight. Studies show that confined aquifers bounded by such lithologies experience limited lateral flow, and flow lines tend to parallel the boundary, confirming its role as a hydraulic barrier (Groundwater Project, 2023; Duffield, G. M. (n.d.)). These ridges often coincide with structural highs and fault zones, which may act as vertical barriers rather than conduits, especially when filled with impermeable volcanic zones. Their alignment with surface water divides further supports the assumption that they also represent groundwater divides, particularly in confined systems. Accordingly, no-flow boundaries are appropriate where a measurable change in hydrogeologic properties occurs, such as at formation contacts or impermeable lithologic transitions. In confined aquifers, these boundaries are valid when the adjacent formations exhibit negligible transmissivity, as is the case with the acidic volcanic centers in the area.

Despite limitations in the availability of direct hydraulic conductivity measurements, the spatial distribution maps for both the unconfined and confined aquifer systems (Figure 4.7a & 4.7b) reveal a consistent trend of reduced hydraulic conductivity in proximity to the acidic volcanic centers and ridges**.** This observed pattern supports the conceptual assumption that these volcanic ridges act as hydraulic barriers**,** thereby validating the use of no-flow boundary conditions in the groundwater flow model. Furthermore, the bottom of the aquifer (Depth > 600 m) and areas not part of the model domain are likewise regarded as inactive or no-flow cells.

5.3.2.2 Constant head

Areas with constant head boundaries, which contain significant surface waters, are where an endless flow of water to the aquifer occurs. Head at a lake or reservoir is an illustration of this circumstance. This model does not provide a constant head boundary because the model domain does not contain any surface water bodies of such type.

5.3.2.3 General Head Boundary (GHB) and Specified flux

Converging evidence from potentiometric and/or piezometric groundwater level, geological, hydrochemical, and isotopic studies ($\delta^{18}O$, $\delta^{2}H$, ^{222}Rn, EC) are in close agreement to suggest that the southeastern section of the study area is considered as a GHB for both layers because it represents the groundwater's outflow zone of the study area.

Furthermore, the planar extent of the General Head Boundary (GHB) surrounding the PUAB exit is designed to simulate hydraulic interaction with external systems, such as regional aquifers, rivers, or discharge zones, without explicitly modeling them. It acts as a head-dependent flux boundary, where the flow rate is proportional to the head difference between the model cell and the external system, scaled by conductance (USGS, 2005; Aquaveo, 2019). The PUAB exit likely represents a regional outflow point, such as a valley outlet or a downgradient basin margin. Assigning a GHB here allows the model to simulate natural drainage or baseflow discharge from the aquifer system into adjacent hydrological domains.

The spatial extent of the GHB was defined based on multiple pieces of evidence, such as

- Hydraulic gradient continuity: extend the GHB along zones where the potentiometric surface consistently trends toward the PUAB exit.

- Geological boundaries: align with lithological transitions or fault zones that facilitate lateral flow
- Model calibration needs: Include enough cells to capture the discharge behavior without overextending into zones better represented by other boundary types (e.g., no-flow or specified flux).
- Avoiding overlap: ensure the GHB does not intersect areas already governed by specified flux or constant head boundaries.

Thus, using a GHB around the PUAB exit avoids the need to extend the model domain to explicitly simulate downstream systems. It also provides flexibility in calibrating conductance values, which can be adjusted to reflect varying transmissivity or connectivity with external systems. Besides, the northern and northwestern plateau and/or escarpment part of the study area of aquifer systems (layer 1. unconfined aquifer, and Layer 3. confined aquifer) is represented by specified flux boundaries, through which groundwater of the model area is recharged mainly from the adjacent Muger sub-basin (Part of the Blue Nile basin) as a sub-surface inflow to the study area as per the converging evidence discussed before (Section-4.7).

Based on convincing sources and hydrogeological principles, the justification for the alignment of the specified flux boundary at the foot of the escarpment, particularly where it intersects tributary rivers, is as follows:

- The specified flux boundary intersects tributary rivers that descend from the escarpment, which are likely to contribute localized recharge to both the unconfined and confined aquifer systems. These rivers represent surface water features hydraulically connected to the subsurface, justifying the use of a Neumann-type boundary condition (prescribed flux) at their interface (Banik, 2023).
- The foot of the escarpment marks a significant topographic break and often coincides with fault zones or fractured volcanic units, which can enhance vertical and lateral groundwater movement. This geomorphic setting supports the assumption that flux enters the aquifer system at this boundary, especially during

seasonal runoff events or sustained baseflow conditions (Groundwater Project, 2023).

- According to MODFLOW documentation, specified flux boundaries are appropriate where external inflows (e.g., river seepage, irrigation return flow, or lateral recharge) are known or estimated. These boundaries allow the model to simulate time-varying or spatially distributed fluxes based on hydrological inputs (USGS, 2005).
- The alignment of the flux boundary along a tractable segment of the model grid ensures consistent cell-based flux assignment and facilitates calibration. It also allows for integration with recharge zones and observation wells, improving the model's ability to simulate inter-basin flow dynamics.

The boundary condition along the hydraulic connection between the Muger sub-basin and the target aquifer system is represented as a head-dependent flux boundary within the Visual MODFLOW grid. This configuration integrates both specified flux inputs and dynamic hydraulic gradients, allowing the model to simulate subsurface inflow as a function of imposed recharge rates and aquifer head responses. Such a dual representation improves the realism of inter-basin flow dynamics, particularly in structurally complex volcanic terrains.

The boundary line intersects zones of verified hydraulic continuity between the Muger sub-basin and the receiving aquifer, as evidenced by regional hydraulic gradients, topographic transitions, and structural controls discussed in earlier sections. The escarpment in this region serves as a preferential flow path, where elevation differences and fault alignments facilitate lateral groundwater movement. This boundary segment is spatially aligned with a tractable portion of the model grid, enabling consistent cell-based flux assignment, calibration, and sensitivity analysis.

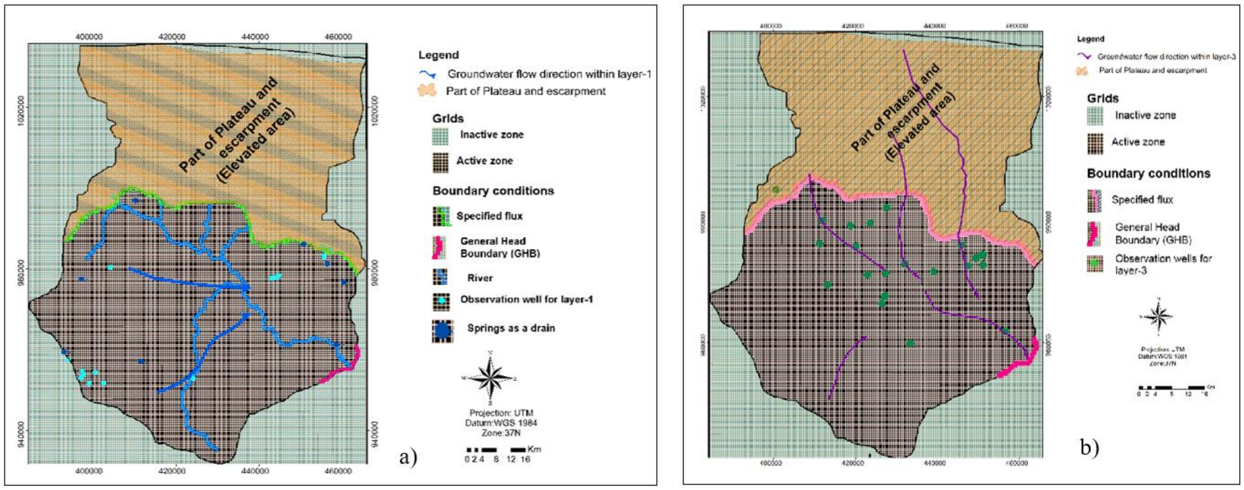

Figure 5.2 Model grid and boundary conditions for a) layer-1 & b) layer-3

The method used to estimate and input fluxes from the neighboring Muger Basin into a Visual MODFLOW Flex model, based on the conceptual understanding, is as follows.

Step 1: Compute average flux using Darcy's Law

Groundwater flux from the Muger sub-basin is estimated using Darcy's Law based on the two flow paths. The flux or recharge as a sub-surface inflow to the unconfined and confined aquifer system from the adjacent Muger sub-basin is 6.9 mm/y and 59.23 mm/y (Based on the computed results: Table 4.15 to 4.17 and Table 4.20 in the dissertation report).

Step 2: Convert Flux to Model Grid

For an unconfined aquifer

- Measure the flux boundary length in the model domain: 89.3km
- Flux average 6.9 mm/y=1.89*10^{-5} m/d
- Number of cells in the boundary=flux boundary length/cell width =89.3km/500m=178.65
- Flux/cell=flux average/# of cells=1.89*10^{-5} m/d/178.65=1.058*10^{-7}m/d
- Flux volume in m^3/d= Area of sub-surface inflow contributing zone (here is the escarpment zone: 2551km^2) *flux in each cell

  =<u>270 m^3/day</u>

For a confined aquifer

- Measure the flux boundary length in the model domain: 89.3km
- Flux average 59.23 mm/y=$1.62*10^{-4}$ m/d
- Number of cells in the boundary=flux boundary length/cell width =89.3km/500m=178.65
- Flux/cell=flux average/# of cells=$1.62*10^{-4}$ m/d/178.65=$9.1*10^{-7}$m/d
- Flux volume in m^3/d= Area of sub-surface inflow contributing zone (here is the escarpment zone: 2551km^2) *flux in each cell

  =2,317.8 m^3/day

Thus, the Darcy-based flux estimation is widely used in regional groundwater modeling, and Visual MODFLOW supports cell-based flux input and interlayer flow simulation.

In general, regional groundwater inflow occurs from the plateau and/or escarpment in the northern and northwestern parts of the study area, whereas outflow generally occurs in the southeast. As a result, a specified flux boundary is used to depict the area where regional inflow occurs, and a general head boundary is used to represent the southeastern border where groundwater exits the research area (Figures 5.2a & 5.2b). The specified flux is computed using the Darcian approach for an unconfined aquifer (layer-1: 6.9 mm/y or 270 m^3/d) and for a confined aquifer (layer-3: 59.23 mm/y or 2,317.8 m^3/d)

5.3.2.4 Recharge

The annual recharge of the model area was estimated using two methods. The WTF approach for the unconfined aquifer and the Darcian method for subsurface inflow to the unconfined and confined aquifers, as detailed in sections 4.6.4 and 4.6.5. Groundwater entering the model area from the northwest and northern plateau or escarpment is categorized as subsurface inflow, moving towards the southeast outlet. Separating recharge from direct precipitation and seepage at the base of the escarpment on superficial deposits and fractured basaltic units is challenging due to variable gradients. Using the groundwater budget concept, the water reaching the southeastern outlet can be divided into two types. seepage and direct precipitation on the unconfined aquifer, and subsurface inflow from the surrounding plateau and escarpment (Section 5.3.2; Table 5.1).

The average annual recharge was estimated at 40.5 mm/y using the WTF method, which represents the unconfined aquifer (Section 4.6.4, Table 4.14). Additionally, the saturated zone sub-surface inflow (groundwater flux or recharge) for both unconfined and confined aquifers in the model area was computed using Darcy's method, yielding a total result of 106.6 mm/y (Section 4.6.5, Table 4.17). Accordingly, conceptualization based on the groundwater balance is made to use the combined results from the two (WTF and Darcian) using the areal extent of aquifers. The classification is based on the areal extent of the model area and the areal extent of the flux or subsurface inflow zone, located on the escarpment and plateau. By subtracting the recharge estimated by the WTF method (40.5 mm/y) from the flux (106.6 mm/y), we obtain a difference of 66.1 mm/y, which represents the flux mainly from the two aquifer systems (6.9 mm/y from the unconfined aquifer and 59.2 mm/y from the regional confined aquifer). Furthermore, the net recharge for the unconfined and confined aquifers is determined as 47.4 mm/y and 59.2 mm/y, respectively, using the two groundwater-related estimation techniques (WTF and Darcy's). This study estimates the subsurface recharge for the regional confined aquifer as 59.2 mm/y.

In general, the recharge estimates are reliable due to two techniques: the WTF method for direct recharge to the unconfined aquifer, and Darcy’s method for assessing subsurface inflow. By considering groundwater balance and areal extent, the study avoids double-counting and accurately allocates recharge between the unconfined (47.4 mm/y) and confined (59.2 mm/y) aquifers. These findings align with regional studies, reinforcing the validity of this approach.

The spatially distributed recharge rate for the model area of the unconfined aquifer was created using the kriging interpolation technique in ArcGIS. This approach was based on point recharge rates estimated from the WTF method of the unconfined aquifer using data from three boreholes (this study) and previous research (three boreholes) conducted in and around the area (Figure 1.1). To accurately apply groundwater recharge to the most active cells, four average recharge zones were identified and incorporated into the model. To align the model with the recharge values, these values were resampled using a grid size of 500 m by 500 m. The recharge flow rate (Q_r) is calculated by the model using the following formula. $Q_r = I_r * DELR * DELC$, where Q_r is the recharge flow rate in m^3/day, I_r is the recharge flux in m/day, and DELR and DELC represent the map area of a model cell in m^2.

5.3.2.5 River

The interaction zones between groundwater and surface water in the model area were determined using various methods discussed in section 5.2. The River package is used to evaluate flow dynamics based on head differences between surface water and groundwater. In losing stream conditions, when the river stage (H_{riv}, in m.a.s.l) exceeds the groundwater head (H_{aq}, in m.a.s.l), water flows from the river to the aquifer (Rate = $C \times (H_{riv} - H_{aq})$). Conversely, in gaining stream conditions, water flows from the aquifer to the river when the groundwater head is higher (Rate = $C \times (H_{aq} - H_{riv})$). The flow is influenced by factors such as the hydraulic gradient, riverbed conductance, river stage, and groundwater head (Anderson & Woessner, 1992). Conductance (C), which quantifies flow resistance, is calculated as $C = (K \times L \times W) / M$, where K is the hydraulic conductivity of riverbed sediments (m/d), L is the river length in the cell (m), W is the river width (m), and M is the riverbed thickness (m).

Since the hydraulic conductivity of the riverbed was not directly measured in the field, average values were assigned to the river nodes based on the hydraulic conductivity of the surrounding rocks and soils (Section 4.4.3.3). This is a common approach when direct measurements of the riverbed are unavailable. River widths in the area were determined using direct field measurements at selected locations, as well as approximations from Digital Elevation Models (DEMs) and Google Earth imagery. The main river and its tributaries varied in width from 6 to 17.3 meters, and the average width for each node was incorporated into the river package for further simulation. This practical method combines field data with remote sensing techniques to characterize river dimensions across the model domain.

Additionally, the thickness of the riverbed sediment was found to range from 0.2 to 0.6 meters, based on lithological logs from boreholes near the river channel. Average values were assigned to each node accordingly. The river's length within a cell was approximately assumed to be equal to the cell size (500 meters) due to the challenges of accurately measuring the river's length within that space. The model uses each river node's conductance, thickness, bed elevation, and river stage to assess whether the node is gaining or losing flow, in conjunction with the main river and its perennial tributaries.

5.3.2.6 Wells

Since there are no injection wells in the area, groundwater extraction was the sole scenario that was simulated. A total of 135 water supply wells were compiled for this study (Annex 5), of which 116 wells fall within the study area boundary and are utilized for various hydrogeological analyses. These wells have depths ranging from 20 to 654 meters below ground level, although not all wells contain complete datasets. For instance, only 60 wells have reliable lithological logs, and 34 wells have properly documented pumping and recovery test data, among other relevant information. Accordingly, only 56 validated wells were selected to represent the two aquifer systems: 36 wells (depth <150 m) for the unconfined aquifer, and 20 wells (depth >250 m) for the confined aquifer. The mean annual abstraction using the 116 wells across the 5,714 km² study area was estimated as 5.25 mm/year, equivalent to approximately 30 MCM/y (Table 4.10).

The model simulates the effects of the wells on groundwater levels and flow dynamics by simulating their presence. Local effects, especially during periods of peak demand, can be substantial even if their impact on regional storage is small. The wells' measured piezometric surfaces provide essential information for calibrating the model. Utilizing actual measurements enhances simulation dependability and guarantees that the model faithfully captures the aquifer's hydraulic conditions. Using piezometric data for calibration enhances the model's accuracy, allowing for better predictions of future groundwater behavior under various scenarios. In general, incorporating the 56 wells and their abstraction rates into unconfined (layer 1) and confined (layer 3) aquifers is essential for capturing the dynamics of groundwater flow in the study area. By using measured piezometric surfaces for calibration, you enhance the model's reliability, which is crucial for effective groundwater resource management and planning.

The total discharge of the wells is the sum of discharges from each layer, and each layer discharge proportion is determined by using the layer transmissivity proportion (McDonald & Harbaugh, 1988).

$$Q_i = Q_t \left((b_i k_i) / (b_1 k_1 + b_2 k_2 + b_3 k_3) \right)$$

Where Q_i is the discharge rate for the i^{th} layer in m^3/d, Q_t is the total measured discharge of the well in m^3/d, $b_i K_i$ is the i^{th} layer thickness and hydraulic conductivity, which is layer transmissivity in m^2/day, b_1K_1, b_2K_2, and b_3K_3 are transmissivity of respective layers in m^2/ day.

Accordingly, the estimated discharge rate of the unconfined aquifer (layer 1) is about 5,784 m^3/d or 2.1 MCM/y. By considering the respective transmissivity values of 76 m^2/day and 483 m^2/day for layer 1 and layer 3, the computed discharge rate for layer 3 using the above expression is about 71,068 m^3/d or 25.9 MCM/y. Thus, the total discharge is estimated to be 28 MCM, which differs from the 30 MCM/y computed abstraction rate (Table 4.10).

The key reasons why the sum of discharge from Layer 1 and Layer 3 (28 MCM/y) does not match the estimated total abstraction of 30 MCM/year in layer-based discharge estimates, even though transmissivity values were used, are as follows:

- Discharge estimates using transmissivity assume uniform aquifer properties and consistent hydraulic gradients, which may not reflect actual spatial variability.
- If the transmissivity values (76 m^2/d for Layer 1 and 483 m^2/d for Layer 3) are averaged or generalized, they may not capture local heterogeneities, leading to under- or overestimation.
- The 30 MCM/year abstraction is based on well withdrawal data, which reflects human-induced extraction, not necessarily the natural discharge capacity of each aquifer layer.
- The transmissivity-based discharge may represent potential flow capacity, not actual abstraction.

- In multi-layered systems, vertical flow between layers (leakage) can redistribute water internally, making it difficult to isolate discharge per layer.
- Some abstraction wells may draw water from multiple layers, especially if screened across both confined and unconfined zones.
- The abstraction estimate (30 MCM/year) is a spatially aggregated value across 116 wells, while transmissivity-based discharge may be calculated over specific zones or cells.

Thus, the discrepancy can be reconciled by considering using zone-based transmissivity averaging tied to well locations and incorporating layer-specific abstraction data if available for future work.

5.3.3 Model initial conditions

5.3.3.1 Hydraulic conductivity

According to the discussion in section 4.4.3.3, the fact that pumping test data is derived from a single well without utilizing data from observation wells makes it challenging to estimate hydraulic conductivity directly. In this study, transmissivity value was analyzed from pumping test and recovery data to calculate the hydraulic conductivities from fifty-six (56) water supply wells, of which thirty-six (36) represent the unconfined aquifer (layer 1. wells shallower than 150 m) and twenty (20) represent the confined aquifer (layer 3. wells deeper than 250 m). Furthermore, thirty-four (34) hydraulic conductivity values are derived from earlier studies. Accordingly, hydraulic conductivity in the range of 0.06 m/d to 1.76 m/d is obtained for shallow to intermediate depth or unconfined aquifer, and in between 0.33 m/d to 17.9 m/d for (Depth > 250 m), which represents the confined aquifer.

A point (well site) hydraulic conductivity value was used as an input for the geostatistical analysis of the kriging interpolation technique in the ArcGIS tool to create spatially distributed hydraulic conductivity zones of the model domain, primarily for both unconfined and confined aquifer systems (Figures 4.7a, 4.7b). Based on the hydraulic conductivity of similar aquifer units, the model domain was characterized by four zones for unconfined (layer 1) and five hydraulic conductivity zones for confined aquifer (layer 3). To fit the model result with the observed head, the calibration process was adjusted after these hydraulic conductivity values from the empirical equation were imposed as the model's starting input.

5.3.3.2 Hydraulic Head

When a flow simulation starts, MODFLOW flex needs initial hydraulic heads. To establish the initial heads, which serve as a starting point for iterations, it is essential to have the measured depth to the groundwater level and the knowledge of the groundwater condition of the area. Groundwater level measurements were made from wells and piezometers following pumping tests and validated during the dry season (January–February 2025). Given the limited groundwater abstraction in the area, aside from localized industrial use, the observed heads remain consistent with those recorded during testing. Although recent groundwater development initiatives by the Ministry of Water and Energy (MoWE) and the Ministry of Irrigation and Lowlands (MoIL) are underway, current measurements show no significant deviation from the one obtained after the pumping test. Of the hydraulic head data from 56 boreholes, 36 represent the upper unconfined aquifer (layer 1) and 20 represent the confined aquifer (layer 3). These values were interpolated using the kriging interpolation technique to generate a continuous potentiometric surface, resampled to a 500m*500m model grid resolution before being imported to the modeling environment as the initial condition for both aquifers. Incorporating this interpolated head surface during model initialization ensures a realistic starting condition, enhancing calibration and numerical stability.

5.3.3.3 Storage coefficients

As mentioned in section 4.4.3.4, the lack of information from observation wells during pumping tests makes it more difficult to estimate aquifer storage values such as specific yield or capacity for unconfined aquifers and storativity or storage coefficient for confined aquifers. Nevertheless, the specific yield value computed for an unconfined aquifer from earlier research (WWDSE, 2008) of a similar geological setting including the present study area, is between 0.01 and 0.3, with an average of 0.15, which is from a small number of unevenly distributed wells. Thus, in this model, the unconfined aquifer is represented by the average value of specific yield (S_y=0.15). For the same reason as an unconfined aquifer, a confined aquifer in the research area has no storativity value. Again, the storativity value of 0.045, determined using information from observation and pumping wells in similar geological settings adjacent to the present study area is adopted for further simulation.

5.4 Model Calibration and Results

Model calibration is a detailed, iterative process that refines the three-dimensional distribution and structure of aquifer properties, including their specific values and the characteristics of boundary conditions. Calibrating a groundwater flow model is critical, as it involves adjusting input data to better match the observed water levels and flow rates in an aquifer system (McDonald & Harbaugh, 1988; Szczepanski, 2004). The importance of careful calibration cannot be overstated, as the quality of this process directly influences the reliability of any findings and recommendations derived from the simulation results (Waterloo Hydrogeologic Inc., 2011). This task must consider the specific conditions of the area and the surrounding factors while keeping errors within an acceptable range. Accurate calibration is essential for effective groundwater management and decision-making.

Calibration was performed with a trial-and-error method by repeatedly adjusting boundary conditions like hydraulic conductivity, recharge, river bed conductance, and specified flux until the simulated heads and fluxes matched field-measured values within a range of error (Kulma, R., & Zdechlik, R., 2009). By comparing the simulated groundwater levels with the measured values, systematically adjust the model parameters to accurately represent the aquifer systems. Through this in-depth change, the model's predictive capabilities are enhanced, ensuring that it reflects the complexities of the subsurface environment more faithfully. After calibration, the simulated head values were closely aligned with the observed values. In this study, 56 observation wells (36 for layer 1 and 20 for layer 3) were employed, for which hydraulic heads were measured. These points served as essential data inputs for calibrating the groundwater model. The calibration process was carried out by comparing the model results with actual measurements of groundwater levels.

Calibration statistics are essential for the accuracy of predictive models. The process starts by calculating the residuals, which are the differences between simulated values and actual observed values. A negative residual indicates an overestimation, while a positive one signals an underestimation. Calibration can be performed through manual trial and error, which involves adjusting parameters based on model runs to match observed data.

A comprehensive statistical comparison was made between the simulated and measured values of hydraulic heads to evaluate the performance of the model. This analysis aimed to evaluate the calibration accuracy of the hydraulic model quantitatively. Key metrics employed in this assessment include the mean error (ME), mean absolute error (MAE), and root mean square error (RMSE). These statistical indicators serve as critical tools for assessing the overall goodness-of-fit between the simulated and observed hydraulic head values, allowing for a thorough understanding of the model's predictive capability, which ultimately facilitates improvements in model calibration and validation processes (Anderson & Woessner,1992).

The mean error (ME) is defined as the average of the differences between the measured water levels (h_m) and the simulated heads (h_s). This statistical metric serves to quantify the disparity between the actual measurements and the model's estimations, providing valuable insight into the accuracy of the simulations. ME provides insight into any consistent bias present in your model, indicating whether it tends to overestimate or underestimate the actual values. A positive ME suggests that the simulated heads are too low, while a negative ME indicates the simulated heads are too high. If the ME is close to zero, it indicates that the model simulations are unbiased on average. It is expressed as;

$$ME = \frac{1}{n}\sum_{i=1}^{n}(hm - hs)\text{i}$$

Where n is the number of calibration measurements. For accurate calibration, this value should be close to zero.

The mean absolute error (MAE) is a quantitative metric that calculates the average of the absolute differences between observed values and their corresponding predicted or simulated values. This measure is particularly valuable as it considers only the magnitude of the errors and treats them equally, effectively ignoring their signs, which allows for a more straightforward evaluation of prediction accuracy. By aggregating these absolute discrepancies, MAE provides a clear and comprehensible assessment of the model's performance, highlighting how well the simulations replicate actual measurements and serving as a crucial indicator in the calibration and validation processes of predictive modeling. It is also expressed as;

$$MAE = \frac{1}{n}\sum_{i=1}^{n} |\,(h_m - h_s)i\,|$$

The root mean squared error (RMSE), also known as the standard deviation of the errors, quantifies the differences between the values predicted by a model and the values observed. It is calculated as the square root of the average of the squared differences between measured and simulated heads, which allows it to capture the magnitude of discrepancies without being affected by the direction of the errors. By squaring the differences before averaging, RMSE emphasizes larger errors, making it a sensitive measure for assessing model accuracy.

$$RMSE = \left[\frac{1}{n}\sum_{i=1}^{n} |\,(h_m - h_s)i^2\,|\right]^{0.5}$$

This metric is particularly valuable to understand the precision of head measurements and a lower RMSE value indicates better model accuracy. Generally, both root mean square error (RMSE) and mean absolute error (MAE) assess the average differences between simulated values and actual measurements, but they approach this task in slightly different manners. RMSE amplifies the discrepancies by squaring them before averaging, which gives heavier emphasis to larger errors. This property makes RMSE quite responsive to outliers, or significant deviations within the data. On the other hand, MAE considers the absolute differences, treating all errors uniformly and offering a clear average of how inaccurate your simulations are. Understanding these metrics helps you identify areas where the model might be falling short and informs adjustments for improved accuracy. The calibration standard for heads necessitates an RMS that is at or below 10 percent of the observed head range in the aquifer being modeled (Anderson & Woessner, 1992).

In general, the evaluation of any model should incorporate both qualitative and quantitative measures, of which quantitative performance measures pertain to the mathematical or statistical analysis of residuals. On the other hand, the qualitative assessment involves scatter plots of measured versus simulated heads and pattern matching like comparisons of contour maps.

69 trial runs were conducted to successfully fit the observed and simulated water levels. The results of the steady-state calibration indicate that the measured water levels in the field (from observation wells) closely match the calculated water levels from the model. A summary of the statistics for the residuals, which represent the differences between simulated and observed values, was generated after the calibration. Specifically, the statistics related to the residuals were computed for 36 wells in layer 1 and 20 wells in layer 3 (Figure 5.3 a, b, c, and Table 5.2).

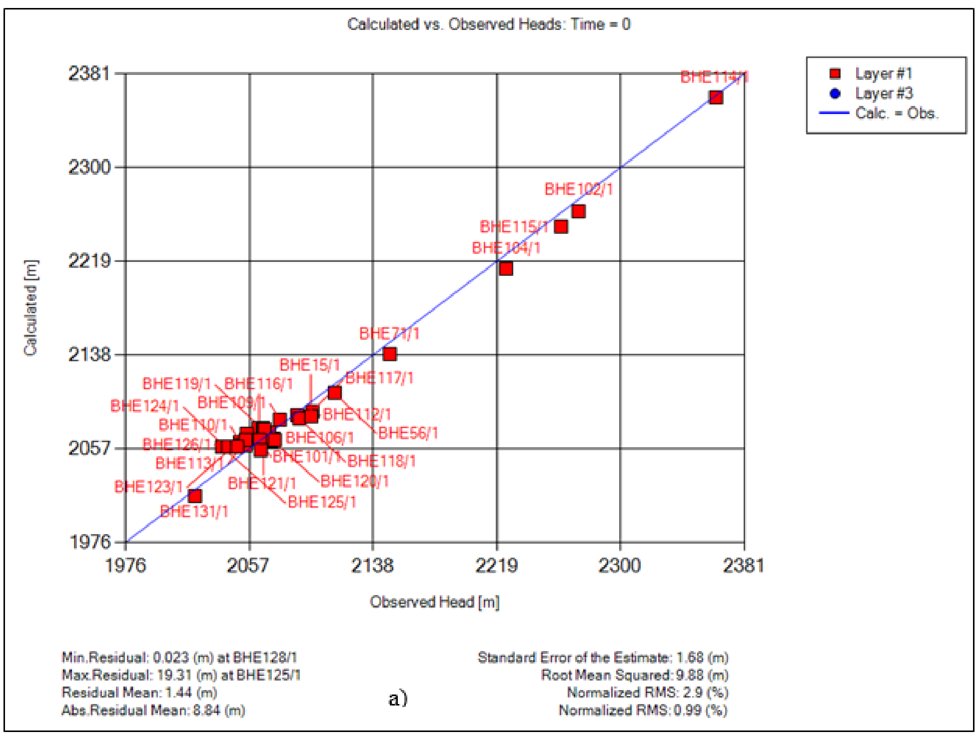

a)

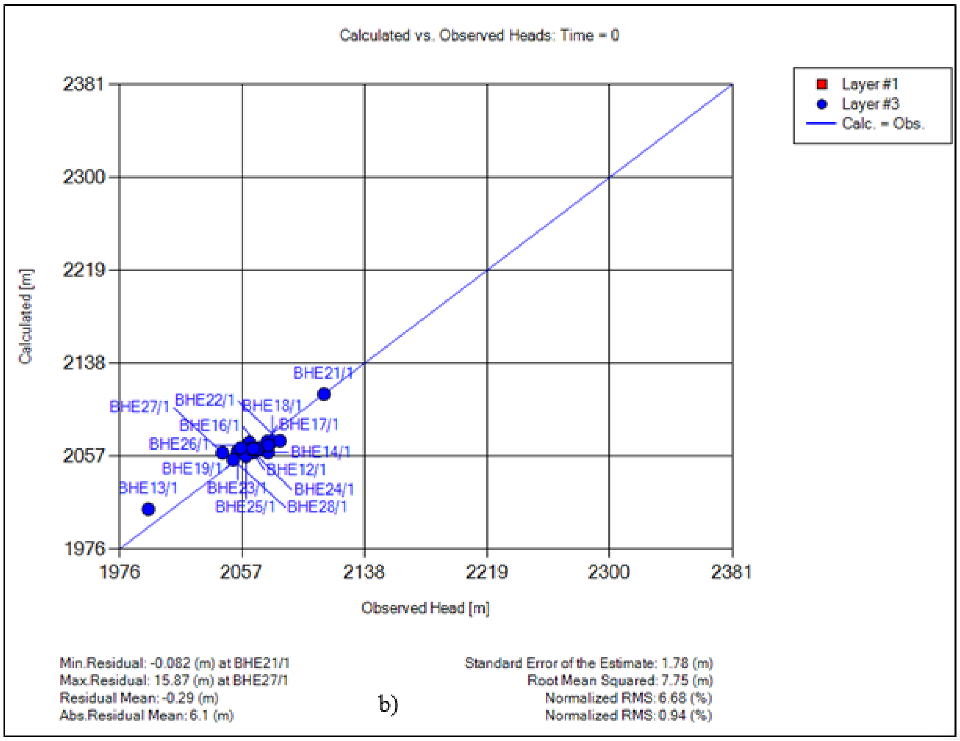

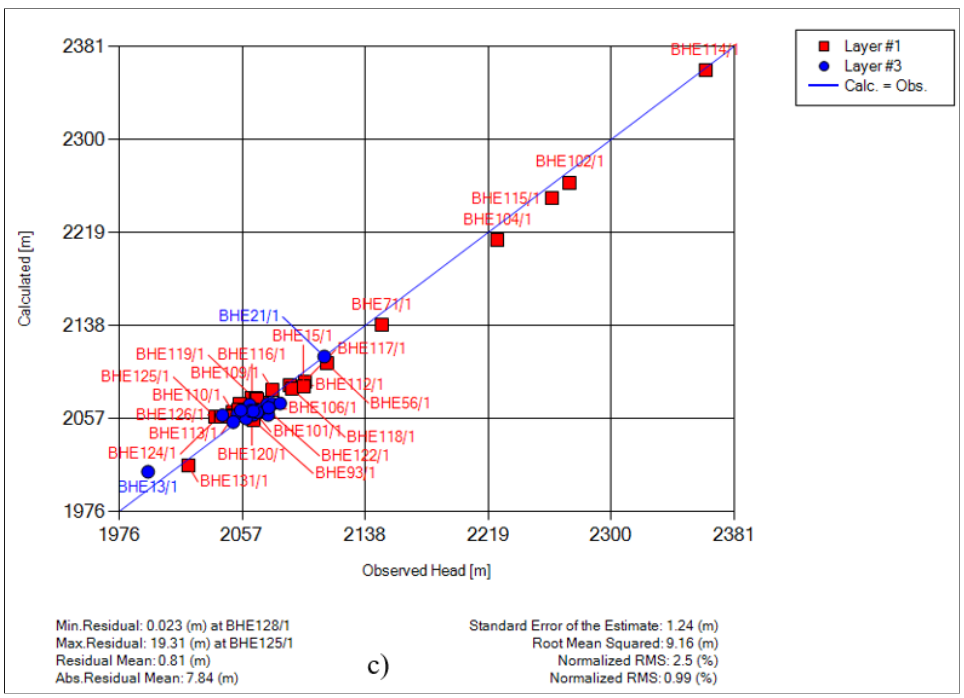

Figure 5.3 Correlation of observed versus simulated groundwater levels for a) layer 1, b) layer 3, and c) both layers together under steady state conditions

To gain deeper insights into the performance of the simulations, a series of key statistical metrics was meticulously calculated from the residuals. These metrics included the mean, minimum, and maximum values, along with the RMSE and AMR, which collectively provide a strong outline for evaluating accuracy. The overall normalized root mean square error of the aquifer systems is 9.16 (<10) with a mean residual of 0.81m and correlation coefficient (R^2) of 0.99, which is a good indicator of calibration quality. A mean close to zero shows a balance between positive and negative residuals, implying less model bias.

Table 5.2 Comparison of observed and simulated groundwater level values under steady-state conditions

No.	Well ID	UTME	UTMN	Elevation, m.a.s.l	The layer it represents	Calibrated groundwater level, m.a.s.l.	Observed groundwater level, m.a.s.l.	Calibrated-Observed
1	BHE101/1	453540	982150	2053	Layer 1	2063.7	2064.8	-1.1
2	BHE102/1	408480	952880	2273		2262.4	2272.9	-10.4
3	BHE104/1	404050	980360	2211		2212.3	2225.3	-13
4	BHE106/1	432820	969800	2075		2065.5	2073	-7.5
5	BHE109/1	429250	993950	2080		2082	2076.9	5.1
6	BHE110/1	429530	987240	2051		2062.6	2051.1	11.5
7	BHE112/1	416950	988220	2088		2085.8	2088.3	-2.5
8	BHE113/1	435990	973760	2052		2059.6	2051.8	7.8
9	BHE114/1	415250	939050	2362		2360.1	2362.1	-2
10	BHE115/1	412830	949740	2261		2248.5	2261.4	-12.9
11	BHE116/1	424090	968970	2081		2072.9	2063.6	9.3
12	BHE117/1	428570	961640	2115		2089.1	2098.1	-8.9
13	BHE118/1	409120	975190	2101		2082.4	2090.3	-7.9
14	BHE119/1	415530	977260	2069		2075.3	2064.5	10.8
15	BHE120/1	416140	977210	2068		2074.4	2063.4	11.1
16	BHE121/1	415720	976670	2070		2075	2066.2	8.8
17	BHE122/1	418710	974900	2073		2073.1	2066.3	6.7
18	BHE123/1	423380	973440	2069		2069.6	2055.4	14.2
19	BHE124/1	441370	977900	2047		2058.4	2041.3	17.1
20	BHE125/1	441900	981390	2043		2058.5	2039.2	19.3
21	BHE126/1	441830	983810	2051		2060	2054.5	5.5
22	BHE128/1	461900	974300	2084		2070.4	2070.4	0
23	BHE129/1	451900	983000	2068		2063.3	2071.3	-8
24	BHE130/1	455530	984000	2096		2064.3	2054.9	9.4
25	BHE131/1	455040	956410	2022		2015.7	2021.6	-5.9
26	BHE132/1	451590	954520	2067		2073.3	2067.2	6
27	BHE135/1	442810	977630	2022		2058.6	2047.1	11.5
28	BHE15/1	433200	959670	2063		2084.8	2097.2	-12.4
29	BHE54/1	442840	977560	2035		2058.6	2042.8	15.8
30	BHE56/1	407400	972710	2097		2105.1	2112.7	-7.5

No.	Well ID	UTME	UTMN	Elevation, m.a.s.l	The layer it represents	Calibrated groundwater level, m.a.s.l.	Observed groundwater level, m.a.s.l.	Calibrated-Observed
31	BHE71/1	423880	953050	2136		2138.3	2149	-10.7
32	BHE76/1	455550	983750	2076		2064.2	2064	0.3
33	BHE93/1	451680	958830	2063		2055.3	2064.6	-9.3
34	BHE94/1	455450	983010	2053		2064.2	2073.5	-9.3
35	BHE97/1	444620	978140	2043		2058.8	2049	9.8
36	BHE97/1	444620	978140	2043		2058.8	2049	9.8
							Min. Residual	-12.9 m
							Max. Residual	19.31 m
							Mean residual	1.44 m
							Absolute mean residual (AMR)	8.84 m
							Root mean squared (RMSE)	9.88 m
							Normalized R^2	0.99
37	BHE12/1	427220	971570	1794	Layer 3	2060.9	2063.2	-2.3
38	BHE13/1	456410	962800	1733		2010.7	1995	15.6
39	BHE14/1	450450	981240	1809		2060.2	2074.1	-13.9
40	BHE16/1	413230	974110	1810		2064.4	2068.6	-4.3
41	BHE17/1	427490	992980	1826		2069.7	2073.7	-4
42	BHE18/1	418770	988570	1815		2069.7	2077	-7.3
43	BHE19/1	423530	989200	1794		2068.9	2061.9	7.1
44	BHE21/1	411870	989880	1853		2111	2111.1	-0.1
45	BHE22/1	411280	984150	1823		2070.2	2082	-11.8
46	BHE23/1	426970	971150	1772		2060.9	2054	6.9
47	BHE24/1	426450	969520	1801		2060.2	2064.6	-4.4
48	BHE25/1	450920	978940	1806		2060.5	2059.6	0.9
49	BHE26/1	450980	981470	1805		2066.5	2074.4	-7.9
50	BHE27/1	438960	977390	1785		2059.8	2044	15.9
51	BHE28/1	447320	978720	1775		2053.9	2051.1	2.8
52	BHE29/1	449170	980610	1796		2057	2059.6	-2.6
53	BHE35/1	445660	983870	1817		2062.5	2066.9	-4.3
54	BHE37/1	427290	976950	1806		2063.6	2062.5	1
55	BHE38/1	431970	979200	1808		2063.4	2064.3	-0.9
56	BHE39/1	422890	976540	1782		2064.1	2056.1	8
							Min. Residual	-13.9 m
							Max. Residual	15.87 m
							Mean residual	0.29 m
							Absolute mean residual (AMR)	6.1 m
							Root mean squared (RMSE)	7.75 m
							Normalized R^2	0.94
Layer 1 and Layer 3 together								
							Min. Residual	-13.9 m
							Max. Residual	19.31 m
							Mean residual	0.81 m
							Absolute mean residual (AMR)	7.84 m
							Root mean squared (RMSE)	9.16 m
							Normalized R^2	0.99

Despite overall consistency in the simulated groundwater flow patterns, notable discrepancies were observed between simulated and measured parameters, such as the normalized RMSE in Layer 3, which reached 94%. These deviations are primarily attributed to the timing and condition of head measurements used during model calibration. The main reason for this is that some observed heads were recorded shortly after the completion of pumping tests, before full stabilization of the dynamic groundwater level to static conditions. These premature data acquisitions likely introduced bias in the input heads, which were subsequently used to compute fluxes and generate groundwater level contours. As a result, the model may reflect errors in both head distribution and water balance components. Such uncertainties underscore the importance of ensuring hydrostatic equilibrium in observation wells before data collection, particularly in stress-based scenario simulations. Future calibration efforts should prioritize stabilized head measurements and consider incorporating uncertainty quantification techniques to constrain model predictions better.

The hydraulic conductivity of aquifer systems is a key input parameter used for calibration purposes. This property is spatially assigned based on a conceptual understanding of the groundwater flow system and the analysis of pumping test data from representative water supply wells in different aquifer layers. The known values of hydraulic conductivity are initially set as pilot points in each aquifer unit, specifically in layer 1 and layer 3.

The simulated hydraulic conductivity values for both the unconfined and confined aquifer systems, as illustrated in Figure 5.4a, b, reveal a distinct spatial variation in groundwater dynamics, mainly in an unconfined aquifer. The northeastern and southeastern regions exhibit notably high hydraulic conductivity, suggesting that these areas facilitate a strong flow of groundwater toward the southeast. In contrast, the western and southwestern sectors present much lower values of hydraulic conductivity, a reflection of the impervious nature of the underlying geological units and the minimal influence of geological structures in these regions, whereas a confined aquifer (layer 3), has little or no significant variation.

The simulated hydraulic conductivity values for the unconfined aquifer range from 0.15 m/day to 8.98 m/day, while those for the confined aquifer range from 7.2 m/day to 22.8 m/day. Whereas, the field-based hydraulic conductivity analysis result shows the value in the range of 0.06 m/d to 1.76 m/d for an unconfined aquifer and 0.33 m/d to 17.9 m/d for a confined aquifer (Figure 4.7a & Figure 4.7b).

The difference between field-based hydraulic conductivity (K) estimates and those obtained after model calibration is a common and well-documented phenomenon in groundwater modeling (*M. El-Rawy et al., 2018*). The justifications for post-calibration changes in hydraulic conductivities are;

- During calibration, the model adjusts parameters, especially hydraulic conductivity values, to minimize the difference between observed and simulated heads. This process, known as inverse modeling, often leads to non-unique solutions, where multiple parameter combinations can yield similar head distributions. As a result, areas with low observed hydraulic conductivity may be assigned higher values to compensate for other uncertainties (e.g., recharge, boundary conditions, or layer connectivity).
- Field measurements reflect local-scale hydraulic conductivity values, while model calibration operates at the grid or zone scale, often averaging heterogeneities. A single well test may underestimate transmissivity if fractures or preferential flow paths are missed, whereas the model may infer higher hydraulic conductivity to match regional flow patterns.
- If boundary conditions (e.g., recharge or flux boundaries) are uncertain or simplified, the model may adjust hydraulic conductivity values to balance the water budget. For example, underestimating recharge may lead the model to increase hydraulic conductivity in certain zones to maintain observed head levels.
- In multi-layered systems, vertical flow between layers can affect calibration. If leakage from upper layers is underestimated, the model may increase hydraulic conductivity in lower layers to simulate observed drawdowns or artesian conditions.
- Calibration often uses zonation, where hydraulic conductivity is assumed constant over large areas. This can mask local variability and lead to generalized hydraulic conductivity values that differ from point-scale observations.

Thus, the observed reversal, where zones with low field-based hydraulic conductivity show higher calibrated values, is a result of either of the following conditions, like the model's compensation for data gaps or simplifications, scale mismatch between field tests and model resolution, structural and boundary condition uncertainties, and the inherent non-uniqueness of inverse modeling. Thus, these adjustments are acceptable as long as the model remains hydrologically consistent, calibrated against reliable head data, and validated through sensitivity analysis.

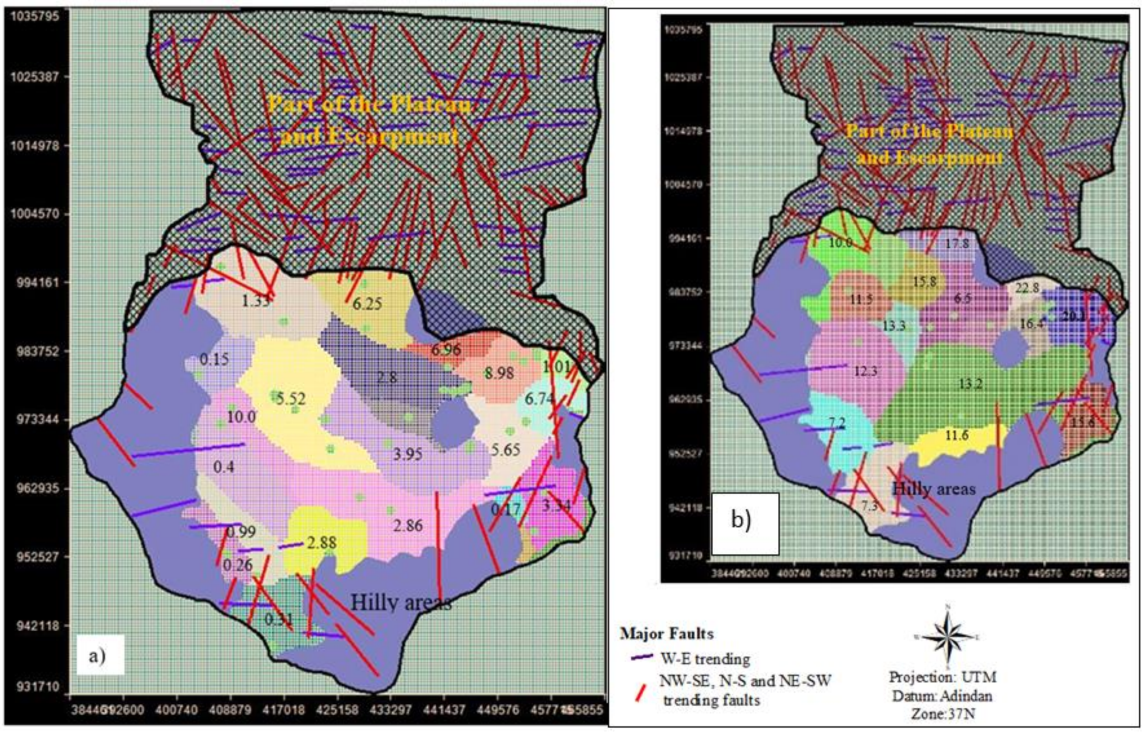

Figure 5.4 Simulated hydraulic conductivity (m/day) distribution under steady-state conditions a) layer 1 and b) layer 3

5.5 Water Budget

The water balance is a crucial performance metric used to assess the accuracy of a calibrated model. It involves comparing the total simulated inflows and outflows within the model to identify any residual errors. The water balance error is expressed as a percentage, representing the discrepancy between total inflows and total outflows, including any changes in storage. To calculate this percentage, you divide the difference between inflows and outflows by either the total inflows or total outflows. For a model to be deemed numerically reliable and acceptable, the water balance error must remain below 1% (Anderson et al., 2015).

In this study, a comprehensive groundwater budget was established following model calibration, yielding a total inflow of approximately 760,095.8 m³/day (equivalent to 277.5 Mm³/year) into the aquifer system (Figure 5.3). The model demonstrates a near-perfect balance between inflow and outflow, with a discrepancy of only 0.001%, indicating a high level of calibration accuracy and numerical stability. To further assess the reliability of the calibrated model, the results were compared against analytically derived estimates, which suggest a total inflow of 844,065.1 m³/day (or 308.1 Mm³/year). Although the calibrated values are slightly lower, the comparison underscores the model's ability to reproduce regional groundwater dynamics within an acceptable margin of error, thereby reinforcing its suitability for predictive simulations and resource management applications.

Table 5.3 Simulated daily water balance for part of the Upper Awash groundwater area

Analyticaly Computed				Model Computed		
No.	Water Balance Components	Inflow	Outflow	Water balance components	Inflow (m^3/d)	Outflow (m^3/d)
		m^3/day	m^3/day	River leakage	275,798.20	704,329.88
1	Recharge from runoff seepage (at the foot of the escarpment, and through stream channels) and direct precipitation on the alluvial plain) computed using WTF method (Area: 3440 km^2)	381,698.73		Head-dependent boundaries	104,365.80	55,777.71
2	Recharge from draining the northwestern and northern plateau & Escarpment as a regional subsurface inflow for unconfined aquifer system (Area: 2552 km^2)	48,243.28		Recharge	325,331.80	-
3	Recharge from draining the northwestern and northern plateau & Escarpment as a regional subsurface inflow for confined aquifer system (Area: 2552 km^2)	414,123.13		Specified flux	54,600.00	-
Total budget for central plain part of the Upper Awash Basin groundwater system estimated by Darcy's method.		844,065.14	844,065.14	Abstraction	-	Negligible
				Total	760,095.80	760,107.58
				Inflow- outflow	-11.8	
				Percent discrepancy, %	0	

A calibrated model reflects observed hydraulic heads and fluxes, ensuring that simulated inflows and outflows are consistent with field conditions. Calibration minimizes the residuals between observed and simulated data, thereby improving confidence in the model's predictive capabilities (Anderson et al., 2015). The near-zero discrepancy (0.001%) between inflow and outflow confirms mass balance closure, a fundamental criterion for model reliability. Analytical methods (Darcy-based recharge estimation and water table fluctuation methods) provide independent benchmarks for model validation. Cross-validation with analytical approaches helps identify potential biases or structural errors in the numerical model (Scanlon et al., 2002). The calibrated inflow (760,095.8 m^3/d) is within ~10% of the analytical estimate (844,065.1 m^3/d), suggesting that the model captures the dominant hydrogeological processes despite simplifications.

Discrepancies below 5 to 10% are generally considered acceptable in regional groundwater models, especially in complex volcanic terrains, like the present study area. Model uncertainty arises from spatial heterogeneity, parameter estimation, and assumptions about boundary conditions (Hill & Tiedeman, 2007). A 0.001% discrepancy is exceptionally low, indicating robust numerical convergence and well-constrained boundary conditions.

Thus, reliable models are essential for scenario-based simulations, policy development, and sustainable groundwater management. A well-calibrated model with validated fluxes can be confidently used for scenario analysis, stress testing, and resource allocation (Barnett et al., 2012). The close agreement between calibrated and analytical budgets supports the model's use in forecasting and decision-making contexts.

5.6 Sensitivity analysis

The primary objective of sensitivity analysis is to quantify uncertainties in a calibrated model resulting in variations in aquifer parameters, stresses, and boundary conditions (Anderson & Woessner,1992). While various methods exist for conducting these analyses, no single approach can definitively determine model sensitivity. This study uses a traditional method, adjusting key parameters by specific percentages to document the resulting changes in simulated outcomes.

A sensitivity analysis was conducted for both unconfined (layer 1) and confined (layer 3) aquifers within the calibrated models to evaluate the uncertainty associated with estimates of aquifer parameters and boundary conditions. The response of the calibrated numerical model was analyzed for variations in hydraulic parameters such as hydraulic conductivity, recharge rates, river-bed conductance, and specified fluxes from the northern and northwestern boundaries of the unconfined aquifer. Additionally, hydraulic conductivity and specified flux were examined for the confined aquifer.

During the simulations, while assessing the impact of one specific parameter, the other parameters were held constant at their calibrated values. A specified percentage across the entire area was uniformly adjusted for each parameter. The resulting changes in heads from the calibrated model were utilized as a measure of the model's sensitivity to particular parameters.

Table 5.4 Result of sensitivity analysis (layer 1)

Parameters	Percent of variation (%)	Resulting change	
		Residual mean (m)	Standard deviation (m)
Hydraulic conductivity, m/day	-50	20.94	33.58
	-25	8.46	12.73
	-10	3.53	9.54
	0	1.44	9.88
	10	-0.48	12.46
	25	-3.4	15.49
	50	-2.3	14.59
River bed conductance, m2/day	-50	-1.7	27.39
	-25	-1.6	26.96
	-10	-1.4	26.74
	0	1.44	9.88
	10	-1.2	26.47
	25	-1.1	26.32
	50	-0.8	26.07
Recharge, m/d	-50	-10.3	26.59
	-25	-4	16.88
	-10	-0.59	12.46
	0	1.44	9.88
	10	3.37	9.69
	25	7.22	11.12
	50	12.9	18.66
Specified Flux, m3/day	-50	1.66	9.86
	-25	1.65	9.87
	-10	1.65	9.86
	0	1.44	9.88
	10	1.65	9.87
	25	1.65	9.87
	50	1.66	9.86

The sensitivity analysis results for the unconfined aquifer (Table 5.4 and Figure 5.5) indicate that the model is very sensitive to changes in hydraulic conductivity and recharge rates. The biggest change in head, which ranges from 20.94 m to -3.4 m, occurs when hydraulic conductivity is adjusted by -50% to +50%. When hydraulic conductivity increases, the head variation reduces to 3.4 m. In contrast, when hydraulic conductivity decreases, the head variation increases significantly to about 21 m from the final calibrated model value. This shows how important hydraulic conductivity is to the behavior of the aquifer.

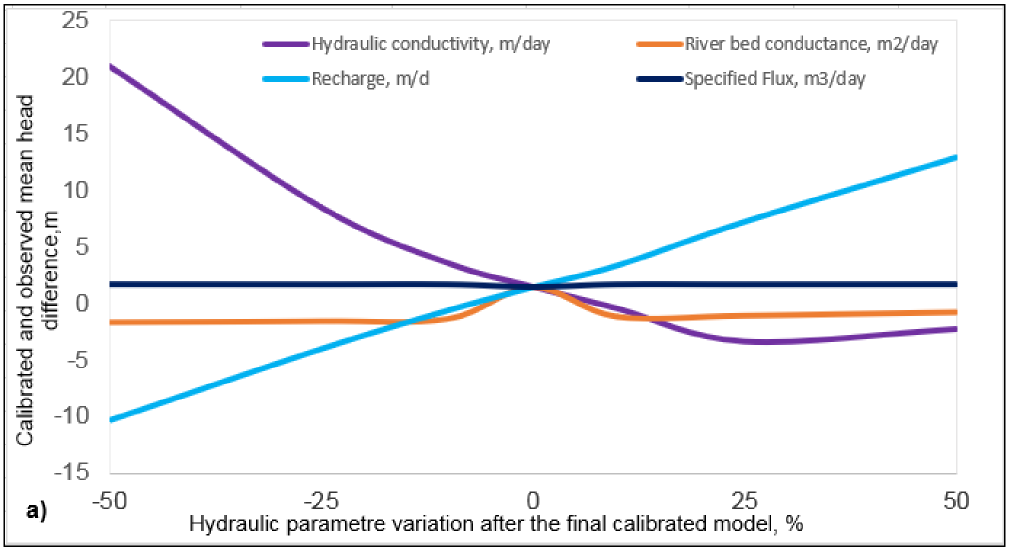

Figure 5.5 Result of sensitivity analysis for unconfined aquifer (layer 1)

The second factor affecting head variation is related to recharge, which varies from -10.3m to 12.9m as recharge values change between -50% and 50%. In an unconfined aquifer, both river-bed conductance and specified flux have little to no significant effect on head variation. In general, the effect of varying hydraulic conductivity and recharge is opposite, i.e., increasing the hydraulic conductivity will decrease the head distribution in the model, while increasing the recharge increases the heads in the model. This indicates that more reliable data on hydraulic conductivity will greatly increase the accuracy of the model outputs.

Table 5.5 Result of sensitivity analysis (Layer 3)

Parameters	**Percent of variation (%)**	**Resulting change**	
		Residual mean (m)	**Standard deviation (m)**
Hydraulic conductivity, m/day	-50	41.8	42.92
	-25	15.6	17.37
	-10	5.8	8.97
	0	-0.3	7.75
	10	-4.6	9.6
	25	-9.9	13.66

Parameters	Percent of variation (%)	Resulting change	
		Residual mean (m)	Standard deviation (m)
	50	-16.3	19.54
Specified Flux, m3/d	-50	-29.1	31.69
	-25	-14.6	17.55
	-10	-5.9	10.28
	0	-0.29	7.75
	10	5.64	9.22
	25	14.3	16.022
	50	28.8	29.98

The results of the sensitivity analysis (Table 5.5 and Figure 5.6) for the confined aquifer show that the model is very sensitive to changes in hydraulic conductivity and specified flux. The largest change in water level, from 41.2m to -16.3m, happened when adjusted the hydraulic conductivity from -50% to +50% of the calibrated value. When hydraulic conductivity increases, the water level change decreases to 16.3m. However, when it decreases, the change in water level increases to about 42m compared to the final calibrated model value. The second key factor that affects the water level change is the specified flux, which changes from -29.1m to 28.8m when the specified flux value is adjusted by -50% to +50% of the calibrated value.

Thus, the sensitivity analysis shows that the unconfined aquifer is highly responsive to changes in hydraulic conductivity and recharge levels, meaning even minor fluctuations can significantly affect its behavior. In contrast, it has less sensitivity to riverbed conductance and specified flux. For the confined aquifer, variations in hydraulic conductivity and specified flux are more impactful. These findings highlight the necessity of accurate and reliable data on hydraulic conductivity, recharge rates, and specified flux to improve groundwater model precision and ensure better water resource management.

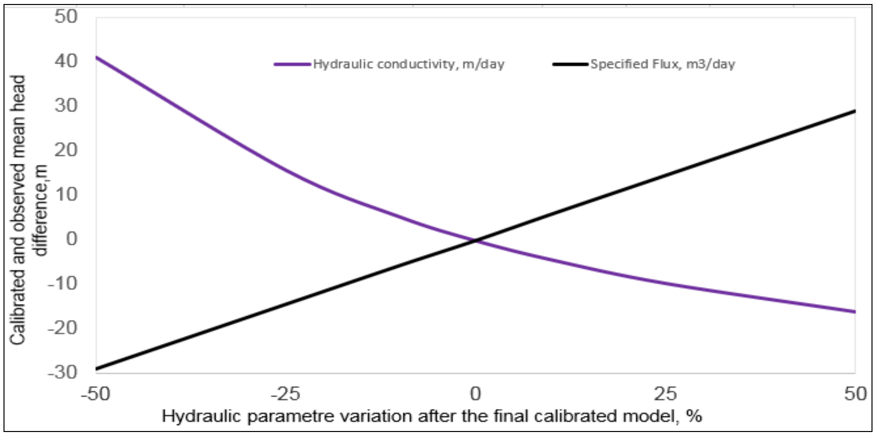

Figure 5.6 Result of sensitivity analysis for confined aquifer (Layer 3)

5.7 Stress-based scenario analysis for resource management

5.7.1 Aquifer response using different scenarios

The significance of groundwater modeling lies in its ability to evaluate the potential impacts on aquifer systems driven by a range of factors, such as climate change and human activities like excessive groundwater extraction. Steady-state models serve as valuable tools for predicting the consequences of sustained stressors over time, including extended drought periods or projected long-term pumping scenarios (Anderson & Woessner, 2015). Through thorough calibration, the final model was utilized to simulate various future scenarios, enabling a comprehensive analysis of the potential changes and challenges that groundwater resources may encounter in the coming years. This not only aids in understanding the dynamics of groundwater systems but also informs better management practices to ensure their sustainability.

Utilizing a calibrated steady-state model, various simulations were made to evaluate the impacts of the adverse effects of climatic conditions, specifically drought, alongside hypothetical increases in well withdrawals. This simulation analyzed the groundwater system's response to various stressors, allowing us to assess how these changes might influence water availability and management. Through situation analysis, valuable insights are provided, which could guide decision-makers in planning and managing groundwater resources within the area. It is anticipated that a significant portion of the withdrawn water may ultimately contribute to river flow or that underflow in the aquifer may become the predominant hydrological process, as indicated by the simulation results.

While all the scenarios considered employed hypothetical values, it is imperative to note that they are representative of conditions that are highly plausible soon, thereby emphasizing the urgency for informed water resource management strategies in the face of changing environmental conditions.

The main assumptions used for the scenario analysis include the initial conditions of the model's head and the flux from steady-state calibration. The simulation period lasts 11,320 days (30 years). It assumes a constant rate of drought condition (a reduced recharge rate and specified flux by 50%) along with both injection and extraction. Furthermore, the response of the groundwater system is analyzed using representative observation wells to assess the drawdown as a function of exploitation time.

5.7.1.1 Scenario I. Decline in recharge and specified flux (Climate Change)

In this scenario, both the calibrated recharge and specified flux values were deliberately reduced by 50 % to simulate the effects of drought. This adjustment was implemented simultaneously within the calibrated model to analyze the groundwater system's response to these considerable changes. By lowering these parameters, the aim was to gain insights into the dynamics of groundwater behavior under modified conditions and evaluate the subsequent impacts on the overall hydrological response.

The simulation results show a decline in groundwater levels on average of 25.8 meters for the unconfined aquifer (layer 1) and 4.3 meters for the regional confined aquifer (layer 3), as recorded by monitored wells (Figures 5.7a & b). The water balance analysis after simulation (Table 5.6) indicates a 10.5% increase in inflows due to river leakage and a 2.5% increase from head-dependent flow. In contrast, the analysis also indicates a significant reduction in outflows, with river leakage experiencing a sharp decline of 19.2%, while outflows through a general head boundary saw a dramatic decrease of 43%.

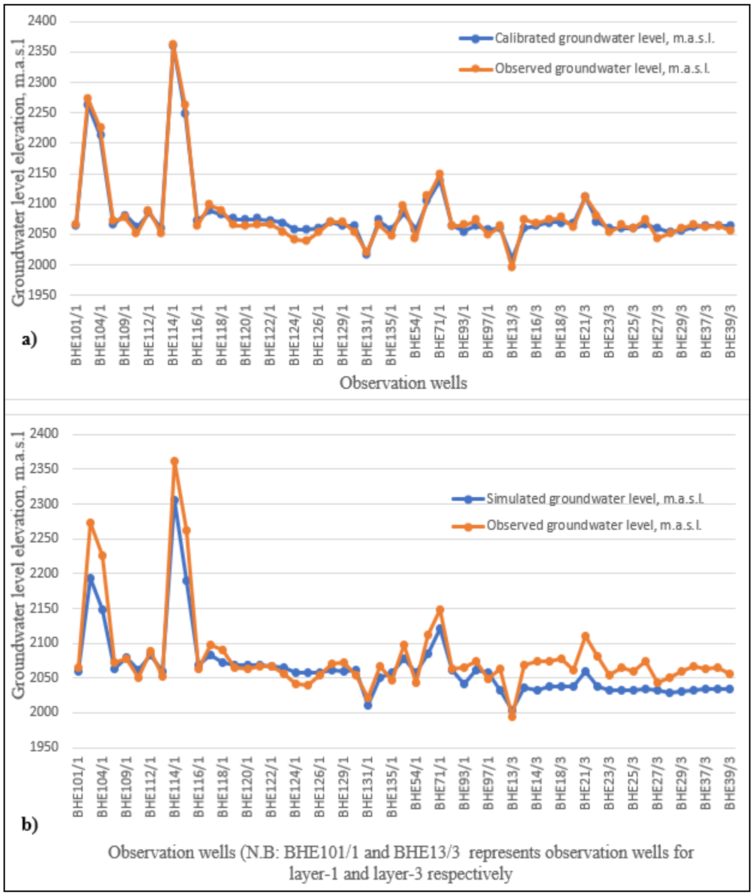

Figure 5.7 Comparison of the simulated and observed heads based on a) the final calibration, and b) after application of the stress-based scenario I simulation

Table 5.6 Changes in water balance components for drought conditions

Water balance after steady state calibration, all in m^3/d		Water balance after simulation of 50 % decline in recharge and specified flux, all in m^3/d
Inflow components		
River leakage	275,813.4	304,498.1
Head-dependent boundary	104,366.8	107,023.9
Recharge	325,331.8	162,564.5
Specified flows	54,565.0	27,265.0
Total Inflow	760,076.9	601,351.6
Outflow components		
River leakage	704,024.13	569,408.80
Head-dependent boundary	56,055.01	31,944.96
Total outflow	760,079.13	601,353.75
Inflow-Outflow	-2.1675	-2.1875
% discrepancy	0.00	0.00

5.7.1.2 Scenario II and III. Using an additional number of water supply wells

The second and third scenarios involve the pumping of 100 and 120 boreholes over 30 years, from January 1, 2026, to December 31, 2055, respectively. The model was used to evaluate the effects of pumping at a mean discharge rate of 4,320 m^3/d, equivalent to 50 l/s. This results in total groundwater extraction of 432,000 m^3/d for the second scenario and 518,400 m^3/d for the third scenario. This assessment aims to understand the future impacts of over-pumping on the aquifer system. During the pumping period, the groundwater levels in the model area were monitored using representative observation wells for both unconfined (layer 1) and confined (layer 3) aquifer systems.

In these scenarios, twelve observation wells represent an unconfined aquifer (layer 1). In the second scenario, six observation wells, including BHE106 and BHE118 to 122, exhibited a significant drawdown of approximately 45 meters from the start, continuing for up to 5,000 days (around 13 years). Following this period, the rate of drawdown slowed, ultimately reaching a total of 50 meters by the end of the extraction phase. Four additional wells (BHE109, 110, 112, and 113) experienced a low drawdown of about 10 meters for only 2,000 days (5 years), with no further drawdown observed in the subsequent pumping intervals. Meanwhile, two wells (BHE15 and BHE17) showed an unusual rise in water levels lasting about 1,500 days (4 years). This rise was attributed to increased water inflow in these areas due to additional aquifer development. After this period, the water levels in these wells dropped rapidly until reaching 5,000 days (13.5 years) and then continued to decline slightly during the remaining pumping interval (Figure 5.8a).

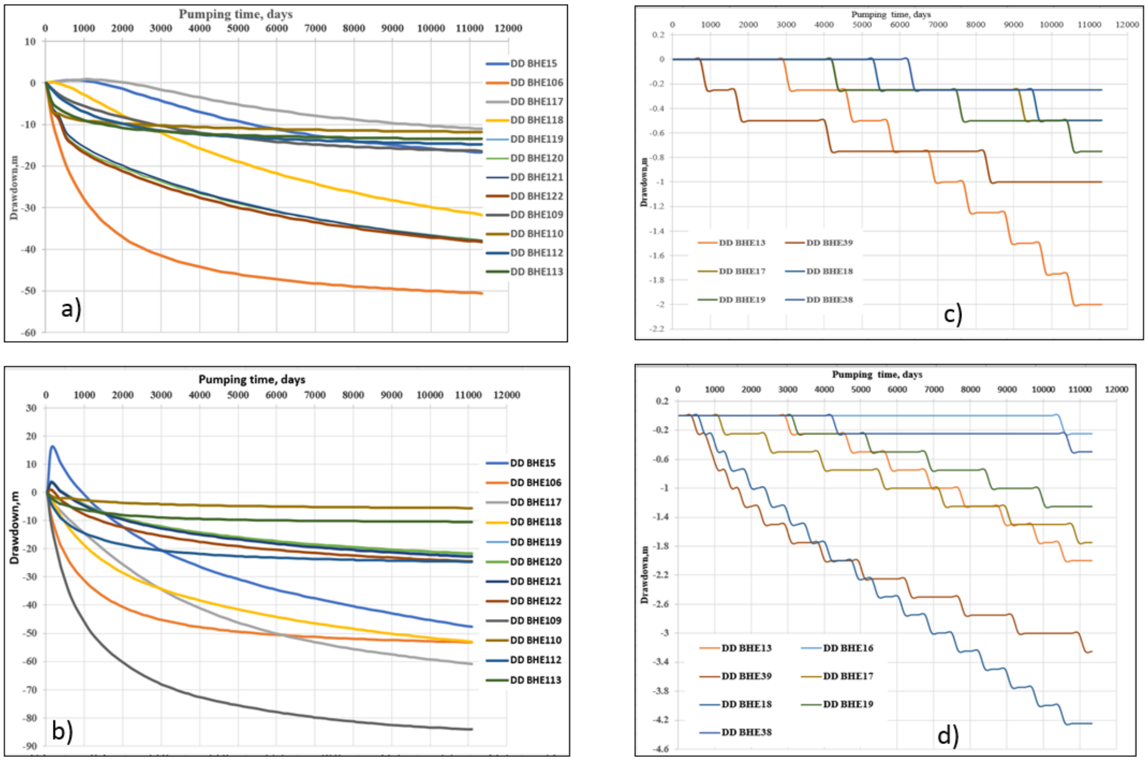

Figure 5.8 Simulated drawdown observed at selected wells after 30 years of varied exploitation rates in layer 1. a) 432,000 m³/day, b) 518,400 m³/day; in layer 3. c) 432,200 m³/day and d) 518,400 m³/day

In the third scenario, which specifically addresses the unconfined aquifer, a significant drawdown was observed in five observation wells. BHE106, BHE109, BHE15, BHE117, and BHE118. This drawdown can be attributed to their proximity to a local barrier located in the central area of the model, as well as the presence of clay layers or lenses at depth that create localized zones of reduced drawdown. In contrast, the lower drawdown recorded in the observation wells labeled BHE15, BHE110, BHE112, BHE113, and BHE119-BHE122 is due to their closeness to the main river or streams, which provide additional water replenishment (Figure 5.8b).

A total of six observation wells (BHE13, BHE17-19, BHE38, and BHE39) serve as key indicators of the regional confined aquifer system. Throughout the entire pumping duration of both scenarios, these wells demonstrated remarkably minimal drawdown, recording less than 2 meters for the second scenario and only about 4.2 meters for the third scenario, as illustrated in Figures 5.8c and 5.8d. This limited response can be attributed to several key factors inherent to the confined regional aquifer system (layer 3).

Notably, a significantly high recharge rate (flux) from the surrounding plateau replenishes the aquifer, while the substantial storage capacity of the fractured scoriaceous basaltic aquifer, characterized by its confined nature, further mitigates the effects of prolonged pumping over an extensive period of 30 years. Analysis of these scenarios revealed that groundwater outflow through rivers decreased by 15.4% in the second scenario and by 23.3% in the third scenario. Conversely, inflow to groundwater increased by 12.8% in the second scenario and by 16.13% in the third scenario.

5.7.1.3 Scenario IV. Recharging using injection wells

In the designated model area, a total of 50 hypothetical deep wells were methodically proposed to facilitate the injection of water at a consistent rate along the rivers and streams, in addition to strategically positioning them at the base of the escarpment. This design carefully considered the intricate alignment of the regional geological structures (Figure 5.9).

To assess the groundwater system's dynamics, a series of independent simulations were conducted, targeting the main regional aquifer system, each employing the calibrated final model result as a reliable baseline. Various injection rates (216,000 m^3/day, 345,600 m^3/day, and 518,400 m^3/day) were experimented. This variability in injection rates allowed for a detailed observation of the groundwater response dynamics across various observation wells, offering insights into how differing volumes of water affect aquifer replenishment, hydraulic gradients, and overall groundwater behavior in the system. The results from these simulations were meticulously analyzed, which are crucial for effective water resource management.

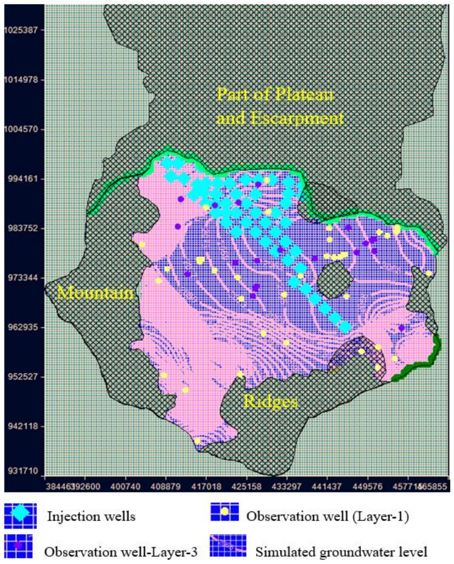

Figure 5.9 Location of injection wells within the model domain

The result of model simulation for the coming 30 years prediction (Figure 5.10 a, b, c) shows that an average rise of groundwater level of only with 1.05 m, 2.38 m, and 4.45 m observed at three observation wells (BHE17, BHE18, and BHE19) for the respective increased injection rate of 216,000 m³/day, 345,600 m³/day, and 518,400 m³/day.

Table 5.7 demonstrates that the result of this scenario led to a 2.03 % increase in groundwater leakage to the river, while the leakage from the river to the groundwater decreased by 4.7%. Overall, as the injection rates increase, groundwater outflow to the river also rises by an average of 7.31%, accompanied by a 2.8% decrease in river leakage to the groundwater, relative to the calibrated model values. Furthermore, the results indicate that outflow at head-dependent flow boundaries increased by approximately five times.

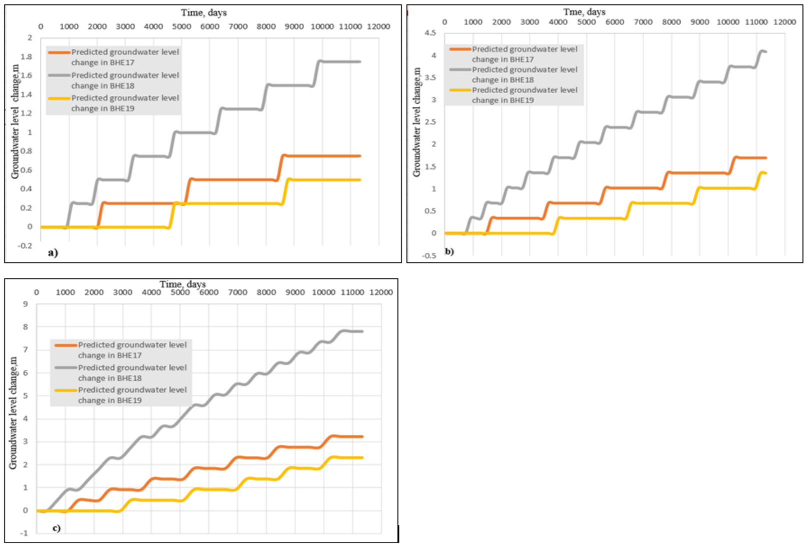

Figure 5.10 The predicted groundwater level rise (for layer-3) over the next 30 years (11,321 days) using different injection rates. a) 216,000 m³/day, b) 345,600 m³/day, and c) 518,400 m³/day

Table 5.7 Changes in water balance components for various injection rates

Water Balance after steady state calibration, all in m^3/d			
Inflow parametres	Value	**Outflow components**	Value
- River leakage	275,813.38	- River leakage	704,024.13
- Head dependant Boundary	104,366.80	- Head dependant Boun	56,055.01
- Recharge	325,331.75	Total outflow	760,079.13
-Specified flows	54,565.00	Inflow-Outflow	-2.1875
Total Inflow	760,076.90	% descrepancy	0.00
The simulated groundwater (model) response after using different rates of injection (Increasing recharge)			
Inflow parametres	Values, m^3/day		
-Storage	343,362.9	342,158.1	369,630.3
-Injection wells	**216,000.0**	**345,600.0**	**518,400.0**
-River leakage	288,728.0	280,888.9	270,635.4
-Head dependant Boundary	100,407.3	100,406.9	98,607.6
-Recharge	325,331.8	325,331.8	325,331.8
-Specified flows	54,530.0	54,530.0	54,530.0
Total Inflow	1,328,360.0	1,448,915.6	1,637,135.1
Outflow components	Values, m^3/day		
-Storage	320,550.40	413,756.09	547,674.06
-River leakage	718,346.43	747,635.12	800,617.87
-Head dependant Boundary	283,710.34	283,710.34	285,081.22
Total outflow	1,322,607.25	1,445,101.55	1,633,373.15
Inflow-Outflow	5,752.75	3,814.03	3,761.91

By facilitating the replenishment of aquifers, this approach mitigates the severe fluctuations in water levels often attributed to over-extraction and ensures the sustainability of groundwater resources during periods of drought. Comprehensive analysis indicates that the strategic implementation of injection wells can significantly improve the flow system within aquifers, effectively enhancing groundwater recharge rates. This, in turn, contributes to a more resilient water supply, vital for both agricultural and urban needs, especially in regions prone to water scarcity.

In general, the calibrated model was subjected to various scenarios to assess the aquifer's response to the imposed stresses, guiding future planning and management. Increasing recharge by developing injection wells at strategically chosen locations would significantly enhance the groundwater potential. While intensive groundwater extraction is unlikely to impact the regional confined aquifer system, it does affect the unconfined aquifer, particularly concerning water supply wells that draw from the unconfined aquifer (with depths ranging from 50 to 80 meters) located near acidic volcanic barriers and distanced from rivers or streams. Under these scenarios, the model indicates substantial drawdown levels of 30 to 45 meters occurring after 4 to 5 years of continuous pumping. Furthermore, the effect of drought was examined by imposing the 50 % reduced recharge and specified flux values into the calibrated model, which reveals a significant impact not only on the unconfined aquifer groundwater level decline but also a significant reduction in outflow and enhancement in inflows.

5.8 Model Limitations

While this model provides valuable insights, it cannot perfectly replicate the complexity of natural groundwater flow. Every effort was made to make this model as reliable as possible, but certain factors can affect its accuracy. These are;

- No water supply well fully penetrated the regional confined aquifer (layer 3)
- Field head measurements are mostly taken right after well completion, before the water level stabilizes. Flux values are derived from water level contours based on this data, which may introduce errors.
- The absence of independently treated aquifer hydraulic properties due to the area's complicated geological setting to accurate representation.
- The time (dry or wet), when the development of water supply wells and water levels are measured can introduce errors into the model.
- The eastern and western parts of the area lack clearly defined aquifer types.
- Limitations in the availability of continuous groundwater level monitoring data.

6. CONCLUSIONS AND RECOMMENDATIONS

6.1 Conclusions

Over the past two decades, Ethiopia has prioritized the development of its groundwater resources to stimulate economic growth, alleviate poverty, and address climate change. The increasing demand driven by urbanization and population growth highlights the necessity for a comprehensive scientific assessment.

The study area covers 9,200 km², encompassing portions of the Upper Awash and Blue Nile Basins, with elevations ranging from 2,050 to 2,850 meters. This region's distinctive topographic variability is indicative of a complex geological history characterized by processes such as topographic uplift, graben formation, and the establishment of significant fault networks-oriented W-E, N-S, NE-SW, and NW-SE. These structural features are crucial in determining the dynamics of groundwater flow in the area. As a result, the geological configuration exhibits substantial spatial variation, which significantly impacts hydrogeological processes and groundwater management strategies.

This study is focused on developing a comprehensive hydrogeological conceptual model and a three-layer groundwater flow simulation for a portion of the Upper Awash Basin. Its objective is to optimize water extraction while minimizing environmental impact. The research adopts a multidisciplinary approach that incorporates geological, geophysical, hydrometeorological, hydrological, hydrogeological, hydrogeochemical, and isotopic methods. By integrating secondary data from prior studies with extensive field investigations, the study identifies key aquifers, recharge zones, and the interactions between groundwater and surface water.

The litho-stratigraphy of the area was established through geological mapping, analysis of borehole logs, and geophysical surveys. A thorough examination of the pumping test data identified the major aquifers and confining units present. Four primary hydrogeological units were distinguished: superficial deposits (alluvial/ash) aquifers, fractured Rift basalt aquifers, acidic rock functioning as an aquiclude, and a confined scoriaceous basalt aquifer. The region's hydrogeology is influenced by its lithological stratigraphy and tectonic activities. Groundwater generally flows southeast within both unconfined and confined aquifers.

The recharge area of the identified aquifers is illustrated by their litho-hydrostratigraphic setup, hydrogeochemical, and stable isotopic insights. As groundwater flows from NW to SE direction, its hydrochemical facies evolve from $CaHCO_3$ / $CaMgHCO_3$ to $NaHCO_3$ water types, the Ca^{2+}/Na^{+} ratio gradually decreases, RA and TDS increase in general. The results illustrate that recharge of superficial deposits and Rift basalt aquifers is from modern precipitation and nearby streams/rivers through fractures, which is characterized by mixed $CaHCO_3$ or $CaMgHCO_3$ water types of low TDS (<200 mg/l), high Ca^{2+}/Na^{+} ratio (>5), low RA (<2.0), enriched isotopic signature, and high deuterium excess (13.3). The highland and transition areas are dominantly the recharge areas for the regional confined scoriaceous basalt aquifer. These areas have high fracture density (0.96 < FD < 3.0 km/km^2), mineralized $NaHCO_3$ water type, high TDS (>468 mg/l), low Ca / Na ratio (<1), high RA (>2.0), highly depleted isotopic signals, and low deuterium excess (<11) relative to the Local Meteoric Water Line. The results also reveal groundwater flux from the adjacent eastern flank of the Blue Nile Basin.

The combined results of environmental tracers (^{222}Rn, $\delta^{2}H$, $\delta^{18}O$, and EC), BFI, and lineament density are used to determine the inferred exchange between surface water and groundwater. Thus, the primary effluent stretches are the headwater portions of both basins, including regions that fall along the surface water divide between portions of the Blue Nile and Upper Awash basins (^{222}Rn values, 100 to 400 Bq/m^3, very high mean annual Baseflow index, BFI > 0.5, high lineament density, 0.9 < LD <3.0). The southern and southeastern (outlet of PUAB) periphery has relatively very high ^{222}Rn values. 400 to 1467 Bq/m^3, and moderate lineament density. 0.35 < BFI < 0.5 is recognized as the regional groundwater outlet zone. The river and streams from the central plain portion of the Upper Awash Basin have little groundwater-surface water connection, which is evidenced by relatively low ^{222}Rn (< 100 Bq/m^3) in both seasons and a low Baseflow index (BFI < 0.35). Furthermore, evidence from analysis of measured electrical conductivity and stable isotopes ($\delta^{18}O$, $\delta^{2}H$) generally agrees with the observed ^{222}Rn value and Baseflow analysis.

For the analytical computation of the groundwater budget in the area, the groundwater that reaches the southeastern outlet zone can be divided into two categories. seepage from runoff and direct precipitation on the fractured basaltic and superficial deposits (unconfined aquifer) and subsurface inflow from the northern, northwest, and southwestern portions of the plateau and/or escarpment. The saturated zone groundwater flux (recharge) is calculated using Darcy's method, essentially for a section of the Upper Awash Basin. The classification is based on the areal extent of the central plain land portion (numerically modeled) and the areal extent of the flux or subsurface inflow zone. The recharge estimated for the seepage from runoff and direct precipitation by the WTF method for the central plain land area to be modeled after multiplying by its area coverage (3440 km^2), results in 40.5 mm/y. Furthermore, subtracting 40.5 mm/y (WTF method) and 6.9 mm/y (sub-surface inflow, Darcy method) combined as 47.4 mm/y (representing recharge for unconfined aquifer) from 106.6 mm/y (recharge estimated as a total using the Darcy approach) becomes 59.23 mm/y, for the subsurface regional groundwater inflow from the plateau and/or escarpment for confined aquifer system.

A hydrogeological model for part of the Upper Awash Basin simulates a three-layer aquifer system (unconfined, aquiclude, confined) under steady-state and predictive stress-based scenario conditions. The confined aquifer is 350 m thick beneath 150 m of unconfined and 100 m of confining layers. The 3,440 km^2 model domain uses a 500 m by 500 m grid with 113,825 active cells. The model establishes no-flow boundaries on multiple sides and at depths beyond 600 m. Groundwater enters from the northern plateau/escarpment and exits southeast. It establishes baseline conditions for 2025 and predicts the response of the aquifer system, like the drawdown, water budget, and boundary conditions, through 2055 (30 years) for sustainable use.

Calibration used trial and error to match simulated and field data, achieving high accuracy (RMS error: 9.16; mean residual: 0.81m; R^2: 0.99). Water balance analysis showed near-perfect agreement, with inflows and outflows balanced and a 0.001%

discrepancy, confirming the model's reliability. Sensitivity analysis reveals that the unconfined aquifer is most affected by changes in hydraulic conductivity and recharge. In contrast, the confined aquifer responds more to variations in hydraulic conductivity and specified flux.

Using a calibrated steady-state model, multiple stress-based scenario simulations were performed to examine the effects of drought alongside a hypothetical increase in well withdrawals and injection, based on the model's initial conditions for head and the steady-state calibration flux, with a simulation period of 11,320 days (30 years). Furthermore, the response of the groundwater system is analyzed using representative observation wells to assess the drawdown (Dd) as a function of exploitation time.

The first scenario simulation modeled drought by reducing recharge and flux by 50%. The result shows that groundwater levels dropped by 25.8 meters in the unconfined aquifer and 4.3 meters in the confined aquifer. Inflows increased through river leakage, rising by 10.5%, and head-dependent flow by 2.5%. Outflows, however, declined significantly. River leakage dropped by 19.2%, and general head boundary outflows decreased by 43%.

The second and third scenarios simulate pumping 100 and 150 boreholes of each 50 l/s over 30 years (2026–2055). In unconfined aquifers, drawdown reached 50 meters in the second scenario and 85 meters in the third. However, observation wells represent the regional confined aquifer system throughout the entire pumping duration of both scenarios, demonstrating remarkably minimal drawdown, recording less than 2 meters for the second scenario and only 4.2 meters for the third scenario. Groundwater outflow through rivers decreased by 15.4% in the second scenario and 23.3% in the third, while inflow increased by 12.8% and 16.13%, respectively. The fourth simulation introduced 50 hypothetical deep wells to inject water into the regional aquifer system. Injection rates of 216,000 m^3/day, 345,600 m^3/day, and 518,400 m^3/day led to groundwater level rises of 1.05 m, 2.38 m, and 4.45 m at observation wells. Water balance analysis showed a 2.03% increase in groundwater leakage to the river, while river-to-groundwater leakage dropped by 4.7%. As injection rates increased, groundwater outflow to the river rose by 7.31%, while river leakage into the groundwater decreased by 2.8%.

In general, the findings of this research build on previous studies, enhancing their conclusions and providing more refined insights into the utilization of groundwater. These results can directly support sustainable groundwater extraction, ensuring balanced usage without overexploitation. Additionally, the model developed in this study can serve as a framework for similar assessments in other wellfields, helping to establish effective utilization of the resource.

6.2 Recommendations

To improve the understanding of the hydrogeological framework in complex systems like the study area and to utilize the groundwater resource without environmental impact, it is essential to make full use of existing records while also collecting new data that covers both temporal and spatial aspects. Addressing the following key points will enhance future groundwater studies, accompanied by sustainable use

- The findings of this study, supported by model simulation results, advocate for sustainable extraction practices from the regional confined aquifer (layer 3) to prevent significant environmental impacts. The study concludes that this aquifer possesses the capacity to accommodate long-term water withdrawals while maintaining groundwater level stability. Furthermore, the minimal environmental impact indicates that crucial factors like recharge rates, river leakage, and the overall water balance remain largely unaffected under these conditions. These results offer essential guidance for water resource management, enabling policymakers and stakeholders to implement responsible extraction strategies that safeguard the aquifer's integrity for long-term use.
- Tracking groundwater levels and quality, alongside abstraction rates and river discharge data, is essential for sustainable groundwater management. Regular monitoring helps ensure resource stability, detect potential overuse or contamination, and support effective long-term planning.

- To improve groundwater management, a centralized national and regional database should be established. This database would store and organize groundwater data, helping track resource availability, monitor trends, and support sustainable usage. It would enable better decision-making for water management, research, and policy development.
- Continuously update numerical models with real-time field data to improve their accuracy and predictive capacity.
- Strengthen regulatory frameworks and promote sustainable groundwater use based on scientifically backed strategies.

REFERENCES

Ahimed Wolela. (2008). Sedimentation of the Triassic-Jurassic Sandstone Formation, Blue Nile Basin, Ethiopia. Journal of African Earth Sciences, 52: 30-42. http://dx.doi.org/10.1016/j.jafrearsci.2008.04.001

Ahimed Wolela. (2009). Sedimentation and Deposition Environments of the Barremian-Cenomanian Debre Libanose Sandstone, Blue Nile Basin, Ethiopia. Cretaceous Research, 30: 1133-1145. http://dx.doi.org/10.1016/j.cretres.2009.04.002

AAWSA, BCEOM, SEURECA, & Tropics. (2000). Addis Ababa Water Supply Project. Stage-IIIA Groundwater-Phase II. Modeling of Akaki well field, V1, main report, Addis Ababa Water and Sewerage Authority, Ethiopia, p 54.

Abebe, T. (1995). The Yerer-Tulu Wellel Extensional Structures Evidences from Remote Sensing, Petrologic and Geochronological Data, Central Ethiopian, Ethiopian Institute of Geological Surveys (unpublished report, Addis Ababa, Ethiopia).

Abebe, T., Mazarini, F., Innocenti, F., & Mmanneti, F. (1998). The Yerer–Tulu–Wellel Volcano-Tectonic Lineament, a Transitional Structure in Central Ethiopia and the Associated Magmatic Activity, Journal of African Earth Sciences, 1. 135-1150. https://doi.org/10.1016/S0899-5362(97)00141-3

Alemayehu, T. (2006). Groundwater Occurrence in Ethiopia. Addis Ababa University Press. Addis Ababa. pp 230.

Alemayehu, T. (2017). Determination of Groundwater - Surface Water Interaction and transboundary flows Using Remote Sensing, Hydrogeological, Hydrogeochemical and Isotopic Techniques. The case of Baro-Akobo Basin, (Unpublished PhD Thesis, Ethiopia).

Anderson, M.P., Woessner, W.W., & Hunt, R.J. (2015). Applied groundwater modeling. simulation of flow and advective transport, Academic press. https://doi.org/10.1016/C2009-0-21563-7

Arnold, J.G., & Allen, P.M. (1999). Automated methods for estimating Baseflow and groundwater recharge from streamflow records, J Am Water Resour Assoc 35.411–424. https://doi.org/10.1111/j.1752-1688.1999.tb03599.x

Aquaveo, (2019). Exploring MODFLOW Head Boundary Packages. https://aquaveo.com/blog/post/exploring-modflow-head-boundary-packages

Assefa, G. (1991). Lithostratigraphy and Environment of Deposition of the Late Jurassic-Early Cretaceous Sequences of the Central Part of Northern Plateau, Ethiopia. N.Jb. Geol, 182. 255-284. https://doi.org/10.1127/njgpa/182/1991/255

Ayenew, T., Kebede, S., & Alemyahu, T. (2007). Environmental isotopes and hydrochemical study applied to surface water and groundwater interactions in the Awash River basin, Hydrol. Process 22, 1548–1563. https://doi.org/10.1002/hyp.6716

Ayenew, T., Demlie, M., & Wohnlich, S. (2008). Hydrogeological framework and occurrence of groundwater in the Ethiopian aquifers, Journal of African Earth Sciences, 52(3), 97-113. https://dx.doi.org/10.1016/j.jafrearsci.2008.06.006

Ayenew, T., Demlie, M., & Wohnlich, S. (2008). Application of numerical modeling for groundwater flow system analysis in the Akaki catchment, Central Ethiopia. Math Geosci 40. 887–906. https://doi.org/10.1007/s11004-008-9144-x

Ayenew et al., (2019). Comparison of Different Baseflow Separation Methods and Drought Vulnerability in a Rift Valley area, Journal of Spatial Hydrology, V.15, n.2, p.1.https://scholarsarchive.byu.edu/josh/vdol15/iss2/2

Azagegn, T. (2008). Hydrochemical Characterization of Aquifer Systems in Upper Awash and Adjacent Blue Nile Plateau using Geochemical Modeling and Isotope Hydrology. Unpublished M.Sc. thesis, Addis Ababa University, Addis Ababa, Ethiopia.

Azagegn, T., Asrat, A., Ayenew, T., & Kebede, S. (2014). Litho-Structural Control on Inter-basin Groundwater Transfer in Central Ethiopia, Journal of African Earth Sciences, 101, 383-395. https://doi.org/10.1016/j.jafrearsci.2014.10.008

Azagegn, T. (2015). Groundwater Dynamics between the Upper Awash and the Left Bank Catchments of the Blue Nile Aquifer Systems. PhD Thesis.

Banik, B. K. (2023). Boundary conditions in groundwater modeling. SlideShare. https://www.slideshare.net/slideshow/boundary-conditions-in-groundwater-modeling/247760774

Banks, D., Røyset, O., Strand, T., & Skarphagen, H. (1995). Radioelement (U, Th, Rn) concentrations in Norwegian bedrock groundwaters, Environ Geol 25.165–180. https://doi.org/10.1007/BF00768546

Barlow, P.M., Cunningham, W.L., Zhai, T., & Gray, M. (2014). US Geological Survey groundwater toolbox, a graphical and mapping interface for analysis of hydrologic data (version 1.0). user guide for estimation of baseflow, runoff, and groundwater recharge from streamflow data. US Geol. Surv Techniques and Methods, book 3, chapter B10. US Geological Survey, Reston, VA. https://doi.org/10.3133/tm3B10

Barnett, B., Townley, L. R., Post, V., Evans, R. E., Hunt, R. J., Peeters, L., ... & Richardson, S. (2012). Australian groundwater modelling guidelines. National Water Commission.

BCEOM, (1997). Blue Nile River Integrated Development Master Plan Project. Ministry of Water Resources, Addis Ababa, Ethiopia, v. II, part 2 Hydrogeology, unpublished report.

BCEOM, (2000). Blue Nile River Integrated Development Master Plan Project. Ministry of Water Resources, Addis Ababa, Ethiopia, v. III, part 2 Hydrology, (Unpublished report).

Bear, J. (1972). *Dynamics of fluids in porous media*. Dover Publications.

Bear, J. (1979). “Hydraulics of groundwater” (New York. Mc-Graw Hill).

Berehanu, B., Azagegn, T., Ayenew, T., & Masetti, M. (2017). Inter-Basin Groundwater Transfer and Multiple Approach Recharge Estimation of the Upper Awash Aquifer System, Journal of Geoscience and Environment Protection, 5, 76-98. https://doi.org/10.4236/gep.2017.53007

Berehanu, B., Kebede, S., Masetti, M., & Ayenew, T. (2018). WEAP-MODFLOW Dynamic Modeling Approach to Evaluate Surface Water and Groundwater Supply Sources of Addis Ababa City, Italian Journal of Groundwater (2018)-AS25-334.15–24. https://doi.org/10.7343/as-2018-334

Beven, K.J. (2001). Rainfall-runoff modeling. John Wiley & Sons ltd., England, 351p.

Bretzler, A., Osenbrück, K., Gloaguen, R., Ruprecht, J.S., Kebede, S., & Stadler, S. (2011). Groundwater Origin and Flow Dynamics in Active Rift Systems a Three-Isotope Approach in the Main Ethiopian Rift, Journal of Hydrology, 402, 274-289. https://doi.org/10.1016/j.jhydrol.2011.03.022

Brindha, K., Neena Vaman, K.V., Srinivasan, K., Sathis Babu., M., & Elango, L. (2013). Identification of surface water-groundwater interactions by hydrogeochemical indicators and assessing its suitability for drinking and irrigational purposes in Chennai, Southern India. https://doi.org/10.1007/s13201-013-0138-6.

Böhlke, J. K., & Denver, J. M. (2022). Groundwater recharge in a changing climate. Methodological advances and case studies, Hydrological Processes*, 36(12), 2701-2719.

Brodie, R. S., & Hosteler, S. (2005). 'A review of techniques for analyzing Baseflow from stream hydrographs' Where Waters Meet, Auckland, New Zealand, New Zealand Hydrological Society. https://api.semanticscholar.org/CorpusID:16890828

Cartwright, I., Hofmann, H., Sirianos, M.A., Weaver, T.R., & Simmons, C. (2011). Geochemical and ^{222}Rn constraints on Baseflow to the Murray River, Australia, and timescales for the decay of low-salinity groundwater lenses. Journal of Hydrology, *405*(3-4), 333-334. https://doi.org/10.1016/j.jhydrol.2011.05.030

Cartwright, I., Hofmann, H., GilfedderB, Smyth, B. (2014). Understanding Para fluvial exchange and degassing to better quantify groundwater inflows using ^{222}Rn. King River, Southeast Australia. Chem Geol 380.48-60. https://doi.org/10.1016/j.chemgeo.2014.04.009

Charles, J.T., & William, M.A. (2001). Groundwater level monitoring and the importance of long-term water level data. U.S. Geological Survey Circular 121, Denver, Colorado.

Chebotarev, I. (1955). Metamorphism of natural water in the crust of weathering. Geochemical et Cosmochimica Acta 8, 22–48, 137–170, 198–212. https.//doi.org/10.1016/0016-7037(55)90015-6.

Chen, WP., & Lee, CH. (2005). Estimation groundwater recharges from stream flow records. Env Geol 44(3), 257-265. https://doi.org/10.1007/s00254-002-0753-2

Cherinet, T. (1997). Hydrogeology of Ethiopia. Addis Ababa, Ethiopia, Ethiopian Institute of Geological Surveys, Addis Ababa, Ethiopia, unpublished Report.

Clark, I., & Fritz, P. (1997). Environmental Isotopes in Hydrogeology, first ed. Lewis Publishers, New York, p. 341pp. https://doi.org/10.1201/9781482242911

Combalicer, E.A., S.H. Lee, S. Kahn, D.Y. Kim, and S. I.m. (2008). Comparing groundwater recharge and Baseflowin the Bukmoongol small-forested Basin, Korea. Journal of Earth System Science, volume 117, number 5, pages 553-366. https://doi.org/10.1007/S12040-008-0052-8

Conant, B.C. Jr., C.E. Tobin son, M.J. Hinton, and H.A.J. Russell (2019). A framework for conceptualizing groundwater-surface water interactions and identifying potential impacts on water quality, water quantity, and ecosystems. Journal of Hydrology, volume 574, pages 609-627. https://doi.org/10.1016/j.jhydrol.2019.04.050

Cook, P.G. (2003). Determining natural groundwater influx to a tropical river using radon, chlorofluorocarbons and ionic environmental tracers. https://doi.org/10.1016/S0022-1694(03)00087-8

Cooper, H.H., & Jacob, C.E. (1946). A generalized graphical method for evaluating formation constants and summarizing well field history. Am. Geophys. Union Trans., vol. 27, pp. 526- 534. https://doi.org/10.1029/TR027i004p00526

Craig, E., Divine, J., McDonell (2005). The future of applied tracers in hydrogeology. Hydrogeology Journal, 13. 255-258. https://doi.org/10.1007/s10040-004-0416-3

Cuthbert, M.O., Taylor, R.G., Favreau, G., Todd, M.C., Shamsudduha, M., Villholth, K. G., MacDonald, A.M., Scanlon,B.R., Kotchoni, D.O.V., Vouillamoz, J.M., Lawson, F. M. A., Adjomayi, P.A., Kashaigili, J., Seddon, D., Sorensen, J.P.R., Ebrahim, G. Y., Owor, M., Nyenje, P.M., Nazoumou, Y., Goni, I., Ousmane, B.I., Sibanda, T., Ascott, M. J., Macdonald, D. M. J., Agyekum, W., Koussoubé, Y., Wanke, H., Kim, H., Wada, Y., Lo, M.-H., Oki, T., & Kukuric, N. (2019a). Observed controls on resilience of groundwater to climate variability in sub-Saharan Africa. Nature, Vol. 572, pp. 230–234. https://doi.org/10.1038/s41586-019-1441-7

Daniel, N. (2016). Temporal changes in Groundwater Recharge in the Upper Awash Basin with particular emphasis to Becho and Koka areas, Central Ethiopia. Unpublished MSc Thesis, Addis Ababa University, Addis Ababa, Ethiopia.

Davis, S.N., De Wiest, R.J.M. (1966). Hydrogeology, Vol. 463. Wiley, New York.

Delin, G., et al., (2007). Comparison of local- to regional-scale estimates of ground-water recharge in Minnesota, USA. Journal of Hydrology, 334 (1–2), 231–249. https://doi.org/10.1016/j.jhydrol.2006.10.010

Demlie, M., Wohnlich, S., & Ayenew, T. (2008). Major Ion Hydrochemistry and Environmental Isotope Signatures as a tool in Assessing Groundwater Occurrence and Its Dynamics in a Fractured Volcanic Aquifer System Located within a Heavily Urbanized Catchment, Central Ethiopia. Journal of Hydrology, 353, 175-188. https://doi.org/10.1016/j.jhydrol.2008.02.009.

De Vries, J. J., & Simmers, I. (2002). Groundwater recharge. an overview of processes and challenges, Hydrogeol. J.,10, 5–17, https://doi.org/10.1007/s10040-001-0171-7

Dieter, C. A., Maupin, M.A., Caldwell, R.R., Harris, M.A., Ivahnenko, T.I., Lovelace, J. K., Barber, N.L. & Linsey, K.S. (2018). Estimated Use of Water in the United States in 2015. U.S. Geological Survey Circular 1441. Reston, Va., U.S. Geological Survey (USGS). https://doi.org/10.3133/cir1441

Domenico, P. A., & Schwartz, F. W. (1998). *Physical and chemical hydrogeology* (2nd ed.). Wiley.

Driscoll, F.G. (1986). Groundwater and wells (2nd ed.). Johnson Division, U.S. Filter.

Duffield, G. M. (n.d.). Pumping tests in bounded aquifers. *AQTESOLV*. http://www.aqtesolv.com/pumping-tests/pumping-tests-in-bounded-aquifers.ht

Durrige Company Inc. (2020). https.//durridge.com/products/big-bottle-system.

ECDSWCo-WEDSWS. (2016). Feasibility study of groundwater source and identification of potential well fields for future abstractions within 100 km radius of Addis Ababa project-unpublished technical report, Ethiopia.

Edmunds, WM., Ma, JZ., Aeschbach-Hertig, W., Kipfer, R., & Darbyshire, DPF. (2006). Groundwater recharge history and hydrogeochemical evolution in the Minqin

Basin, North West China. Appl Geochem 21(12). 2148–2170. https://doi.org/10.1016/j.apgeochem.2006.07.016.

Ellins, K.K., Roman-Mas, A., & Lee, R. (1990). Using ^{222}Rn to examine groundwater/surface discharge interactions in the Rio Grande de Manati, Puerto Rico. J Hydrol 115.319–341. https://doi.org/10.1016/0022-1694(90)90212-G

El-Rawy, M., De Smedt, F., & Zijl, W. (2018). Zone-integrated double-constraint methodology for calibration of hydraulic conductivities in grid cell clusters of groundwater flow models. Transport in Porous Media, 122, 633–645. https://link.springer.com/article/10.1007/s11242-018-1018-1.

ESRI Inc. (2006). GIS and mapping software, Technical paper, USA.

European Commission. (2008). Groundwater Protection in Europe. The New Groundwater Directive. Consolidating the EU Regulatory Framework. Luxembourg, Office for Official Publications of the European Communities. https.//op.europa.eu/en/publication-detail/-/publication/4f3c68f2- 464d-4502-9086-6fcd1be8ab01. https://doi.org/10.2779/84304

EVDSA. (1989). Awash River Basin Master Plan Study: Technical report, Ethiopia.

FAO. (1984). Soil and Land use/land cover Map of Africa. Food and Agriculture Organization of the United Nations.

Fetter, C.W. (1994). Applied hydrogeology: Prentice-Hall, Upper Saddle River.

Fetter, G.W. (2001). Applied Hydrogeology: University of Wisconsin Oshkesh, USA. pp 598.

Fetter, C.W. (2018). Applied hydrogeology: Waveland, Long Grove IL Findlay S-Importance of surface-subsurface exchange in stream ecosystems. the hyporheic zone. Limnol Oceanogr 40.159-164.

Foster, S., Tuinhof, A., & Van Steenburgen, F. (2012). Managed groundwater development for water-supply security in Sub-Saharan Africa. Investment priorities. Water SA, Vol. 38, No. 3, pp. 359–366. https://doi.org/10.4314/wsa.v38i3.1

Franke, O.L., & Reilly, T.E. (1987). The effects of boundary conditions on the steady state response of three hypothetical ground-water systems - results and implications of numerical experiments, U.S. Geological Survey Water-Supply Paper 2315, 19 pp. https://doi.org/10.3133/wsp2315

Freeze, R.A., & Cherry, J.A. (1979). Groundwater: Prentice-Hall Inc., New Jersssy. pp 604.

Furi, W. (2011). Hydrogeological System Analysis of the Middle Awash Basin: Ethiopia. Unpublished PhD Thesis. University of Poitiers. Poitiers.

Giordano, M. (2009). Global groundwater? Issues and solutions. Annual Review of Environment and Resources, Vol. 34, No. 1, pp. 153–178. https://doi.org/10.1146/annurev.environ.030308.100251.

Gani, N. DS., Abdusalam, M.G., (2006). Remote Sensing Analysis of the Gorge of the Blue Nile, Ethiopia, with Emphasis on Dejen-Gohatsion Region. Journal of African Earth Sciences, 44: 135-150. http://dx.doi.org/10.1016/j.jafrearsci.2005.10.007

Gani, N., Abdelsalam, S., & Gani, D.S. (2008). Stratigraphy and Structural Evolution of the Blue Nile North Western Ethiopia Plateau, Geological Journal, 44. 30-56. https://doi.org/10.1002/gj.1127.

Gaye, C.B. & Tindimugaya, C. (2018). Review, Challenges and opportunities for sustainable groundwater management in Africa, Hydrogeol. J., 27, 1099–1110, http://dx.doi.org/10.1007/s10040-018-1892-1

Geosoft Inc. (2012b). Oasis Montaj v7.2 Software (Standard Edition): Integrated Platform Software for Earth Exploration. Geosoft Inc., Toronto.

Gerhart, J.M. (1986). Ground-water Recharge and its Effects on Nitrate Concentration beneath a Manured Field Site in Pennsylvania, vol. 24. No. 4. 483-489.

Gossel, W., Neukum, C., & Hötzl, H. (Eds.). (2007). *Groundwater modelling in arid and semi-arid areas*. Cambridge University Press. https://www.cambridge.org/core/books/groundwater-modelling-in-arid-and-semiarid-areas/2B997E3C0E5A9670973D3C25F0A7FF7C

Grey, D., & sadoff, C.W. (2007). Sink or swim? Water security for growth and development. Water Policy, Vol. 9, No. 6, pp. 545–571. http://dx.doi.org/10.2166/wp.2007.021

Groundwater Project. (2023). The influence of boundary conditions. https://books.gw-project.org/hydrogeologic-properties-of-earth-materials-and-principles-of-groundwater-flow/chapter/the-influence-of-boundary-conditions

HALCROW-EVDSA. (1989). Master Plan for the Development of Surface Water Resources in the Awash Basin: Final Report Vol.2, Main Report.

Hamada, H., & Komae, T. (1994). Application of ^{222}Rn to the analysis of the exchange between river water and groundwater, Radioisotopes (Tokyo) 43.770-775. https://doi.org/10.3769/radioisotopes.43.12_770

Harbaugh, A.W., & McDonald, M.G. (1996). User's documentation for MODFLOW-96: an update to the U.S. Geological Survey modular finite-difference ground-water flow model. U.S. Geological Survey Open-File Report 96–485 56 p.

Hatch, C.E., Fisher, A.T., Revenaugh, J.S., Constantz, J., & Ruehl, C. (2006). Quantifying surface water-groundwater interactions using time series analysis of streambed thermal records. method development. Water Resour Res 42, https://doi.org/10.1029/2005WR004787.

Heath, R.C. (1983). Basic Groundwater hydrology, U.S. Geological survey Water Supply Paper 2220, 86p, https://doi.org/10.3133/wsp2220

Healy, R.W., & Cook, P.G. (2002). Using groundwater levels to estimate recharge. Hydrogeology Journal 10, 91–109 (2002),https://doi.org/10.1007/s10040-001-0178-0.

Healy, R.W., & Sophocleous, M. (2004). Groundwater Recharge and Discharge: A Review of the Methods. Ground Water. 42(3), 386-397.

Healy, R.W. (2010). Estimating groundwater recharge. Cambridge University Press, Cambridge, UK, https://doi.org/10.1017/CBO9780511780745

Hem, J. D. (1985). Study and Interpretation of the Chemical Characteristics of Natural Water (3rd edition), U.S Geological Survey Water Supply Paper 2254. 1- 263, https://doi.org/10.3133/wsp2254

Hill, M. C., & Tiedeman, C. R. (2007). Effective groundwater model calibration: With analysis of data, sensitivities, predictions, and uncertainty. Wiley.

IAEA. (2000). Environmental isotopes in the hydrological cycle: principles and applications, v. II: Atmospheric water.

IGRAC. (2020). National Groundwater Monitoring Programmes. A Global Overview of Quantitative Groundwater Monitoring Networks. Delft, The Netherlands, IGRAC. www.un-igrac.org/stories/national-groundwater-monitoring-programmes.

Jr, W.V., & Lewis, G.L. (2003). Introduction to Hydrology: Pearson Education inc., pp 589.

Kazmin, V. (1979). Stratigraphy and Correlation of Volcanic Rocks in Ethiopia: Note No. 106, EGS, Addis Ababa, Ethiopia.

Kebede, S., Travi, Y., Alemayehu, T., & Ayenew, T. (2005). Groundwater Recharge, Circulation and Geochemical Evolution in the Source Region of the Blue Nile River, Ethiopia. Applied Geochemistry, 20, 1658-1676, https://doi.org/10.1016/j.apgeochem.2005.04.016

Kebede, S., Travi, Y., Asrat, A., Alemayehu, T., Ayenew, T., & Tessema, Z. (2007). Groundwater origin and flow along selected transects in Ethiopian Rift volcanic aquifers. Hydrogeology Journal, 10.1007-1040, https://doi.org/10.1007/s10040-007-0210-0

Kebede, S., & Travi, Y. (2012). Origin of the $\delta^{18}O$ and $\delta^{2}H$ composition of meteoric waters in Ethiopia, Quaternary International, 257. 4-12, https://doi.org/10.1016/j.quaint.2011.09.032

Kebede, S. (2013). Groundwater in Ethiopia: Features, vital numbers and opportunities, 297pp, Springer, ISBN 978-3-642-30390-6, Berlin.

Kebede, S., Abdalla, O., & Sefelnasr, A. *et al.* (2016). Interaction of surface water and groundwater in the Nile River basin: isotopic and piezometric evidence. *Hydrogeol J* **25**, 707–726 (2017), https://doi.org/10.1007/s10040-016-1503-y

Kebede, S., & Zewdu, S. (2019). Use of ^{222}Rn and $\delta^{18}O$-$\delta^{2}H$ isotopes in Detecting the Origin of Water and in Quantifying Groundwater Inflow Rates in an Alarmingly Growing Lake, Ethiopia. Water, 11, 2591, https://doi.org/10.3390/w11122591.

Kebede, S., Charles, K., Samuel Godfrey, S., MacDonald, A., & Taylor, R.G. (2021). Regional-scale interactions between groundwater and surface water under changing aridity, evidence from the River Awash Basin, Ethiopia, Hydrological Sciences Journal, 66.3, 450-463, https://doi.org/10.1080/02626667.2021.1874613.

Kovalevsky, V., Kruzman, G., & Rashton, K. (2004). International Guide for Hydrogeological investigations, UNESCO, France, pp 430, https://coilink.org/20.500.12592/vmcvg5z

Kruseman, G.P., & De Ridder, N.A. (1990). Analysis and evaluation of pumping test data: Second Edition, pub Ser. No 47, 377p.

Kruseman, G. P., & de Ridder, N. A. (1994). *Analysis and evaluation of pumping test data* (2nd ed.). International Institute for Land Reclamation and Improvement (ILRI), Publication 47.

Kulma, R., & Zdechlik, R. (2009). Groundwater modelling. Institutional Educational and Scientific Publishing AGH, Kraków, (in Polish).

Kunianisky, E.L. (1989). Geohydrology and Simulation of groundwater flow in the "400-foot" "600-foot", and adjacent aquifers, Baton Rouge area, Louisiana. Louisiana Department of transportation and Development technical report 49.

Lerner, D.N., Issar, A.S., & Simmers, I. (1990). Groundwater Recharge. A Guide to Understanding and Estimating Natural Recharge, International Contributions to Hydrogeology, Verlag Heinz Heise, P.O.B. 610407, D-3000 Hannover 61, Germany, 1990, https://doi.org/10.2134/jeq1992.00472425002100030036x

Lyne, V., & Hollick, M. (1979). Stochastic time variable rainfall-runoff modeling. Hydrology and Water Resources Symposium Berth, 1979, Proceedings, National Committee on Hydrology and Water Resources of the Institution of Engineers, Australia, pp. 89–92, https://www.researchgate.net/publication/381094299_Automated_Baseflow_Separation_for_Changing_Catchments

Lubczynski M.W., & Gurwin, J. (2005). Integration of various data sources for stress-based scenario groundwater modeling with spatio-temporally variable fluxes, Sardon study case, Spain. Journal of Hydrology, 306 (1–4), 71–96, https://doi.org/10.1016/j.jhydrol.2004.08.038

Mandle, R.J. (2002). Groundwater modeling guidance: groundwater modeling program. Michigan Department of Environmental Quality. 54pp.

Mazor, E. (1997). Chemical and isotopic groundwater hydrology: The applied approach. NY, 413 pp.

MacAllister, D. J., MacDonald, A. M., Kebede, S., Godfrey, S., & Calow, R. (2020). Comparative performance of rural water supplies during drought. Nature Communications, Vol. 11, Article 1099, https://doi.org/10.1038/s41467-020-14839-3

MacDonald, M.G., & Harbaugh, A.W. (1988). A modular three-dimensional finite-difference ground-water flow model, USGS TWRI Chapter 6-A1, 586 pp https://doi.org/10.3133/twri06A1

MacDonald, A.M., & Calow, R.C. (2009). Developing groundwater for secure rural water supplies in Africa. Desalination, Vol. 248, No. 1–3, pp. 546–556. https://doi.org/10.1016/j.desal.2008.05.100

MacDonald, A.M., Bonsor, H.C., Dochartaigh, B.É.Ó., & Taylor, R.G., (2012). Quantitative maps of groundwater resources in Africa. Environmental Research Letters, Vol. 7, No. 2, https://doi.org/10.1088/1748-9326/7/2/024009

MacDonald, A. M., Bell, R.A., Kebede, S., Azagegn, T., Yehualaeshet, T., Pichon, F., Young, M., McKenzie, A. A., Lapworth, D. J., Black, E., & Calow, R. C. (2019). Groundwater and resilience to drought in the Ethiopian highlands. Environmental Research Letters, Vol. 14, No. 9, Article 095003, https://doi.org/10.1088/1748-9326/ab282f

MacDonald, A.M., Lark, R.M., Taylor, R.G., Abiye, T., Fallas, H. C., Favreau, G., Goni, I. B., Kebede, S., Scanlon, B., Sorensen, J. P. R., Tijani, M., Upton, K. A., & West, C. (2021). Mapping groundwater recharge in Africa from ground observations and implications for water security. Environmental Research Letters, Vol. 16, No. 3, https://doi.org/10.1088/1748-9326/abd661

Meinzer, O.E. (1923). The Occurrence of Groundwater in the United States, with a Discussion of Principles. U.S. Geological Survey Water Supply Paper 489, https://doi.org/10.3133/wsp489

Meinzer, O.E., & Stearns, N.D. (1929). A Study of Ground Water in the Pomperaug, Connecticut. With Special Reference to Intake and Discharge, USGS, Water Supply Paper, 597-B. 73-146, https://doi.org/10.3133/wsp597B

Melaku, B. (1982). Hydrogeology of Upper Awash basin up stream of Koka dam, Ministry of Mines and Energy, Ethiopian Institute of Geological Survey (EIGS), Note No. 171, Ethiopia.

Melaku, T., Chernet, T., & Haro, W. (1996). Geological Map of Ethiopia: Ministry of Mines and Energy, EIGS, Ethiopia.

Meyboom, P. (1961). Estimating groundwater recharge from stream hydrographs. J Geophys Res 66(4).1203-1214, https://doi.org/10.1029/JZ066i004p01203

Morris, J.T., & Bartels, E. (2023). Evaluating the impact of land use on groundwater recharge using Darcy's law, Journal of Hydrology*, 604, 127166.

MS Consultancy. (2024). Adama well field completed production wells pumping test analysis for Adama town water supply project (Unpublished technical report), Ethiopia.

Müller-Schmied, H., Cáceres, D., Eisner, S., Flörke, M., Herbert, C., Niemann, C., Peiris, T.A., Popat, E., Portmann, F.T., Reinecke, R., Schumacher, M., Shadkam, S., Telteu, C.E., Trautmann, T., & Döll, P. (2021). The global water resources and use model WaterGAP v2.3D, model description and evaluation, Geosci. Model Dev., 14, 037–1079, https.//doi.org/10.5194/gmd-14-1037-2021

Nathan, R.J., & McMahon, A.T. (1990). Evaluation of automated techniques for Baseflow and recession analysis, Water Resour. Res. 26 (7), 1465-1473. https://doi.org/10.1029/WR026i007p01465

Neuman, S. P. (2005). Trends, prospects and challenges in quantifying flow and transport through fractured rocks. *Hydrogeology Journal*, 13(1), 124–147. https://doi.org/10.1007/s10040-004-0397-2

Nimmo, J.R., Healy, R.W., & Stonestrom, D.A. (2005). Aquifer recharge, In. Anderson MG, Bear J (eds) Encyclopedia of hydrological science, vol 4. Wiley, Chichester, UK, pp 2229–2246. https://doi.org/10.1002/0470848944.hsa161a

Petermann, E., Gibson, J.J., Knöller, K., Pannier, T., Weiß, H., & Schubert, M. (2018). Determination of groundwater discharge rates and water residence time of groundwater-fed lakes by stable isotopes of water (^{18}O, ^{2}H) and radon (^{222}Rn) mass balances, Hydrol Process 32. 805–816. https://doi.org/10.1002/hyp.11456

Pik, R., Catherine, D., Yirgu G., Corine, H., & Ayalew, D. (1997). The northwestern Ethiopian Plateau Flood Basalts, Classification and Spatial Distribution of Magma Types, Journal of Volcanology and Geothermal Research, 81. 91-111. https://doi.org/10.1016/S0377-0273(97)00073-5

Piper, A.M. (1944). A graphic procedure in the geochemical interpretation of water analysis, Trans. Am. Geophysical Union 25, 914-923. https://doi.org/10.1029/TR025i006p00914.

Rango, T., Petrini, R., Stenni, B., Bianchini, G., Slejko, F., Beccaluva, Luigi., & Ayenew, T. (2010). The dynamics of central Main Ethiopian Rift waters, Evidence from δD, $\delta^{18}O$ and $^{87}Sr/^{86}Sr$ ratios, Applied Geochemistry, 25.1860–1871. https://doi.org/10.1016/j.apgeochem.2010.10.001

Rapti, D. (2025). Hydrogeology of a Volcano-Sedimentary Multi-Aquifer System: The Skydra, Northern Greece, Case Study. Water, 17(5), 755. MDPI Article.

Rasmussen, W.C., & Andreasen, G.E. (1959). Hydrologic budget of the Beaverdam Creek Basin, U.S. Geol. Surv, 106, Water Suppl Paper 1472. https://doi.org/10.3133/wsp1472

Riser, D.W., Gruber, W.J., & Folmer, G.J. (2005). Comparison of methods for estimating groundwater recharge and Baseflow at a small watershed underlain by fractured bed rock in the eastern United States, U.S geological survey scientific investigation, Report 2005-5038, 31.

Rosi, M., & Gattinoni, P. (2013). Groundwater modeling of fractured aquifers in mines: A case study from Tuscany, Italy. *Rock Mechanics and Rock Engineering*, *46*(6), 1351–1364. https://link.springer.com/article/10.1007/s00603-013-0444-1

Rotzoll, K., El-Kadi, A. I., & Gingerich, S. B., (2007). Estimating hydraulic properties of volcanic aquifers using constant-rate and variable-rate aquifer tests. Journal of the American Water Resources Association. USGS Publication.

Scanlon, B. R., Healy, R. W., & Cook, P. G. (2002). Choosing appropriate techniques for quantifying groundwater recharge, Hydrogeology Journal, Vol. 10, pp. 18–39. http://dx.doi.org/10.1007/s10040-001-0176-2.

Scanlon. B.R., Keese, K.E., & Flint, A.L, et al., (2006). Global synthesis of groundwater recharge in semiarid and arid regions, Hydrol Process 20.3335–3370. https://doi.org/10.1002/hyp.6335

Schmidt, A., et al., (2008). Continuous and discrete on-site detection of Radon-222 in ground- and surface waters by means of an extraction module. Applied Radiation and Isotopes, 66 (12), 1939-1944. https://doi.org/10.1016/j.apradiso.2008.05.005

Shaw, E. M. (1994). Hydrology in practice: Taylor & Francis e-Library. pp 613.

Simmers, I. (1988). Estimation of natural groundwater recharge: Springer Science & Business Media.

Singal, B.B.S, & Gupta, R.P. (1999). Applied Hydrogeology of Fractured Rocks: Springer. London. pp 429.

Singh, K., Hundal, H.S., & Singh, D. (2011). Geochemistry and assessment of hydrogeochemical processes in groundwater in the southern part of Bathinda district of Punjab, northwest India. https://doi.org/10.1007/s12665-011-0989-9 .

Singh, K.P., & Kumar, P. (2015). Assessing groundwater recharge using dynamic modeling and the Darcy method, Hydrological Sciences Journal, 65(9), 1566-1582. http://dx.doi.org/10.14760/SNAP-2015-007-EN

Sloto, R.A., & Crouse, M.Y. (1996). HYSEP. a computer program for streamflow hydrograph separation and analysis. US Geol Surv Water Resour Invest Rep 96-4040. https://doi.org/10.3133/wri964040

Sophocleous, M. (2002). Interactions between groundwater and surface water. the state of the science. Hydrogeol J 10.52-67. https://doi.org/10.1007/s10040-001-0170-8.

Stat Soft Inc. (2008). STATISTICA data analysis software version 8.0, 2300 East 14th Street, Tulsa, OK 74104.

Stewardson, M., & Marsh, N. (2003). Using the river analysis package (RAP) for environmental flow studies. 28th International Hydrology and Water Resources Symposium, 2.

Stricker, V. (1983). Baseflow of streams in the outcrop area of Southeastern sand aquifer: South Carolina, Georgia, Albania and Mississippi, US Geological Survey water resources investigations report 83-4106.

Szczepaski, A. (2004). Methodology to determine operating resources of groundwater intakes. A methodological guide. POLGEOL S.A., HYDROCONSULT Sp. z o.o. Warsaw, (in Polish).

Tadesse, E., Azagegn, T., Alemayehu, T. (2023). Characterizing groundwater and surface water interaction using geological, environmental tracers (222Rn, EC, δ18O, and δ2H) and baseflow index methods for part of the Upper Awash and the adjacent Blue Nile Basin, Ethiopia. J. Afr. Earth Sci. 205 (2023), 104992 https://doi.org/10.1016/j.jafrearsci.2023.104992.

Tadesse, E., Azagegn, T., Alemayehu, T. (2024). Identifying recharge areas for the upstream portion aquifers of Awash Basin, Ethiopia. Journal of Hydrology: Regional Studies 54 (2024) 101890 https://doi.org/10.1016/j.ejrh.2024.101890.

Tadesse, M., & Alemayehu, T. (2023). Numerical groundwater modelling in Weyib watershed, Ethiopia. Cogent Engineering, 10(1), 2283297. https://www.tandfonline.com/doi/pdf/10.1080/23311916.2023.2283297

Tefera, M., Chernet, T., & Haro, W. (1996). Geological Map of Ethiopia: Ministry of Mines and Energy. EIGS, Addis Ababa, Ethiopia.

Tafesse, N. T., (2019). Characteristics and Productivity of Volcanic Rock Aquifers in the Upper Part of Blue Nile Basin, Ethiopia. Universal Journal of Geoscience. Academia.edu PDF.

Tesfaye, A. (2009). Steady State Groundwater Flow and Contaminant Transport Modeling of Akaki Well Field and Its Surrounding Catchment (Addis Ababa, Ethiopia): Unpublished MSc Thesis, Addis Ababa University, Addis Ababa.

Theis, C.V. (1935). The relation between the lowering of the piezometric surface and the rate and duration of discharge of well using groundwater storage, Am. Geophys. Union Trans., vol. 16, pp.519-524. https://doi.org/10.1029/TR016i002p00519

Thornthwaite, C.W. (1948). An approach towards a rational classification of climate. Geographical Review 38. 55–94. https://doi.org/10.2307/210739

Thornthwaite, C.W., Mather, J.R., Carter, D.B., & Drexel Institute of Technology. (1957). Instructions and tables for computing potential evapotranspiration and the water balance, Publ. Climatol. Lab. Drexel Inst. Technol 10(3).185-311.

Tirumalesh, K., Shivanna, K., Sriraman, A.K., & Tyagi A.K. (2010). Assessment of quality and geochemical processes occurring in groundwaters near central air conditioning plant site in Trombay, Maharashtra, India. Environ Monit Assess 163(1-4).171-184. https://doi.org/10.1007/s10661-009-0825-9

Tsegaye, A., Mazzarini, F., Innocenti, F., & Manetti, P. (1998). The Yerer-Tulu Wellel volcano-tectonic Lineament. a transtensional structure in central Ethiopia and the associated magmatic activity. J. Afr. Earth Sci. 26, 135–150. https://doi.org/10.1016/S0899-5362(97)00141-3

Todd, D.K. (1980). Groundwater hydrology: Wiley, New York, U.S.A.

Tóth, J. (1963). A theoretical analysis of groundwater flow in small drainage basins. J. Geophys. Res. 68, 4795-4812. https://doi.org/10.1029/JZ068i016p04795

Turc, L. (1961). Water requirements assessment of irrigation, potential evapotranspiration. Simplified and updated climatic formula. Annales Agronomiques, 12, 13-49.

UNEP. (2010). Africa Water Atlas, Division of Early Warning and Assessment (DEWA), UNEP-United Nations Environment Programme, https://wedocs.unep.org/20.500.11822/7919 .

UN/UNESCO. (2022). The United Nations World Water Development Report, Groundwater. making the invisible visible. https://en.unesco.org/wwap, https://en.unesco.org/wwap.

U.S. Geological Survey. (2005). MODFLOW-2005 guide: Specified flux boundaries. https://water.usgs.gov/ogw/modflow/MODFLOW-2005- Guide /specified flux boundaries.html

Waterloo Hydrogeologic Inc. (2002). Aquifer test pro (Pumping Test & Slug Test Analysis) Software version 3.5, Ontario, Canada.

Waterloo Hydrogeologic Inc. (2011). Visual MODFLOW Flex User's Manual. A Professional Application for 3D Groundwater Flow and Contaminant Transport Modeling, Ontario, Canada.

Wetzel, L.K., & Newell, J.A. (2006). Groundwater Budgets: Part 1- Terminology, Forms, and Use. U.S. Geological Survey Circular 1314.

WEDSWS. (2017). Feasibility study of groundwater source and identification of potential well fields for future abstractions within 100kms radius of Addis Ababa project: Geomorphology, lithology and structure of prospective sites; Unpublished report, Addis Ababa, Ethiopia.

WHO/UNICEF. (2021). Progress on Household Drinking Water, Sanitation and Hygiene, 2000–2020. Five Years into the SDGs. Geneva, WHO/UNICEF. http://data.unicef.org/resources/progress-on-household-drinking-water-sanitation-and- hygiene-2000-2020.

Woessner, W.W. (2020). Groundwater-Surface water Exchange: Groundwater Project. Principles and Field applications, Guelph, Ontario, Canada, pages 1-32.

World Bank. (2018a). Assessment of Groundwater Challenges and Opportunities in Support of Sustainable Development in Sub-Saharan Africa. Washington, DC. http://documents.worldbank.org/curated/en/420291533931251279

World Bank. (2021). *Managing groundwater for drought resilience in South Asia*. https://openknowledge.worldbank.org/server/api/core/bitstreams/eb9ff6f0-ff8c-5ba5-83Df-6d015729b19a/content

WWDSE. (2008). Adaa-Becho Groundwater Resource Evaluation for Irrigation. Unpublished Report, Addis Ababa, Ethiopia.

WWDSE. (2008-2014). Compiled Mapping, Test and production wells accomplishment reports within Ada'a and Becho plains, unpublished report, Addis Ababa, Ethiopia.

WWDSE. (2009). Evaluation of water resources of the Ada'a and Becho plains ground water basin for irrigation development project: Unpublished technical report, Addis Ababa, Ethiopia.

WWDSE. (2010). Raya valley Groundwater resources: Volume III, Groundwater modeling of Raya Valley alluvial aquifers. Unpublished technical report, Addis Ababa, Ethiopia.

Yeh, H.F., Cheng, Y.S., Lin, H.I., & Lee, C.H. (2016). Mapping groundwater recharge potential zone using a GIS approach in Hualian River, Taiwan. Sustainable Environment Research 26 (1), 33e43. http://dx.doi.org/10.1016/j.serj.2015.09.005.

Zektser, I.S., & Everett, L.G. (2004). Groundwater Resources of the World and Their Use, IHP-VI, SERIES ON GROUNDWATER NO. 6, UNESCO 2004. https://coilink.org/20.500.12592/k0p2q0t

Yitbarek, A. (2009). Hydrogeological and Hydrochemical Framework of Complex Volcanic System in the Upper Awash River Basin, Central Ethiopia. Unpublished PhD Thesis, University of Poitiers, Poitiers.

Yitbarek, A., Razack, M., Ayenew, T., Zemedagegnehu, E., & Azagegn, T. (2012). Hydrogeological and Hydrochemical Framework of Upper Awash River Basin, Ethiopia. With Special Emphasis on Inter-Basins Groundwater Transfer between Blue Nile and Awash Rivers. Journal of African Earth Sciences, 65, 46-60. https://doi.org/10.1016/j.jafrearsci.2012.01.002.

Zhang, Y., & Schwartz, F. W. (1995). Simulation of solute transport in fractured porous media. *Water Resources Research*, 31(5), 1137–1145.

Zhao, M., & Zhang, L. (2021). A framework for simulating groundwater recharge based on Darcy's law, Water Resources Research, 57(6), e2020WR028230.

APPENDICES

Appendix 1. ^{222}Rn, EC, and Temperature measurements during non-rainy season

No	ID	Measurement sites	Longitude	Latitude	Electrical Conductivity, µS/cm	Temperature, ^{0}C	Mean ^{222}Rn, Bq/m^3
1	ENrREC1	Main Awash River	404089	997852	235	23.6	354.7
2	ENrREC2	Upper Awash tributary	416186	995306	384	27.1	240.2
3	ENrREC4	Main Awash River	456505	962163	525	24.8	667
4	ENrREC5	Upper Awash tributary	433034	959184	677	23.2	465.1
5	ENrREC6	Main Awash River	417433	988934	267	22.3	53.1
6	ENrREC7	Upper Awash tributary	446133	1003882	275	18.8	91.1
7	ENrREC8	Upper Awash tributary	429166	997165	399	21.3	65.6
8	ENrREC9	Main Awash River	435097	978088	286	21	24
9	ENrREC11	Upper Awash tributary	445399	1008379	191	20.92	114
10	ENrREC12	Upper Awash tributary	445407	1005268	189	20.9	153
11	ENrREC13	Upper Awash tributary	445374	1004738	293	20.94	160
12	ENrREC15	Upper Awash tributary	446245	1002787	172	20.74	107
13	ENrREC16	Upper Awash tributary	446465	1001086	289	20.9	34.1
14	ENrREC17	Upper Awash tributary	445913	997622	285	20.86	40
15	ENrREC20	Upper Awash tributary	443118	995089	206	21.06	244
16	ENrREC24	Upper Awash tributary	445231	996952	173	20.75	17.1
17	ENrREC26	Upper Awash tributary	443517	1014536	287	20.88	269.2
18	ENrREC27	Upper Awash tributary	444339	1012018	286	20.87	385.4
19	ENrREC28	Upper Awash tributary	434517	1021884	293	20.94	40.2
20	ENrREC29	Upper Awash tributary	436105	1012425	285	20.86	51.6
21	ENrREC30	Muger tributary	458840	1028965	196	20.97	22.7
22	ENrREC31	Muger tributary	446718	1033658	255	21.51	195
23	ENrREC32	Muger tributary	457556	1023901	293	20.94	203
24	ENrREC33	Muger tributary	456055	1020515	191	20.92	133
25	ENrREC34	Muger tributary	459274	1031367	201	21.01	48.5
26	ENrREC35	Muger tributary	458411	1027297	299	20.99	77.1
27	ENrREC36	Muger tributary	447579	1026018	298	20.98	215
28	ENrREC37	Muger tributary	453806	1018451	300	21	94
29	ENrREC38	Muger tributary	470173	1039641	355	22.43	218
30	ENrREC39	Muger tributary	470918	1028879	352	20.9	196
31	ENrREC40	Muger tributary	456078	1047291	186	21.79	20.7

No	ID	Measurement sites	Longitude	Latitude	Electrical Conductivity, µS/cm	Temperature, ^{0}C	Mean ^{222}Rn, Bq/m^3
32	ENrREC41	Muger tributary	469647	1047056	369	22.56	53
33	ENrREC42	Muger tributary	421045	1040594	142	20.12	22.83
34	ENrREC43	Main Awash River	417478	988970	363	19.5	80.8
35	ENrREC44	Main Awash River	435015	977947	317	19.7	28.6
36	ENrREC45	Main Awash River	443133	965791	580	19.8	27.3
37	ENrREC48	Upper Awash tributary	453984	976412	558	20.2	528.4
38	ENrREC49	Spring	400482	999171	627	25.9	318.7
39	ENrREC50	Spring	460900	976902	358	23.9	2498
40	ENrREC51	Well	456231	962375	546	27.9	2049
41	ENrREC52	Well	433416	959506	609	21.1	660.2
42	ENrREC53	Spring	447864	1009140	228	21.26	300.5
43	ENrREC54	Spring	454700	995350	231	21.29	573.6
44	ENrREC55	Well	421795	1040108	224	33.5	1005

NB. Under ID field **ENrREc** or **ER*REc** represents. E-Author's name first word, Nr-Non-rainy season, R*-rainy season, R-^{222}Rn, EC-Electrical Conductivity)

Appendix 2. ^{222}Rn, EC, and Temperature measurements during the rainy season

No	ID	Water Source	Longitude	Latitude	Electrical Conductivity, µS/cm	Temperature, ^{0}C	Mean ^{222}Rn, Bq/m^3
1	ER*REC1	Upper Awash tributary	404089	997852	210	18.5	107
2	ER*REC2	Upper Awash tributary	416186	995306	170	17.2	61.8
3	ER*REC3	Main Awash River	456505	962163	260	21.9	467.8
4	ER*REC4	Upper Awash tributary	433034	959184	270	21.8	387.3
5	ER*REC5	Main Awash River	417433	988934	160	19.5	32.3
6	ER*REC6	Upper Awash tributary	446133	1003882	140	19.7	97.4
7	ER*REC7	Upper Awash tributary	429166	997165	158	17.5	42.9
8	ER*REC8	Main Awash River	435097	978088	110	19.1	28.6
9	ER*REC9	Main Awash River	404171	997868	180	19	96.5
10	ER*REC10	Main Awash River	417478	988970	235	20	38.0
11	ER*REC11	Main Awash River	443133	965791	170	20.4	2.7
12	ER*REC12	Upper Awash tributary	460858	974217	140	24.8	210
13	ER*REC13	Upper Awash tributary	426967	971988	120	21.7	36.1
14	ER*REC14	Upper Awash tributary	440007	1001102	160	19.2	187
15	ER*REC15	Upper Awash tributary	436106	1012816	140	21.2	82

NB. Under ID field **ENrREc** or **ER*REc** represents. E-Author's name first word, Nr-Non-rainy season, R*-rainy season, R-^{222}Rn, EC-Electrical Conductivity)

Appendix 3. Summarized lithology logs (Data source. WWDSE, 2008)

A. Representing Plateau and Escarpment

Inchini area (BHE10)

Depth (m)		Lithologic Description
From	to	
0	146	Fractured basalt

Holeta town (BHE11)

Depth (m)		Lithologic description
From	to	
0	6	Red topsoil
6	236	Slightly fractured basalt
236	300	Scoriaceous basalt

Holeta Sara Yimer Water Bottling PLC well (BHE7)

Depth (m)		Lithologic description
From	To	
0	6	Reddish brown topsoil
6	52	Tuff
52	96	Weathered and moderately fractured basalt
96	98	Paleosol
98	198	Massive basalt
198	222	Unwelded Tuff
222	406	Slightly fractured basalt
406	426	Scoriaceous basalt
426	654	Highly fractured and altered Scoriaceous basalt

Ginchi Agriculture Centre Well (BHE2)

From	To	Lithological Description
0	12	Topsoil
12	92	Boulder, Gravel, and Pyroclastic deposit
92	156	Basalt
156	246	Scoriaceous basalt

Ginchi Kegga Beverages deep well (BHE5)

Depth (m)		Lithologic description
From	To	
0	64	Topsoil, gravel, and Tuff
64	72	Weathered vesicular basalt
72	90	Fresh basalt
90	102	Weathered and moderately fractured basalt
102	130	Massive basalt
130	148	Highly weathered and fractured basalt
148	160	Massive basalt
160	194	Welded tuff
194	208	Ignimbrite
208	294	Trachyte
294	502	Scoriaceous basalt (altered)

B. Representing the Central plain portion of the Upper Awash Basin

Becho plain exploratory deep well (BHE19)

Depth (m)		Lithologic description
From	To	
0	42	Top Soil, Silty clayey gravel
42	74	Tuff
74	150	Massive basalt
150	250	Trachyte and trachybasalt
250	348	Slightly to moderately fractured Basalt
348	450	Highly fractured and altered Scoriaceous basalt

Becho plain exploratory deep well (BHE23)

Depth, m		Lithologic description
From	To	
0	26	Topsoil
26	100	Unwelded tuff
100	168	Slightly fractured basalt
168	248	Fresh to Slightly fractured trachyte
248	262	Moderately weathered and Fractured basalt
262	402	Highly fractured Scoriaceous basalt

Becho plain exploratory deep well (BHE25)

Depth (m)		Lithologic description
From	To	
0	44	Black cotton topsoil, silty clay, and loose tuff
44	150	Slightly fractured Basalt
150	246	Slightly fractured ignimbrite and Rhyolite
246	254	Scoria
254	352	Fractured Scoriaceous basalt

Becho plain exploratory deep well (BHE26)

Depth (m)		Lithologic description
From	To	
0	40	Topsoil and Silty sandy clay
40	152	Slightly fractured Basalt
152	184	Slightly fractured Rhyolite and Ignimbrite
184	186	Welded Tuff
186	192	Loose Tuff
192	196	Welded Tuff
196	244	Slightly fractured Rhyolite
244	250	Loose Tuff
250	268	Moderately fractured Rhyolite
268	436	Highly fractured Scoriaceous basalt

Becho mapping well (BHE12)

Depth, m		Lithologic description
From	to	
0	2	Black topsoil
2	24	Weathered tuff
24	154	Moderately fractured Basalt
154	164	Massive basalt
164	184	Highly weathered ignimbrite
184	212	Moderately weathered ignimbrite
212	224	Pumice
224	225	Paleosols
225	308	Scoriaceous basalt

Sebeta Meta Brewery well (BHE32)

Depth (m)		Lithologic description
From	to	
0	2	Top dark brown clay soil
2	18	River deposit of boulders, gravel, and sands
18	26	Massive volcanic rock
26	42	Fractured basalt
156	163	Massive basalt

Sebeta Meta Brewery well (BHE34)

Depth (m)		Lithologic description
From	To	
0	22	Top Unconsolidated Clay Formation
22	86	Pyroclastic ash deposit
86	118	Massive Basalt intercalated with fine ash deposit
118	130	Scoria
130	201	Fractured Scoriaceous Basalt

Appendix 4. Stable isotope data from previous works

No	Locality	UTME	UTMN	Elevation, m.a.s.l	Water Source	δ^2H, ‰	$\delta^{18}O$, ‰	d-excess, ‰	Physiography	Data Source	Sample ID from Data source
1	Derba town	463209	1038637	2398	DW	-11.33	-3.28	13.7	P	Azagegn, 2015	BHT47
2	Gimbichu town	472973	1062101	2640	DW	-20.29	-3.97	10	P		BHT56
3	Gonoyo	462806	1072054	2784	DW	-13.02	-3	9.9	P		BHT58
4	Segnogebeya	453986	1025102	2591	DW	-14.15	-4.22	18	P		BHT41
5	Shino	420012	1030815	2606	DW	-9.85	-2.99	13	P		BHT108
6	Segnogebe	455702	1027244	2585	DW	-16.3	-3.5	10.4	P	Yitbarek et al., 2012	Ay31
7	Chancho	473819	1031909	2502	DW	-21.2	-4.1	10.1	P		Ay32
8	Inchini	421722	1040053	2447	DW	-14.8	-3.6	12.7	P		Ay33
9	Bikate Shallw well	435083	1016838	2560	DW	-12.75	-3.17	11.4	P	Azagegn, 2015	BHT112
10	Moye goje	475578	1035082	2608	SW	-7.31	-2.75	13.7	P		BHT54
11	Robe Gebeya	464387	1034248	2441	SW	-7.2	-2.7	13.4	P		BHT48
12	Sululta China Leather	473064	1016698	2558	SW	-3.12	-2.41	15.3	P		BHT86
13	Werers	475154	1018844	2582	SW	-2.42	-1.64	10.1	P		BHT84
14	J.J.Kotar	472599	1012757	2590	SW	-2	-2	13.3	P	Yitbarek et al., 2012	Ay28
15	Sur	432020	1025151	2600	SW	-6.8	-2.5	12.3	P	Azagegn, 2015	BHT111
16	Ginchi China	401795	996642	2311	DW	-9.53	-3	13.4	E		BHT90
17	Holota Ros	444475	998414	2273	DW	-13.85	-3.32	11.5	E		BHT102
18	Mapping well at Melkakunture	433200	959670	2096	DW	-27.07	-5.39	14.1	E		BHT204
19	Mark flower	449572	1002149	2476	DW	-20.65	-4.24	11.7	E		BHT103
20	Tatek Mugher cement	460254	997269	2583	DW	-16.18	-3.92	13.7	E		BHT118
21	Wolenkomi	416279	995355	2139	DW	-10.42	-2.95	12.1	E		BHT94
22	Asgori well	420207	971573	2073	DW	-23	-5	15.2	E	Yitbarek et al., 2012	Ay66
23	Awash melka	456307	962581	1994	DW	-23	-5	15.2	E		Ay67
24	Asgori	427210	971573	2069	DW	-28.7	-4.9	8.7	E		Ay68
25	Dimajalewa	413274	974205	2084	DW	-26.7	-4.9	10.7	E		Ay69
26	Jawarokora	433511	959708	2094	DW	-18.1	-3.7	10.1	E		Ay70
27	Tefki	450472	981241	2067	DW	-14.3	-3.1	9.4	E		Ay71
28	Melkakunture	456318	962383	1989	DW	-24.9	-4.6	10.2	E		Ay73
29	kimoye	427491	992970	2084	DW	-29.2	-5.3	11.2	E		Ay74
30	Holeta	448440	1001427	2393	DW	-23.9	-5.04	14.6	E	Hailu, 2016	HW1
31	Holeta	446117	990929	2246	DW	-12.3	-2.35	5.6	E		HW2
32	Holeta	440379	1006281	2509	SW	-8.4	-2.9	13.7	E	Yitbarek et al., 2012	Ay34
33	Ginch BH	406143	996474	2198	SW	-1	-1.8	12.7	E	Azagegn, 2015	BHT161
34	Gurjo gerjera	409131	990434	2156	SW	-1.32	-1.95	13.6	E		BHT164
35	Kimoye	427131	996390	2137	SW	-2.71	-1.92	11.9	E		BHT101
36	Koftu shallw well	418798	988451	2078	SW	-2.13	-2.02	13.3	E		BHT100
37	Tita Maru	405640	970310	2175	SW	-7.45	-2.88	14.5	E		BHT165
38	Holeta	440379	1006281	2509	SW	-8.4	-2.9	13.7	E	Yitbarek et al., 2012	Ay34
39	Asgori area	418884	963344	2132	SW	-10	-2.85	11.7	E	Azagegn, 2015	BHT121
40	Muger	434606	1052723	1673	R	5.76	-0.19	7.2	P		RVT1
41	Muger	458600	1028944	2533	R	-9.1	-2.51	10.1	P	Hailu, 2016]	MR1
42	Muger	451485	1027273	2660	R	-1.2	-0.73	4.4	P		MR2
43	Muger	458689	1030535	2548	R	-10.6	-2.57	9	P		MR5

No	Locality	UTME	UTMN	Elevation, m.a.s.l	Water Source	δ^2H, ‰	$\delta^{18}O$, ‰	d-excess, ‰	Physiography	Data Source	Sample ID from Data source
44	Muger	457900	1027030	2563	R	-9.8	-2.69	10.7	P		MR6
45	Muger	454540	1024628	2590	R	-4.3	-1.55	7.5	P		MR7
46	Holeta	447638	1012559	2650	R	3.7	-0.01	3.8	P		HR18
47	Holeta	443517	1014536	2596	R	21.8	3.53	-5.1	P		HR19
48	Holeta	446596	1013226	2660	R	21.5	3.48	-5.1	P		HR20
49	Holeta	440295	1013053	2683	R	7	1.54	-4.8	P		HR21
50	Holeta	439310	1010218	2588	R	-3.9	-1.37	6.6	P		HR22
51	Muger	455762	1020665	2628	R	-14.9	-2.86	6.9	P		MR4
52	Muger	463275	1038355	2397	R	-9.2	-1.78	4.4	P		MR9
53	Muger	464619	1033828	2449	R	-0.8	-0.62	3.9	P		MR10
54	Muger	456078	1047291	1491	R	-4.8	-0.23	-3	P		MR11
55	Muger	462392	1041185	2373	R	0.5	-0.43	3.8	P		MR12
56	Baka	420268	1022766	2776	S	-0.31	-2.13	15.9	P		SPT26
57	Biriti	418000	1079000	2509	S	-6.69	-2.49	12.3	P		SPT25
58	Burke Gebero	459525	1066280	2603	S	-16.56	-3.19	7.8	P		SPT18
59	Daleti	454415	1063647	2569	S	-10.33	-3.11	13.4	P		SPT132
60	Eka Gogna	470338	1035426	2549	S	-9.16	-3.14	14.8	P	Azagegn, 2015	SPT16
61	Muger cement	431391	1048275	2259	S	-4.16	-2.26	13.1	P		SPT28
62	Muger	426391	1042935	2513	S	-3.7	-2.07	12.1	P		SPT135
63	Awash river at MelkaKunture	458564	960032	1892	R	-0.76	-1.12	7.8	E		RVT4
64	Awash	404143	997941	2227	R	2	-1	9.6	E	Yitbarek et al., 2012	Ay13
65	Holeta	445374	1004738	2374	R	-2.8	-1.32	7.3	E		HR4
66	Holeta	446465	1001086	2357	R	-3.1	-1.14	5.6	E		HR7
67	Holeta	445913	997622	2210	R	0.2	-0.88	6.9	E		HR8
68	Holeta	452911	1000512	2494	R	-4.8	-1.89	9.6	E		HR9
69	Holeta	454221	999759	2509	R	-11	-3.13	12.9	E		HR10
70	Holeta	443118	995089	2190	R	-4.5	-1.72	8.6	E		HR11
71	Holeta	433043	995231	2126	R	-1.9	-1.06	6.2	E	Hailu, 2016	HR12
72	Holeta	435104	989707	2071	R	4.3	-0.61	9	E		HR13
73	Holeta	434980	998207	2240	R	4.8	-1.01	12.5	E		HR14
74	Holeta	446492	995599	2235	R	-4.8	-2.2	12	E		HR15
75	Holeta	445890	987801	2146	R	-8.2	-2.47	10.6	E		HR16
76	Holeta	445231	996952	2220	R	-0.7	-1.22	8.6	E		HR17
77	Boda	399152	978471	2667	S	-9.3	-3.39	16.6	E	Azagegn, 2015	SPT57
78	Tulubolo town	412199	957215	2176	S	-10.78	-3.72	17.6	E		KSP9
79	Roge sp	457026	981375	2075	S	-23	-5	15.2	E	Yitbarek et al., 2012	Ay52
80	HS2	454700	995350	2670	S	-5.6	-2.51	13.6	E	Hailu, 2016	HS2
81	HS3	446601	987634	2167	S	-7.4	-2.08	8.5	E		HS3

N.B. DW-Deep well, SW-Shallow well, R-River, S-Spring, P-Plateau, E-Escarpment

Appendix 5. Boreholes data

No	Researcher ID	Clients Well Index	UTM East	UTM North	Elevation, m	Depth, m	Static water level, m	Dynamic water level, m	Drawdown , m	Discharge, L/s	Transmissivity, m2/day	Specific well yield, l/s/m
1	BHE1	GW#1	401157	996412		302	24.5	31.4	6.9	17	69.4	2.5
2	BHE2	GW#2	401801	996640		246	31.2	66.4	35.2	20	29.5	0.6
3	BHE3	GW#3	401587	997298		302	21.5	27.6	6.1	26.6	207	4.4
4	BHE4	GW#4	400975	997008		302	19	28.7	9.7	28	205	2.9
5	BHE5	BTPW-1	400575	997156	2284	502	8.5	72.6	64.1	88	252	1.4
6	BHE6	SPW-1	446356	1005421	2408	400	9	95	85.6	31.8	147	0.4
7	BHE7	SPW-2	446347	1002761	2388	654	53	241.3	188	20	19	0.1
8	BHE8	National Biotech	445556	1001719	2355	400	59.6	171.8	112.5	2	1	0.02
9	BHE9	Sara coffee	446296	1002676	2380	308.6	18.3	245.3	221.7	3	2.4	0.014
10	BHE10	AMW1	421795	1040108	2457	146	18.1	27.95	9.85	16	109	1.6
11	BHE11	AMW2	440274	1006055	2525	300	12.33	37.5	25.17	35.5	75.4	1.41
13	BHE12	AMW3	427126	971361	2075	308	4.2	7.86	3.66	35.5	994	9.7
14	BHE13	AMW4	456314	962592	2014	290	Artesian	2.65	2.65	35.5	1350	13.4
15	BHE14	AMW14	450359	981037	2084	280	11	30.95	41.95	19	667	0.45
16	BHE15	AMW18	433200	959670	2111	194	Artesian	16.86	16.86	19.2	150	1.13
17	BHE16	AMW20	413137	973900	2090	311	8.5	26.88	35.38	16.74	58.8	0.47
18	BHE17	AMW26	427395	992768	2109	243	4	32.35	36.35	17.47	46.1	0.48
19	BHE18	BTW1	418679	988365	2082	445	(+)1 Artesian	125.45	95	62.05	76.9	0.65
20	BHE19	BTW2	423439	988990	2077	450	(+)1 Artesian	107.22	74.3	34.05	46.9	0.46
21	BHE20	BTW3	420071	983317	2071	350	3.2	73.72	54.8	19.12	45.9	0.35
22	BHE21	BTW4	411777	989671	2119	250	25.83	31.75	4.71	56	589	11.89
23	BHE22	BTW5	411189	983944	2091	301	(+0.53) Artesian	100.25	100.78	38.58	61.9	0.35
24	BHE23	BPW-02	426873	970945	2082	402	0.3	44.74	44.44	98	312	2.21
25	BHE24	BPW-03	426362	969316	2018	420	0.6	36.66	36.06	84.3	583	2.34
26	BHE25	BPW-012	454868	963109		352	3.3	10.17	6.87	63.4	1240	9.3
27	BHE26	BPW-018	450887	981258	1841	436	12.17	34.96	22.79	58	312	2.54
28	BHE27	STTW-01	438871	977181	2053	443	12.65	58.72	46.07	41	31	0.88
29	BHE28	STTW-02	447224	978514	2055	440	13.44	99.47	86.03	20	32.1	0.23
30	BHE29	STTW-03	449082	980399	2066	440	10.67	104.38	93.68	13.12	26.4	0.14
31	BHE30	APW-013	433672	1023691		602	45.9	181.36	135.46	9	7.7	0.07
32	BHE31	Sebeta Meta Abo Community well	455282	984682	2152	135	74.1	78.06	3.96	7.5	875	1.89
33	BHE32	Meta Abo Brew well #11	455255	985646	2197	163	25.6	81.33	55.73	13.2	27.9	0.24
34	BHE33	Meta Abo Brew well #12	455342	985531	2206	185	33.95	126.92	92.97	12	6.23	0.13
35	BHE34	Meta Abo Brew well #13	455470	984876	2175	201	104.56	128	23.44	3.5	10	0.15
36	BHE35	STTW4	445565	983665	2088	550	5.4	No pumping test data				
37	BHE36	STTW5	450949	1000247		186	Artesian					
38	BHE37	STTW6	427193	976742		500	Artesian					
39	BHE38	STTW9	431873	978996		500	Artesian					

No	Researcher ID	Clients Well Index	UTM East	UTM North	Elevation, m	Depth, m	Static water level, m	Dynamic water level, m	Drawdown, m	Discharge, L/s	Transmissivity, m2/day	Specific well yield, l/s/m
40	BHE39	STTW10	422802	976337		500	Artesian					
41	BHE40	Adbh0153	447200	998889	2290	126			45.4	14		0.3
42	BHE41	AdBh0156	453522	1001474	2562	115.3	57.8		1.3	14.6	No pump test data	11.6
43	BHE42	AdBh0182	378447	991365	2189	130	32.9	83.9	51	2		0
44	BHE43	AdBh0187	404656	997733	2235	81	21.5	42.2	20.7	3.5		0.2
45	BHE44	AdBh0193	434015	1000129	2554	147	4.8	74.7	69.9	1.5		0
46	BHE45	AdBh0194	440110	1001337	2419	153	36.6	136.7	100.1	1.5		0
47	BHE46	AdBh0198	461930	970844	2201	183.2	144.4	146	1.6	2.3		1.4
48	BHE47	AdBh0217	459928	941554	2175	134	77.9	103.1	25.2	2.5	8.6	0.1
49	BHE48	AdBh0247	463635	988675	2296	83	26.8	36.1	9.2		No Pumping test data	0.4
50	BHE49	AdBh0249	455450	983014	2110	120	14.6	54	39.4	6.6		0.2
51	BHE50	AdBh0250	455426	982736	2099	150	16.3	83.2	66.8	5.4		0.1
52	BHE51	AdBh0255	444624	978143	2074	65.4	9.6	54.6	45	0.8		0.02
53	BHE52	AdBh0281	463286	1038986	2420	78	4.2	10.3	6.1	3.2		0.5
54	BHE53	AdBh0283	473871	1024156	2605	15	6	11	5	2		0.4
55	BHE54	AdBh0300	442842	977555	2074	100	14.2	66.4	52.2	3.4		0.1
56	BHE55	AdBh0314	404050	980200	2150	98.5	10	14.4	4.5	8		1.8
57	BHE56	AdBh0318	407400	972711	2140	172	19.5	33	13.6	4		0.3
58	BHE57	AdBh0328	463599	988583	2283	130	19.5	24.5	5	4		0.8
59	BHE58	AdBh0339	436160	1000453	2370	153	36.6	136.7	100.1	1.5		0.01
60	BHE59	AdBh0340	435382	1000251	2358	206	9.9	31.1	21.2	7.9		0.4
61	BHE60	AdBh0357	445180	1002459	2393	101	23.3	38.1	14.8	3.5		0.2
62	BHE61	AdBh0362	432432	1024464	2598	161	11.5	116.6	105.1	2.5		0
63	BHE62	AdBh0426	440595	1000333	2374	170	81.5	92.2	10.7	7.4		0.7
64	BHE63	AdBh0428	402350	951544	2440	60	26.7	43.1	16.4	0.2		0.01
65	BHE64	AdBh0429	393964	957477	2497	61.3	39.1	47.7	8.6	0.1		0.02
66	BHE65	AdBh0430	397276	954511	2400	61.3	17.5	54	36.6	0.6		0.02
67	BHE66	AdBh0431	397540	953574	2393	60	17.9	52.8	34.9	0.2		0
68	BHE67	AdBh0432	396861	952816	2380	36	20.5	24.7	4.2	2.2		0.5
69	BHE68	AdBh0434	400409	954207	2379	48	21.6	26.2	4.7	4		0.9
70	BHE69	AdBh0435	398901	951499	2402	60	24.4	45.5	21	1.3		0.1
71	BHE70	AdBh0437	394200	944338	2207	62	36.5	54.9	18.4	0.2		0
72	BHE71	AdBh0444	424000	952736	2169	112	5.4	50.4	45	10		0.2
73	BHE72	AdBh0527A	463600	988200	2280	64	27.5	33.6	6.1	3	50.99	0.5
74	BHE73	AdBh0723	455000	985200	2200	126	50.9	84.7	33.8	3.5	10.72	0.1
75	BHE74	AdBh0751	463700	988500	2280	130	19	24.5	5.5	4	75.4	0.7
76	BHE75	AdBh0889	455300	985250	2218	101	37.5	55.3	17.8	4.5	25.92	0.3
77	BHE76	AdBh0891	455550	983750	2138	181	46.8	71.7	24.9	4	16.64	0.2
78	BHE77	AdBh0892	444000	977700	2055	100	17.1	113.8	96.7	0.4	0.43	0
79	BHE78	AdBh0895	460850	985850	2260	106	43	45.8	2.8	6.5	240.69	2.3
80	BHE79	AdBh0896	460500	986500	2285	100	27.1	44	16.9	9.1	55.89	0.5

No	Researcher ID	Clients Well Index	UTM East	UTM North	Elevation, m	Depth, m	Static water level, m	Dynamic water level, m	Drawdown , m	Discharge, L/s	Transmissivity, m2/day	Specific well yield, l/s/m
81	BHE80	AdBh0981	460121	985966	2239	120	39.7	43.7	4	6.7	173.76	1.7
82	BHE81	AdBh1037	457030	984617	2200	140	_	107	18.5	5	28.02	0.3
83	BHE82	AdBh1059	472975	1011144	2650	114	11.7	22.4	10.7	2.2	21.32	0.2
84	BHE83	AdBh1103	462260	984901	2294	180	82.8	100	17.3	6.7	No pumping test data	0.4
85	BHE84	AdBh1152	460295	986769	2222	158	31	81	50	17		0.3
86	BHE85	AdBh1153	447549	1007893	2520	203	24.5	8	4	2	350	0.5
86	BHE86	AdBh0190	427193	994953	2145	0	2	_	_	_	No pumping test data	_
87	BHE87	AdBh0191	427164	996290	2158	37		_	_	_		_
88	BHE88	AdBh0196	460810	981473	2228	102	67.1	_	_	4		_
89	BHE89	AdBh0197	460464	974637	2101	61.1	38.14	_	_	3.5		_
90	BHE90	AdBh0199	456740	962388	2007	39	3	_	_	_		_
91	BHE91	AdBh0200	454852	962780	2009	56	2	_	_	38		_
92	BHE92	AdBh0202	455040	956408	2103	170	_	_	_	_		_
93	BHE93	AdBh0204	451590	954524	2118	156	_	_	_	_		_
94	BHE94	AdBh0207	444924	954222	2260	184	_	_	_	4		_
95	BHE95	AdBh0208	448328	957872	2142	139	85.4	_	_	3.25		_
96	BHE96	AdBh0212	444245	956023	2220	158	96.38	_	_	2		_
97	BHE97	Adbh0213	451681	958830	2123	120.75	_	_	_	_		_
98	BHE98	AdBh0249	455450	983014	2110	120	14.56	53.95	39.39	6.6		0.17
99	BHE99	AdBh0253	453850	973096	2065	59	56.3					_
100	BHE100	AdBh0254	451420	971692	2083	60	57.92					_
101	BHE101	AdBh0255	444624	978143	2074	65.4	9.6	54.55	44.95	0.75		_
102	BHE102	AdBh0256	445643	973409	2132	141.8	_	_	_	_		_
103	BHE103	AdBh0257	445354	969451	2100	71.25	39	_	_	_		_
104	BHE104	AdBh0258	445144	969045	2087	85.5	45	_	_	_		_
105	BHE105	AdBh0259	453538	982154	2087	80	8	_	_	_		_
106	BHE106	AdBh0301	442811	977625	2073	179	9.9	_	_	_		_
107	BHE107	AdBh0312	408475	952876	2280	50	10	_	_	_		_
108	BHE108	AdBh0313	407460	953526	2288	36	9	_	_	_		_
109	BHE109	AdBh0315	404051	980357	2150	83	3.8	_	_	_		_
110	BHE110	AdBh0316	401219	985083	2130	50	_	_	_	_		_
111	BHE111	AdBh0322	432820	969800	2100	50	_	_	_	_		_
112	BHE112	AdBh0323	447966	980422	2070	80	53.88	_	_	_		_
113	BHE113	AdBh0334	427635	994816	2132	125	7	_	_	15		_
114	BHE114	AdBh0335	429252	993949	2115	45	15	_	_	_		_
115	BHE115	AdBh0337	429529	987244	2075	37	_	_	_	_		_
116	BHE116	AdBh0338	433722	996293	2167	50	_	_	_	_		_
117	BHE117	AdBh0341	416945	988222	2101	49.2	_	_	_	_		_
118	BHE118	AdBh0346	435988	973764	2078	50	_	_	_	_		_
119	BHE119	AdBh0397	415254	939047	2399	47	_	_	_	_		_
120	BHE120	AdBh0398	412826	949736	2274	50	_	_	_	_		_
121	BHE121	AdBh0399	424094	968971	2104	24	22	_	_	_		_

No	Researcher ID	Clients Well Index	UTM East	UTM North	Elevation, m	Depth, m	Static water level, m	Dynamic water level, m	Drawdown, m	Discharge, L/s	Transmissivity, m2/day	Specific well yield, l/s/m
122	BHE122	AdBh0400	428566	961644	2141	24	21.5	_	_	_		_
123	BHE123	AdBh0402	409122	975187	2106	15	14	_	_	_		_
124	BHE124	AdBh0403	415528	977263	2079	7.5	6.5	_	_	_		_
125	BHE125	AdBh0404	416140	977209	2079	7.5	6.5	_	_	_		_
126	BHE126	AdBh0405	415715	976666	2076	6.5	5.5	_	_	_		_
127	BHE127	AdBh0406	418707	974898	2082	12	10	_	_	_		_
128	BHE128	AdBh0407	423375	973439	2093	19.5	18.5	_	_	_		_
129	BHE129	AdBh0408	441366	977899	2070	10	8	_	_	_		_
130	BHE130	AdBh0409	441901	981393	2074	7	5.5	_	_	_		_
131	BHE131	AdBh0410	441831	983807	2090	50	6	_	_	_		_
132	BHE132	AdBh0725	445000	978200	2060	120	_	_	_	_		_
133	BHE133	AdBh0739	461900	974300	2120	-	38.1	38.1	_	0.6		_
134	BHE134	AdBh0740	451900	983000	2140	40	_	_	_	6.3		_
135	BHE135	AdBh0890	455525	984000	2140	124	63.3	_	_	_		_

Appendix 6. Water chemistry data

SN	Researcher ID	UTME	UTMN	Elevation, m.a.s.l	Depth, m	Temp, °C	EC, µS/cm	TDS	PH	Na+	K+	Ca2+	Mg2+	HCO_3^{3-}	Cl-	F-	$SO_4$2-	NO_3-	$PO_4$3-	Hardness	Water Type	Water Source
1	BHE2	401801	996640	2311.6	246		552	352	7.6	37	6.7	72	14.4	356.2	2.8	0.7	4.2	0.5	4.2	240	Ca-Na-HCO3	BH
2	BHE6	446356	1005421	2390.8	400	32	315	173	8.3	57	2.6	11.8	1.5	150.7	8	1	2	0.1	2	35.8	Na-HCO3	BH
3	BHE7	446347	1002761	2371.6	654	34	397	218	9.1	81	2.8	6.7	4.5	119.5	18.9	2.7	8.4	1	8.4	35.4	Na-HCO3	BH
4	BHE8	445556	1001719	2355.9	400	25	397	219	8.3	61	1.9	15.5	7	125.1	12.3	0.5	17.1		17.1	67.9	Na-Ca-HCO3	BH
5	BHE11	440274	1006055	2504.2	300	23	260	162	9	53	1	4.4	0.5	113.1	13.4	0.5	0.5	0.3	0.5	13.2	Na-HCO3	BH
6	BHE12	427126	971361	2064.4	308	23	229	142	8.4	27	2.1	19.3	5.6	117.2	4.8	0.3	5.8	0.4	5.8	71.3	Na-Ca-HCO3	BH
7	BHE13	456314	962592	1995	290	30	534	360	7.2	44	10.7	68.6	10.3	339.7	8.6	1.3	3.2	0.7	3.2	213.4	Ca-Na-HCO3	BH
8	BHE14	450359	981037	2075.1	280	26	487	312	7.6	49	5.4	54.6	4.3	255.5	13.4	1.1	7.5	5.3	7.5	154	Ca-Na-HCO3	BH
9	BHE15	433200	959670	2096	194	23	605	404	7.3	52	8	75	13.3	445.8	9.9	1.3	0.9	1.7	0.9	243.6	Ca-Na-HCO3	BH
10	BHE16	413137	973900	2072.1	311	27	822	540	7.6	69	13.5	94.1	21.4	588.5	4.1	2.4	1.7	7.1	1.7	323.4	Ca-Na-HCO3	BH
11	BHE17	427395	992768	2077.7	243	20	430	282	8.8	102	1.3	12.6	3.4	158.6	34.8	1	15.6	5.8	15.6		Na-HCO3-Cl	BH
12	BHE18	418679	988365	2077	445	37	945	572	8.4	216	4.9	9.1	7.3	491.2	41.9	1.9	13.4	1.1	13.4	53.2	Na-HCO3	BH
13	BHE19	423439	988990	2061.9	450	34	555	350	8.3	120	3	12	5.3	234.2	56	1	18.9	0.5	18.9	52	Na-HCO3-Cl	BH
14	BHE20	420071	983317	2061.5	350	33	776	466	7.4	142	12.7	11.2	4.8	362.3	50.2	1.2	3.6	0.3	3.6	48	Na-HCO3	BH
15	BHE22	411189	983944	2082	301	39	655	420	7.6	107	12.8	14.4	6.9	341.6	15.1	0.7	41.8	0.3	41.8	64.8	Na-HCO3	BH
16	BHE23	426873	970945	2054	402	38	929	600	8.7	166	27.5	23	5.5	278.2	70	1.1	66.7	0.3	66.7	80.5	Na-HCO3-Cl	BH
17	BHE24	426362	969316	2064.6	420	40	953	628	7.2	160	21	19	4.1	380.2	62.5	1.2	70.3	1.9	70.3	64.6	Na-HCO3	BH
18	BHE25	454868	963109	1991.3	352	30	521	322	6.9	46	11	59.2	8.6	322.1	7.3	0.7	5.3	3.7	5.3	184	Ca-Na-HCO3	BH
19	BHE26	450887	981258	2074.4	436	25	405	230	7	26.5	5.9	59.2	1.9	253.8	3.6	0.7	0.1	4.4	0.1	156	Ca-Na-HCO3	BH
20	BHE27	438871	977181	2044	443	35	658	392	7.9	130	5.1	6.1	2.7	233.1	69.2	0.9	36.8	0.6	36.8	26.6	Na-HCO3-Cl	BH
21	BHE28	447224	978514	2051.1	440	28	590	383	7.1	91	8.7	36.8	8.8	229.5	42.8	0.7	72.5	0.8	72.5	128.8	Na-Ca-HCO3-SO4	BH
22	BHE29	449082	980399	2059.6	440	30	490	322	7.2	83	8.1	29.6	6.4	259.6	23.7	0.9	17.6	2.8	17.6	100.7	Na-Ca-HCO3	BH
23	BHE30	433672	1023691	2563.9	602	28	242	156	8.8	42.5	0.7	7.6	2.7	61	5.7	0.5	7.2	12.9	7.2	30.4	Na-HCO3	BH
24	BHE32	455255	985646	2185.7	163		256	160	6.6	13	6.1	36.5	7.8	165.9	6.4	0.6	1.6	0.8	1.6	123.5	Ca-Mg-HCO3	BH
25	BHE34	455470	984876	2169.5	201		317	204	6.9	30.5	3.8	41.6	6.2	209.8	4.6	0.6	1.6	1.1	1.6	130	Ca-Na-HCO3	BH
26	BHE40	447200	998889	2273.7	126		225	146	7.9	24.5	2	24.9	3.8	138.3	5.8	0	1.3	10	1.3	77.7	Ca-Na-HCO3	BH

SN	Researcher ID	UTME	UTMN	Elevation, m.a.s.l	Depth, m	Temp, °C	EC, µS/cm	TDS	PH	Na+	K+	Ca2+	Mg2+	HCO_3^{3-}	Cl-	F-	$SO_4$2-	NO_3-	$PO_4$3-	Hardness	Water Type	Water Source
27	BHE41	453522	1001474	2549.9	115.3	18.1	206	144	7.7	7.6	1.8	29.4	7	133.2	3.8	0	1.3	4.8	1.3	102.1	Ca-Mg-HCO3	BH
28	BHE50	455426	982736	2085	150	21	422	273	6.7	17	4.2	68.3	9.4	218.4	4.8	0.4	1.3	10.5	1.3	208.8	Ca-HCO3	BH
29	BHE51	444624	978143	2048.1	65.4	23.5	726	455	7.4	116	6.6	36.4	6.1	345.9	56.6	3.6	15.6	4.8	15.6	115.8	Na-Ca-HCO3-Cl	BH
30	BHE73	455000	985200	2202.4	126	-	191	117	7.7	23.8		24.1	3.9	122	14.2	-	-	9.3	-	76	Ca-Na-HCO3	BH
31	BHE74	463700	988500	2249.6	130	-		336	8.5	19.7	4.9	60.1	15.8	256.2	10.6	1	-	6.5	-	251	Ca-Mg-HCO3	BH
32	BHE75	455300	985250	2162.1	101	21.6		139	7.3	14	6.6	20	46	122	7.1	0.7	-	0.1	-	69	Mg-Ca-HCO3	BH
33	BHE78	460850	985850	2240.1	106		244	159	6.7	16	3.1	28.8	4.8	141.5	3.9		1.8	14	1.8	92	Ca-Na-HCO3	BH
34	BHE86	401886	996858	2303.4	NK	22.9	597	329	7.4	33	6.5	60.1	1.2	409.9	6	0.6	11.8	0.4	11.8	250.5	Ca-Na-HCO3	BH
35	BHE87	456231	962375	1982.5	NK	27.9	547	301	7.1	48	11	46.1	0.9	371.5	10.9	1	8.3	0.6	8.3	191.9	Ca-Na-HCO3	BH
36	BHE88	431706	960084	2113.9	NK	22.6	586	322	6.8	21	5	62.5	1.2	333.1	15.9	1.8	13.8	4.8	13.8	260.6	Ca-HCO3	BH
37	BHE89	427340	971039	2056.4	NK	-	428	235	6.9	11.8	4.8	48.5	0.9	294.6	2	1.2	2.4	0.4	2.4	202	Ca-HCO3	BH
38	BHE90	415762	959878	2149.5	NK	22	474	261	6.8	17	1.6	49.9	1	307.4	1	0.8	3	1.6	3	208.1	Ca-HCO3	BH
39	BHE91	427981	973260	2078	NK	22.4	755	415	7.2	125	3	30.1	0.6	422.7	37.8	1.8	1.6	9.9	1.6	125.2	Na-HCO3	BH
40	BHE92	416268	995349	2138.9	NK	24.2	509	280	7.5	68	3.1	31.5	0.6	320.3	13.9	2.6	14.7	0.3	14.7	131.3	Na-Ca-HCO3	BH
41	BHE93	463033	985920	2277	NK	21.6	428	236	7.9	19.5	4.7	45.6	0.9	299.8	3	0.7	3.3	0.4	3.3	189.9	Ca-Na-HCO3	BH
42	BHE94	448785	980205	2058.7	NK	23.3	509	280	6.9	18	1.8	58.2	1.1	315.1	13.9	1	5.6	4.1	5.6	242.4	Ca-HCO3	BH
43	BHE95	422250	967800	2088.7	NK	27	633	348	7.1	55	2.8	46.1	0.9	409.9	1	1.2	3.4	0.4	3.4	191.9	Na-Ca-HCO3	BH
44	BHE96	418082	962641	2133	NK	24.9	548	301	7	43	12.5	49.9	1	397.1	6	1.2	5.2	0.5	5.2	208.1	Ca-Na-HCO3	BH
45	BHE97	406956	955338	2281	NK	23.5	633	348	6.7	26	10.4	61.1	1.2	420.2	5	0.9	2.6	0.4	2.6	254.5	Ca-HCO3	BH
46	BHE98	403914	954147	2388.8	NK	20.5	236	130	6	7.5	4.1	22.3	0.4	58.9	23.9	0.1	15.3	17.3	15.3	92.9	Ca-HCO3-Cl	BH
47	BHE99	427748	995043	2107.4	NK	-	606	33	7.3	60	7.1	48.5	0.9	358.7	32.8	0.5	21.9	0.5	21.9	202	Na-Ca-HCO3	BH
48	BHE100	425776	989648	2070.4	NK	-	639	351	7.2	60	4	58.2	1.1	461.2	10.9	0.9	9.5	0.4	9.5	242.4	Ca-Na-HCO3	BH
49	BHE101	448532	1008047	2510.2	50	20	258	174	6.3	6	1.4	44.5	4.9	117.9	7.8	0	6	25	6	131	Ca-HCO3	BH
50	BHE102	449177	1002158	2452.2	0	-	146	88	8.3	19	1.4	12.2	1.6	79.3	1	0	1.8	0.8	1.8	369	Na-Ca-HCO3	BH
51	BHE103	445773	1001323	2380.1	74.5	-			8	9.5	1.8	32.1	18.5	196.2	11.3	1	0	14.9	0	156	Ca-Mg-HCO3	BH
52	BHE104	441584	1003445	2446	50	-	263	170	7.1	6.6	1.5	46.3	7.6	179.3	1	0	0.5	7	0.5	146.5	Ca-HCO3	BH
53	BHE105	439632	993521	2180.6	39	-	447	300	7.1	9.6	1.8	78.3	12.4	256.2	5.8	0	7.4	23.3	7.4	246.4	Ca-HCO3	BH
54	BHE106	404656	997733	2230.3	81	21.5	663	434	7.7	12	2.3	114	15.1	384.3	15.5	0	9	25	9	346.3	Ca-HCO3	BH
55	BHE107	460464	974637	2081	61.1	20	376	236	7.1	15.5	1.8	47	13.8	226.5	5.8	2.6	0.6	11.5	0.6	173.6	Ca-Mg-HCO3	BH
56	BHE108	456740	962388	1996.6	39	21	510	350	7.2	42	9.8	62.8	9.4	333.1	6.7	1.3	2.6	7.5	2.6	195.2	Ca-Na-	BH

SN	Researcher ID	UTME	UTMN	Elevation, m.a.s.l	Depth, m	Temp, °C	EC, µS/cm	TDS	PH	Na+	K+	Ca2+	Mg2+	HCO_3^{3-}	Cl-	F-	$SO_4$2-	NO_3-	$PO_4$3-	Hardness	Water Type	Water Source
																					HCO3	
57	BHE109	451590	954524	2103.4	156	20	430	280	7.2	20	11	50.5	14.8	273.8	7.7	1.6	0.6	11.5	0.6	186.6	Ca-Mg-HCO3	BH
58	BHE110	444924	954222	2237.3	184	21.7	546	372	7	28	7.2	81.9	13.2	296.1	6.7	1	0.5	10.7	0.5	258.8	Ca-Na-HCO3	BH
59	BHE111	459658	946538	2114.5	103	20	378	258	8.5	32	9.5	44.6	7.2	217.6	2.9	1.1	0.8	3.2	0.8	140.7	Ca-Na-HCO3	BH
60	BHE112	462875	950361	2055.4	187	20	383	250	7.8	28	9.9	41.8	9	238.9	5.8	1.4	0.3	5	0.3	141.1	Ca-Na-HCO3	BH
61	BHE113	462554	944481	2097	127	20	400	280	7.6	27	8.2	52.8	9.4	276.7	3.8	1.8	0.3	3	0.3	170.3	Ca-Na-HCO3	BH
62	BHE114	466690	976790	2060.8	93	20	588	376	7.4	67	9.5	41.8	13.8	266.3	20.2	0.8	17.3	32.5	17.3	160.6	Na-Ca-HCO3	BH
63	BHE115	464607	973547	2123.2	135	20	507	312	7.8	20	6.1	68.7	17.5	316.1	3.8	1.2	0.6	8.5	0.6	243	Ca-Mg-HCO3	BH
64	BHE116	466662	970715	2043	148	20	427	276	7.3	24	6.1	67.3	6.1	284.4	5.8	0.8	1.3	7	1.3	192.9	Ca-Na-HCO3	BH
65	BHE117	445643	973409	2106.9	141.8	-	333	219	7.1	17	4.2	50	8.3	235.7	2.9	0.8	0.5	7.5	0.5	158.9	Ca-HCO3	BH
66	BHE118	471304	1027754	2546.5	65	20	257	146	6.5	20.5	0.9	32.2	4.2	154.3	1.9	0	0.8	2.9	0.8	97.7	Ca-Na-HCO3	BH
67	BHE119	463742	985378	2346.2	125	-			7.9	20.4	4	56.1	9.7	268.4	7.1	0.7	-	-	-	180	Ca-HCO3	BH
68	BHE120	393191	944399	2150.3	46.9	40.5	741	488	7.4	147	8.6	11.4	1.1	438.1	11.3	6.1	7.2	0.3	7.2	33	Na-HCO3	BH
69	BHE121	482263	1038145	2558.8	66	-	257	146	6.5	20.5	0.9	32.2	4.2	154.3	1.9	0	0.8	2.9	0.8	97.7	Ca-Na-HCO3	BH
70	BHE122	465410	1002944	2575.8	NK	-	135	89	6.8	11.5	4.6	9.6	3.4	76.9	2	1.7	1.6	1.5	1.6	-	Na-Ca-HCO3	BH
71	BHE123	465161	1003103	2603	NK	-	201	130	7.8	18	4.9	21.6	4	136.6	8	0.9	3.2	0.5	3.2	-	Ca-Na-HCO3	BH
72	BHE124	430267	987498	2060.4	NK	-	630	380	7.4	42	3.6	82.7	14.3	350	19.2	1.7	21.7	7	21.7	-	Ca-Na-HCO3	BH
73	BHE125	460810	981473	2204	NK	-	344	222	7	15	4.8	43.7	13.2	217.8	0.5	0.2	0	7.5	0	-	Ca-Mg-HCO3	BH
74	BHE126	474740	1028068	2599.1	NK	-	342	222	7.5	8	0.7	45	15	195	6	0.1	25	17.3	25	-	Ca-Mg-HCO3	BH
75	BHE127	453776	998997	2590.9	NK	-	154	100	7.5	9	0.8	20	3	95	1	0.1	6	0.4	6	-	Ca-Na-HCO3	BH
76	BHE128	451196	1027438	2660.5	NK	-	278	181	7.5	10	0.6	36	7	173	2	0.3	1	2.7	1	-	Ca-HCO3	BH
77	BHE129	479695	1073212	2582.7	NK	-	488	395	7	13	2.2	57	16	215	14	0.3	11	18	11	-	Ca-Mg-HCO3	BH
78	BHE130	473911	1031930	2509.7	NK	-	166	108	7.6	30	0.7	5.3	0.5	90.3	1.9	0.2	7.2	0.8	7.2	-	Na-HCO3	BH
79	BHE131	463376	1036389	2485.3	NK	-	156	101	7.8	21.5	9.5	32.2	7.4	189.1	5.8	0.5	0.8	8	0.8		Ca-Na-HCO3	BH
80	BHE132	464070	1034816	2458.4	NK	-	156	101	7.8	21.5	9.5	32.2	7.4	189.1	5.8	0.5	0.8	8	0.8		Ca-Na-HCO3	BH
81	BHE133	464387	1034248	2440.6	NK	-	156	101	7.8	21.5	9.5	32.2	7.4	189.1	5.8	0.5	0.8	8	0.8		Ca-Na-HCO3	BH
82	BHE134	443048	1001649	2384.9	NK	-	693	450	7.8	94	9	48	9	390	18	4	26	2	26		Na-Ca-HCO3	BH
83	BHE135	446260	1004149	2383.3	NK	-	211	137	8.6	24	0.3	18	3	107	7	0.4	2	6.7	2		Na-Ca-HCO3	BH
84	BHE136	473800	1024726	2651.1	NK	-	319	200	7.3	17	1.1	44	11	200	4.6	0.5	1.1	5.9	1.1	-	Ca-Mg-HCO3	BH
85	BHE137	455620	1026514	2591.2	NK	-	237	152	8.2	34	1.5	16	1.1	118.9	6.7	0.3	13.2	2.5	13.2	-	Na-Ca-HCO3	BH

SN	Researcher ID	UTME	UTMN	Elevation, m.a.s.l	Depth, m	Temp, °C	EC, μS/cm	TDS	PH	Na+	K+	Ca2+	Mg2+	HCO_3^{3-}	Cl-	F-	$SO_4$2-	NO_3-	$PO_4$3-	Hardness	Water Type	Water Source
86	BHE138	474421	1013070	2592.7	NK	-	291	172	8.6	54	1	1.8	1.1	86	21	0.1	24	0.2	24	-	Na-HCO3-Cl	BH
87	BHE139	473621	1013070	2593.9	NK	-	277	186	7.8	46	1.2	12.9	4.6	141	10	0.1	11.3	1.6	11.3	-	Na-Ca-HCO3	BH
88	BHE140	448502	978502	2044.4	NK	-	1074	520	7.4	53	7	118.8	59.8	258.2	99	1.6	306	0	306	-	Ca-Mg-SO4-HCO3-Cl	BH
89	BHE141	441088	1013105	2684.3	NK	-	164	112	7.4	6.5	1.4	23.1	6.5	105	0.5	0.4	1.1	8.5	1.1	-	Ca-Mg-HCO3	BH
90	BHE142	442661	1079441	2550.9	NK	-	395	257	7.8	8	2	50	13	250	3	0.6	1	3	1	-	Ca-Mg-HCO3	BH
91	BHE143	483800	1065398	2588.7	NK	-	459	298	7.3	16.5	1.2	67.2	16	231.8	15.1	0.6	13.5	25.9	13.5	-	Ca-Mg-HCO3	BH
92	BHE144	447488	1004519	2406.2	NK	-	258	168	8	12	1.2	30	8	159	3	0.2	3	5.3	3	-	Ca-Mg-HCO3	BH
93	BHE145	464607	973547	2123.2	NK	20	507	312	7.8	20	6.1	68.7	17.5	316.1	3.8	1.2	0.6	8.5	0.6	-	Ca-Mg-HCO3	BH
94	BHE146	448254	1081234	2863.4	62	20	213	198	7.4	9	2	26	6	121	2	0.1	1	6	1	-	Ca-Mg-HCO3	BH
95	BHE147	424260	1052339	2530	NK	20	364	237	7.9	7	1	45	12	220	2	0.8	1	15	1	-	Ca-Mg-HCO3	BH
96	BHE148	460564	1061005	2489.9	NK	20	452	294	7.2	18	3.2	37	20	226	13	0.4	9	4	9	-	Ca-Mg-HCO3	BH
97	BHE149	406469	1009401	3000.1	150	20	395	257	7.8	10	2	50	13	250	3	0.6	1	3	1	-	Ca-Mg-HCO3	BH
98	BHE150	406144	996681	2215.1	NK	20	510	332	8	52	2	39	12	296	11	0.6	12	8	12	-	Na-Ca-HCO3	BH
99	BHE151	428348	1027771	2492.8	440	20	322	209	7.8	12	1	35	9	182	5	0.3	1	12	1	-	Ca-Mg-HCO3	BH
100	BHE152	474590	1068254	2642.5	43.4	20	302	291	7.7	10	0.1	48	8	167	11	0.7	1	12	1	-	Ca-HCO3	BH
101	BHE153	420001	1030799	2606.9	104	20	312	203	7.9	7	2	33	12	182	2	0.2	1	15	1	-	Ca-Mg-HCO3	BH
102	BHE154	475621	1065990	2643.4	43	20	267	259	7.7	8	0.5	32	8	160	2	0.2	3	7	3	-	Ca-Mg-HCO3	BH
103	BHE155	473024	1008828	2619.2	NK	22	130	92	6.4	17	2.9	12.2	2.7	85.4	3.6	0.4	6	0.2	6	-	Na-Ca-HCO3	BH
104	BHE156	415726	995659	2154	NK	20	469	305	6.9	75	2.8	37.2	4.1	312.6	14.4	1.1	1.8	0.4	1.8	-	Na-Ca-HCO3	BH
105	SPE1	400482	999171	2267.6	HS	25.9	612	336	7.6	24.5	2.3	71.3	1.4	435	12.9	0.8	6.5	0.5	6.5	296.9	Ca-HCO3	Spring
106	SPE2	431584	998853	2309.4	V	22	415	269	7	9.6	1.7	63.2	20	286.9	1.9	0	1.6	8	1.6	239.8	Ca-Mg-HCO3	Spring
107	SPE3	459831	985582	2210.7	HS	22	201	138	6.6	9.1	4.6	26.4	5	123	9.6	0.8	0.3	3	0.3	86.3	Ca-HCO3	Spring
108	SPE4	412197	957215	2175.7	F	20	324	216	7.1	21.5	9.5	32.2	7.4	189.1	5.8	0.5	0.8	8	0.8	110.7	Ca-Na-HCO3	Spring
109	SPE5	457146	1004953	2657	F	17	84	54.6	7	3	0.8	10	2.3	44	1	0.2	2	3.5	2	-	Ca-Mg-HCO3	Spring
110	SPE6	471668	1040491	2466.5	F	17	316	205	7.8	4	0.6	40	15	190	3	0.3	8	9.8	8	-	Ca-Mg-HCO3	Spring
111	SPE7	486175	1045151	2517.2	F	20	358	240	6.6	11.5	0.9	52.9	12.1	192.8	9.5	0.5	1.8	35.8	1.8	-	Ca-Mg-HCO3	Spring
112	SPE8	474208	1005540	2976.8	F	16	196	127	7.6	4	1.4	28	5	107	4	0.1	4	8.4	4	-	Ca-Mg-HCO3	Spring
113	SPE9	473540	1004307	2896	V	17.8	58.5	38	6.7	3	2.1	7	0.8	29	1	1	3	3.1	3	-	Ca-Na-HCO3	Spring

SN	Researcher ID	UTME	UTMN	Elevation, m.a.s.l	Depth, m	Temp, ºC	EC, µS/cm	TDS	PH	Na+	K+	Ca2+	Mg2+	HCO_3^{3-}	Cl-	F-	$SO_4$2-	NO_3-	$PO_4$3-	Hardness	Water Type	Water Source
114	SPE10	454124	1002590	2605.4	V	20	240	148	7	5.3	1.1	40.9	4.9	148.6	4.8	0.4	0.5	8.5	0.5	-	Ca-HCO3	Spring
115	SPE11	465505	1075390	2851.9	HS	16	365	237	7.8	12	0.6	48	12	212	4	0.4	2	15	2	-	Ca-Mg-HCO3	Spring
116	SPE12	455086	1053735	1947.8	HS	16	1304	848	7	75	31	124	39	543	63	0.8	76	8	76	-	Ca-Na-Mg-HCO3	Spring
117	SPE13	454500	1063823	2566.4	HS	16	335	218	7.2	11	2	38	11	210	3	0.5	2	4.5	2	-	Ca-Mg-HCO3	Spring
118	SPE14	459509	1066272	2603.2	HS	16	333	217	7.2	11	2	40	11	220	3	0.5	2	4.5	2	-	Ca-Mg-HCO3	Spring
119	SPE15	447470	1064576	1985.3	V	16	488	317	7.1	14	4	48	22	237	10	0.4	27	3.5	27	-	Ca-Mg-HCO3	Spring
120	SPE16	459951	1048382	1741.6	V	23.1	499	324	8.1	12	0.4	60	20	287	6	0.3	5	29	5	-	Ca-Mg-HCO3	Spring
121	SPE17	464186	1065719	2543.4	V	16	388	252	7.2	16	4	42	12	216	9	0.3	6	15	6	-	Ca-Mg-HCO3	Spring
122	SPE18	446945	1066467	2241.2	HS	17	512	333	7.2	9	2.1	62	18	251	8	0.3	12	16	12	-	Ca-Mg-HCO3	Spring
123	SPE19	385386	1052257	1912.2	HS	20	395	257	7.8	10	2	50	13	250	3	0.6	1	3	1	-	Ca-Mg-HCO3	Spring
124	SPE20	454415	1063647	2569.4	HS	16	330	212	7.3	12	1.5	37	11.5	205	3	0.5	2	4.5	2	-	Ca-Mg-HCO3	Spring

N.B. Except PH all chemical parameters are in mg/l, HS-Hill side, F-Flat area, V-Valley, NK-Not known, BHE-Borehole with researcher-Ephrem ID, SPE-Spring

Appendix 7. Geophysical survey data

Researcher ID	Clients ID	UTME	UTMN	Elevn, m.a.s.l	Apparent resistivity, ohm-m																	
					1.5	2.1	3	4.2	6	9	13.5	20	30	45	66	100	150	220	330	500	750	1000
VE1	T1	420144	995576	2146.5	7.6	6.6	5.6	5.7	6.0	6.6	8.0	9.3	13.0	18.0	24.0	32.0	43.0	46.0	47.0	53.0	60.0	-
VE2	T4	405850	1012333	3068.9	130.0	74.0	37.0	22.5	19.0	18.5	21.7	25.0	23.0	40.0	50.0	60.0	56.0	50.0	34.0	30.0		-
VE3	T5	406104	1009841	2959.7	63.0	49.0	35.0	25.0	24.0	21.0	22.0	22.0	21.0	20.0	29.0	31.0	30.0	30.2	27.0	25.0	23.0	-
VE4	T7	389885	1047850	1949.2	12.0	10.0	10.0	11.0	13.5	17.0	20.0	24.0	27.0	35.0	45.0	65.0	100.0	130.0	160.0	230.0		-
VE5	T9	395206	1036965	2536.0	13.0	8.0	6.0	4.7	4.7	4.7	5.1	5.0	8.5	12.0	17.0	24.0	42.0	50.0	54.0	57.0	64.0	73.0
VE6	T11	420512	987101	2067.1	8.3	5.9	5.1	5.2	4.9	5.0	5.8	6.0	7.0	7.0	7.5	7.0	8.0	9.0	10.0	11.0	11.0	11.5
VE7	T12	417596	990897	2089.1	6.5	5.1	5.0	4.2	4.0	4.6	6.0	8.0	10.0	14.0	18.0	24.0	28.0	30.0	35.0	44.0	50.0	56.0
VE8	T13	417340	992791	2104.1	20.0	16.0	13.0	10.8	10.0	10.0	11.4	10.0	11.3	11.2	15.3	20.0	21.5	30.0	34.0	32.0	31.0	30.0
VE9	T14	416788	995949	2152.5	8.0	7.8	7.8	7.1	7.5	7.9	9.4	11.0	14.0	15.0	18.0	30.0	34.0	30.0	29.0	37.0	53.0	68.0
VE10	T15	433753	979297	2050.3	9.8	8.0	6.7	6.6	6.5	6.5	9.0	11.0	14.7	16.9	20.0	14.0	7.0	6.0	6.5	12.0	20.0	-
VE11	T16	435533	975713	2043.9	7.0	6.4	6.7	7.0	7.6	8.5	8.5	9.3	11.3	9.8	8.0	7.0	9.0	10.0	11.0	15.0	18.0	21.0
VE12	T17	438653	974227	2055.7	13.0	10.0	9.0	8.5	7.5	7.6	8.0	9.4	10.0	7.8	5.3	7.0	8.0	11.0	13.0	18.0	25.0	
VE13	T18	438954	971215	2046.7	7.4	7.1	6.5	6.5	5.7	6.5	7.0	10.0	14.0	17.0	23.0	25.0	26.0	12.0	16.0	23.0	28.0	30.0
VE14	T19	453740	966247	2002.7	48.0	28.0	22.0	16.0	14.0	13.0	13.0	19.0	25.0	36.0	44.0	60.0	40.0	36.0	32.0	34.0	40.0	43.0
VE15	T20	454588	964633	2015.1	6.0	7.2	6.5	5.8	6.3	7.4	9.4	11.0	13.0	15.0	19.0	22.0	26.0	33.0	34.0	41.0	51.0	
VE16	T21	455204	959520	2089.9	17.7	15.3	12.6	9.6	6.7	5.8	5.5	8.0	10.5	15.0	21.0	28.0	32.0	40.0	58.0	55.0	50.0	49.0
VE17	VESB-1	411861	959422	2166.7	14.0	13.0	16.0	17.0	18.0	20.0	22.0	24.0	26.0	38.0	44.0	48.0	44.0	38.0	40.0	43.0	48.0	-
VE18	VESB-2	419789	950958	2190.6	13.0	12.0	10.0	9.3	8.3	8.4	9.5	11.0	13.0	17.0	20.0	26.0	30.0	32.0	33.0	29.0	25.0	-
VE19	VESB-3	430458	951259	2178.4	13.0	8.5	8.5	9.0	11.2	12.0	16.0	17.0	15.0	10.0	9.9	11.7	13.0	15.0	20.0	23.0	27.0	-
VE20	VESB-4	440364	951942	2254.5	28.0	14.0	12.0	11.0	9.0	9.4	9.0	9.0	10.0	15.0	21.0	28.0	38.0	50.0	55.0	52.0	42.0	36.0
VE21	VESB-6	405372	961931	2233.5	19.0	12.5	11.0	8.4	7.4	7.3	6.8	7.5	8.5	10.0	12.0	16.0	18.0	28.0	35.0	43.0	54.0	62.0
VE22	VESB-7	412051	960145	2156.8	9.0	7.5	8.0	9.0	11.4	14.7	19.0	24.0	24.0	22.0	16.0	15.0	14.0	18.0	25.0	29.0	35.0	-
VE23	VESB-8	418930	960765	2125.5	10.5	9.4	8.7	7.7	8.5	9.3	10.3	10.5	11.0	14.3	18.5	24.0	25.0	23.0	15.0	11.0		-
VE24	VESB-9	430097	960258	2124.3	7.5	7.0	6.6	6.0	6.0	6.0	6.1	6.2	6.0	5.8	6.0	6.5	8.0	8.5	9.0	9.5	7.0	-
VE25	VESB-10	440212	963453	2101.3	16.0	15.0	15.0	15.0	17.0	23.0	29.0	34.0	36.0	38.0	32.0	26.0	25.0	30.0	33.0	31.0	29.0	28.0

Researcher ID	Clients ID	UTME	UTMN	Elevn, m.a.s.l	Apparent resistivity, ohm-m																	
					1.5	2.1	3	4.2	6	9	13.5	20	30	45	66	100	150	220	330	500	750	1000
VE26	VESB-11	454133	964975	2011.8	17.5	14.0	10.8	9.5	8.6	9.4	11.0	13.0	17.0	22.0	28.0	37.0	47.0	50.0	55.0	56.0	55.0	50.0
VE27	VESB-12	402363	969729	2231.0	7.2	6.4	6.6	6.5	7.3	8.6	11.4	16.0	22.0	32.0	40.0	47.0	43.0	37.0	31.0	26.0	16.0	
VE28	VESB-13	408008	970392	2127.2	6.0	6.0	7.2	7.2	7.7	9.0	11.0	15.0	22.0	26.0	34.0	38.0	44.0	42.0	40.0	36.0	30.0	25.0
VE29	VESB-14	420583	969253	2088.1	7.5	7.4	7.3	7.5	8.0	9.0	12.6	16.0	21.0	22.0	24.0	26.0	24.0	23.0	18.0	17.0	21.0	-
VE30	VESB-15	429643	969127	2089.2	13.6	9.7	10.0	9.8	10.0	11.0	12.4	15.0	18.0	17.0	17.0	16.0	14.0	15.0	16.0	18.0	21.0	-
VE31	VESB-16	437111	971581	2049.2	11.0	10.0	9.5	9.0	9.0	8.8	8.8	8.0	9.0	11.0	14.0	17.0	15.0	13.0	16.0	22.0	40.0	55.0
VE32	VESB-17	451306	972219	2053.0	10.0	9.0	8.0	6.4	6.5	6.6	8.5	12.0	14.0	19.0	22.0	24.0	22.0	21.0	27.0	31.0	34.0	-
VE33	VESB-18	460887	969065	2243.4	20.0	14.0	12.7	12.3	14.0	17.0	20.0	22.0	26.0	34.0	44.0	52.0	65.0	74.0	75.0	80.0	80.0	80.0
VE34	VESB-19	404260	984021	2311.4	44.0	38.0	40.0	44.0	55.0	68.0	86.0	98.0	92.0	80.0	73.0	75.0	85.0	100.0	110.0	100.0	85.0	73.0
VE35	VESB-20	409026	980059	2099.5	4.2	5.2	5.5	6.5	6.1	6.2	6.4	6.4	7.1	8.3	10.4	15.6	23.0	25.0	30.0	37.0	42.0	35.0
VE36	VESB-21	426513	978953	2060.6	6.5	6.4	6.4	6.5	7.5	8.0	8.6	9.0	8.0	6.5	6.5	7.0	7.5	8.0	8.5	8.5	9.0	-
VE37	VESB-22	441527	979145	2044.4	8.0	7.6	8.2	8.0	9.3	9.4	9.3	10.0	9.4	8.0	8.5	10.4	12.0	14.0	17.0	22.0	25.0	27.0
VE38	VESB-23	450483	980504	2057.9	18.0	16.0	18.0	20.0	24.0	30.0	38.0	44.0	53.0	60.0	65.0	75.0	85.0	80.0	77.0	62.0	45.0	38.0
VE39	VESB-24	461380	979460	2166.0	13.0	9.2	8.0	9.0	8.7	9.2	9.7	9.0	8.6	10.3	13.5	18.4	28.0	41.0	53.0	66.0	68.0	55.0
VE40	VESB-25	402505	990787	2261.6	14.2	11.0	13.6	10.0	10.0	11.1	14.0	17.0	21.0	24.0	27.0	31.0	35.0	45.0	55.0	63.0	63.0	64.0
VE41	VESB-26	409236	989695	2159.1	19.5	7.0	6.5	5.5	5.2	5.6	7.4	9.7	13.6	19.0	28.0	36.0	42.0	46.0	50.0	48.0	45.0	42.0
VE42	VESB-28	432551	959137	2102.2	19.0	12.0	8.0	5.7	5.0	4.8	5.0	5.5	5.8	7.3	7.4	9.0	11.0	12.0	14.0	18.0	22.0	-
VE43	VESB-29	403669	998459	2228.4	9.0	7.0	6.3	6.0	6.0	5.7	6.3	7.0	8.4	9.0	13.0	14.6	17.5	20.0	21.0	26.0		-
VE44	VESB-31	430906	998839	2303.1	70.0	54.0	38.0	32.0	22.0	14.0	12.0	5.5	6.5	9.0	12.0	16.0	17.0	17.0	16.0	12.0	13.0	14.0
VE45	VESB-32	438936	999920	2404.4	127.0	59.0	35.0	28.0	32.0	44.0	61.0	75.0	83.0	70.0	60.0	46.0	42.0	43.0	48.0	50.0	50.0	45.0
VE46	S2	422654	1043121	2544.8	4.6	5.7	7.3	9.7	13.4	18.8	26.5	36.7	45.9	55.6	53.1	47.2	31.2	18.0	22.1	28.6	90.2	136.5
VE47	S3	431635	1027616	2597.1	21.2	10.9	6.4	6.8	6.5	6.4	6.4	7.6	11.0	15.2	19.6	27.3	42.3	48.0	58.5	60.6	47.0	129.5
VE48	S4	432287	1025698	2573.7	9.5	4.2	4.1	4.1	4.0	3.8	4.6	6.0	7.9	10.0	12.1	15.5	22.9	27.7	31.1	37.2	44.3	55.7
VE49	S5	436281	1013451	2558.6	13.4	11.8	10.1	9.6	8.3	8.8	10.5	12.4	18.1	26.2	29.5	39.6	49.5	57.0	51.4	69.2	125.4	237.4
VE50	S6	438957	1007817	2561.3	17.5	7.2	7.0	7.0	8.2	11.8	18.7	23.8	34.3	47.5	52.6	54.8	49.4	45.4	49.9	46.3	56.8	122.5
VE51	S7	446542	952495	2355.5	12.0	14.7	16.2	17.4	17.5	18.7	16.9	18.3	20.6	24.8	31.3	35.9	38.0	34.5	35.6	60.6	113.9	217.0

Researcher ID	Clients ID	UTME	UTMN	Elevn, m.a.s.l	Apparent resistivity, ohm-m																	
					1.5	2.1	3	4.2	6	9	13.5	20	30	45	66	100	150	220	330	500	750	1000
VE52	S8	442516	989991	2174.9	12.3	5.6	5.2	6.3	7.1	8.1	9.4	11.0	13.0	16.0	24.9	32.5	26.2	30.0	38.5	60.6	105.4	266.0
VE53	S9	420395	1104037	2530.7	10.4	8.0	9.2	12.0	13.9	16.7	18.7	22.2	30.0	40.1	46.8	62.4	83.5	115.7	135.0	143.6	78.4	49.3
VE54	S10	438090	1082149	2560.7	16.4	19.0	23.8	40.1	53.3	95.1	113.6	127.4	21.3	30.0	41.4	61.8	94.1	116.5	142.5	143.6	98.0	77.0
VE55	S11	457323	1084282	3073.3	9.1	8.3	9.8	12.9	13.6	19.6	22.7	23.3	27.7	29.7	19.9	22.8	26.2	39.2	63.4	99.5	96.0	-
VE56	S12	467260	1081926	2960.3	15.2	18.3	22.5	29.5	37.3	45.4	65.0	89.4	89.5	99.0	99.3	99.8	82.8	78.4	80.6	80.5	80.5	80.5
VE57	S13	465104	1073374	2743.7	5.7	5.2	6.2	7.9	8.9	9.8	10.7	11.0	12.9	13.4	15.5	20.2	28.9	39.5	53.3	66.6	103.9	122.5
VE58	S14	480009	1067922	2615.8	3.6	2.8	3.3	4.2	6.5	9.7	13.0	18.2	31.9	52.5	72.0	95.4	122.3	129.4	127.9	123.0	119.6	112.5
VE59	S15	482195	1063318	2620.8	10.7	11.5	14.6	17.4	18.2	26.5	32.5	40.3	52.4	58.0	61.5	63.9	97.0	164.3	157.5	159.2	129.4	119.0
VE60	S16	486284	1053126	2649.4	7.0	7.9	8.5	9.3	10.2	13.2	15.7	13.9	17.1	18.6	24.9	39.6	50.3	67.7	71.6	83.0	121.5	157.5
VE61	S17	487760	1046033	2554.2	7.0	8.0	10.2	14.4	19.2	23.7	28.5	35.0	45.6	55.2	58.1	55.5	48.2	51.5	54.4	63.5	90.2	-
VE62	S18	482619	1037585	2582.8	10.5	7.9	7.5	7.9	8.6	9.0	9.7	11.9	14.7	16.8	21.2	32.5	43.5	58.3	67.1	85.6	109.8	133.0
VE63	S19	474683	1028442	2606.1	4.9	5.9	6.7	7.8	11.8	16.9	26.5	37.9	48.5	65.6	90.0	119.5	150.7	150.8	139.5	138.4	98.0	-
VE64	S20	473228	1011884	2597.8	4.2	3.3	3.6	4.2	4.2	4.6	4.9	5.4	7.1	8.8	11.0	14.7	22.3	28.4	34.1	42.0	54.9	66.5
VE65	S21	472424	1020860	2542.7	6.0	4.2	4.9	5.5	5.5	6.3	7.7	7.7	11.8	15.6	20.9	30.1	37.0	49.9	63.4	70.1	88.2	136.5
VE66	S22	455713	1026721	2591.2	5.2	3.7	4.2	4.2	4.4	5.4	6.5	8.1	13.2	17.6	25.7	32.0	46.5	50.4	40.1	33.7	60.8	108.5
VE67	S23	472276	1026242	2546.6	13.8	6.9	6.5	7.5	9.0	11.5	15.9	21.0	29.5	37.3	46.9	59.2	64.1	67.1	76.5	90.8	98.0	84.0
VE68	Mkv1	453784	967447	2013.0	20.0	17.0	18.2	17.1	15.6	19.5	21.9	21.6	21.4	26.3	26.2	27.0	38.3	43.9	50.9	65.6	64.2	57.6
VE69	Mkv2	449831	962742	2003.3	20.2	14.1	11.5	9.5	10.2	14.7	19.5	21.6	24.5	33.2	42.0	47.3	53.5	53.1	58.1	69.0	75.5	76.8
VE70	Mkv3	456706	965747	2041.0	13.1	12.5	10.5	9.5	8.8	7.4	8.5	9.5	10.7	16.4	17.4	27.0	30.6	40.8	50.9	57.4	66.0	64.0
VE71	Mkv4	458366	965993	2048.2	16.8	13.6	19.1	27.6	37.1	47.3	53.6	51.4	52.0	67.1	72.7	74.3	76.5	103.0	130.8	147.5	150.9	192.1
VE72	Mkv5	456181	967170	2029.8	16.4	12.7	11.0	10.5	9.8	11.6	12.2	13.5	15.3	21.0	26.2	30.4	38.3	50.2	58.1	65.6	66.0	66.6
VE73	Mkv6	454939	964416	2015.1	22.0	19.7	20.6	20.7	23.4	35.8	43.8	51.4	57.5	65.7	69.8	81.1	72.1	62.7	65.4	76.1	80.0	75.1
VE74	Mkv7	453183	969514	2039.2	10.9	9.1	9.1	7.6	7.4	8.4	9.7	10.8	12.2	18.4	20.4	30.3	38.3	50.2	58.1	65.6	66.0	64.0
VE75	Mkv8	451059	967023	2052.9	42.3	34.3	28.2	25.7	23.4	22.1	23.9	27.0	36.7	42.1	46.5	54.1	61.2	69.0	72.7	70.5	75.5	79.4
VE76	Mkv9	448636	963509	2055.1	33.7	31.8	27.2	26.6	25.4	27.6	30.1	32.5	40.9	57.8	69.8	81.1	91.8	87.8	87.2	65.6	56.6	64.0
VE77	Mkv10	449119	960527	2098.3	57.4	65.9	70.3	79.8	95.7	101.0	116.9	124.4	122.4	121.0	127.9	135.2	122.4	125.4	130.8	131.1	132.1	115.3
VE78	Mkv11	455173	960732	2055.2	65.6	60.2	75.5	73.2	84.0	101.0	121.7	129.8	146.9	130.1	115.3	108.2	122.4	112.9	116.3	131.1	132.1	128.1
VE79	Mkv12	451026	961049	2047.8	163.9	156.8	155.3	153.9	152.4	142.0	114.4	86.5	67.3	57.8	52.3	54.1	55.0	56.4	58.1	65.6	75.5	76.8

Researcher ID	Clients ID	UTME	UTMN	Elevn, m.a.s.l	Apparent resistivity, ohm-m																	
					1.5	2.1	3	4.2	6	9	13.5	20	30	45	66	100	150	220	330	500	750	1000
VE80	Mapping Well	455040	963127	1992.9	39.9	45.3	63.6	78.1	89.0	100.1	102.3	94.1	79.9	63.1	52.3	48.0	54.0	62.7	72.7	76.9	75.5	72.9
VE81	BVES-2	400668	997363	2281.8	7.0	6.4	5.7	5.4	5.6	6.4	8.4	11.6	16.4	23.0	28.7	34.5	37.1	39.8	44.5	50.3	53.2	47.7
VE82	BVGPW-1	401206	996611	2298.3	9.1	8.0	7.7	7.9	7.0	5.9	6.5	8.6	10.0	14.9	20.7	29.1	38.8	47.8	51.1	49.2	45.1	50.6
VE83	BVES-3	400735	996620	2281.4	6.4	5.8	5.5	5.4	5.9	7.4	9.8	14.2	20.5	27.3	34.3	45.4	52.2	59.5	60.4	54.7	55.7	61.8
VE84	BVES-1	400536	998330	2268.8	4.7	4.7	4.7	4.8	4.7	4.9	5.2	6.0	7.9	11.0	15.8	23.2	32.7	43.7	54.8	61.4	61.9	58.5
VE85	BVES-11	399714	996683	2296.9	12.8	10.6	8.9	7.8	7.3	7.0	6.8	7.6	9.8	13.2	17.7	23.3	29.4	35.9	42.5	46.8	46.9	43.2
VE86	BVGPW-3	401663	997569	2297.0	11.0	10.9	10.2	9.0	7.5	6.3	6.1	6.8	8.2	10.7	14.3	20.0	26.9	34.9	41.6	48.6	50.0	47.5
VE87	HWV1	446709	1001916	2377.6	45.0	26.0	13.0	8.5	7.3	7.0	7.4	7.9	11.0	14.8	20.7	29.4	39.1	44.6	49.0	-	-	-
VE88	HWV2	445400	1002149	2365.9	93.0	80.0	64.0	51.0	42.0	41.0	46.5	59.0	76.0	102.0	123.0	137.0	131.0	111.0	91.0	-	-	-
VE89	HWV3	445960	1002606	2367.3	73.0	64.0	51.0	39.0	32.0	32.0	40.0	47.0	63.0	84.5	102.0	110.0	91.0	76.1	66.0	65.0	69.0	-
VE90	HWV4	445810	1001591	2387.7	15.0	9.0	6.0	5.6	5.9	6.6	7.5	8.9	11.0	13.8	18.2	24.2	32.0	38.5	44.0	49.0		-
VE91	AB1	445295	969842	2076.2	33.3	32.1	32.8	34.3	31.9	17.7	15.2	24.5	24.9	37.8	44.6	46.9	45.9	42.8	44.6	47.6	45.1	45.5
VE92	AB2	445940	965636	2061.0	8.6	11.6	14.7	16.5	15.7	14.2	14.0	23.2	17.0	30.3	33.2	34.3	41.8	51.7	51.4	48.4	43.1	35.0
VE93	AB3	428532	950054	2225.6	17.5	15.4	14.6	14.8	15.3	14.8	14.0	12.4	11.9	11.3	11.8	13.6	16.5	21.4	24.8	26.0	25.5	23.8
VE94	AB4	429885	945010	2483.3	82.6	88.3	94.4	103.0	117.3	126.0	126.0	130.9	80.1	37.1	25.5	30.9	38.2	54.2	55.1	60.6	64.7	66.5
VE95	AB5	416012	951342	2220.1	66.3	18.5	8.9	8.7	8.1	10.6	15.1	17.5	19.7	19.7	20.6	24.3	29.3	33.6	40.5	67.6	107.2	162.1
VE96	AB6	417238	947316	2252.7	12.2	7.1	4.8	4.7	4.0	3.0	3.0	4.3	6.7	9.6	11.7	14.5	16.1	18.2	26.3	30.5	38.2	49.7
VE97	AB7	430519	960132	2119.0	5.1	4.4	4.1	3.8	3.9	3.8	4.1	5.2	5.0	6.0	6.5	7.9	9.5	10.8	12.7	12.1	9.3	6.6
VE98	AB8	427275	959882	2116.3	10.6	8.0	6.7	7.2	7.1	6.8	7.0	4.8	6.5	5.9	7.0	8.7	10.4	12.6	16.0	15.6	13.7	11.2
VE99	AB9	429299	956197	2126.6	9.6	9.2	8.5	7.8	7.3	7.0	7.1	6.5	8.7	9.3	11.6	14.2	17.2	18.9	21.7	20.6	18.5	15.9
VE100	AB10	440461	959119	2134.4	11.2	8.2	7.1	6.9	6.4	7.4	9.4	10.6	15.6	20.2	26.9	37.5	44.1	51.7	41.3	36.3	27.4	18.2
VE101	AB11	446949	958188	2167.0	11.1	13.9	17.5	21.3	26.2	32.6	40.0	54.5	56.9	59.9	47.8	31.4	22.5	21.9	28.5	27.7	23.5	18.9
VE102	AB12	443464	945492	2707.8	77.8	56.9	41.3	32.0	25.6	21.6	20.0	18.7	26.3	33.9	44.2	57.3	68.7	65.3	43.5	37.1	32.2	29.0
VE103	AG2	418920	981251	2065.1	7.0	4.5	4.2	5.0	5.0	4.9	5.3	4.7	4.9	4.9	7.0	7.5	7.6	9.6	12.9	18.4	34.8	66.5
VE104	AG4	407875	975644	2117.8	29.5	15.0	11.9	12.0	12.3	12.4	13.4	14.9	16.4	20.8	25.0	25.9	28.5	36.0	36.0	44.7	76.8	147.4
VE105	AG5	411209	972169	2085.4	10.4	4.4	4.3	4.7	4.9	5.2	5.4	5.6	6.9	9.2	10.6	16.7	19.2	22.2	30.2	55.0	92.8	133.5
VE106	AG7	416112	965051	2108.8	14.9	9.6	8.6	8.4	7.0	6.1	6.2	6.4	6.8	8.5	13.0	15.0	15.8	16.4	14.9	13.1	10.3	14.8

Researcher ID	Clients ID	UTME	UTMN	Elevn, m.a.s.l	Apparent resistivity, ohm-m																	
					1.5	2.1	3	4.2	6	9	13.5	20	30	45	66	100	150	220	330	500	750	1000
VE107	AG8	418046	966388	2101.4	25.3	16.4	13.7	13.9	13.4	13.2	13.9	14.3	18.1	24.9	35.1	44.8	57.3	56.5	55.9	38.2	35.9	47.7
VE108	AG9	417318	970184	2077.5	10.3	9.7	9.0	8.7	8.5	8.7	9.3	9.1	14.1	15.1	18.8	23.0	26.4	26.6	20.2	15.2	10.7	8.4
VE109	AG10	422561	976060	2059.1	12.2	10.5	8.2	6.2	5.1	4.9	5.5	6.7	6.8	7.7	7.9	8.0	7.9	7.9	9.4	9.5	9.8	10.1
VE110	AG11	429723	985702	2049.2	6.0	5.3	4.6	5.7	5.7	6.4	7.3	8.6	9.8	10.0	8.1	8.9	10.4	10.7	10.8	18.9	27.1	39.8
VE111	AG12	431815	993154	2069.8	15.7	6.7	6.1	6.9	6.6	6.1	5.9	6.1	7.1	7.6	8.0	10.4	13.9	19.6	28.5	34.5	47.1	63.4
VE112	HIM2	413337	1028725	2447.6	24.1	14.5	10.0	10.4	12.3	13.6	16.1	18.6	22.6	23.3	38.2	42.5	44.3	45.4	55.5	62.4	77.6	94.3
VE113	HIM9	422554	1030000	2480.9	20.1	13.9	11.3	8.8	7.9	7.9	7.5	7.2	7.9	8.0	10.7	14.6	18.5	29.3	39.0	51.3	71.3	115.2
VE114	HIM10	429915	1029743	2543.8	23.4	17.1	14.9	10.6	7.8	6.1	6.5	7.3	7.4	9.2	10.2	13.6	19.1	22.7	31.7	42.1	66.4	89.2
VE115	HIM13	434838	1018622	2557.3	6.6	5.7	5.7	4.9	5.3	6.0	6.8	7.1	7.4	7.6	8.6	9.6	16.0	17.8	43.5	70.0	123.5	181.4
VE116	HIM14	435630	1016743	2546.9	18.4	15.1	14.5	13.3	12.7	11.3	10.9	10.2	11.1	14.1	18.5	25.4	30.2	36.3	46.1	59.8	76.8	80.2
VE117	HIM15	429716	1012923	2584.4	18.3	15.8	9.4	8.0	7.0	5.4	4.8	5.5	5.5	5.2	4.7	4.6	3.5	4.8	8.7	18.3	24.7	29.7
VE118	HIM16	431225	1013975	2597.9	64.2	45.8	33.7	22.1	16.9	12.5	12.1	13.3	17.2	24.7	28.6	49.8	52.4	42.0	32.1	37.7	54.5	60.9
VE119	HIM17	432983	1011845	2590.6	90.8	54.1	34.6	18.4	14.5	13.5	11.6	10.2	12.1	15.4	21.5	27.5	32.4	26.2	19.2	24.1	44.3	67.4
VE120	HIM20	423674	1011057	2673.4	87.1	39.9	27.5	14.2	10.7	8.6	11.0	19.5	27.1	42.8	67.2	84.4	126.4	132.2	104.6	67.1	57.2	89.6
VE121	IW-1	427894	979049	2057.5	16.2	11.0	9.9	9.7	10.2	9.8	10.1	10.6	9.6	8.5	7.4	7.3	8.8	14.3	23.4	34.3	66.8	112.0
VE122	IW-2	428834	978804	2047.2	15.2	13.5	13.9	14.3	19.4	23.6	27.9	28.3	22.8	15.2	14.6	16.7	30.1	38.3	43.8	57.1	98.1	153.0
VE123	IW-3	429625	978987	2057.3	10.0	5.3	4.6	4.3	4.9	5.5	7.0	10.1	12.4	13.0	14.1	14.4	12.9	12.3	19.1	40.6	91.5	167.0
VE124	IW-4	430459	978994	2054.8	4.8	4.5	4.5	4.9	5.4	6.2	6.7	7.8	8.1	9.1	10.3	10.6	9.0	8.8	10.9	17.4	38.1	66.8
VE125	IW-5	427849	978018	2057.5	9.5	9.8	10.7	14.2	18.1	21.1	23.0	21.7	15.3	10.6	10.9	11.0	11.5	16.8	19.9	30.9	75.1	237.0
VE126	IW-6	429545	978092	2049.7	7.1	7.4	6.9	7.0	6.2	6.1	6.9	7.6	7.6	9.1	10.3	10.7	10.4	11.3	18.6	36.3	66.0	124.0
VE127	IW-7	430590	978182	2052.0	5.5	6.0	5.8	6.2	6.7	7.8	8.3	8.4	9.6	13.2	15.8	19.4	25.0	35.1	41.2	73.3	143.5	194.0
VE128	IW-8	428044	977107	2056.6	8.4	9.2	15.3	27.2	41.2	47.9	48.5	28.6	15.9	14.1	13.9	12.7	11.7	9.8	4.6	2.0	12.0	633.2
VE129	IW-9	429340	977013	2055.9	3.7	4.0	4.6	4.4	4.5	4.0	3.7	4.3	6.8	11.9	20.9	29.4	32.1	33.2	32.1	41.9	87.3	146.8
VE130	IW-10	430567	977001	2048.7	5.0	5.0	4.8	4.9	5.5	6.6	7.6	8.2	9.9	16.6	21.9	27.3	29.7	28.2	26.0	38.2	74.6	107.4
VE131	IW-11	428777	976151	2061.2	7.9	7.9	6.8	6.3	6.4	6.6	6.7	7.1	8.0	10.1	11.9	13.0	14.7	17.2	30.3	56.2	106.2	253.0
VE132	IW-12	429801	976356	2055.6	6.7	6.2	6.3	6.4	6.9	8.0	8.8	8.5	7.1	6.8	7.1	9.7	10.4	10.8	17.9	35.6	47.5	49.8

Researcher ID	Clients ID	UTME	UTMN	Elevn, m.a.s.l	Apparent resistivity, ohm-m																	
					1.5	2.1	3	4.2	6	9	13.5	20	30	45	66	100	150	220	330	500	750	1000
VE133	BWV-01	423646	968370	2082.8	7.6	6.6	6.3	7.0	7.7	8.4	10.3	11.4	12.5	13.5	13.7	13.4	13.9	14.7	20.6	28.2	54.2	104.4
VE134	BWV-02	422984	967603	2088.3	8.1	7.0	5.7	5.6	6.1	6.7	7.9	9.3	9.9	10.8	11.3	12.4	15.0	17.7	28.0	41.7	81.4	131.5
VE135	BWV-03	422336	966838	2092.6	5.4	5.0	4.8	4.8	4.8	5.5	7.2	10.1	13.0	14.4	16.3	19.1	20.5	21.1	26.4	30.1	47.8	92.6
VE136	BWV-04	423063	966359	2086.9	8.0	7.0	6.3	6.4	6.7	8.2	9.6	10.2	9.9	10.3	10.5	10.3	11.1	13.1	24.3	44.2	108.4	193.3
VE137	BWV-05	421519	966134	2110.6	10.3	7.6	6.5	6.3	6.1	6.0	6.6	7.5	9.3	12.2	15.9	17.7	18.9	20.7	29.0	43.7	82.7	126.5
VE138	BWV-06	422296	965657	2099.2	6.0	5.3	5.1	5.4	5.5	6.7	8.8	11.1	14.1	17.0	18.9	19.4	19.9	21.2	26.2	39.8	75.4	120.2
VE139	BWV-07	420785	965468	2128.2	11.2	9.9	8.1	6.5	5.5	4.4	4.2	4.7	5.9	8.3	10.2	14.2	17.6	19.2	32.0	51.5	95.0	155.4
VE140	BWV-08	422622	964714	2102.1	10.2	8.8	8.5	9.0	10.7	15.9	19.5	21.3	20.7	19.9	17.1	13.5	13.5	14.8	22.3	33.7	64.7	126.5
VE141	BWV-09	423460	965499	2093.3	10.4	9.8	10.0	10.6	11.0	11.4	11.7	10.9	10.6	10.5	11.3	12.9	13.5	14.8	24.5	38.7	90.8	166.5
VE142	BWV-10	421499	964851	2112.3	8.0	7.3	6.3	6.1	6.2	6.7	7.3	9.1	9.7	10.3	11.8	13.8	15.7	18.2	29.0	38.3	73.9	134.9
VE143	BWV-11	424076	966948	2072.0	9.4	8.5	7.7	7.9	7.2	7.2	7.2	7.9	9.1	9.8	9.0	10.0	10.2	11.2	14.9	17.4	15.5	13.1
VE144	BWV-12	424358	966274	2076.9	11.5	10.4	10.3	9.9	10.1	9.7	9.7	10.6	10.9	10.4	9.5	9.7	10.5	11.7	14.1	14.8	14.9	13.7
VE145	DB1V1	436551	968193	2085.5	17.5	13.9	16.8	20.9	24.6	31.2	35.5	33.2	31.1	21.9	15.2	14.5	14.0	14.8	18.2	21.1	21.7	19.5
VE146	DB1V2	437546	968190	2067.0	7.9	7.0	6.5	5.9	5.7	6.7	7.8	9.2	11.0	11.8	12.7	15.7	17.9	19.7	22.6	24.8	20.8	17.6
VE147	DB1V3	437631	967824	2067.1	17.9	11.9	12.1	10.7	10.1	11.4	13.8	12.9	16.7	17.4	17.6	19.3	19.8	22.4	26.0	27.7	23.7	19.0
VE148	DB1V4	437182	968166	2078.0	4.0	4.2	2.7	4.6	4.2	4.9	6.2	7.1	7.6	11.8	11.1	23.0	14.0	27.3	31.6	47.1	99.2	168.7
VE149	DB1V5	436078	968432	2093.1	3.7	4.1	4.9	6.1	9.6	13.5	16.9	21.6	26.1	27.2	30.7	32.1	27.4	25.4	30.3	47.4	80.5	142.6
VE150	DB2V1	438471	967113	2073.2	7.3	5.7	5.5	5.0	5.2	5.1	5.9	8.2	10.6	14.3	15.0	19.2	23.0	25.2	27.4	27.7	22.4	17.2
VE151	DB2V2	439278	968414	2092.6	11.5	10.5	9.6	10.3	9.2	8.8	8.8	10.5	13.1	19.0	24.8	35.9	40.9	42.3	31.4	26.4	18.5	13.5
VE152	DB2V3	439437	969099	2070.6	16.4	14.6	17.3	19.1	23.7	27.0	31.5	43.7	49.3	71.9	74.2	69.1	64.9	53.2	43.9	38.8	19.2	24.5
VE153	DB2V4	438982	968377	2086.1	8.9	8.9	9.1	9.4	10.3	12.0	14.6	17.7	21.1	25.2	30.2	37.0	44.3	49.2	56.9	60.5	63.1	64.2
VE154	DB2V5	440960	968084	2077.0	46.7	46.6	46.3	45.7	44.4	42.1	39.7	38.1	37.2	36.8	36.7	36.9	37.7	39.0	43.7	47.9	52.3	54.9
VE155	JAV1	425455	965142	2086.2	11.9	5.6	4.7	5.5	6.1	7.0	7.5	8.5	8.8	9.9	9.1	10.6	11.1	11.9	13.6	14.9	14.7	15.6
VE156	JAV2	425495	964537	2075.3	7.5	7.7	6.8	6.8	7.2	7.6	7.7	7.6	8.5	8.2	7.7	8.8	10.1	11.2	13.9	15.6	14.2	13.9
VE157	JAV3	426115	965852	2087.7	5.5	4.7	4.6	4.6	4.7	5.1	5.8	6.3	6.9	7.4	7.0	8.4	9.4	10.5	11.8	12.8	13.2	16.7
VE158	JAV4	426167	964722	2095.3	13.2	9.3	8.7	8.9	9.0	9.3	13.4	14.7	9.5	8.2	7.9	9.0	9.5	10.3	12.6	14.3	14.2	13.5
VE159	JAV5	426105	965091	2089.5	5.3	5.8	6.5	7.4	8.2	8.5	9.4	9.8	9.8	9.2	7.9	8.2	12.4	15.9	30.3	47.6	167.4	233.1
VE160	JAV6	426117	963866	2093.0	3.8	3.7	3.8	4.3	5.0	5.4	5.5	5.5	6.4	9.9	16.5	25.8	29.2	28.3	31.6	49.7	101.3	179.7
VE161	SWV-1	423646	968370	2082.8	7.4	6.5	5.4	5.5	5.3	5.3	5.8	6.3	7.6	9.7	14.7	19.9	25.8	35.0	49.8	66.6	90.7	107.1
VE162	SWV-2	422984	967603	2088.3	6.0	6.7	10.9	20.2	60.1	153.4	206.1	222.6	193.3	143.0	115.6	105.7	96.6	90.8	84.5	83.9	111.0	129.8
VE163	SWV-3	422336	966838	2092.6	5.4	4.7	4.6	4.5	4.2	4.1	4.1	4.4	4.8	6.3	8.6	11.0	14.3	18.3	33.4	52.9	89.0	91.8
VE164	SWV-4	423063	966359	2086.9	6.8	5.6	4.3	3.9	4.4	4.7	5.7	6.2	7.6	10.3	12.7	18.5	26.8	35.0	58.9	79.7	102.5	133.2
VE165	SWV-5	421519	966134	2110.6	4.4	4.4	4.4	4.5	4.9	5.6	6.1	6.9	8.1	11.6	16.3	23.0	29.9	34.8	42.9	45.0	41.8	42.7
VE166	SWV-6	422296	965657	2099.2	4.9	4.1	3.6	3.4	3.2	3.5	4.4	5.7	8.5	10.8	14.8	21.7	31.2	36.0	56.1	68.3	93.1	107.1
VE167	SWV-7	420785	965468	2128.2	4.6	4.6	4.4	4.5	5.0	6.8	10.8	13.9	15.9	16.8	20.1	24.5	29.8	33.1	36.7	45.3	79.4	112.7
VE168	SWV-8	422622	964714	2102.1	4.4	4.4	4.6	4.7	4.9	5.6	6.8	7.7	9.6	11.9	15.5	22.7	26.3	31.0	36.6	39.7	42.5	44.0

Researcher ID	Clients ID	UTME	UTMN	Elevn, m.a.s.l	Apparent resistivity, ohm-m																	
					1.5	2.1	3	4.2	6	9	13.5	20	30	45	66	100	150	220	330	500	750	1000
VE169	SWV-9	423460	965499	2093.3	5.1	5.0	4.9	4.8	4.7	4.7	5.3	6.5	8.5	11.8	13.6	18.1	24.2	30.0	46.0	39.7	63.4	108.5
VE170	SWV-10	421499	964851	2112.3	4.9	4.8	4.9	5.5	6.3	7.6	9.8	12.3	15.4	19.4	26.2	35.7	42.9	48.7	51.5	50.9	47.3	45.5
VE171	SWV-11	424181	967041	2071.0	4.6	4.4	4.0	3.9	3.9	4.2	5.5	7.1	9.7	12.6	17.3	22.7	26.5	29.4	34.2	35.2	36.3	38.0
VE172	SWV-12	424358	966274	2076.9	4.3	4.3	4.7	4.9	5.4	5.7	5.8	6.3	7.1	8.7	10.4	12.3	15.2	18.8	23.8	26.3	26.9	27.2
VE173	SWV-13	451994	978425	2071.7	4.5	4.6	4.5	4.9	5.1	6.2	7.9	10.0	13.7	18.3	23.3	33.3	43.6	50.9	66.2	79.7	91.9	104.4
VE174	SHV1	411559	946481	2318.8	8.9	8.1	7.5	7.3	7.7	9.0	11.2	13.8	16.8	19.7	22.9	27.0	32.2	36.0	47.2	58.3	78.8	100.2
VE175	SHV2	411203	947066	2334.8	6.0	10.2	10.5	12.5	16.6	23.3	30.6	30.1	27.6	29.7	26.5	29.8	34.5	40.7	49.9	51.8	42.0	40.6
VE176	SHV3	411336	947283	2329.6	12.8	10.6	10.2	9.3	8.7	7.9	7.9	9.3	11.2	14.8	18.7	24.1	27.9	34.5	41.4	40.1	32.5	28.1
VE177	SHV4	411706	947932	2306.4	12.6	10.6	8.8	7.9	7.6	7.8	8.7	10.1	12.0	14.6	17.8	23.5	32.3	39.8	64.1	86.3	120.2	151.8
VE178	SHV5	411354	946981	2326.8	15.0	10.6	6.9	6.4	7.1	8.6	11.6	14.4	13.7	11.5	12.8	25.6	27.2	30.5	33.8	31.2	25.9	20.9
VE179	SHV6	412902	947065	2282.0	23.7	21.6	26.4	36.1	46.1	57.8	73.9	74.1	85.9	71.2	57.3	37.8	37.1	44.8	8.4	8.7	8.7	17.4
VE180	AB3	435512	977812	2041.6	6.0	5.4	4.5	5.6	6.3	6.8	7.4	7.7	7.5	7.4	6.4	6.7	6.5	7.0	9.4	12.2	15.1	17.1
VE181	AB2	437040	978775	2053.0	9.8	8.5	8.4	6.6	5.8	5.6	5.3	5.0	5.9	5.4	5.6	6.4	7.2	7.9	10.6	14.9	17.3	27.8
VE182	AB1	436192	979611	2047.0	4.1	4.4	4.8	5.2	5.9	6.4	6.5	6.6	7.0	7.5	7.0	6.9	7.1	7.7	10.7	12.7	16.1	17.1
VE183	ATC2V1	432569	973928	2067.9	24.2	13.7	10.3	7.8	6.7	6.7	7.6	8.0	8.8	9.8	9.9	9.1	13.8	16.8	27.8	26.1	32.0	22.9
VE184	ATC2V2	432046	976381	2062.3	17.8	13.1	8.4	7.4	7.4	7.0	6.6	6.4	6.3	6.8	6.6	7.5	7.7	7.9	9.5	11.5	13.6	15.1
VE185	ATC2V3	433692	976335	2053.8	5.5	5.0	4.8	5.3	5.9	6.8	7.7	8.4	8.2	9.0	8.4	9.1	8.8	8.5	10.2	12.6	15.3	16.9
VE186	DBV1	467227	963957	2065.7	9.8	7.1	4.2	5.1	5.5	7.0	10.3	13.8	18.0	21.4	24.3	27.1	28.5	36.6	37.4	38.2	39.4	40.7
VE187	DBV2	468028	964298	2044.4	191.4	140.4	88.6	65.6	38.8	18.1	16.0	16.9	20.5	25.7	31.5	25.6	28.0	25.5	35.5	35.5	31.8	31.4
VE188	DBV3	467838	965055	2041.5	15.4	10.2	8.8	9.6	10.6	11.5	12.4	13.8	12.7	14.8	16.6	19.6	22.3	31.3	30.9	30.6	30.2	29.7

Appendix 8. Hydrograph separation results after RAP analysis for existing gauged stations

A. EGS1-Station (Upper Awash at Wolonkomi)

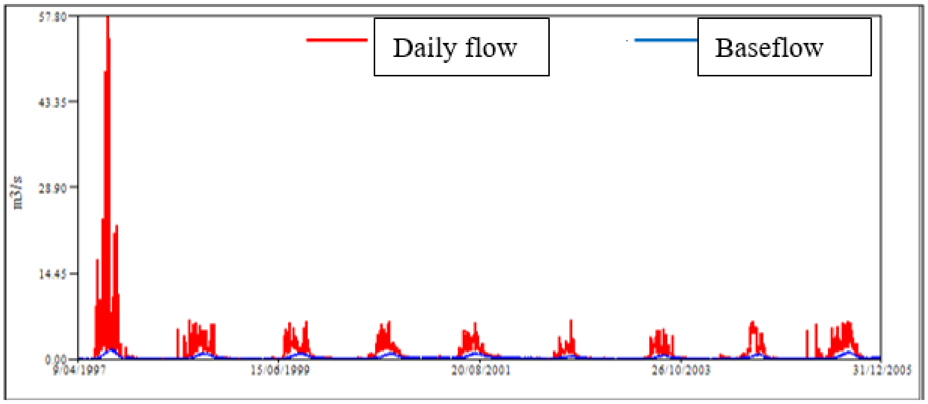

B. EGS2-Station (Upper Awash at Ginchi)

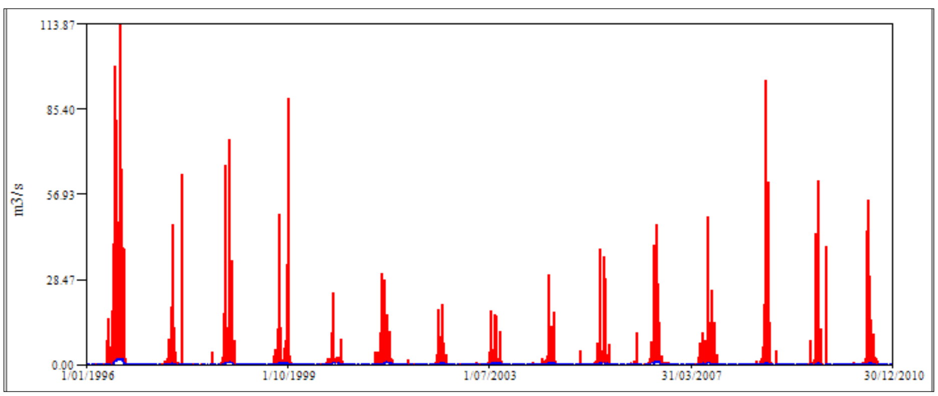

C. EGS3-Station (Upper Awash at Holeta)

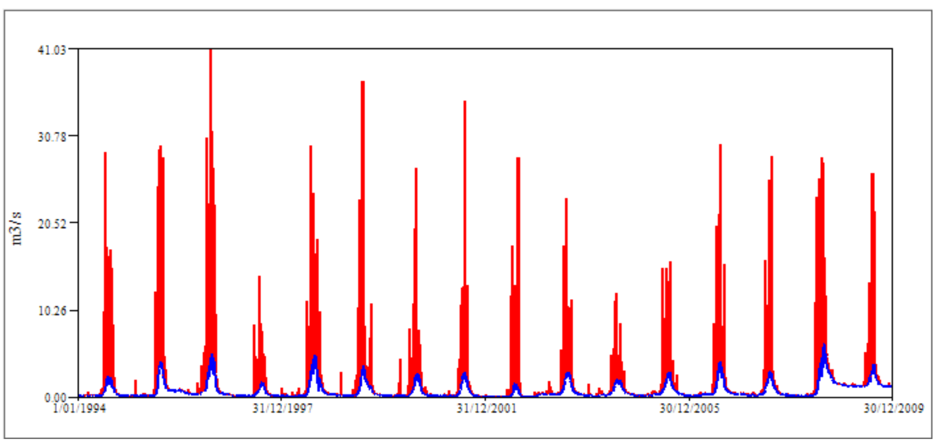

D. EGS4-Station (Upper Awash at Addisalem)

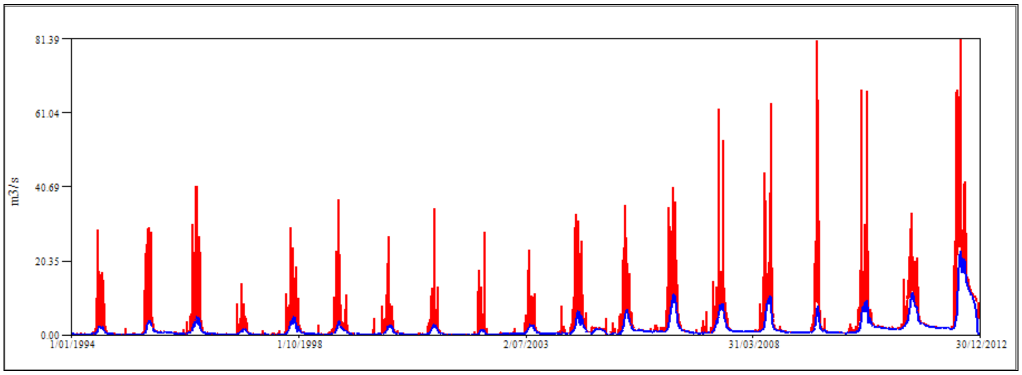

E. EGS5-Station (Upper Awash at Asgori)

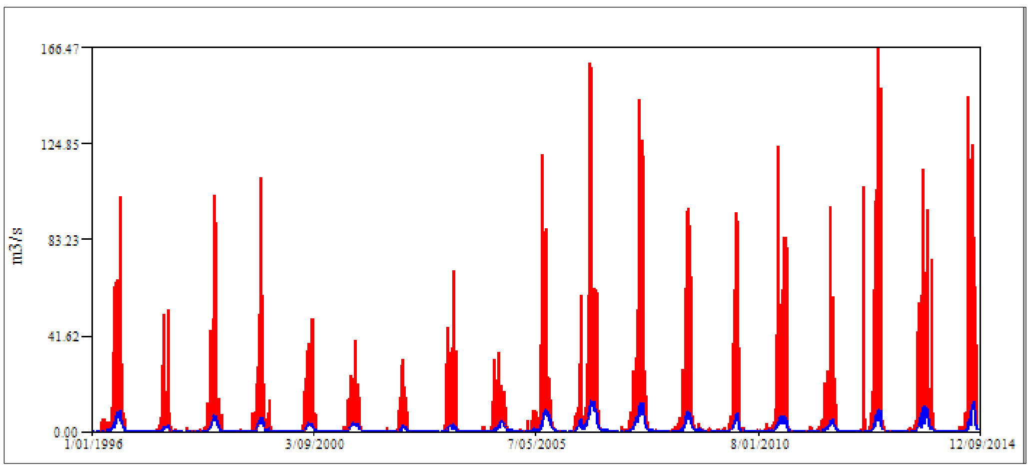

F.

EGS6-Station (Upper Awash at Awash Belo)

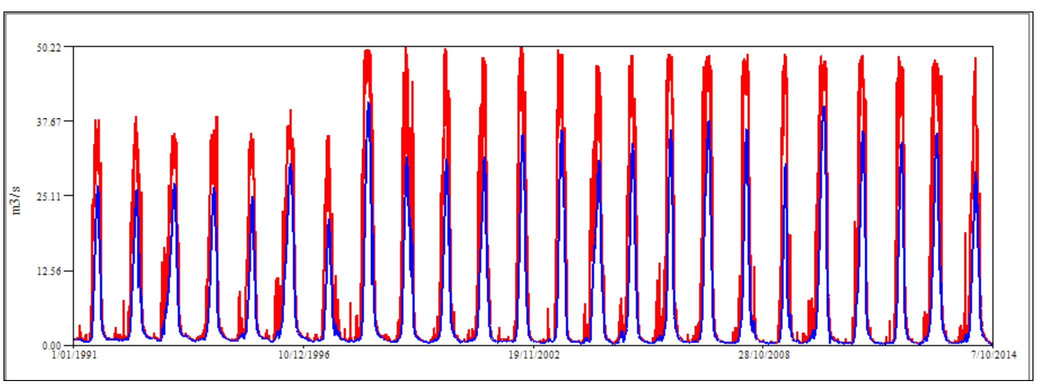

G. EGS8- Mugher at Roba

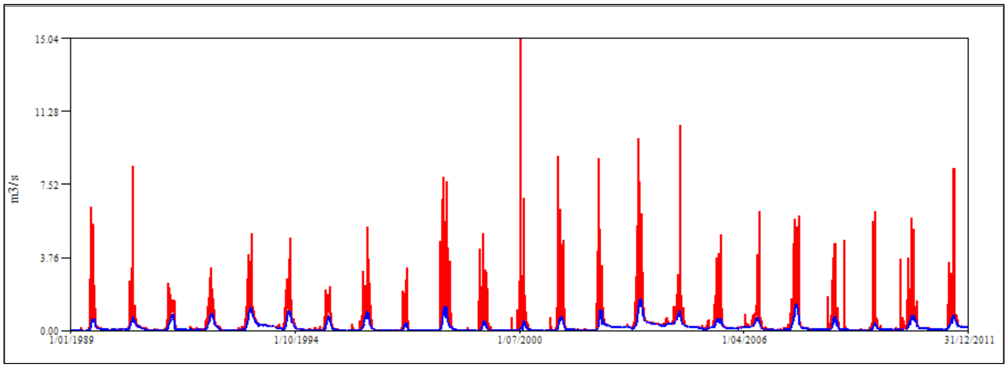

H. EGS9- Mugher at Gerbi

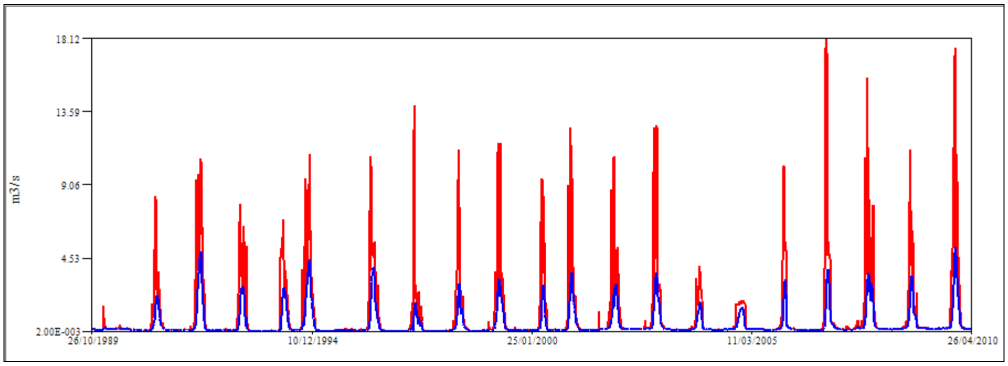

I. EGS10- Mugher at Sibilu

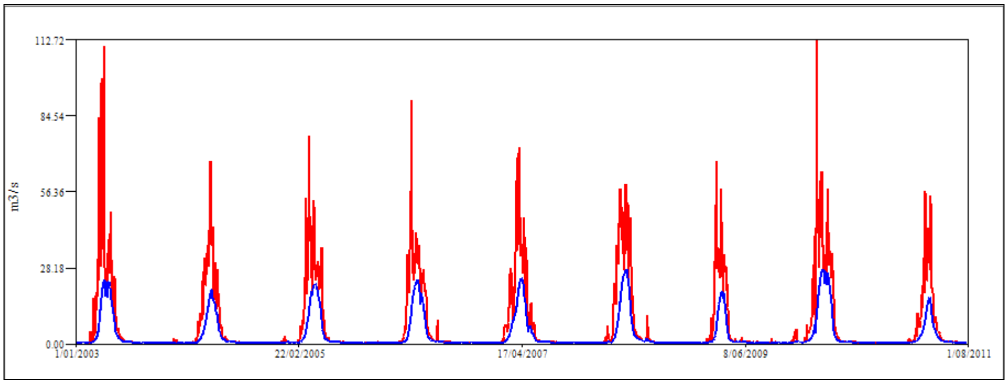

J. EGS11- Mugher at Muger

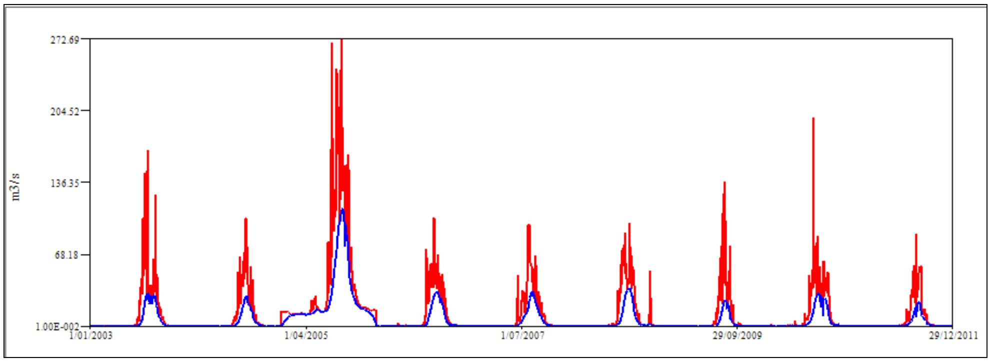

Appendix 9. Hydrograph separation results after TIMESPLOT analysis for existing gauged stations

A. EGS1-Station (Upper Awash at Wolonkomi)

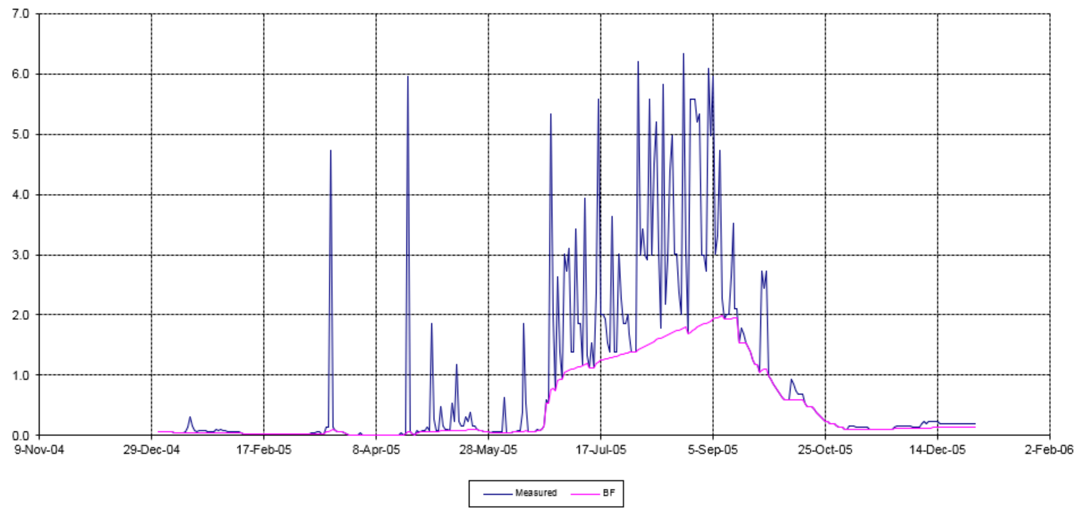

B. EGS2-Station (Upper Awash at Ginchi)

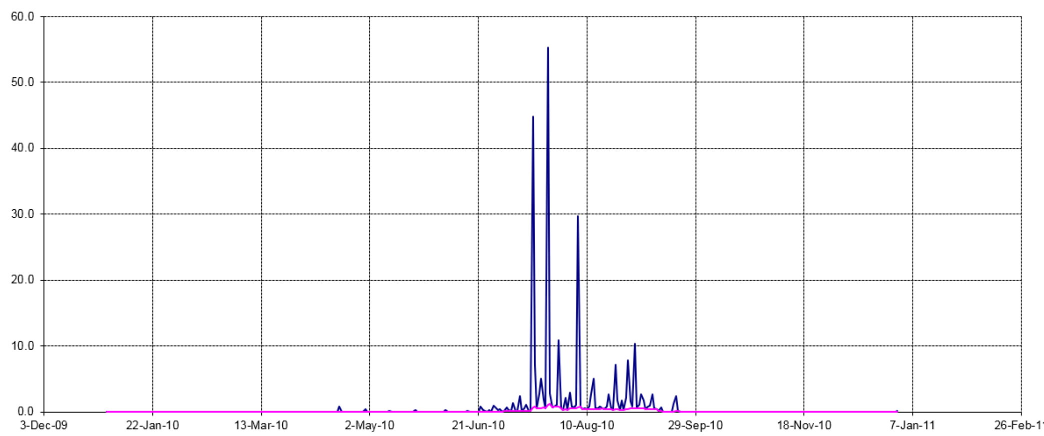

C. EGS3-Station (Upper Awash at Holeta)

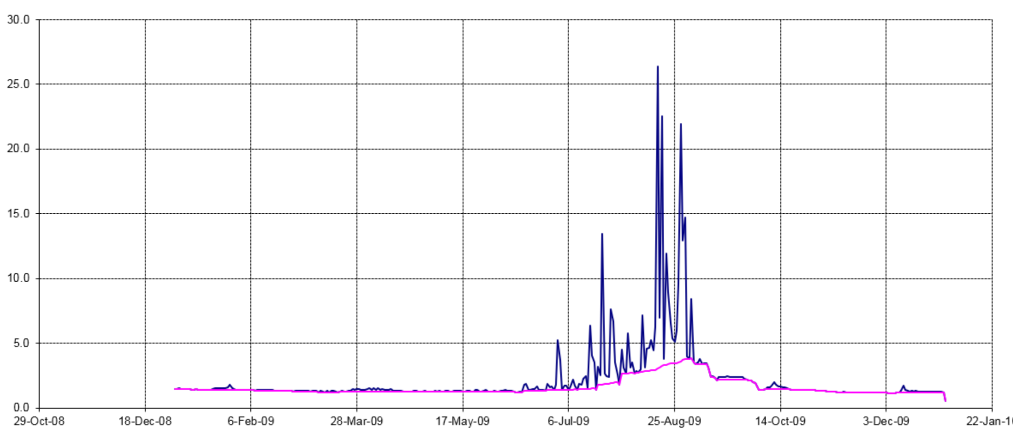

D. EGS4-Station (Upper Awash at Addisalem)

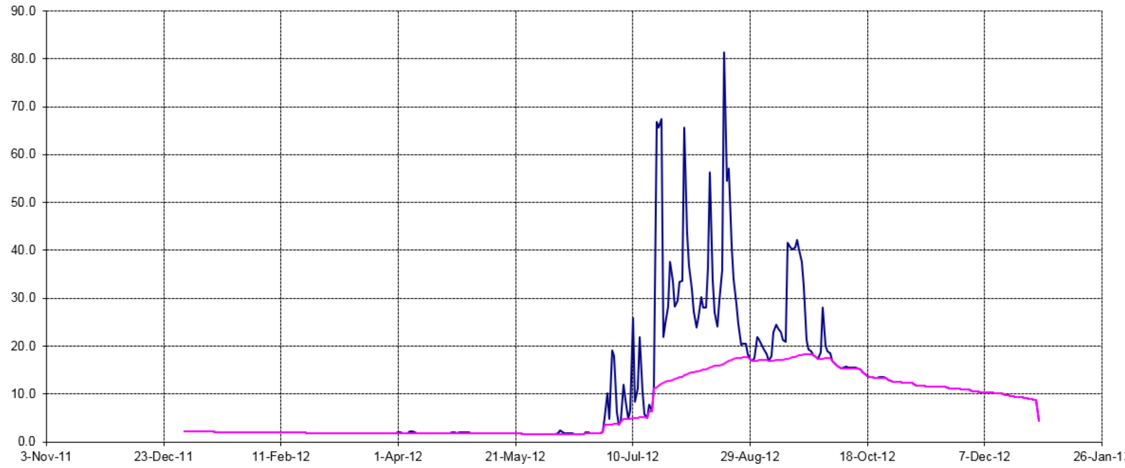

E. EGS5-Station (Upper Awash at Asgori)

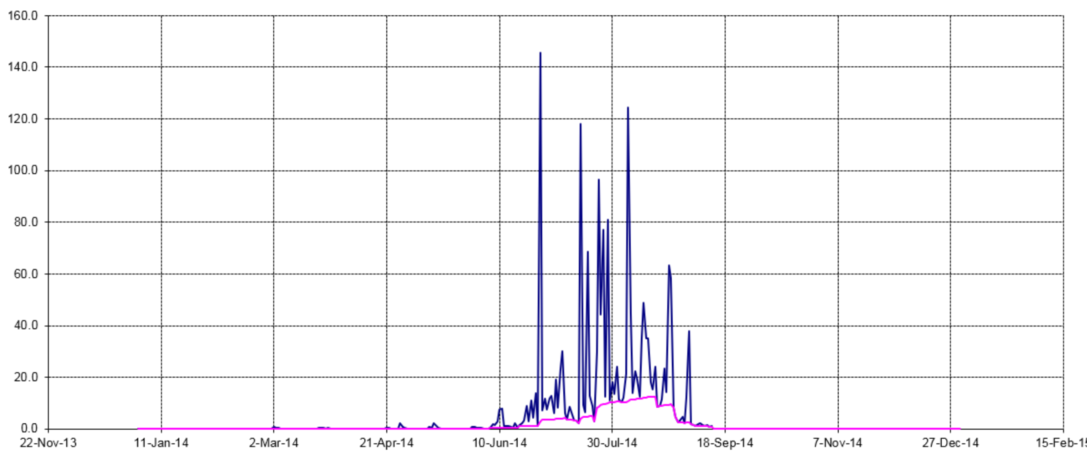

F. EGS6-Station (Upper Awash at Awash Belo)

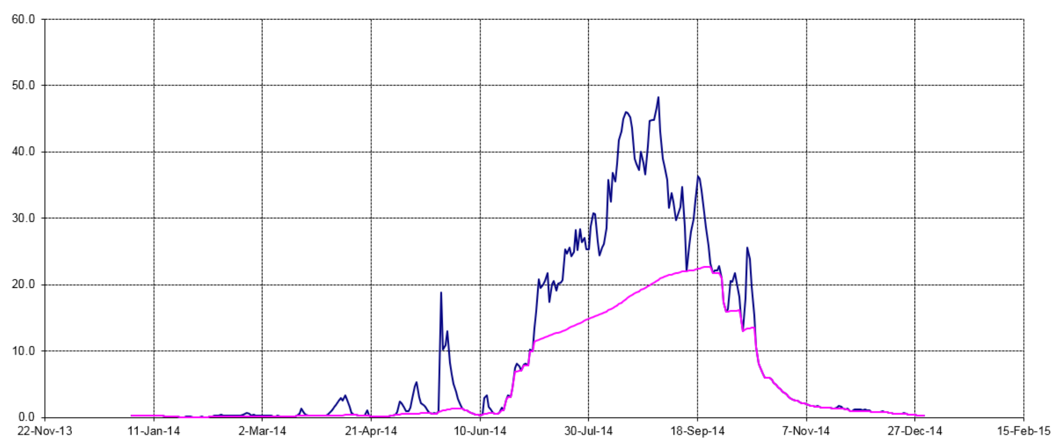

G. EGS8- Mugher at Roba

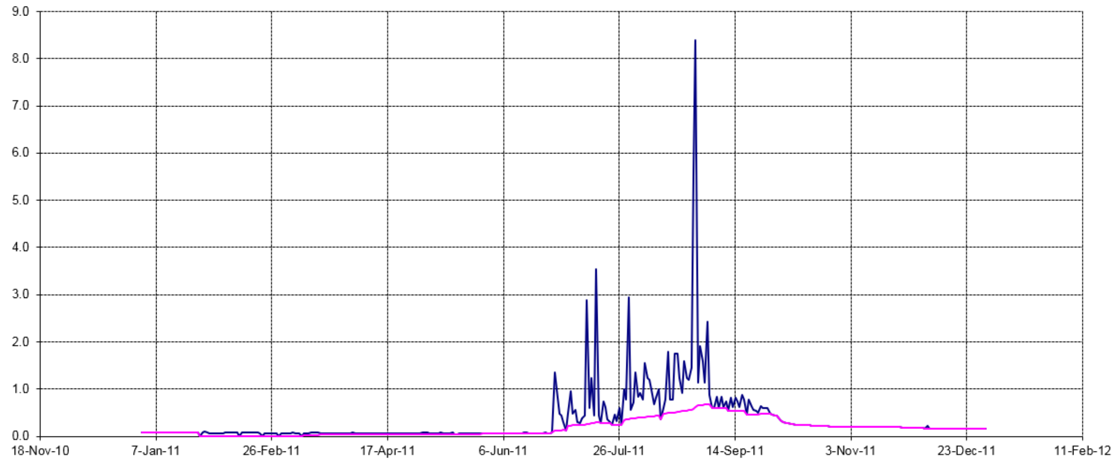

H. EGS9- Mugher at Gerbi

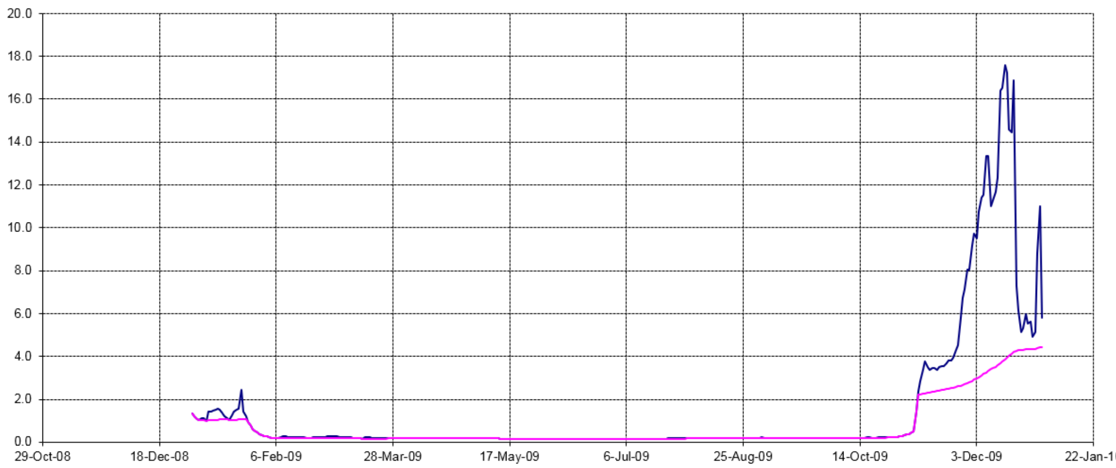

I. EGS10- Mugher at Sibilu

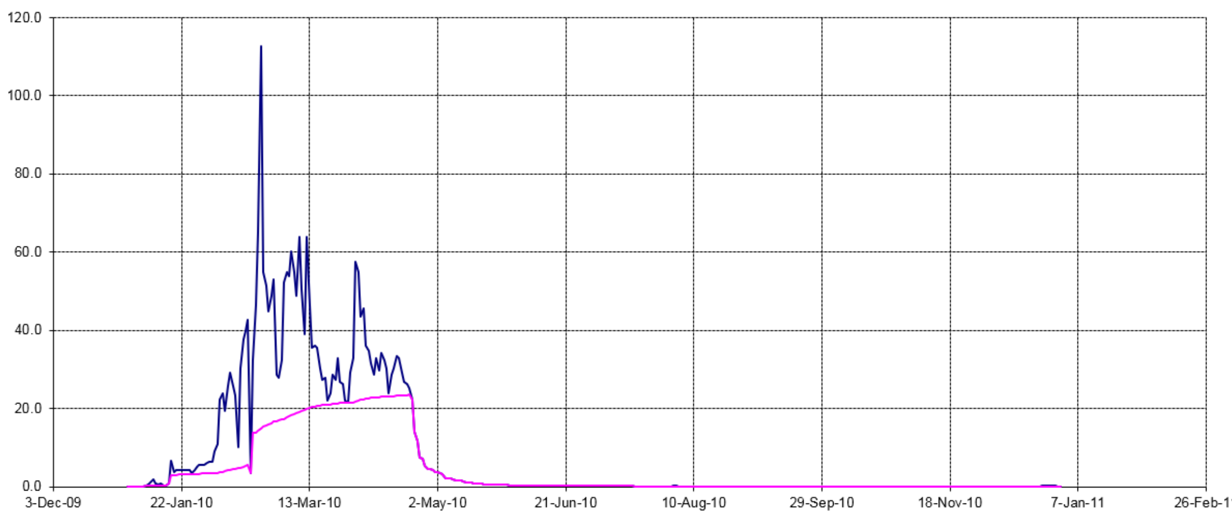

J. EGS11- Mugher at Muger

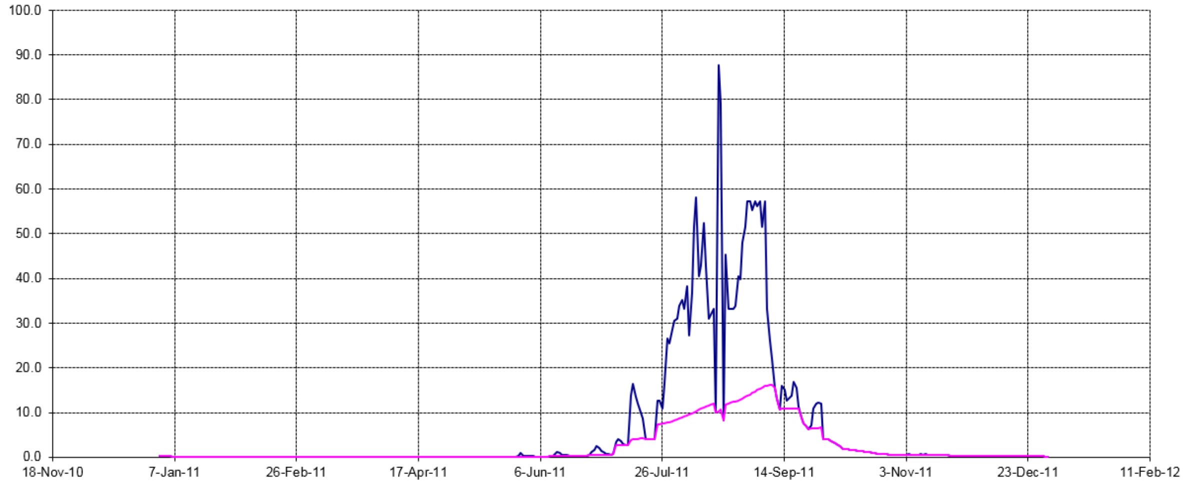

Appendix 10. List of published articles

1. Tadesse, E., Azagegn, T., Alemayehu, T. (2023). Characterizing groundwater and surface water interaction using geological, environmental tracers (222Rn, EC, δ18O, and δ2H) and baseflow index methods for part of the Upper Awash and the adjacent Blue Nile Basin, Ethiopia. J. Afr. Earth Sci. 205 (2023), 104992 https://doi.org/10.1016/j.jafrearsci.2023.104992.

Journal of African Earth Sciences 205 (2023) 104992

Contents lists available at ScienceDirect

Journal of African Earth Sciences

journal homepage: www.elsevier.com/locate/jafrearsci

Characterizing groundwater and surface water interaction using geological, environmental tracers (^{222}Rn, EC, $\delta^{18}O$, and $\delta^{2}H$) and baseflow index methods for part of the Upper Awash and the adjacent Blue Nile Basin, Ethiopia

Ephrem Tadesse[a,*], Tilahun Azagegn[b], Taye Alemayehu[a]

[a] Ethiopian Institute of Water Resources, Addis Ababa University, Addis Ababa, Ethiopia
[b] Department of Earth Sciences, Addis Ababa University, Addis Ababa, Ethiopia

ARTICLE INFO

Handling Editor: M Mapeo

Keywords:
Groundwater-surface water interaction
Environmental tracers
^{222}Rn
Baseflow
Awash Basin
Ethiopia

ABSTRACT

Characterization of groundwater-surface water interaction using a combined approach of geological, environmental tracers (^{222}Rn, EC, $\delta^{18}O$, and $\delta^{2}H$) and baseflow index in a complex geological environment was carried out for part of the Upper Awash and adjacent Blue Nile Basins. In this work, total measurements of 59 water samples were used (52 from different reaches of main Rivers and tributaries, 4 from springs, and 3 from boreholes) for ^{222}Rn analysis in dry and wet seasons, along with recent 8–20 years of daily stream flow records from 11-gauge stations. For sub-surface inference, regional geological structures and lineament density zones were determined using Kriging interpolation techniques. ^{222}Rn values for the river and streams show 2.7–468 Bq/m^3 during the rainy season and 17.1–1467 Bq/m^3 for the non-rainy season. The credible justification related to moderate to high seasonal ^{222}Rn values (100–400 Bq/m^3) in the upstream parts of the two Basins, including areas falling along the surface water divide between the two adjacent Basins, shows a link between groundwater and surface water systems. In the same area, a very high mean annual baseflow index (BFI >0.5) is dominantly associated with high lineament density (0.9 < LD < 3.0), regional faults, and geologic units of highly permeable scoriaceous basalt, rift basalt, and fractured ignimbrite units. Relatively, low ^{222}Rn (<100 Bq/m^3) in both seasons and low baseflow index (BFI <0.35) values mainly in the central part of the Upper Awash basin are attributed to existing impervious superficial deposits (alluvial, tuff and ash). This, in turn, shows the poor connection between the groundwater and surface water systems in the central plain part of the Upper Awash Basin and, as also evidenced by the storage of floodwater for an extended time after the end of the rainy season, prove poor connectivity between groundwater and surface water systems. The very high ^{222}Rn (400–1467 Bq/m^3) with varied mean annual baseflow index (0.35 < BFI <0.5) at different stations in the extreme southern and southeastern parts of the Upper Awash Basin show Awash River is gaining from the aquifer system through highly fractured basalt and fractured ignimbrite geologic units. Evidence from analysis of measured electrical conductivity and stable isotopes ($\delta^{18}O$, $\delta^{2}H$) generally agree with the observed ^{222}Rn value and baseflow analysis.

2. Tadesse, E., Azagegn, T., Alemayehu, T. (2024). Identifying recharge areas for the upstream portion aquifers of Awash Basin, Ethiopia. Journal of Hydrology: Regional Studies 54 (2024) 101890 https://doi.org/10.1016/j.ejrh.2024.101890.

Journal of Hydrology: Regional Studies 54 (2024) 101890

Contents lists available at ScienceDirect

ELSEVIER

Journal of Hydrology: Regional Studies

journal homepage: www.elsevier.com/locate/ejrh

Identifying recharge areas for the upstream portion aquifers of Awash Basin, Ethiopia

Ephrem Tadesse[a,*], Tilahun Azagegn[b], Taye Alemayehu[a]

[a] Ethiopian Institute of Water Resource, Addis Ababa University, Addis Ababa, Ethiopia
[b] School of Earth Sciences, Addis Ababa University, Addis Ababa, Ethiopia

A R T I C L E I N F O

Keywords:
Aquifers
Recharge area
Groundwater chemistry
Stable isotopes
Part of the Upper Awash Basin
Ethiopia

A B S T R A C T

Study area: The western and eastern flanks of Ethiopia's Awash and Abay Basins, respectively.
Study focus: Identifying recharge zones of the main aquifers in the Upper Awash Basin, which are water resources targeted for long-term sustainable use. In this work, lithohydrostratigraphic concepts with fracture density, hydrogeochemical and stable isotopic insights were applied using information from 94 water-supply wells, 188 geoelectrical resistivity, 124 hydrochemistry, and 81 stable isotopic data sets.
New hydrogeological insights of the area: The results illustrate that recharge of superficial deposits and Rift basalt aquifers is from modern precipitation and from nearby streams/rivers through fractures, which is exemplified by mixed $CaHCO_3$ or $CaMgHCO_3$ water types of low TDS (<200 mg/l), high Ca/Na ratio (>5), low RA (<2.0), enriched isotopic signature, and high deuterium excess (13.3). Seepage from the overlying aquifers, as well as direct precipitation in locations where the unit is exposed, form the mechanisms of recharge for fractured ignimbrite aquifer. The highland and transition areas are dominantly the recharge areas for the regional scoriaceous basalt aquifer. These areas have high fracture density ($0.96<FD<3.0$ km/km^2), mineralized $NaHCO_3$ water type, high TDS (>468 mg/l), low Ca/Na ratio (<1), high RA (>2.0), highly depleted isotopic signals, and low deuterium excess (<11) relative to the Local Meteoric Water Line. The results also reveal groundwater flux from the adjacent eastern flank of Abay Basin.

Appendix 11. Communications

A. Paper presented during the 9th Ethiopian Geoscience and Mineral Engineering Association (EGMEA) Congress with Theme. The Role of Geoscience and Mining for Sustainable Socio-economic Development (August 2-3, 2024)


ETHIOPIAN GEOSCIENCES AND MINERAL ENGINEERING ASSOCIATION

Certificate

AWARDED TO

Ephrem Tadesse

In recognition of presenting a paper entitled "**Characterizing Groundwater and Surface Water Interaction Using Geological, Environmental Tracers (222Rn, EC, δ18O, and δ2H) and Baseflow Index Methods for part of the Upper Awash and the Adjacent Blue Nile Basin, Ethiopia**" at the Ninth EGMEA Congress held in the FDRE Ministry of Mines, Addis Ababa from 2-3 August 2024.

Tarekegn Tadesse
President, EGMEA

B. Paper presented during **AAU Research Week (May 09-12, 2022)** in Addis Ababa University. Ethiopian Institute of Water Resources.

Characterizing groundwater and surface water interaction using geological, environmental tracers (^{222}Rn, EC, δ^{18}O, and δ^{2}H) and Baseflow index methods for part of the Upper Awash and the adjacent Blue Nile Basin, Ethiopia

Appendix 12. Signed plagiarism check

turnitin Page 1 of 232 - Cover Page Submission ID trn:oid:::1:3227143226

Ephrem Tadesse

final paper

Hydro chem

Mr Ephrem

Addis Ababa Science and Technology University

Document Details

Submission ID

trn:oid:::1:3227143226

Submission Date

Apr 24, 2025, 12:09 PM GMT

Download Date

Apr 24, 2025, 5:00 PM GMT

File Name

Draft_Final13.pdf

File Size

10.3 MB

209 Pages

64,728 Words

322,514 Characters

17% Overall Similarity

The combined total of all matches, including overlapping sources, for each database.

Filtered from the Report

- Bibliography

Exclusions

- 3 Excluded Sources
- 219 Excluded Matches

Match Groups

- **698Not Cited or Quoted 14%**
  Matches with neither in-text citation nor quotation marks
- **142Missing Quotations 3%**
  Matches that are still very similar to source material
- **3 Missing Citation 0%**
  Matches that have quotation marks, but no in-text citation
- **0 Cited and Quoted 0%**
  Matches with in-text citation present, but no quotation marks

Top Sources

13%	Internet sources
12%	Publications
2%	Submitted works (Student Papers)

Integrity Flags

1 Integrity Flag for Review

- **Replaced Characters**
  163 suspect characters on 43 pages
  Letters are swapped with similar characters from another alphabet.

Our system's algorithms look deeply at a document for any inconsistencies that would set it apart from a normal submission. If we notice something strange, we flag it for you to review.

A Flag is not necessarily an indicator of a problem. However, we'd recommend you focus your attention there for further review.